

In-flight Calibration of Space-borne Magnetometers

Ph.D. Thesis

by
Hannes Karl Leinweber

Graz University of Technology
December 2011

External Advisor: Prof. Christopher T. Russell,
Institute of Geophysics and Planetary Physics at
University of California, Los Angeles

1st Advisor: Prof. Klaus Torkar
Graz University of Technology and
Austrian Academy of Sciences, Space Research Institute

2nd Advisor: Prof. Martin Friedrich
Graz University of Technology

Acknowledgments

I would like to express my deep and sincere gratitude to my external Ph.D. advisor Professor Christopher T. Russell for his guidance. This thesis would not exist without his well meaning support and advice.

I also would like to thank Professor Vassilis Angelopoulos for his support on THEMIS related topics of this thesis.

Furthermore, I would like to thank my advisors from Graz University of Technology, Professors Klaus Torkar and Martin Friedrich for their support and for allowing me to have an external advisor.

Additionally, I would like to thank Professor Krishan K. Khurana for introducing me to the field of “In-flight calibration of space-borne magnetometers” and for his scientific input on Chapter 3.

I would like to express my deepest gratitude to my wife Anita, for always standing by me during difficult times and to my little son Mika for shining light into our lives.

Abstract

Calibration parameters of space-borne magnetometers can change in-flight, compared to their values that were measured on ground before launch. This thesis contains a variety of methods for recovering calibration parameters in-flight. The theory of previously published methods for finding magnetometer zero levels inside the interplanetary magnetic field has been generalized and an improved method that provides error estimates is presented. Furthermore, a new method for finding zero levels and their error estimates, inside the low field regions of a magnetosphere is described. Three improvements on in-flight orthogonalization of sensor triads on spinning spacecraft are presented. First, the existing equations have been improved, so that they converge for large errors in the spin axis tilt angles. Second, a new method for orthogonalization of sensor triads onboard fast moving and slow spinning spacecraft where FFT based methods do not work is introduced. Third, a method for recovering short term variations of calibration parameters is described. Methods for recovering calibration parameters via comparisons with model fields for spinning, as well as three axis stabilized spacecraft are provided. Magnetometer calibration has been combined with attitude determination for spinning spacecraft. Additionally, a method that allows recovering attitude, calibration parameters and varying spin angle corrections is described, which is especially important for eclipsed periods of spacecraft that only have a Sun sensor. A new method for finding spin axes offsets via comparison of accurate measurements of the field magnitude is presented, that additionally matches the gains of the two instruments that are being compared. The technique has been applied to EDI and FGM data for the Cluster 3 satellite and EDI noise distributions were analyzed. Results of minimizing curl and divergence of the magnetic field via adjustment of calibration parameters are presented, using data measured by the four Cluster satellites inside the tail lobes with equations that are an order of magnitude shorter than the previously published ones.

Kurzfassung

Kalibrierparameter von Magnetometern, die sich auf Raumsonden befinden, können sich im Flug ändern, sodass sie von den Werten, die vor dem Start gemessen wurden abweichen. Diese Dissertation beinhaltet eine Reihe von Verfahren, die dazu dienen, Kalibrierparameter im Flug neu zu berechnen. Die Theorie von bereits publizierten Methoden, die dazu verwendet werden um Offsets im interplanetaren Raum zu bestimmen, wurde vereinheitlicht und eine neue Methode, die auch Fehlerabschätzungen beinhaltet, wird präsentiert. Zusätzlich wurde eine neue Methode entwickelt, mit der man Offsets und deren Fehlerabschätzungen, in den Regionen innerhalb der Magnetosphäre, die niedriges Feld aufweisen, bestimmen kann. Drei Verbesserungen von Methoden zur Orthogonalisierung von dreiachsigem Sensoren, die sich auf rotierenden Raumsonden befinden, wurden entwickelt. Erstens: Die Gleichungen wurden so geändert, dass sie auch bei grösseren Neigungswinkeln der Rotationsachse konvergieren. Zweitens: Eine Methode wurde entwickelt, die auch bei langsam rotierenden und schnellen Raumsonden funktioniert, wo Methoden die auf FFT basieren nicht funktionieren. Drittens: Eine Methode wurde entwickelt, die kurzzeitige Schwankungen der Kalibrierparameter bestimmen kann. Methoden um Kalibrierparameter von Vergleichen mit dem Erdmagnetfeldmodell zu bestimmen werden präsentiert für rotierende und für dreiachsenstabilisierte Raumsonden. Die Berechnung von Kalibrierparametern wurde mit der Berechnung der Ausrichtung einer Raumsonde kombiniert. Zusätzlich wurde eine Methode entwickelt die, die Ausrichtung, Kalibrierparameter und zeitlich veränderliche Korrekturen des Sonnenwinkels bestimmt. Das ist insbesondere für Raumsonden die nur einen Sonnensensor haben wichtig, wenn sie sich im Schatten (z.B. Erdschatten) befinden. Eine Methode zur Bestimmung des Rotationsachsen-Offsets durch Vergleich mit genauen Messungen der totalen Feldstärke, die auch den Verstärkungsfaktor der beiden Instrumente abgleicht, wird präsentiert. Diese Methode wurde mit Daten von EDI und FGM (auf dem Cluster 3 Satelliten) angewandt und auch die Verteilungen des Rauschens von EDI wurde untersucht. Resultate vom Minimierungen (durch Kalibrierparameter) von Rotor und Divergenz der Magnetfelder werden präsentiert, mit Daten von den vier Cluster Satelliten, die innerhalb des Magnetfeldschweifes gemessen wurden. Die Minimierungen wurden mit Hilfe von Gleichungen die um Faktor 10 kürzer sind als die, die bisher publiziert wurden bewirkt.

Table of Contents

1.	Introduction	1
1.1.	Basic Equations	2
1.2.	Magnetic Field Measuring Techniques	4
1.2.1.	Scalar Magnetometers	4
1.2.1.1.	Proton Precession Magnetometer	4
1.2.1.2.	Overhauser Magnetometer	4
1.2.1.3.	Optically Pumped Magnetometers	5
1.2.2.	Vector Magnetometers	6
1.2.2.1.	Search Coil Magnetometer	6
1.2.2.2.	Fluxgate Magnetometer	6
1.2.2.3.	Vector Helium Magnetometer	6
1.2.2.4.	Coupled Dark State Magnetometer	7
1.2.3.	Comparison of Space-borne Magnetometers	7
1.3.	The Interplanetary Magnetic Field	8
1.4.	Planetary Magnetic Fields	12
1.4.1.	Earth's Geomagnetic Field	12
1.4.2.	Internal Magnetic Fields of Other Planets	13
1.4.3.	Internal Magnetic Field of Ganymede	15
1.5.	Solar System Magnetospheres	16
1.5.1.	Earth's Magnetosphere	17
1.5.2.	Magnetospheres of Other Planets	19
1.5.3.	Other Magnetospheres	21
1.6.	Space Weather	23
1.6.1.	Reconnection	24
1.6.1.1.	Northward IMF	24
1.6.1.2.	Southward IMF	25
1.6.1.3.	Substorm	25
1.6.2.	Slow and Fast Solar-wind Streams	27
1.6.3.	Coronal Mass Ejection (CME) Events	27
1.6.4.	Flares and Solar Energetic Particles (SEP)	27
1.6.5.	Geomagnetic Storms	27
1.6.6.	Galactic Cosmic Rays	29
1.6.7.	Consequences of Space Weather	29
1.6.8.	Space Weather Forecasting	31
1.7.	Historical Overview and Magnetometer Configurations	32

1.8.	Introduction to Calibration of Space-borne Magnetometers	37
1.8.1.	Ground Calibration and Magnetic Cleanliness	37
1.8.2.	Calibration Parameters and In-flight Calibration of Space-borne Magnetometers from Natural Constraints and Comparisons to Model Fields (Thesis Overview)	40
1.8.2.1.	Summary	44
2.	In-flight Determination of Magnetometer Zero Levels	45
2.1.	Introduction	45
2.2.	An Advanced Approach to Finding Magnetometer Zero Levels in the Interplanetary Magnetic Field	46
2.2.1.	Belcher's Method	47
2.2.2.	Hedgecock Method	48
2.2.3.	Davis-Smith Method	50
2.2.4.	Mathematical Insights on the Davis-Smith Equation	52
2.2.4.1.	Derivation of the Davis-Smith Equation using Correlations	52
2.2.4.2.	Davis-Smith Equation for First Differences	53
2.2.4.3.	Davis-Smith Equation for Filtered Data	54
2.2.4.4.	Mathematical Superiority of the Davis-Smith Equation	56
2.2.5.	Selection Criteria for the Davis-Smith Method	57
2.2.5.1.	First Selection Criterion	64
2.2.5.2.	Second Selection Criterion	64
2.2.5.3.	Third Selection Criterion	64
2.2.5.3.1.	Making the Third Selection Criterion Robust	65
2.2.6.	Windowing	66
2.2.7.	Combination of Data-windows and Overall Inversion	68
2.2.8.	Monte Carlo Simulation	69
2.2.9.	Application of the Algorithm to Space-borne Magnetometer Data	70
2.3.	An Advanced Approach to Finding Magnetometer Zero Levels Inside the Low-field Regions of a Magnetosphere	78
2.3.1.	Introduction	78
2.3.2.	Algorithm	81

2.3.2.1.	Criteria: First Category	81
2.3.2.2.	Criteria: Second Category	82
2.3.2.3.	Overall Inversion and Monte Carlo Simulation	84
2.3.2.4.	Application	85
2.4.	Conclusions	87
3.	Orthogonalization of a Sensor Triad on Spinning Spacecraft	88
3.1.	Introduction	88
3.2.	Removal of Spin Harmonics via Fourier Transforms	95
3.2.2.	Least Squares Inversions and Iterations	96
3.2.3.	Application of the Technique	97
3.3.	Removal of Spin Harmonics for Fast Changing Magnetic Fields (Envelope-Method)	100
3.3.1.	Introduction	100
3.3.2.	Algorithm	101
3.3.3.	Application of the Envelope-Method	102
3.4.	Resolving Short Term Variations in the Calibration Parameters via Spin Tone Removal	103
3.4.1.	Introduction	103
3.4.2.	Equations and Algorithm	103
3.4.3.	Application of the Technique to Cluster Data	107
3.5.	Conclusions	112
4.	Comparison with Model Fields	113
4.1.	Transformation of Model Fields into Spacecraft Coordinates	114
4.1.1.	Spinning Spacecraft (Transformation to Spacecraft Coordinates)	114
4.1.2.	Three Axis Stabilized Spacecraft (Transformation to Spacecraft Coordinates)	115
4.2.	Spinning Spacecraft (Model Comparison)	116
4.2.1.	Application to Galileo's Second Earth flyby	117
4.3.	Three Axis Stabilized Spacecraft (Model Comparison)	118
4.3.1.	Application to STEREO Data	120
4.4.	Attitude Determination of a Spinning Spacecraft (First Method)	121

4.4.1.	Attitude Determination of a Spinning Spacecraft with Variable Phase Angle Correction (Second Method)	122
4.4.2.	Application to Polar Data with Constant Phase Corrections	124
4.4.3.	Application to THEMIS Data with Variable Phase Corrections	127
4.5.	Conclusions	129
5.	Calibration of Triaxial Fluxgate Magnetometers from Accurate Measurements of the Field Magnitude	130
5.1.	Measuring Scalar Magnetic Fields with the <u>Electron Drift Instrument</u> (EDI)	131
5.2.	Calibration of a Triaxial Magnetometer with the Electron Drift Instrument (EDI) Onboard a Spinning Spacecraft	134
5.3.	Conclusions	147
6.	Precise Calculation of Current Densities via Four Spinning Spacecraft in a Tetrahedron Configuration	148
6.1.	Application to Cluster Data	154
6.2.	Conclusions	156
7.	Discussion and Future Work	157
7.1.	Chapter 2.2	157
7.2.	Chapter 2.3	158
7.3.	Chapter 3	158
7.4.	Chapter 4	159
7.5.	Chapter 5	159
7.6.	Chapter 6	159
Appendix A		A1
Appendix B		A3
Appendix C		A6

References

List of Figures

Figure 1.1. The “Parker Spiral” in the solar equatorial or ecliptic plane. The spirals are magnetic field lines that start out radially and make a large angle to the radial direction by the time they reach 1AU (the dotted circle). Arrows added to the field directions indicate their polarity at the Sun. The pluses designate outward-directed (positive) fields and the minuses inward-directed (negative) fields. The field lines divide the circle into two magnetic ‘‘sectors’’. Two of the spirals are the boundaries between the sectors (designated S/B for sector boundary). The straight lines emanating from the Sun at the center are radial solar-wind velocity vectors with speeds of 300 km/s (considered slow wind today). Taken from Smith (2007).

Figure 1.2. Interaction of fast and slow solar wind that form a so-called corotating interaction region. Adapted from Russell (2001).

Figure 1.3. Heliospheric current sheet near the Sun. The magnetic axis is tilted with respect to the rotation axis. Taken from Smith (2007).

Figure 1.4. Artist’s view of the heliosphere, (the magnetosphere of our Sun) carved by the solar wind into the flow of the interstellar medium. Taken from Blanc (2005).

Figure 1.5. Rate of change of declination at Greenwich (GRW), Abinger (ABN), Hartland (HAD), Eskdalemuir (ESK) and Lerwick (LER) observatories 1900-2008. Courtesy of British Geological Survey.

Figure 1.6. The relative geometries of the solar-wind direction (opposite to vector \mathbf{R} here), planetary spin vectors $\mathbf{\Omega}$ and dipole moments \mathbf{M} are illustrated in this figure for Earth, Mercury and the giant planets. They play an important role in the way solar-wind forcing and planetary motion interplay to determine a global pattern of plasma and magnetic flux circulation in each magnetosphere. In addition the planetary obliquity angle determines the importance of seasonal variations in magnetospheric phenomena, and the angle between \mathbf{M} and $\mathbf{\Omega}$ determines the importance of diurnal variations in magnetospheric flows. Taken from Blanc (2005).

Figure 1.7. Earth’s magnetosphere. Adapted from Parks (1991).

Figure 1.8. Magnetospheric current systems. Modified from Kivelson and Russell (1995).

Figure 1.9. Induced magnetosphere of Venus. Taken from Zhang et al. (2008).

Figure 1.10. Magnetosphere of Mercury. Taken from Kivelson (2007).

Figure 1.11. Giant magnetospheres. Taken from Bennet (2004).

Figure 1.12. Magnetosphere of Ganymede. Taken from Kivelson (2007).

Figure 1.13. Effects of space weather. Adapted from Lanzerotti et al. (1997).

Figure 1.14. The reconnecting magnetosphere for northward (top panel) as well as southward IMF (bottom panel). The points labeled “N” are neutral points where the magnetic field goes to zero (also called X-points). Straight arrows show regions with accelerated flow. Taken from Russell (2007).

Figure 1.15. Dynamics of a magnetospheric substorm. Depicted is the noon-midnight meridian. Taken from Russell (2007).

Figure 1.16. The top panel shows the Dst-index a ICME storm during solar maximum. The bottom panel shows a geomagnetic storm caused by a co-rotating interaction region during solar minimum. Taken from Tsurutani (2000).

Figure 1.17. Magnetic field strength (top panel) and cosmic ray intensity (bottom panel) at the termination shock as measured by the Voyager 1 spacecraft. Taken from Burlaga et al. (2005).

Figure 1.18. Curves 1 and 2 represent calculated magnetic field models along the trajectory from two different magnetic field models. Curve 3 (short dashes) represents the measured and corrected magnetic field data. Curve 4 represents the height of the spacecraft. Curve 5 represents the measured (uncorrected) data (Dolginov et al., 1962).

Figure 1.19. Some of the first precise measurements of the interplanetary magnetic field. The top three panels show the magnetic field in the two angle representation and the bottom three panels show the variance of the solar ecliptic components (Ness et al., 1964).

Figure 1.20. Magnetometer configuration on the ATS-1 satellite (Barry and Snare 1966).

Figure 1.21. Helmholtz coil system for ground calibration (Photo: Imperial College, London).

Figure 1.22. Gradiometer setup for magnetic measurements on spacecraft sub-systems (as used for the Rosetta Lander magnetic cleanliness program).

Figure 2.1. Relationship between the actual field magnitude B_{t_A} , the measured field magnitude B_{t_M} and the offset O .

Figure 2.2. Artificially generated data that contain pure rotations while the field strength B_t is smoothly and slightly non-linearly decreasing.

Figure 2.3a. A short example of STEREO-A data in the spacecraft coordinate system. The thin black lines are the magnetic field magnitude and its negative value plotted on the same scale to illustrate when the field was largely along or orthogonal to the sensors. The zero levels are incorrect. $O_1=1$ nT, $O_2=-1$ nT and $O_3=2$ nT.

Figure 2.3b. Same data as in Figure 2.3a but rotated into the minimum variance coordinate system to show that there is variance along all three axis of the principal coordinate system. The square roots of the eigenvalues (same as standard deviations in the minimum variance coordinate system) are given in descending order: 3.03 nT, 0.48 nT and 0.38 nT.

Figure 2.3c. Squared magnitude (B_t^2) versus component plots. The averages have been subtracted to center the plots at the origin.
 Gray: before zero Levels have been applied.
 Black: after zero levels have been applied.

Figure 2.3d. Black: O_1 is incorrect whereas O_2 and O_3 are correct. This causes a slope with gradient of $2O_1$ that is close to linear. $O_1=1$ nT.
 Gray: O_1 and O_3 are incorrect whereas O_2 is correct. The introduction of an offset in another component causes a highly nonlinear slope. $O_1=1$ nT and $O_3=2$ nT.

Figure 2.3e. The data in Figure 2.3a after the zero levels have been applied. The thin black traces are the mirrored field magnitude. The variance of the squared magnitude (thin black traces) has been greatly reduced compared to Figure 2.3a confirming that the variances in the component axes are mostly rotational.

Figure 2.4. A theoretical example of a pure compression. Magnitude squared versus the component along which there is a pure compression. For this example I chose the other two components (B_1 and B_2) to be zero.

Black: upper and lower quartile of B_3 .
 The straight slopes represent twice the offsets that would be calculated using only the upper and lower quartile. The difference of those offsets is used for the third selection criterion (the linearity criterion).

Figure 2.5. Magnetic field data of STEREO-A as it passes through the interior of an ICME. Shown in black are the outputs of the three magnetometer sensors at 1 sec resolution. The light gray lines are the magnetic field magnitude B_t and its negative value plotted on the same scale to illustrate when the field was largely along or orthogonal to the sensors. Zero-phase high-pass filtering is applied on these data before the zero level determination algorithm. The filter is a fourth order (eighth order when zero-phase filtering) butterworth-type filter with a cutoff frequency of 8.9 mHz.

Figure 2.6. Example of spin averaged THEMIS-B data. The roughly 7 hour long subset that is marked in gray has been used as input for an offset calculation. B_3 represents the spin-plane component. The spin period of the THEMIS spacecraft is roughly 3 sec.

Figure 2.7a. Example of detection of changing offsets using four days of Venus Express data. The input data are unfiltered. The horizontal lines show the timeframe for a particular offset estimate. The vertical black lines represent the error bars for the offset estimates.

Figure 2.7b. Example of detection of changing offsets using four days of Venus Express data. The input data are high-pass filtered using a cutoff frequency of 8.9 mHz. The horizontal lines show the timeframe for a particular offset estimate. The vertical lines represent the error bars for the offset estimates.

Figure 2.8. Example of an interval consisting of four magnetic field vectors in the XZ-plane. The black vectors are all aligned and represent a pure change of field magnitude. The red arrows introduce a change of the zero level along the Z-axis. The blue vectors are the result of the changed zero level. Thus the blue vectors do not have uniform direction.

Figure 2.9. Example of mirror-mode waves as observed by the THEMIS-B spacecraft.

Figure 2.10. Example of drift mirror-mode waves as observed by the THEMIS-B spacecraft.

Figure 2.11. THEMIS-A magnetic field data. The area highlighted in gray is one independent interval that was chosen by the algorithm. B_{12} (4th panel) is the sum of the squares of the spin plane components.

Figure 2.12. THEMIS-B magnetic field data. The area highlighted in gray is one independent interval that was chosen by the algorithm. B_{12} (fourth panel) is the sum of the squares of the spin plane components.

Figure 3.1. Definition of the six angles that are required to calibrate a magnetometer.

Figure 3.2. Example of Cluster magnetic field data that were measured in 3 different ranges (magnetometer gains).

Figure 3.3. First and second harmonics in a spin plane component for three different ranges (magnetometer gains).

Figure 3.4. First harmonics in the spin axis component for three different ranges (magnetometer gains).

Figure 3.5. Removed spin tone in one of the spin plane components. Shown are data that cover three different ranges (magnetometer gains).

Figure 3.6. Removed spin tone in the spin axis component. Shown are data that cover three different ranges (magnetometer gains).

Figure 3.7. Magnetic field data in non-orthogonal despun spacecraft coordinates as measured by the Galileo spacecraft during its second Earth flyby.

Figure 3.8. The first and second panels show magnetic field values that contain spin harmonics plus envelopes. The bottom panel shows the amplitudes of the spin harmonics as calculated from the envelopes.

Figure 3.9. Magnetic field data in non-orthogonal despun spacecraft coordinates as well as in orthogonolized (red) despun spacecraft coordinates (measured by the Galileo spacecraft during its second Earth flyby).

Figure 3.10. Cluster-3 magnetic field data in range 4 (range 4: ± 1024 nT).

Figure 3.11. Dynamic amplitude spectrum of Cluster-3 data after application of a single set of calibration parameters, in despun spacecraft coordinates (spin plane component).

Figure 3.12. Dynamic amplitude spectrum of Cluster-3 data after application of a single set of calibration parameters, in despun spacecraft coordinates (spin plane component).

Figure 3.13. Dynamic amplitude spectrum of Cluster-3 data after application of a single set of calibration parameters, in despun spacecraft coordinates (spin axis component).

Figure 3.14. Time varying calibration parameters that are required to completely remove faint spin harmonics. The vertical labels of the top two panels (O_1' and O_2') are a simplification. The fully correct labels should be $B_z \Delta \theta_1 + O_1'$ and $B_z \Delta \theta_2 + O_2'$ which leads to altogether eight time varying parameters.

Figure 3.15. Dynamic amplitude spectrum of Cluster-3 data after application of a single set of calibration parameters, plus time varying calibration parameters, in despun spacecraft coordinates (spin plane component).

Figure 3.16. Dynamic amplitude spectrum of Cluster-3 data after application of a single set of calibration parameters, plus time varying calibration parameters, in despun spacecraft coordinates (spin plane component).

Figure 3.17. Dynamic amplitude spectrum of Cluster-3 data after application of a single set of calibration parameters, plus time varying calibration parameters, in despun spacecraft coordinates (spin axis component).

Figure 4.1. Galileo's second Earth flyby: Top two panels show the field magnitude and the field values of the three components. The bottom three panels show the residuals in percent of the field magnitude.

Figure 4.2. The top panel shows the perigee pass of STEREO-B with the closest magnetic field measurements to Earth. The bottom three panels show the residuals of the Earth field comparison in percent of the field magnitude.

Figure 4.3. Required rotations for transformation into spacecraft coordinates.

Figure 4.4. Combined results from the first and second methods. The quantities $d\varphi_{12}$, $dRAS$ and $dDEC$ are in degree and dO_3 is in nano Tesla.

Figure 4.5. A perigee pass with only ~ 25 min of data. The second and third component are similar in shape (panels 2 and 3). Data are black and the model is red.

Figure 4.6. Data (black) and the model (red) before calibration with the second method. The required time varying correction to the phase angle ($d\varphi_{12}$) is given in degree.

Figure 4.7. Data (black) and the model (red) after calibration with the second method. The black traces are below the red traces.

Figure 5.1. The basic operating principle of an electron drift instrument.

Figure 5.2. The triangulation process.

Figure 5.3. Comparison of EDI magnetic field magnitude and FGM magnetic field magnitude (red) at ~ 88 nT.

Figure 5.4. Comparison of EDI magnetic field magnitude and FGM magnetic field magnitude (red) at ~ 325 nT. EDI changes ranges at 325 nT.

Figure 5.5. Comparison of EDI magnetic field magnitude and FGM magnetic field magnitude (red) at ~ 590 nT.

Figure 5.6. Number of EDI measurements per bin.

Figure 5.7. RMS differences between EDI and FGM per bin (before calibration).

Figure 5.8. Histograms of differences between EDI and FGM (before calibration).

Figure 5.9. Line fit across all the mean differences between EDI and FGM of all the bins (before calibration).

Figure 5.10. RMS differences between EDI and FGM for each bin after minimum search.

Figure 5.11. Histograms of differences between EDI and FGM (after calibration).

Figure 5.12. Line fit across all the mean differences between EDI and FGM of all the bins (after calibration).

Figure 5.13. Zero level calculations for fields smaller 120 nT. The data were binned to 10 bins with equal number of points. The data in the first bin were measured before the data in the second bin and so forth.

Figure 6.1. Blue: best effort calibration; Red: best effort calibration plus inter spacecraft calibration. The top panel shows a comparison of current density before and after inter spacecraft calibration. The second panel shows a comparison of divergence before and after inter spacecraft calibration. The third panel shows B_x and the bottom panel shows the inter spacecraft distances from a principal coordinate system. The three traces are largest, intermediate and smallest spacecraft distance.

Figure B.1. Six differences before zero level matching, of three components of four Cluster spacecraft (one component per panel).

Figure B.2. Six differences after zero level matching, of three components of four Cluster spacecraft (one component per panel).

List of Tables

Table 1.1. *Typical specifications of space-borne magnetometers.*

Table 1.2. *Planetary data. Adapted from Kivelson (2007).*

Table 1.3. *Advances to the field of in-flight calibration of space-borne magnetometers.*

Table 2.1. *Three examples of empirically determined criteria used in calculations. STEREO is a dual-spacecraft mission with three-axis stabilization where the zero levels of all three component axes need to be calibrated. THEMIS is a five-spacecraft mission with spin stabilization where only the zero level of the component that lies along the spin axis needs to be calculated. Venus Express (VEX) is a three-axis stabilized spacecraft.*

Table 2.2a. *Example of STEREO-B zero level calculations for day 224, of 2007. For the filtered case the cutoff frequency of the high-pass filter is 3.3 mHz. The fields that are marked in gray represent violations of criteria which lead to dismissal of O_1 from the filtered case and the dismissal of O_3 from both cases. The full set of selection criteria is given in Table 2.1.*

Table 2.2b. *Rerun of the algorithm in order to solve for O_3 . Before I performed the rerun I applied the corrected zero levels O_1 and O_2 as given in Table 2.2a to the input data.*

Table 2.3. *Example of a zero level calculation for THEMIS-B. For the filtered case the cutoff frequency of the high-pass filter is 3.3 mHz. The full set of selection criteria is given in Table 2.1.*

Table 2.4. *Table of results.*

Table 4.1. *Thresholds for interpreting the Monte Carlo simulation.*

Table 5.1. *Results of various fits.*

1. Introduction

The spirit of exploration is an important characteristic of modern human societies. Inspiring new discoveries through space exploration increase knowledge, imagination and thus human capabilities.

Our home star, the Sun provides energy input via radiation to sustain the terrestrial biosphere. Our Sun also generates magnetic fields and emits plasma. A plasma is a gas of charged particles having equal numbers of free positive and negative charge carriers. The Sun's emitted plasma is called solar-wind plasma and travels away from the Sun far beyond the known planets of our solar system. The solar-wind plasma is highly conducting and carries along the Sun's magnetic field. The region in interstellar space that is filled with solar-wind plasma and its accompanying magnetic field (interplanetary magnetic field) is called heliosphere. Solar-wind plasma travels from the Sun to Earth typically within several days. Earth has an internal magnetic field also called a planetary magnetic field that is generated by flow patterns in the conducting liquid of its core similar to a Faraday's disk dynamo. The interaction of the solar-wind plasma with the Earth's magnetic field forms a cavity called the Earth's magnetosphere. The interplanetary environment that is created and influenced by the Sun is highly variable and has effects on Earth as well as in space. Such effects can cause telecommunication problems, power outages, malfunctioning electronic systems, satellite damage, radiation hazards to astronauts and airline passengers as well as effects on biological systems on the surface of Earth. Long term variability of the interplanetary environment may cause climate changes. Recent studies have proposed a relevant connection of solar combined with cosmic ray activity to Earth's climate. A positive effect is the generation of beautiful auroras.

Space-borne magnetometers are devices that are carried by spacecraft to measure magnetic fields in space. Typically the sensors of such magnetometers are mounted on a boom so that the influence of spacecraft generated magnetic fields at the location of the sensor is minimized. It is possible to check important performance parameters of such magnetometers (calibration parameters) by examination of the very data that the magnetometer transmitted back to Earth. How this can be done in different environments in the magnetized plasmas of the solar system is the underlying theme of this dissertation.

1.1. Basic Equations

Charged particles at rest cause an electrostatic field which is the origin of the Coulomb force.

$$\mathbf{F}_C = q\mathbf{E}$$

E	electrostatic field
<i>q</i>	single point charge
F_C	Coulomb Force

Charged particles in motion are current elements that generate a magnetic field which is the origin of the Lorentz force.

$$\mathbf{F}_L = q(\mathbf{v} \times \mathbf{B})$$

v	velocity of the charged particle
B	magnetic induction

The equation of motion for a single point charge in the presence of Coulomb and Lorentz forces is

$$m \frac{d\mathbf{v}}{dt} = q(\mathbf{E} + \mathbf{v} \times \mathbf{B})$$

<i>m</i>	particle mass
<i>t</i>	time

The coupling between electric and magnetic fields can be expressed by two of Maxwell's equations namely, Ampere's and Faraday's law.

$$\nabla \times \mathbf{B} = \mu_0 \mathbf{j} + \epsilon_0 \mu_0 \frac{\partial \mathbf{B}}{\partial t} \quad \text{Ampere's law}$$

j electric current density

$$\nabla \times \mathbf{E} = - \frac{\partial \mathbf{B}}{\partial t} \quad \text{Faraday's law}$$

As one can see from Ampere's and Faraday's laws the electric and the magnetic fields are coupled via their spatial as well as their temporal variations. The above equations need to be supplemented by two more of Maxwell's equations namely the Gauss's law for magnetism and the Gauss's law.

$$\nabla \cdot \mathbf{B} = 0$$

Gauss's law for magnetism

$$\nabla \cdot \mathbf{E} = \frac{\rho}{\epsilon_0}$$

Gauss's law, often called Poisson equation

ρ electric space charge density (see below)

Gauss's law for magnetism means that magnetic field lines are always closed. This statement is equivalent to the statement that magnetic monopoles do not exist. Gauss's law means that the electric space charge density is the source of the electric field. The difference between the charge densities of the ions and electrons gives the space charge density.

$$\rho = e(n_i - n_e)$$

e unit charge ($e = 1.602176487 \times 10^{-19}$ C)

n_i positive ion number density (assumed single charged)

n_e electron number density

Another definition of the current density besides Ampere's law is the difference between the electron and ion fluxes that can be seen as current density as well

$$\mathbf{j} = e(n_i \mathbf{v}_i - n_e \mathbf{v}_e)$$

\mathbf{v}_e electron velocity

\mathbf{v}_i ion velocity

1.2. Magnetic Field Measuring Techniques

1.2.1. Scalar Magnetometers

Scalar magnetometers are magnetic field measuring devices that measure the total strength or magnitude of the magnetic field but provide no directional information of the magnetic vector field.

1.2.1.1. Proton Precession Magnetometer

Many kinds of atoms possess a net magnetic moment and thus behave as small magnets. If electromagnetic pulses are applied to such atoms they can absorb the applied energy and radiate it out again at a certain resonance frequency which depends on the ambient magnetic field strength. This phenomenon is called nuclear magnetic resonance.

A proton precession magnetometer basically consists of a sample of a liquid that is rich in protons (hydrogen nuclei). The sample is surrounded by a coil to magnetically polarize the protons so that all of the small magnetic moments are aligned with the applied magnetic field. The applied magnetic field is then removed (switched off) and the sample is exposed to the ambient magnetic field. The protons will then start to precess around the ambient magnetic field (similar to spinning tops in a gravity field) and induce an AC-signal in the coil that was used to polarize the protons. The frequency of the signal is proportional to the magnitude of the ambient field and is called Larmor frequency.

$$f = \frac{\tau_p B}{2\pi} \quad \text{Larmor frequency}$$

$$\begin{aligned} B & \quad \text{magnitude of the external field} \\ \tau_p & \quad \text{gyromagnetic ratio of the proton} \end{aligned}$$

The gyromagnetic ratio is very accurately derived from quantum mechanical principles ($\frac{2\pi}{\tau_p} = 23.4874 \frac{\text{nT}}{\text{Hz}}$), thus the proton precession magnetometer is an absolute reference magnetometer.

1.2.1.2. Overhauser Magnetometer

The overhauser magnetometer can achieve polarization much more effectively than the proton precession magnetometer. Additionally it can produce a continuous Larmor precession signal. The proton-rich sample is doped with a free radical as a source of electrons. The electrons are pumped with RF-energy at ~20-60 MHz and are efficiently

coupled to the protons which are then polarized dynamically by the pumping RF. The achievable Larmor signal amplitudes with this principle are 100 times larger than the amplitudes from the DC-method that is used for the traditional proton precession magnetometer as described in Sec. 1.2.1.1. Additionally the power consumption for excitement is reduced from tens of watts to just a few watts.

1.2.1.3. Optically Pumped Magnetometers

Optically pumped magnetometers use energy that is required to transfer atomic electrons from one energy level to another as means of measuring magnetic fields. Such magnetometers consist of a certain gas which is irradiated by a discharge lamp. A certain quantum level becomes overpopulated (due to forbidden transitions) when the irradiation is done at a proper frequency. The gas cell then becomes transparent to the irradiating beam. Such a process is called optical pumping. The electrons in the gas cell then start to precess about the axis of the external magnetic field at the Larmor frequency of the element in the gas cell.

$$f = \frac{\tau_e B}{2\pi} \quad \text{Larmor frequency}$$

B	magnitude of the external field
τ_e	electron gyromagnetic ratio

A photodetector is used to measure the intensity-modulated light at the same rate (Larmor frequency). The cell can be made opaque again by an RF-signal at the proper energy level. For helium $\frac{\tau_e}{2\pi} = 28 \frac{\text{Hz}}{\text{nT}}$ and is much larger than the value for proton precession magnetometers of $0.04257602 \frac{\text{Hz}}{\text{nT}}$. Thus higher time resolution can be achieved with optically pumped magnetometers. Besides helium, alkali metals such as cesium, rubidium and sodium are as well used for optically pumped magnetometers.

If the external magnetic field is aligned with the gas cell, the amplitude of the signal that is modulated with the Larmor frequency decreases to a minimum ('null zones'). This is the reason why most optically pumped magnetometers for space missions consist of two cells oriented at different angles.

1.2.2. Vector Magnetometers

Vector magnetometers can measure the total field strength or magnitude as well as the direction of the magnetic vector field.

1.2.2.1. Search Coil Magnetometer

The search coil magnetometer cannot measure DC-magnetic fields, but it is capable of measuring AC-magnetic fields extremely accurately up to high frequencies. It obtains the AC-magnetic field vector using Faraday's law of magnetic induction.

$$\nabla \times \mathbf{E} = -\frac{\partial \mathbf{B}}{\partial t} \quad \text{Faraday's law}$$

It consists of orthogonal coils. The voltage induced in the coils by time varying magnetic fields is proportional to the ambient AC-magnetic field.

$$V = \oint \mathbf{E} \cdot d\mathbf{s} = \iint \nabla \times \mathbf{E} \cdot d\mathbf{A} = -\iint \frac{d\mathbf{B}}{dt} \cdot d\mathbf{A}$$

1.2.2.2. Fluxgate Magnetometer

The fluxgate magnetometer is based on a saturated transformer. If a transformer operates in saturation, even harmonics are produced that are proportional to the ambient magnetic field. The largest of the even harmonics is the second harmonic which is used for magnetic field detection. The fluxgate magnetometer basically consists of three orthogonal transformers which are tuned in a way that the excitation signals do not appear on the pick up coils (balanced arrangement) and are optimized for the second harmonic. The signals at the pick up coils are fed into an electronic system that can generate a feedback current in an additional feedback coil so that the ambient field is canceled out.

1.2.2.3. Vector Helium Magnetometer

The vector helium magnetometer consists of an optically pumped helium scalar magnetometer with an added Helmholtz coil system around the gas cell, which is used to derive directional information of the ambient field. The directional information is derived electronically and thus is not directly related to mechanical alignments. The Helmholtz coil is used to generate synchronous orthogonal sweep fields in two planes that intersect along the optical axis and thus synchronously modulate the photodetector light output.

The photodetector light output is synchronously rectified to cancel out the field applied, via current feed back, similar to the fluxgate magnetometer.

1.2.2.4. Coupled Dark State Magnetometer

This is a new type of magnetometer that is currently under development for space-borne applications. In principle it can be configured as a scalar and a vector magnetometer. It is based on two-photon spectroscopy of free alkali atoms. Compared to other scalar magnetometers it has much lower mass and power consumption. Additionally, it produces no artificial magnetic fields for excitation. For more information see Pollinger *et al.* (2010) and references therein.

1.2.3. Comparison of Space-borne Magnetometers

The table below represents the typical instrument specifications of each type. Specific applications may require magnetometers to have different specifications than in the table.

	dynamic range [nT]	noise [pT/sqrt(Hz)]	frequency range [Hz]	power [W]	weight [kg]	zero level stability
proton precession (scalar)	20000-100000	10 @ 1 Hz	0-1	>20	3-4	absolute 0.1 nT
overhauser (scalar)	20000-200000	10 @ 1 Hz	0-1	>2	1-2	absolute 0.1 nT
optically pumped (scalar)	20000-200000	10 @ 1 Hz	0-2	>2	1-2	absolute 0.1 nT
search coil (vector)	0.01-1000 @ 1 Hz	10 @ 1 Hz 0.01 @10 kHz	1-50000	0.5	0.8	N A
fluxgate (vector)	0.05-60000	10 @ 1 Hz	0-100	0.5	0.5	1-10 [nT/year]
vector helium (vector)	0.05-150000	10 @ 1 Hz	0-10	4-6	2-3	0.05-0.2 [nT/year]

Table 1.1. Typical specifications of space-borne magnetometers.

1.3. The Interplanetary Magnetic Field

The perfectly conducting solar-wind plasma that flows radially out of the solar corona carries the Sun's magnetic field with it. While the Sun rotates with a 27 day rotation period (as observed from Earth) the magnetic field lines stay anchored at the same footprint in the solar atmosphere. This causes the field lines to be bent due to the radially out flowing plasma to form an Archimedean spiral (also referred to as "Parker Spiral"). Field lines that are carried by a highly conducting plasma flow are called "frozen-in" field lines (see Fig. 1.1). At the distance of 1 AU the angle between the spiral and the Earth-Sun line is about 45° (the Sun-Earth distance is referred to as an astronomical unit, $1 \text{ AU} = 149.597.870 \text{ km}$). The typical solar-wind speed is 500 km s^{-1} . At this speed the solar-wind needs 4 days to travel from Sun to Earth. The typical range of solar-wind velocity lies between 300 km s^{-1} and 1400 km s^{-1} . Regions of flow with velocities below 400 km s^{-1} are called low-speed streams, whereas regions with flow velocities exceeding 600 km s^{-1} are called high-speed streams. Because of the azimuthal velocity of Earth of about 30 km s^{-1} the solar-wind arrives at Earth with about 5° aberration from the radial direction. The typical magnetic field strength of the interplanetary field at 1 AU is in the order of 5 nT rarely exceeding 20 nT . The solar wind propagates faster than its speed of sound as well as faster than magnetic signals can be transported inside the solar-wind. Thus the solar-wind can be seen as a supersonic as well as a super-Alfvénic flow. At 1 AU the solar-wind plasma is fully ionized and consists of protons, electrons and α -particles.

There are several periodic cycles of solar activity. The Sun's activity varies with an 11 year cycle. The direction of the Sun's magnetic field changes polarity during each 11 year cycle, thus forming a 22 year magnetic cycle, commonly referred to as "Hale Cycle". Other cycles are the roughly 90 year Gleissberg cycle and the roughly 210 year De Vries or Suess cycle. At low solar activity the Sun's magnetic field is more similar to the field of a magnetic dipole.

High-speed streams originate from coronal holes that rotate with the Sun's surface. Thus an observer at e.g. in front of the magnetosphere of Earth sees a repeating pattern of high-speed streams and low-speed streams with a 27 day periodicity, especially during low solar activity (see Fig. 1.2). The proton density for high-speed streams is $\sim 3 \text{ cm}^{-3}$ and the proton temperature is $2 \times 10^5 \text{ K}$. The proton density for low-speed it is $\sim 7-10 \text{ cm}^{-3}$ and the proton temperature is $4 \times 10^4 \text{ K}$. The magnetic field fluctuations of the high-speed streams are mostly Alfvénic fluctuations (changes in direction of the field rather than changes in magnitude). Magnetic fluctuations of the low-speed streams are mostly changes in field magnitude related to density fluctuations.

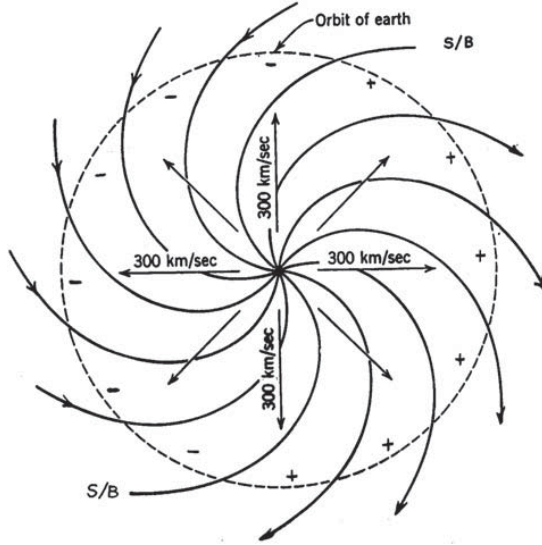


Figure 1.1. The “Parker Spiral” in the solar equatorial or ecliptic plane. The spirals are magnetic field lines that start out radially and make a large angle to the radial direction by the time they reach 1AU (the dotted circle). Arrows added to the field directions indicate their polarity at the Sun. The pluses designate outward-directed (positive) fields and the minuses inward-directed (negative) fields. The field lines divide the circle into two magnetic ‘‘sectors’’. Two of the spirals are the boundaries between the sectors (designated S/B for sector boundary). The straight lines emanating from the Sun at the center are radial solar-wind velocity vectors with speeds of 300 km/s (considered slow wind today). Taken from Smith (2007).

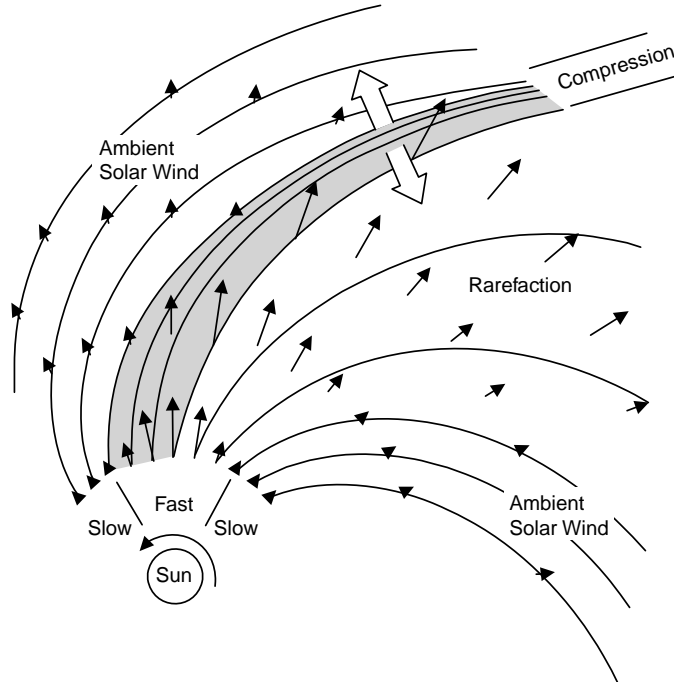


Figure 1.2. Interaction of fast and slow solar wind that form a so-called corotating interaction region. Adapted from Russell (2001).

The average direction of the interplanetary magnetic field along the Parker spiral is pointing away from the Sun in one hemisphere and towards the Sun in the other hemisphere (directions are reversed during each 11 year solar cycle). The magnetic field goes through zero in between the hemispheres and thus the interplanetary current sheet is formed (see Fig. 1.3). An observer in front of Earth's magnetosphere sees a sector structure of alternating polarities of the interplanetary magnetic field. Typically there are two to four sectors (see Fig. 1.1).

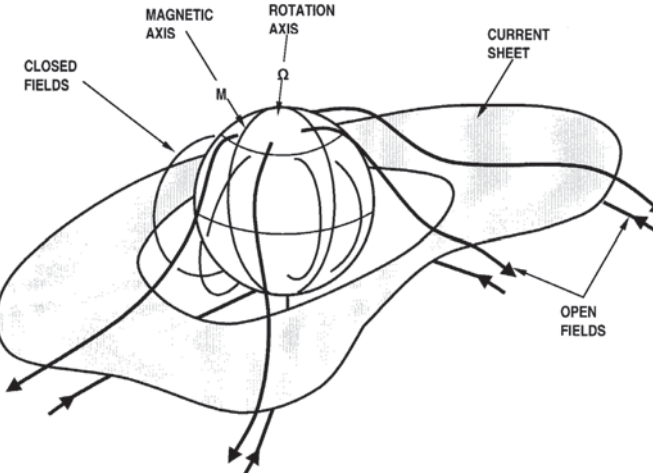


Figure 1.3. *Heliospheric current sheet near the Sun. The magnetic axis is tilted with respect to the rotation axis. Taken from Smith (2007).*

The interplanetary magnetic field has a so-called termination shock where the supersonic solar-wind plasma becomes subsonic and enters the heliosheath. Both Voyager spacecraft have crossed the termination shock taking first in-situ measurements of this boundary. Voyager 1 crossed on 11 Nov., 2004 at a distance from the Sun of 94 AU (Burlaga *et al.*, 2005). Voyager 2 followed on 30 Aug., 2007 at 84 AU (Burlaga *et al.*, 2008). The next boundary past the termination shock is the heliopause where the field lines stop being “frozen” into the solar-wind plasma and is expected to be located at around 200 AU. Additionally, if the local interstellar medium is supersonic, a bow shock may exist as well (see Fig. 1.4). The magnetic field strength at the termination shock is roughly 0.1 nT (Burlaga *et al.*, 2005).

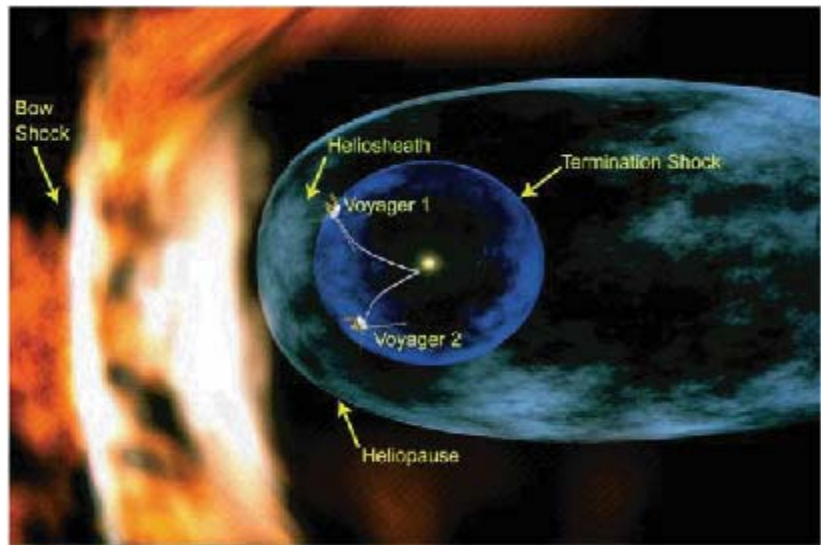


Figure 1.4. Artist's view of the heliosphere, (the magnetosphere of our Sun) carved by the solar wind into the flow of the interstellar medium. Taken from Blanc (2005).

1.4. Planetary Magnetic Fields

Magnetohydrodynamic dynamos create planetary magnetic fields also called internal fields in many of the planets. Such dynamos are formed inside liquid cores. Basically the dynamo creates (induces) an electromotive force (EMF) because of motion of a conducting liquid across magnetic field lines. The EMF causes currents that produce a magnetic field in such a way that the dynamo is self-exciting. For more information see Parker (1979). Magnetic fields generated by such dynamos can be modeled by using the negative gradient of the scalar potential that satisfies Laplace's equation. For the case that the solution to Laplace's equation was found in spherical coordinates it is called a spherical harmonic expansion. The required parameters are called Gauss coefficients.

Besides the magnetohydrodynamic dynamos another important component of planetary magnetic fields are crustal magnetic fields, generated from magnetic material of the planet's crust. The crustal magnetic field is often called an anomaly field because of its general high spatial variability.

1.4.1. Earth's Geomagnetic Field

The geomagnetic field is observed by ground based geomagnetic stations, ship-towed magnetometers, magnetometers on aircraft as well as by space-borne magnetometers (MAGSAT, Ørsted and CHAMP see Sec. 1.7.). The Earth's magnetic field can roughly be approximated by a dipole that is located at the center and tilted with respect to the rotation axis by about 10° . The magnetic field strength at the surface ranges from 24,000 nT to 66,000 nT. For more data about Earth see Table 1.2 and Figure 1.6. Significant derivations from a pure dipole field exist. Several spherical harmonic models exist, commonly used is the International Geomagnetic Reference Model (IGRF) (see e.g. Maus *et al.*, 2005).

The Earth's magnetic field is not constant. Studies of the magnetic field of rocks revealed that reversals of the geomagnetic field have occurred in the past. When a rock is formed it can acquire a magnetic field that is parallel to the ambient field. The time frame between reversals is several thousand years. Reversals take place slowly and without a constant periodicity. Currently the strength of Earth's magnetic dipole is decreasing with a rate of about 6% per century. The so-called westward drift is another change of the geomagnetic field. During the last century the field drifted westward at a rate of about 0.15° per year (Wei and Xu, 2001). There are changes of the Earth's field called Geomagnetic Jerks. Such changes of secular variations have happened in 1925, 1969, 1978 and 1992 and are currently not predictable (see Fig. 1.5). The crustal magnetic field can vary as well. Such changes occur mainly along mid-ocean ridges when liquid material from molten mantle reaches the ocean bottom. The new material pushes older material aside that has the current geomagnetic field frozen into it, thus causing local magnetic field changes.

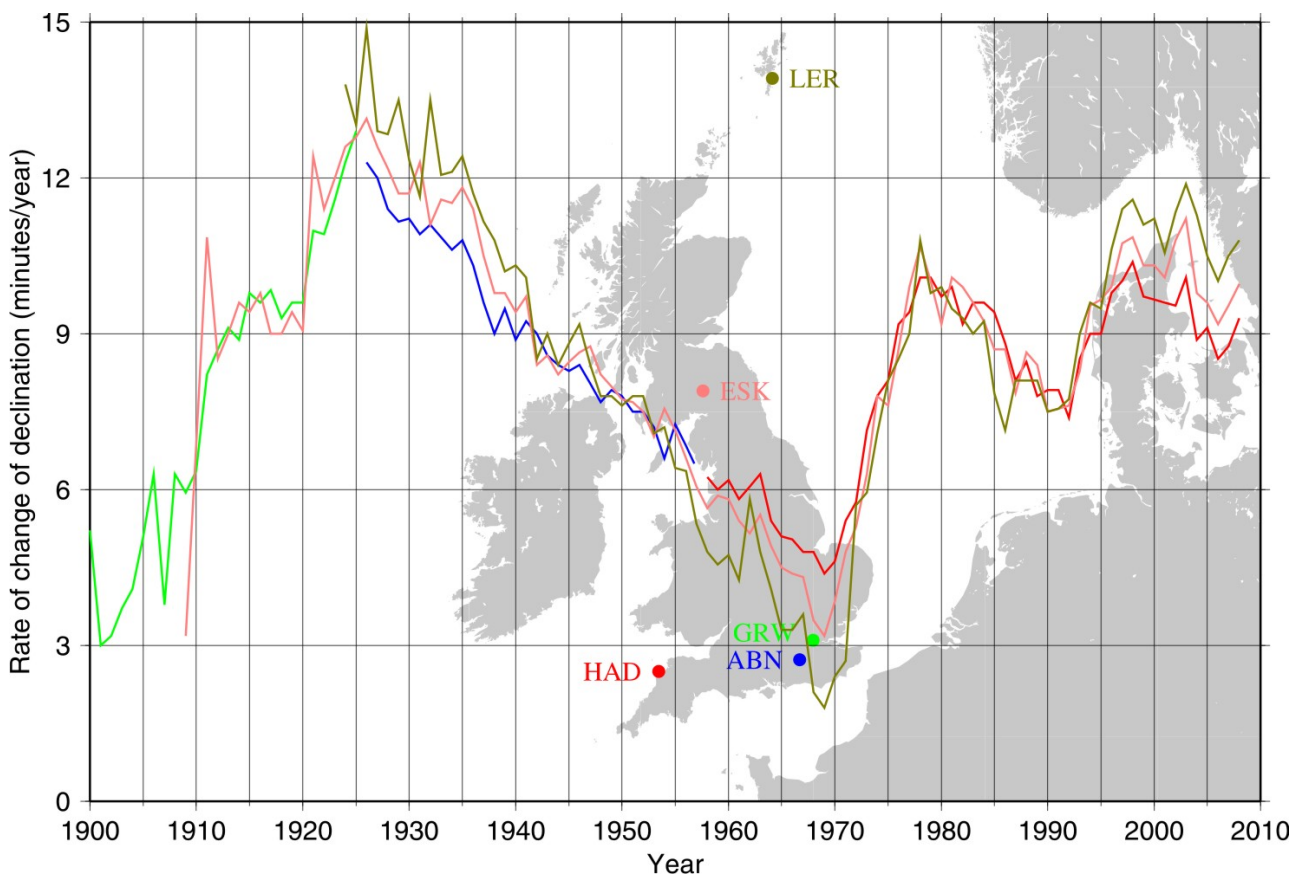


Figure 1.5. Rate of change of declination at Greenwich (GRW), Abinger (ABN), Hartland (HAD), Eskdalemuir (ESK) and Lerwick (LER) observatories 1900-2008.
Courtesy of British Geological Survey.

Additionally, ocean currents and tidal flows can generate magnetic fields. For more details on the interaction of ocean currents and magnetic fields see Manoj *et al.* (2006).

1.4.2. Internal Magnetic Fields of Other Planets

Similar to Earth, other planets are likely to have magnetohydrodynamic dynamos. Figure 1.6 shows the magnetic dipole fields of all the planets of our solar system that have measurable internal fields. Their dipole strengths and directions vary. There is evidence that Mars once had an internal field until the dynamo stopped generating a magnetic field. Venus is a likely candidate for having a liquid outer core but magnetic field measurements show no sign of an internal magnetic field. See Table 1.2 for data about planets.

	Radius [km]	Surface equatorial field [nT]	Dipole tilt and sense	Sidereal rotation period	Density of external plasma**	Dynamic pressure of external plasma [nPa]**	Magnetic field of external plasma [nT]**
Mercury	2440	140 - 400	$\sim 10^\circ$ *	59 days	$\sim 50/\text{cm}^{-3}$	15	20
Venus	6052	-	-	243 days	$16/\text{cm}^{-3}$	4	10
Earth	6373	31000	$+10.8^\circ$	23.9 h	$8/\text{cm}^{-3}$	2	8
Mars	3390	<10	-	24.6 h	$3.5/\text{cm}^{-3}$	1	3.5
Jupiter	71398	428000	-9.6°	9.8 h	$0.3/\text{cm}^{-3}$	0.1	1
Saturn	60330	22000	0.0°	10.7 h	$0.1/\text{cm}^{-3}$	0.03	0.5
Uranus	25559	23000	-59°	15.5 h	$0.02/\text{cm}^{-3}$	0.005	0.3
Neptune	24764	14000	-47°	15.8 h	$0.008/\text{cm}^{-3}$	0.002	0.2
Ganymede	2634	720	4°	7.2 days	$100 \text{ AMU}/\text{cm}^{-3}$	1	100

* Value from Slavin (2004)

** The properties of the solar-wind vary greatly; hence the values are approximate.

Table 1.2. Planetary data. Adapted from Kivelson (2007).

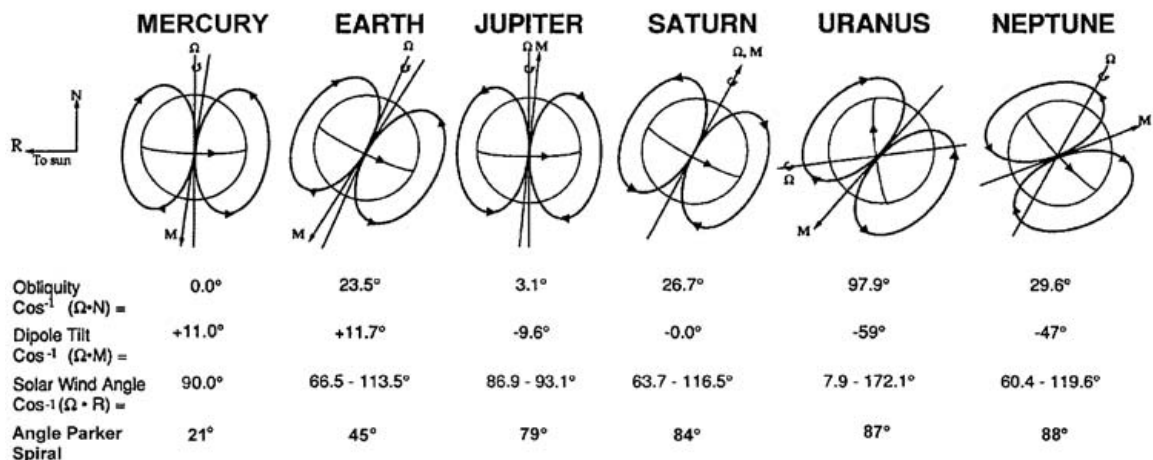


Figure 1.6. The relative geometries of the solar-wind direction (opposite to vector \mathbf{R} here), planetary spin vectors $\boldsymbol{\Omega}$ and dipole moments \mathbf{M} are illustrated in this figure for Earth, Mercury and the giant planets. They play an important role in the way solar-wind forcing and planetary motion interplay to determine a global pattern of plasma and magnetic flux circulation in each magnetosphere. In addition the planetary obliquity angle determines the importance of seasonal variations in magnetospheric phenomena, and the angle between \mathbf{M} and $\boldsymbol{\Omega}$ determines the importance of diurnal variations in magnetospheric flows. Taken from Blanc (2005).

1.4.3. Internal Magnetic Field of Ganymede

Ganymede is a moon of Jupiter. It is the only moon in our solar system for which an internal magnetic field has been observed, thus it is likely to have a magnetohydrodynamic dynamo. Ganymede is the smallest known body within or solar system to have such a dynamo. For data on Ganymede see Table 1.2.

1.5. Solar System Magnetospheres

Planets can be seen as obstacles that slow down the supersonic solar wind, divert and heat its flow around the planetary obstacle. There are three different types of such obstacles. The solar wind can be slowed down by:

- 1) a planet that does not have a magnetic field nor a dense atmosphere or ionosphere may have an “induced magnetosphere” in an electrically conducting core. This magnetosphere is transient with a time scale dependent on the size and conductivity of the core.
- 2) a planet’s atmosphere (or ionosphere), the resulting magnetosphere is called “induced magnetosphere” as well
- 3) or by a planet’s magnetic field, the resulting magnetosphere is then called “intrinsic magnetosphere”.

Mars represents a special case because of larger crustal fields that reach up to the ionosphere. The solar wind is slowed down by the planets atmosphere/ionosphere and magnetic field (Winterhalter *et al.*, 2004).

The so-called standoff distance of the magnetopause (see Figure 1.7) is the distance from the “nose” of the magnetopause (subsolunar point) to the planet, moon or comet (obstacle). This standoff distance is a result of an equilibrium (pressure balance) of pressures of the surrounding plasma with pressures of generated by the obstacle.

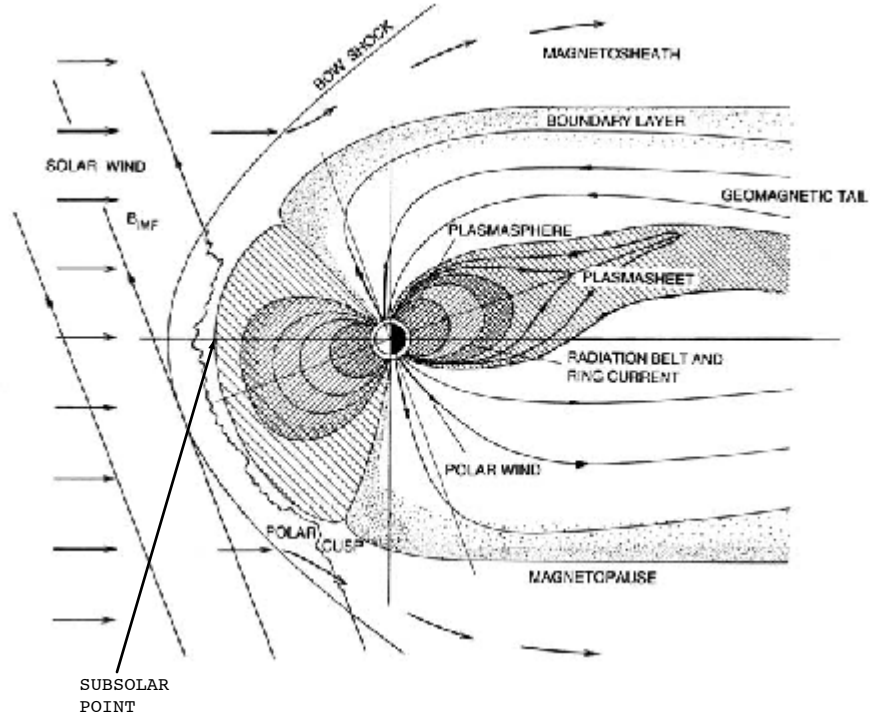


Figure 1.7. Earth's magnetosphere. Adapted from Parks (1991).

1.5.1. Earth's Magnetosphere

Earth's magnetosphere falls under category three as described above. The interaction of the supersonic solar wind with the Earth's magnetosphere causes a bow shock (see Fig. 1.7) which precedes the magnetosphere and is located at a distance of about 13 Re (1 Re is the average radius of Earth of 6371 km) in front of Earth. Behind the bow shock there is another boundary called the magnetopause where the hydrodynamic pressure of the solar wind of about 0.17 nPa (nano Pascal) is balanced by the magnetic pressure of the internal magnetic field of Earth, thus the plasma flow is diverted around the magnetopause including the "frozen-in" magnetic field lines. This boundary is about 10 Re in front of Earth. The region between bow shock and magnetopause is called magnetosheath. Inside the magnetosheath the solar-wind plasma is slowed down while its thermal energy increases. The plasma types outside and inside of the magnetosphere are very different. The magnetosheath plasma mainly comes from the solar wind (see Sec. 1.3.) while the plasma on the opposite side of the magnetopause is mainly fed by ions from the ionosphere. The Archimedean spiral shaped magnetic field that is carried by the solar wind arrives at Earth at an average angle of 45°. This generally causes so-called parallel shocks at the morning side and perpendicular shocks at the afternoon side. Parallel shocks are highly oscillatory and cause upstream waves that are observable within a region called foreshock region, thus "letting the plasma know" that a shock is ahead. Towards the night side the magnetosphere extends far beyond the orbit of the Moon to about 1000 Re.

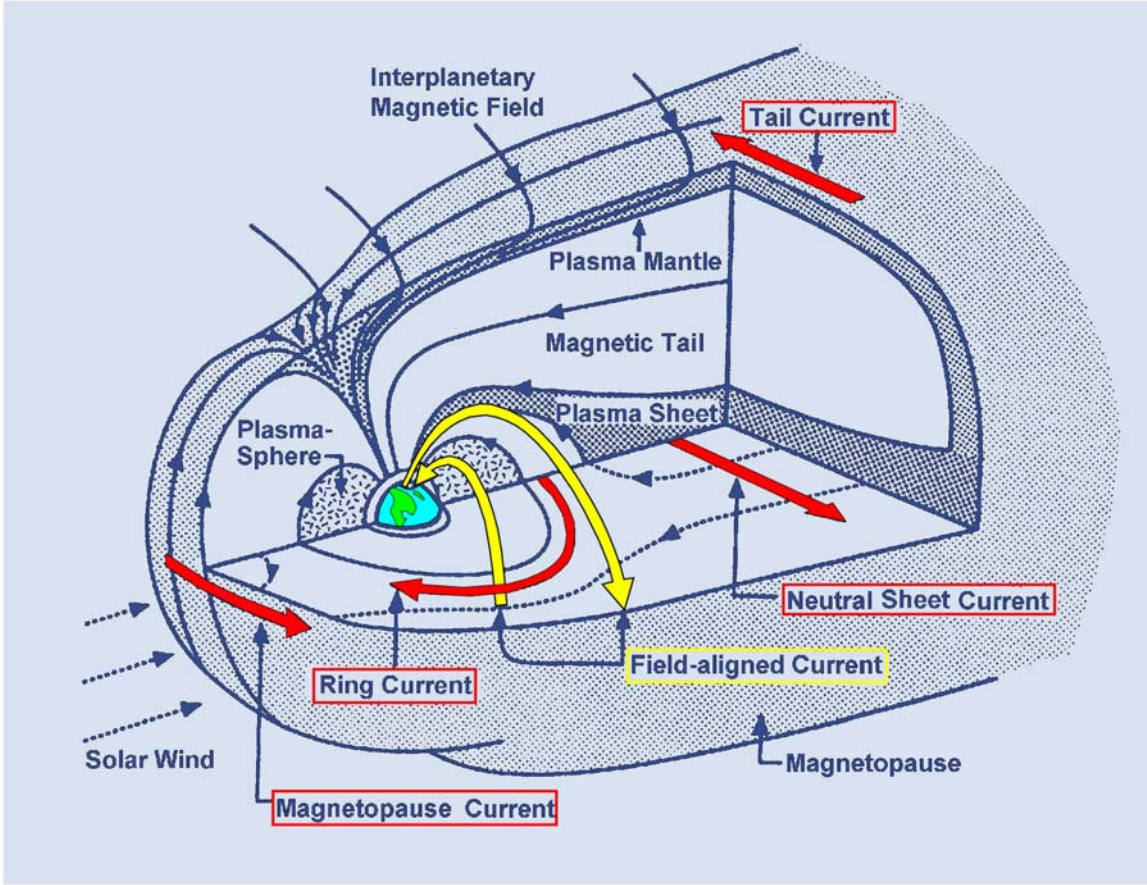


Figure 1.8. Magnetospheric current systems. Modified from Kivelson and Russell (1995).

There are several current systems within the Earth's magnetosphere as well as several regions of different charged particles (see Figure 1.8). The coupling of the solar-wind plasma together with the interplanetary magnetic field to the Earth's magnetosphere causes flow and an electric field ($E = -v \times B$) which leads to magnetospheric current systems. The innermost region of the magnetosphere, the plasmasphere consists of low energy plasma and represents the extension of the ionosphere. The latter can be seen as a transition region between the fully ionized magnetospheric plasma to the neutral atmosphere. Ionospheric ionization of neutral atmospheric particles is caused by solar ultraviolet as well as extreme solar ultraviolet radiation. The mantle is a layer of plasma with tail ward bulk flow. Mantle plasma eventually reaches the center of the magnetotail where it can be accelerated to higher energy levels. The dashed lines in Figure 1.8 show the average flow of low-energy particles both inside and outside the magnetosphere. Together with the presence of magnetic fields, those flows cause electric fields which can accelerate charged particles to very high energies that populate the so-called Van Allen radiation belts. The discovery of the radiation belts was made by Van Allen's group (Van Allen, 1959) with Geiger-Müller tubes onboard the Explorer 1 spacecraft (launched on 1958-02-01). The Van Allen radiation belts are located between about 2 Re and 6 Re (geocentric distances) and consist of high energy particles (electrons and ions) that bounce back and fourth along dipolar field lines. Currents are generated when the magnetic field is not curl free (in the mathematical sense). The thick, red arrows in

Figure 1.8 show flows of major electric currents. The pressure gradient of the shocked magnetosheath plasma when it reaches the magnetic field of Earth causes the magnetopause currents. The tail current (or also called neutral sheet current) is part of the magnetopause current. It separates both tail lobes which contain magnetic fields of opposite directions. The ring current consists of charged particles that are trapped by the Earth's dipolar field. The most energetic of those particles comprise the radiation belts. The trapped particles drift azimuthally due to gradient and curvature of the magnetic field. Ions and electrons drift in opposite directions, thus generating a current. The ring current extends from about 2 Re to 9 Re (geocentric distances) and flows westward thus causing a magnetic field that is opposite to the Earth's dipolar field. Currents that flow along magnetic field lines are called field-aligned currents. Field-aligned currents apply drag to the ionospheric plasma via Lorentz or $\mathbf{J} \times \mathbf{B}$ force as they close inside the resistive ionosphere and cross field lines on pressure gradients. Thus field-aligned currents can transport stresses from the outer magnetosphere to the ionosphere and hence to the atmosphere. Such an energy transfer as well depends on the direction of the interplanetary field (see Sec. 1.6.).

1.5.2. Magnetospheres of Other Planets

Venus has no measurable internal magnetic field. It has an induced magnetosphere (see Fig. 1.9). Due to its dense atmosphere it falls under category two in Sec. 1.5. Mercury, Earth, Jupiter, Saturn, Uranus and Neptune have intrinsic magnetospheres (category three in Sec. 1.5.).

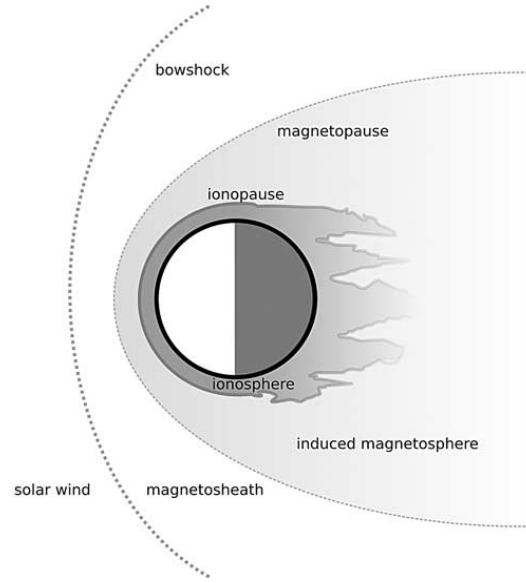


Figure 1.9. Induced magnetosphere of Venus. Taken from Zhang et al. (2008).

The magnetosphere of Mercury is a “mini magnetosphere” because of the relative small planetary size and the short standoff distance of Mercury’s magnetosphere (see

Fig. 1.10). Due to the small size radiation belts cannot form and due to the slow rotation period there is no Earth-like plasmasphere.

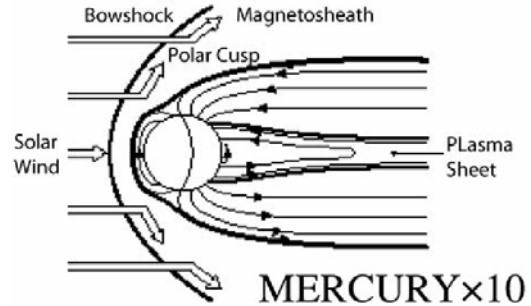


Figure 1.10. Magnetosphere of Mercury. Taken from Kivelson (2007).

Mars represents a special case because its magnetohydrodynamic dynamo has stopped but crustal magnetic fields in some regions are large enough to prevent the solar wind from reaching its surface and form so-called solar arcs.

The magnetospheres of Jupiter and Saturn represent so-called “giant magnetospheres”. Large magnetic moments together with fast rotation, moons and rings form extremely large and complex magnetospheres (see Fig. 1.11).

Uranus and Neptune as well produce very large magnetospheres but their dipole tilts are extremely large. Large dipole tilts produce highly varying structural features and asymmetries in these magnetospheres throughout a planetary rotation (see Fig. 1.11).

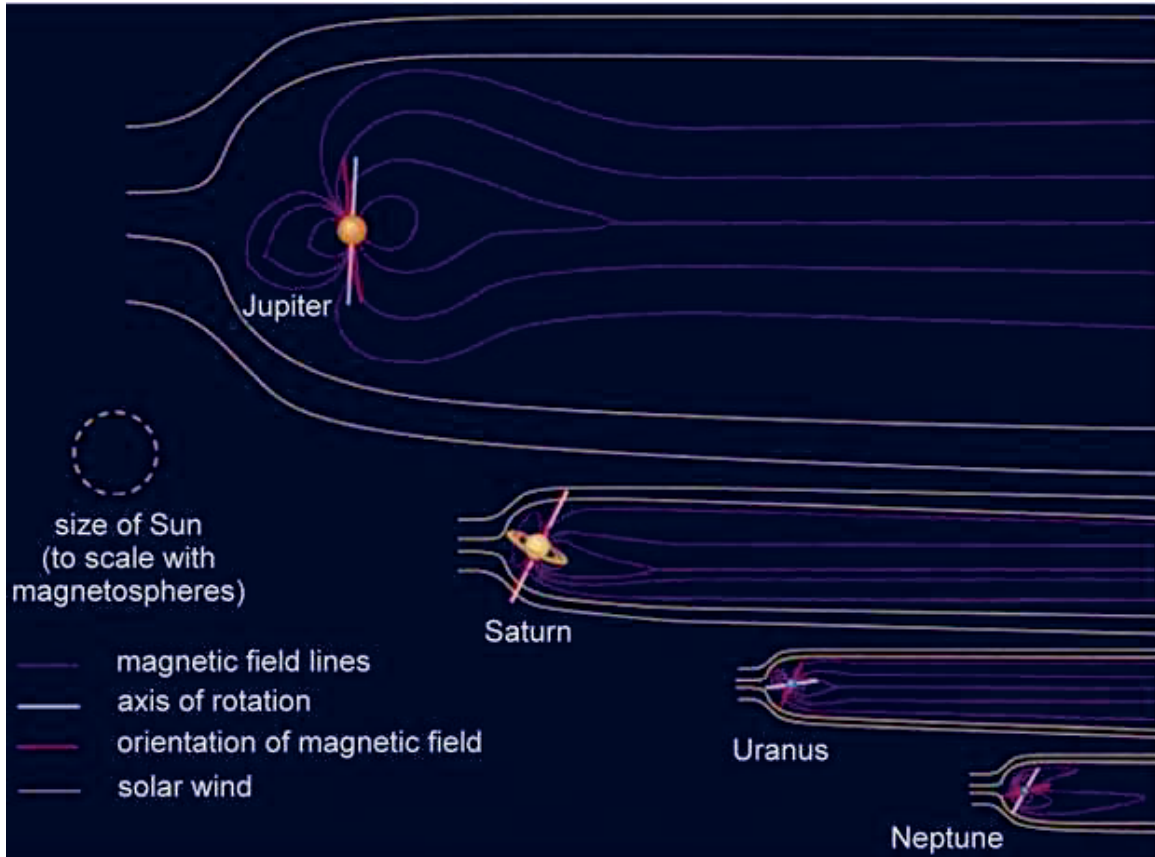


Figure 1.11. Giant magnetospheres. Taken from Bennet (2004).

1.5.3. Other Magnetospheres

Magnetospheres can be inside magnetospheres. The magnetospheres of moons orbiting planets are such cases. Most moons in our solar system do not have an internal magnetic field, their magnetospheres are “induced magnetospheres” (categories one and two in Sec. 1.5.). The Jupiter moon Titan has a dense atmosphere but no internal magnetic field (category two in Sec. 1.5.). Our moon is a typical example of surface interaction with the ambient plasma (category one in Sec. 1.5.).

The Jupiter moon Ganymede is an exception. Ganymede has an internal magnetic field, thus has an “intrinsic magnetosphere” that is inside another “intrinsic magnetosphere” (see Fig. 1.12). The magnetic pressure dominates the plasma pressure at Ganymede’s orbit inside Jupiter’s magnetosphere. This causes Ganymede’s magnetosphere to be more cylinder-shaped.

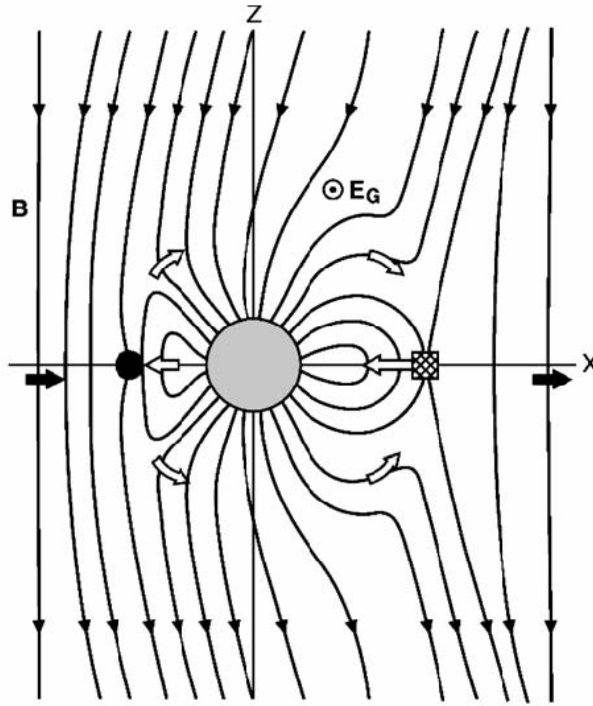


Figure 1.12. Magnetosphere of Ganymede. Taken from Kivelson (2007).

Magnetospheres of comets are “induced magnetospheres”. A comet emits neutral gas and dust. There are two boundary regions. One is the cometary bow-shock and the other is the boundary between the region where the pressure of gas and dust dominate and the region where solar-wind plasma pressure and magnetic field dominate.

Most asteroids and moons without dense atmosphere and magnetic field do not form bow shocks. The surrounding plasma directly interacts with the surface of such a body (absorption).

1.6. Space Weather

The field of research that describes how interplanetary space, Earth and its technological systems, biological systems as well as its climate are affected by solar activity and other cosmic sources is called ‘space weather’. Examples of affected technological systems are space probes and satellites, telecommunication systems, transformers connected to electric energy supplying power grids as well as electronic systems and very long conductors (power lines or telecommunication cables). Examples that fall under the category biological systems are humans as astronauts and airline passengers (see Fig. 1.13). More recent studies suggest that even humans that are located on the surface of Earth are as well influenced by space weather conditions. Besides humans other species such as pigeons and whales on the Earth’s surface can be influenced by space weather as well. The general processes of influence are magnetic field reconnection and plasma acceleration processes as well as direct impacts of highly charged particles. The solar wind controls both, the size of the magnetosphere and the amount of energy that enters the magnetosphere.

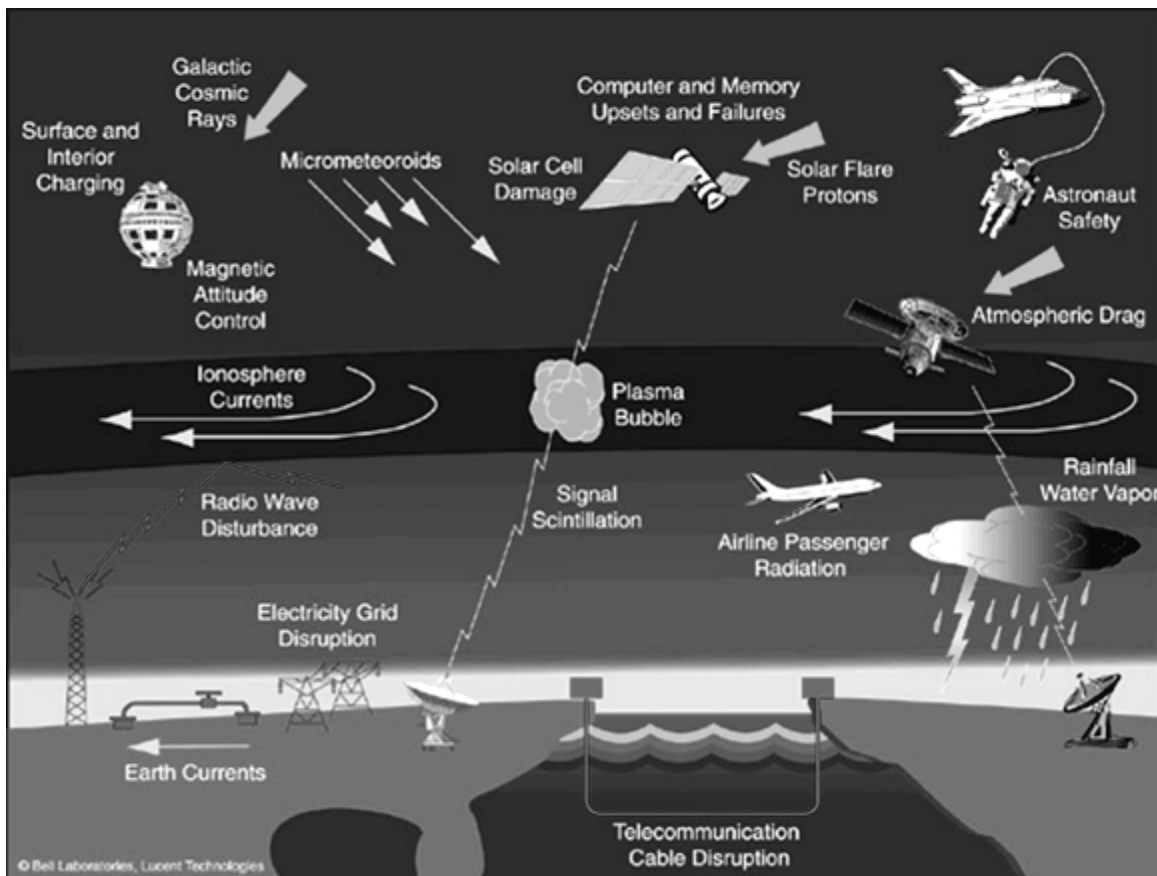


Figure 1.13. Effects of space weather. Adapted from Lanzerotti et al. (1997).

1.6.1. Reconnection

If the magnetic field is northward at the subsolar point (parallel to the internal field), the energy transfer into the Earth's magnetosphere is minimal (see Fig. 1.14). If the interplanetary magnetic field (IMF) turns southward the field lines at the subsolar point become anti-parallel and reconnect (see Fig. 1.14). The size of this dayside reconnection region is highly variable and thus the amount of energy that is transported into the magnetosphere is highly variable as well. The reconnection processes described below were first suggested by Dungey (1961; 1963), and are still hot scientific topics (see e.g. Treumann *et al.*, 2010).

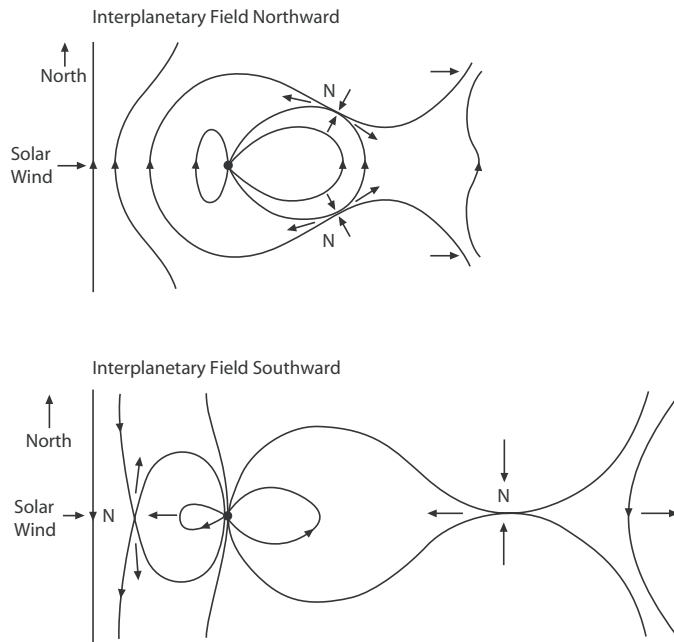


Figure 1.14. The reconnecting magnetosphere for northward (top panel) as well as southward IMF (bottom panel). The points labeled “N” are neutral points where the magnetic field goes to zero (also called X-points). Straight arrows show regions with accelerated flow. Taken from Russell (2007).

1.6.1.1. Northward IMF

In case of northward IMF, reconnection regions form behind Earth as marked with “N” in Fig. 1.14 (top panel). As depicted with arrows, plasma flows into the reconnection region from above and below and is accelerated towards and away from the Sun by straightening field lines. Magnetic flux is transported towards the dayside magnetosphere and removed from the back. Magnetic flux that was removed from the night side is eventually replenished from the dayside. This reconnection transfers momentum from the solar wind into the magnetosphere. This energy transfer is much weaker compared to the energy transfer that occurs for southward IMF.

1.6.1.2. Southward IMF

For southward IMF the reconnection region can become as large as the entire dayside magnetopause (see Fig. 1.14). Reconnection regions are marked with “N”. Additionally the field strength on the dayside is higher and the field geometry altogether is encouraging reconnection. Thus the entry of mass, momentum and energy into the magnetosphere can be much larger than it is for northward IMF. Plasma is transported from the subsolar point over the polar caps into the tail where reconnection occurs. Plasma is then further transported towards Earth and away from Earth.

1.6.1.3. Substorm

The process of magnetospheric energy storage and release is called a substorm. Such a substorm consists of three phases: growth, expansion and recovery. During the growth phase magnetic flux builds up in the tail (see top panel in Fig. 1.15). This process typically lasts about one hour (inside Earth’s magnetosphere). After that too much energy has built up in the tail and it becomes unstable. This is the beginning of the expansion phase which typically lasts between 30 and 60 minutes and can cause bright auroras. A second reconnection region on the night side forms (see second panel in Fig. 1.15) which is closer to Earth (near-Earth neutral line). Between the two reconnection regions on the night side a plasmoid is formed. This plasmoid grows and is eventually ejected towards the night side and thus energy is released (see bottom panel in Fig. 1.15). After that, the recovery phase starts and the magnetosphere goes back to the quiet state typically within 1 to 2 hours.

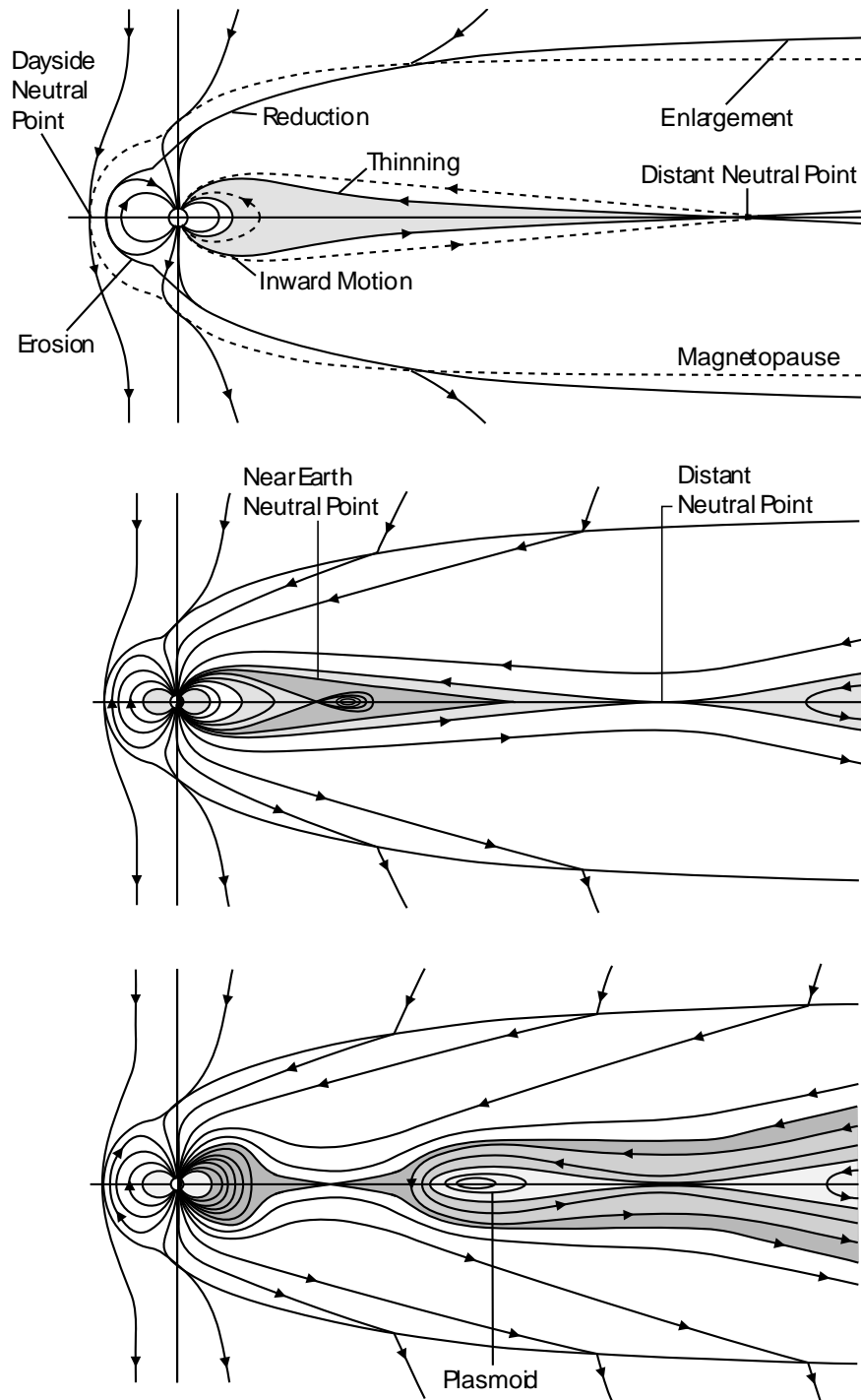


Figure 1.15. Dynamics of a magnetospheric substorm. Depicted is the noon-midnight meridian. Taken from Russell (2007).

1.6.2. Slow and Fast Solar-wind Streams

As described in Sec. 1.3., there is a 27-day recurrence period of fast and slow solar-wind streams which is linked to the rotation period of the Sun. Sources of fast solar-wind streams are coronal holes. Co-rotating interaction regions are formed when fast solar wind catches up with slow solar wind (see Fig. 1.2). This feature is especially pronounced during declining solar cycles. Inside the co-rotating interaction regions both the fast as well as the slow solar-wind streams are compressed, the magnetic field strength is enhanced and (interplanetary) shocks can occur. Fast solar-wind streams lead to so-called geomagnetic storms as described in Sec. 1.6.5.

1.6.3. Coronal Mass Ejection (CME) Events

CMEs are large ejections of magnetized plasma from the Sun, expanding outwards from the corona and rapidly develop into objects that are larger than the Sun itself. The average speed of CMEs ranges from below 400 km s^{-1} to above 3000 km s^{-1} and the mass estimate for a typical CME is 10^{12} kg . As a CME propagates outward from the Sun into the interplanetary medium it becomes an interplanetary coronal mass ejection (ICME). Ahead of the fastest CMEs particle accelerations of up to 100 MeV can take place. Such accelerated particles travel along interplanetary magnetic field lines. CMEs cause large scale disturbances of the solar-wind plasma and can cause geomagnetic storms as described in Sec. 1.6.5.

1.6.4. Flares and Solar Energetic Particles (SEP)

Solar flares are sudden and rapid releases of magnetic energy that take place in the solar atmosphere. Energy is explosively released in various forms such as particle acceleration, plasma heating and acceleration as well as increased radiation fields. The amount of energy that can be released by solar flares is in the order of 10^{25} J . High energy particles propagate away from the Sun along interplanetary field lines and can cause geomagnetic storms as described in Sec. 1.6.5.

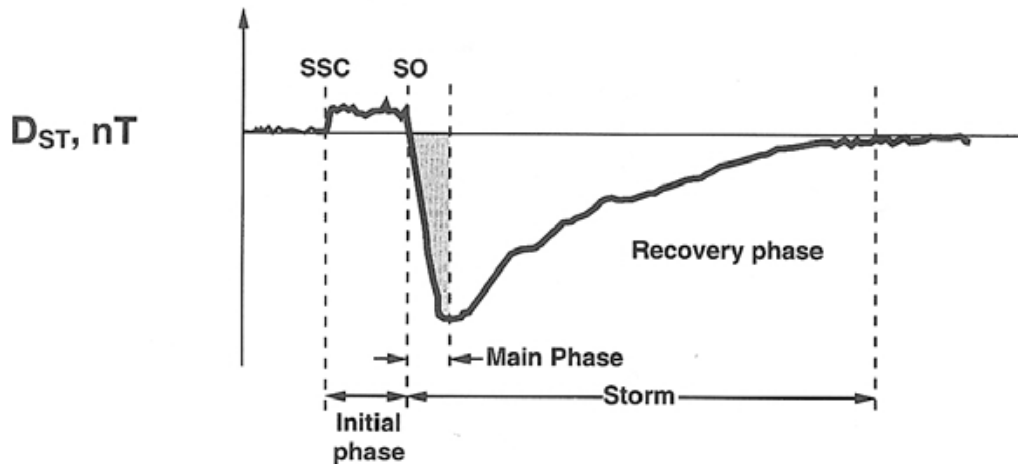
1.6.5. Geomagnetic Storms

Besides substorms which are caused by the general variability of the interplanetary magnetic field, geomagnetic storms occur. Such geomagnetic storms are caused by continuous (over many hours) enhanced stress imposed onto the magnetosphere by the solar wind. Similar to a substorm a geomagnetic storm consists of three phases. The first phase is called sudden commencement. During this phase the magnetic field is compressed caused by an increase of the solar-wind dynamic pressure. The second phase is called the main phase where the magnetic field rapidly decreases. This is caused by a

higher amount of energetic plasma in the tail and thus a higher than usual amount of particles is injected into the ring current, mainly by an enhanced dusk ward electric field ($\mathbf{E} \times \mathbf{B}$ -drift). An enhanced ring current causes a weakening of the overall magnetic field. If the field strength decreases by more than 50 nT a geomagnetic storm is said to have occurred. Finally the third phase is called the recovery phase where the field strength returns to normal.

The Dst-index represents the disturbance of the Earth's magnetic field close to the equator. It is calculated from four low latitude magnetic observatories. Fig. 1.16 shows the Dst-index for two different geomagnetic storms. One is caused by an ICME (see Sec. 1.6.3.) and the other is caused by a co-rotating interaction region (see Sec. 1.6.2.).

Solar Maximum (ICME) Storm



Solar Minimum (CIR) Storm

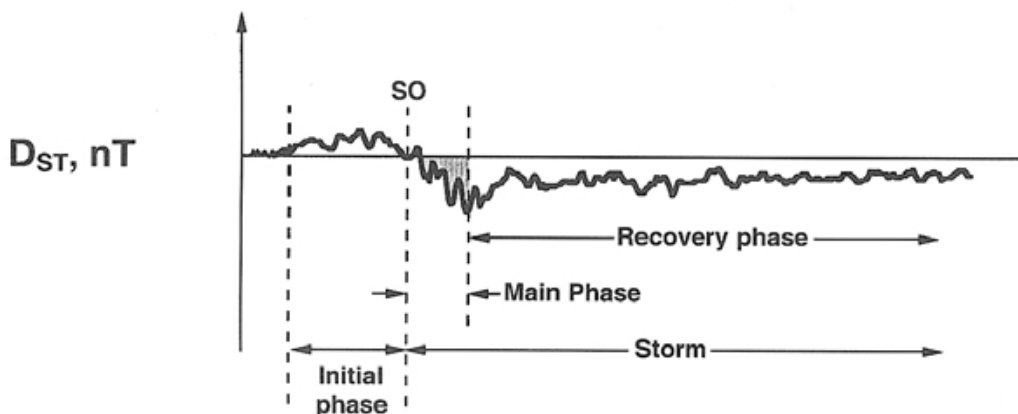


Figure 1.16. The top panel shows the Dst-index a ICME storm during solar maximum. The bottom panel shows a geomagnetic storm caused by a co-rotating interaction region during solar minimum. Taken from Tsurutani (2000).

1.6.6. Galactic Cosmic Rays

The most energetic particles with energies up to 10^{21} eV, that can be found in our Solar System, originate from far outside of our Solar System. Such particles are called galactic cosmic rays (GCRs). All GCRs consist of nuclei only and thus are fully ionized. Acceleration processes in space strip off electrons, leaving behind separated nuclei and electrons. The ratio of nuclei to electrons is such that there are about one percent electrons. As GCRs travel through space they collide with matter and are deflected by magnetic fields so that directional information obtained inside our solar system does not contain information about their origins. Since GCRs are deflected by magnetic fields, there are less GCRs in the inner solar system than in the outer solar system. The termination shock of the solar wind as well provides some shielding against GCRs (see Fig. 1.17). As described above the strength of the interplanetary field undergoes an eleven year cycle and thus the amount of GCRs that reach the inner solar system shows an eleven year modulation.

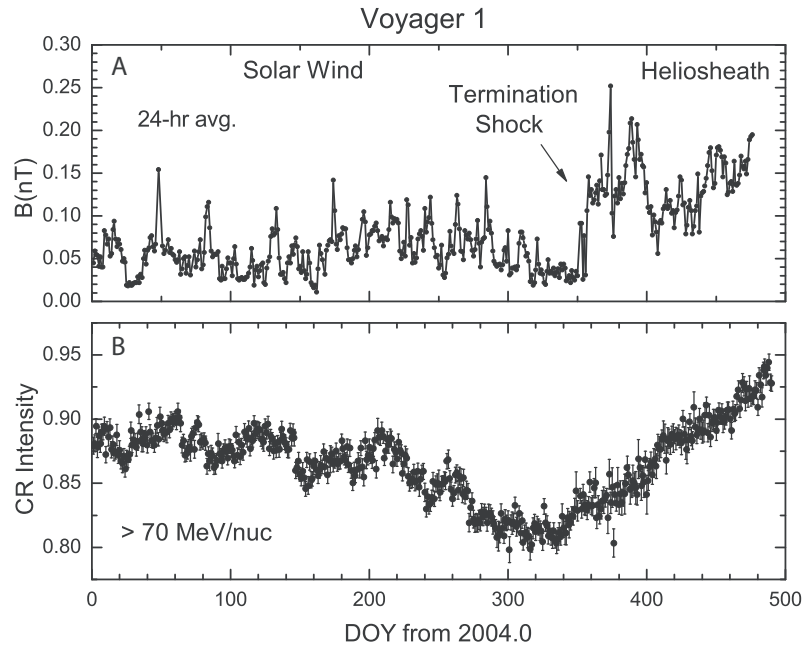


Figure 1.17. Magnetic field strength (top panel) and cosmic ray intensity (bottom panel) at the termination shock as measured by the Voyager 1 spacecraft. Taken from Burlaga et al. (2005).

1.6.7. Consequences of Space Weather

In interplanetary space, exposure to SEPs (see Sec. 1.6.4.) and GCRs (see Sec. 1.6.6.) represent the major threats for space probes and astronauts. SEPs can lead to large electron densities in the D-region of the ionosphere and together with the large electron to neutral collision frequencies cause strong absorption of electromagnetic waves. This can cause interruptions for short (MHz) and medium (kHz) wave

communication systems that use the ionosphere as a reflector. The production of ‘bubbles’ in ionospheric densities can cause interruptions of satellite-to-ground signals. During geomagnetic storms, disturbed ionospheric currents can cause severe problems for the accuracy of the Global Positioning System (GPS) as well as the forthcoming European Galileo Navigation Satellite System (GNSS), thus causing problems for e.g. air traffic control or ship navigation. Another consequence of SEPs is that via a complicated chain of reactions SEPs can cause a reduction of ozone in the mesosphere. Thus frequent flares may have an influence on Earth’s climate (Kallenrode, 2003). All the consequences of ionization of SEPs as well apply to GCRs. Additionally the flux of GCRs is anti-correlated with solar activity (as described in Sec. 1.6.6.). Thus the ionization of the mesosphere and the stratosphere is generally higher during solar minimum years. There is evidence that this has consequences for the Earth’s climate (see e.g. Scherer *et al.* 2007 and references therein) but this is still a controversial topic (see e.g. Kristjansson *et al.*, 2004). Changes of the magnetic field as seen on the Earth’s surface caused by disturbed ionospheric currents during geomagnetic storms can induce large potential differences across large areas of the surface of Earth. Such potential differences can drive additional currents through power lines. Transformers connected to power lines can see large potential differences, thus operating in saturation and overheat. Telecommunication lines that use ground as return for their circuits are also affected as well as certain rail equipment. Today’s fiber optic cables are not directly affected but power supplies to amplifiers that compensate signal damping can be affected. Pipelines corrode faster due to enhanced pipe-to-soil voltages and their electronic protection systems and control surveys may experience problems. Satellite attitude control is often managed by measuring the Earth’s magnetic field. During enhanced geomagnetic activity the magnetotail plasma sheet can convect earthward due to an enhanced cross-magnetosphere electric field. Thus surface charging of geosynchronous satellites may occur that can lead to malfunctioning onboard electronics. This effect is strongest seen in the midnight-to-dawn sector. Enhanced solar-wind dynamic pressure can push the magnetopause much closer towards Earth than its usual position of about 10 Earth radii distance. In extreme cases the magnetopause can pushed in as close to Earth as the geosynchronous orbit. The magnetic field then changes so dramatically that it points into the opposite direction. Thus geosynchronous satellites that control their attitude via magnetic field measurements might be unable to maintain the desired attitude.

Some species use magnetoreception as a tool for navigation. Such species are e.g. pigeons, sea dwellers, lobsters, sea turtles, salmon, trout and certain bacteria (e.g. Kirschvink, 1997; Walker *et al.*, 1997; Scheffel *et al.*, 2005; Lohmann *et al.*, 1995; Irwin *et al.*, 2004). Geomagnetic activity can have an influence on their ability to navigate. It has recently been suggested that there is a correlation between fatal whale strandings and solar activity (Vanselow and Ricklefs, 2005).

There is evidence that humans on the surface of Earth are also influenced by space weather conditions. After the second largest SPE event of the space era on 29 September 1989 a doubling of heart attacks was registered in Tbilisi, Georgia. Some studies suggested a link between solar activity and numbers of car accidents (see e.g. Roederer, 1995; Temuriantz *et al.*, 2007 and references therein).

1.6.8. Space Weather Forecasting

Space weather forecasting relies on the ability to model different space environments. Space weather modeling is used to predict space weather conditions. It is desirable that such models predict in an accurate, reliable and timely manner. For that reason accurate input data are required. The magnetic field is one of the most important input parameters because charged particles move more easily along magnetic field lines. Their transverse motion is opposed by the Lorentz force. Real-time input data are much desired for space weather models in order to predict in a timely manner.

1.7. Historical Overview and Magnetometer Configurations

Sputnik III was the first satellite that measured magnetic fields in space. Launched on 1958-05-15 it surveyed the magnetic field from 225 km to 800 km altitude mainly above the former Soviet Union for a 22 day period. Prior to Sputnik III sounding rockets carried magnetometers up to a height of 200 km. The magnetometer onboard of Sputnik III was a self-orientating triaxial fluxgate magnetometer (Dolginov *et al.*, 1960). The orientation of the sensor triad was adjusted so that the field at two of the three orthogonal sensors became zero. From the required angular adjustments it was possible to determine the orientation of the spacecraft by comparison with magnetic field models of Earth. Fig. 1.18 shows some of the early Sputnik III data (Dolginov *et al.*, 1962). Magnetic interferences from the spacecraft had to be modeled and subtracted from the measured data (see curves 3 and 5 in Fig. 1.18). For an introduction to fluxgate magnetometers see Sec. 1.2.2.2. More detailed information can be found in e.g. Ness (1970) or Acuña (2002) and references herein.

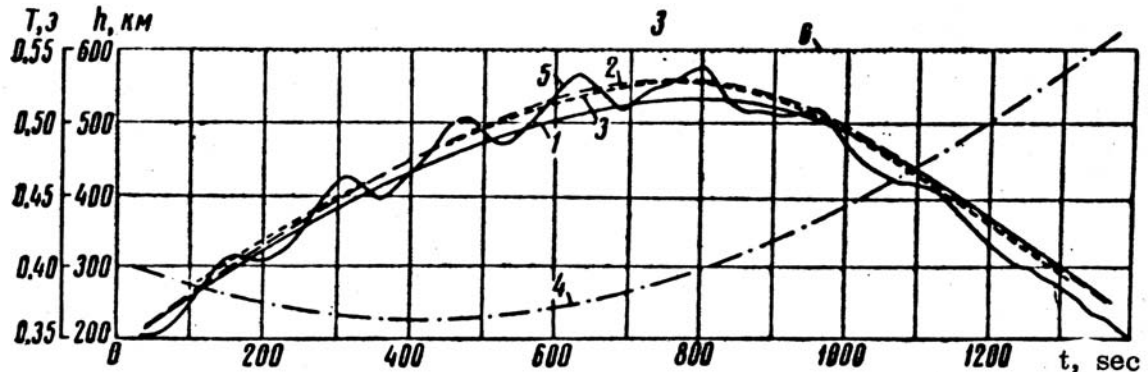


Figure 1.18. Curves 1 and 2 represent calculated magnetic field models along the trajectory from two different magnetic field models. Curve 3 (short dashes) represents the measured and corrected magnetic field data. Curve 4 represents the height of the spacecraft. Curve 5 represents the measured (uncorrected) data (Dolginov *et al.*, 1962).

After taking magnetic field measurements in space one of the next challenges was taking precise vector measurements of the weak interplanetary magnetic field. The expected strength of the interplanetary field at 1 AU is about 7 nT. This task requires stable zero levels of the magnetometer and digitization steps that are smaller than 1 nT. Additionally magnetic interferences from the spacecraft at the location of the magnetometer sensors should be kept at low levels. For example the magnetometer that was placed on Sputnik III had a zero level drift of about 12 nT per day (Dolginov *et al.*, 1962) and digitization steps of ± 40 nT (Ness, 1970). From Fig. 1.18 curve 5 one can see that there were substantial interferences from the spacecraft. Pioneer 5 launched on 1960-03-11 was the first spacecraft to take in situ measurements of the interplanetary magnetic field. It carried a search coil magnetometer (Coleman *et al.*, 1960) that only measured the component perpendicular to the spacecraft's spin axis. The vector measurements taken by the triaxial fluxgate magnetometer onboard the Mariner II spacecraft launched on 1962-08-27 were contaminated by spacecraft magnetic interferences in a way that studies of the interplanetary magnetic field were hindered

(Coleman, 1966). It was not until after the launch of the IMP 1 (Explorer 18) spacecraft until precise vector measurements of the weak interplanetary field could be obtained (Ness *et al.*, 1964). The spacecraft was launched on 1963-11-27, equipped with two mono-axial fluxgate magnetometers and a rubidium vapor magnetometer for in-flight calibration of the fluxgate magnetometers (Ness *et al.*, 1964). Fluxgate magnetometers tend to have slight drifts of the zero levels (see Table 1.1). Each of the three magnetometers was capable of producing full vector measurements. This was possible because they were oriented at angles that were neither perpendicular nor parallel to the spin axis of the spacecraft. In such a placement a mono-axial magnetometer measures a constant component that is proportional to the field parallel to the spin axis plus a spin modulated component that is proportional to the field perpendicular to the spin axis. Separation of the two components yields full vector measurements in steady fields if the phase angle of the spin modulated component is taken into account as well. For more information see Ness (1970) or Ness *et al.* (1964). Fig. 1.19 shows an example of IMP 1 measurements of the interplanetary magnetic field. The digitization steps were ± 0.25 nT. One surprising outcome of the IMP 1 interplanetary magnetic field investigation was that fluctuations of the interplanetary field are primarily changes in the direction rather than in the magnitude so that the field magnitude is more constant than any of its three component axes (Ness *et al.*, 1964). After a high amount of post processing the power spectra and histograms of the Mariner II data in Coleman (1966) reflected this property of the solar wind as well.

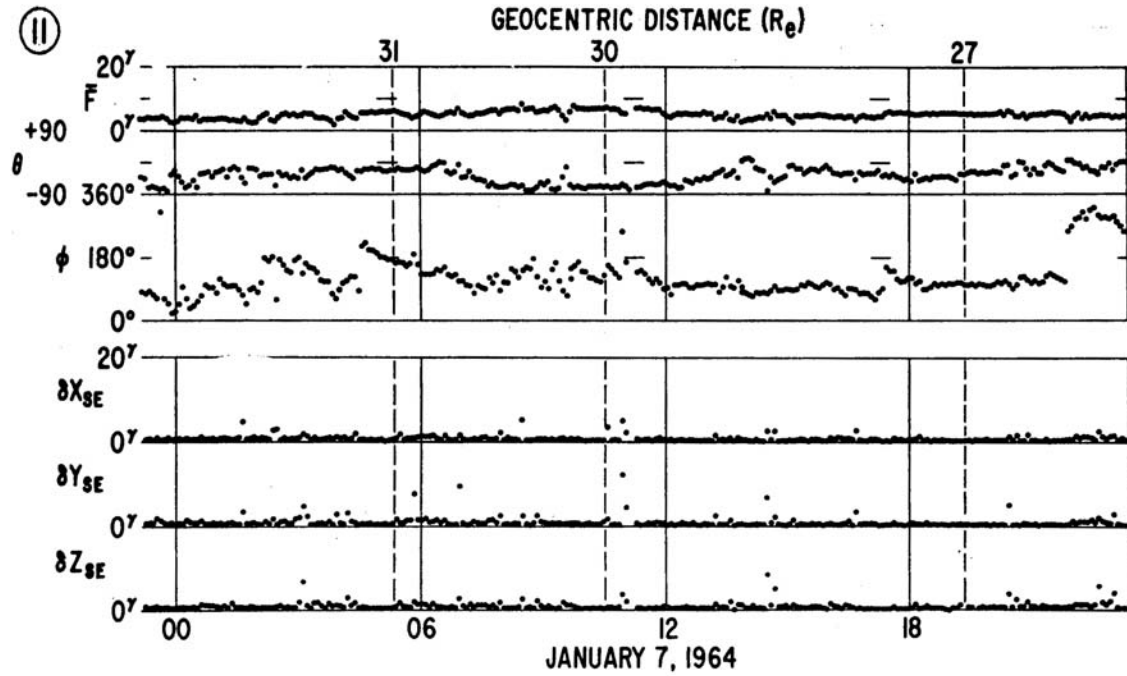


Figure 1.19. Some of the first precise measurements of the interplanetary magnetic field. The top three panels show the magnetic field in the two angle representation and the bottom three panels show the variance of the solar ecliptic components (Ness *et al.*, 1964).

Early magnetometer experiments on spinning spacecraft used a variety of sensor configurations to achieve redundancy and low weight but conserve the ability to obtain vector measurements in quiet fields. If a sensor is placed at an angle of $54^\circ 45'$ from the spin axis, vector measurements can be obtained simply by using a sampling frequency that is three times the spin frequency (Ness *et al.*, 1966). This configuration was placed on the Pioneer 6, 7 and 8 spacecraft launched on 1965-12-16, 1966-08-17 and 1967-12-13. Another configuration that was used on the ATS-1 satellite (launch date: 1966-12-07) consisted of two sensors that were placed at angles of 45° from the spin axis (see Fig. 1.20). This configuration allows the separation of the magnetic field components that are parallel and perpendicular to the spin axis by calculating the sum and the difference of the two sensor outputs (Barry and Snare, 1966).

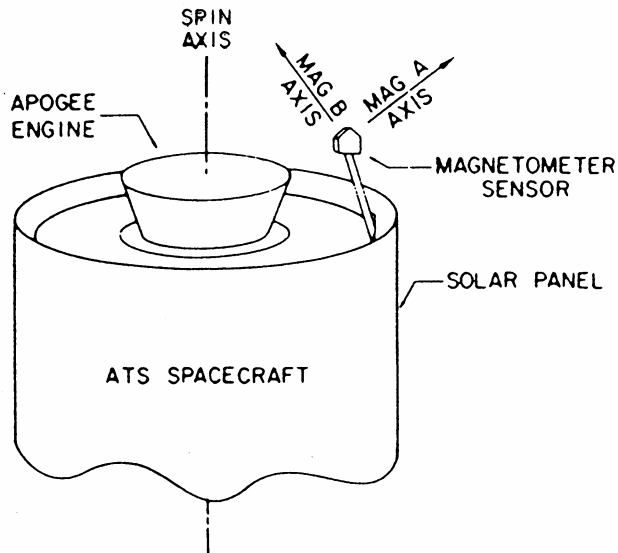


Figure 1.20. Magnetometer configuration on the ATS-1 satellite (Barry and Snare, 1966).

The magnetic field experiment on the Pioneer Venus Orbiter launched on 1978-05-20 had another interesting configuration. It consisted of two sensors parallel and perpendicular to the spin axis. A third sensor was placed at two thirds of the magnetometer boom. This sensor was tilted with respect to the spin axis by 45° and at right angles with respect to the spin plane sensor. This configuration ensured redundancy and gave the possibility to provide two full vector measurements at the end of the boom as well as at two thirds of the boom length for steady fields (Russell *et al.*, 1980, Snare 1998). Additionally vector measurements at high resolution were also possible. The differences in the vector measurements at the end of the boom and at two thirds of the boom length could be used to determine spacecraft-generated fields (gradiometer configuration). This technique was first proposed by Ness *et al.* (1971) and conceptually generalized by Neubauer (1975).

Voyager 1 and Voyager 2 are three-axis stabilized spacecraft launched on 1977-09-05 and 1977-08-20. Both spacecraft are identically equipped with four triaxial

fluxgate magnetometers (Behannon *et al.*, 1977) forming two dual magnetometers (gradiometers), one for low fields and one for high fields. The magnetometers for low fields are equipped with mechanic as well as electronic flippers. The mechanic flippers can rotate each sensor by 180° so that it points in the opposite direction. Flipping of sensors by 180° yields the zero levels. The electronic flippers reverse the sensor signal polarity for determination of zero level drifts due to radiation effects, component aging and temperature and voltage variation but not those due to changes in the magnetic properties of the materials used in the sensors. The boom length of the spacecraft is 13 meters. Tests on ground have shown that the boom deployment could cause an unknown angle around the boom axis (torsional) of up to $\pm 7^\circ$, thus requiring in-flight correction. This can be done by generating a known field on the spacecraft. For this purpose a coil was wound around the periphery of the high gain antenna. For more details see Behannon *et al.* (1977).

Explorer 33 launched on 1966-07-01 carried a triaxial fluxgate magnetometer (Ness *et al.*, 1967). The triaxial sensor set could be flipped by 90° so that the sensor that is aligned with the spin axis could be rotated into the spin plane for zero level determination. After Explorer 33 various different flipper mechanisms have been flown on a number of different missions. Flipper mechanisms that flip only one or two sensors instead of the whole sensor triad, can cause a change of the cross coupling between the individual sensors. Such a change of cross coupling can lead to a slightly non-orthogonal sensor triad (Russell *et al.*, 1995). Examples of magnetometer experiments that flipped two sensors are ISEE 1, ISEE 2 (Russell, 1978) both launched on 1977-10-22 and Galileo (Kivelson *et al.*, 1992) launched on 1989-10-18.

Besides fluxgate magnetometers, another common type of magnetometer that is used for magnetic field investigations in space is the Vector Helium Magnetometer also called Low-Field Vector Helium magnetometer. A scalar Helium Vapor Magnetometer can be turned into a Low-Field Vector Helium Magnetometer by adding a Helmholtz Coil around the gas cell (Shapiro *et al.*, 1960). Another way of obtaining vector measurements is the use two sets of deflection coils. This configuration gives the total field and two angles that can define a field vector. On a spinning spacecraft and for the case of a steady field only one set of deflection coils is required (Heppner *et al.*, 1963). It is important to point out that there are fundamental differences between the Low-Field Vector Helium Magnetometer and the scalar Helium Vapor Magnetometer, besides vector versus scalar measurements. Unlike the scalar Helium Vapor Magnetometer, the different types of Alkali Vapor Magnetometers and the Proton Precession Magnetometer and its modified version the Overhauser Magnetometer, the accuracy of the Low-Field Vector Helium Magnetometer is not directly derived from intrinsic magnetic properties of the fundamental particles in the atom. Thus it is not an absolute magnetometer. Its operation is somewhat similar to the fluxgate magnetometer (Ness, 1970) because it operates with field cancellation loops. Vector Helium Magnetometers outperform fluxgate magnetometers in sensitivity and stability but at the expense of lower bandwidth, weight, power consumption and cost (Acuña, 2002). Some of the space missions that carried Low-Field Vector Helium Magnetometers were, Mariner 3, 4 and 5 (launched on 1964-11-05, 1964-11-28 and 1967-06-14), Pioneer 10 and 11 (launched on 1972-03-03

and 1973-04-06), ISEE 3 (launched on 1978-08-12), Ulysses (launched on 1990-10-06), Cassini-Huygens (launched on 1997-10-15). More information on Vector Helium Magnetometers can be found in, Frandsen *et al.* (1978), Balogh *et al.* (1992), Southwood *et al.* (1992), Acuña (2002) and Dougherty (2004).

Proton Precession Magnetometers have been flown on early space missions such as Vanguard 3 launched on 1959-09-18 (Cain *et al.*, 1962), Cosmos 26 launched on 1964-03-18 and Cosmos 49 launched on 1964-10-24. Another interesting reference is Hurwitz and Nelson (1960). Proton Precession Magnetometers have not been carried into space recently. Overhauser magnetometers are onboard the Danish Ørsted satellite launched on 1999-02-23 (Duret *et al.*, 1995) as well as on the German satellite CHAMP launched on 2000-07-15.

Precise scalar magnetometer can be put together with triaxial fluxgate magnetometers onto a spacecraft. Such a configuration can improve the in-flight calibration of the fluxgate magnetometer. Space missions with such a configuration are MAGSAT (Langel *et al.*, 1982) launched on 1979-10-30, Ulysses, Cassini-Huygens, Ørsted and CHAMP. The theory behind this type of cross-calibration was published by Merayo *et al.* (2000). The application of this type of calibration is described in Olsen (2003). Another interesting reference is Dougherty (2004).

An Electron Drift Instrument can measure the scalar magnetic field with high precision and can be used to cross-check the calibration of fluxgate magnetometers. Electron Drift Instruments together with fluxgate magnetometers have been flown on the ESA-GEOS 1 satellite (Melzner, 1978) launched on 1977-04-20, on the EQUATOR-S mission (Paschmann *et al.*, 1999) launched on 1997-12-02 and on the four Cluster satellites launched on 2000-07-16 and 2000-08-09 (Paschmann *et al.*, 1988 and 1997).

Another common type of space-borne magnetometer is the Search Coil Magnetometer. Search coil magnetometers have been carried into space on various space missions starting as early as Pioneer 1 launched on 1958-10-11 (Sonett, 1962) until more recently on the Cluster mission (CornilleauWehrlin 1997) and the THEMIS mission launched on 2007-02-17 (Roux, 2008).

1.8. Introduction to Calibration of Space-borne Magnetometers

1.8.1. Ground Calibration and Magnetic Cleanliness

Space-borne magnetometers are calibrated before launch most commonly inside a ground calibration facility (see Fig. 1.21). Helmholtz coils are used to compensate the Earth's magnetic field. Well-defined reference fields are then generated inside the Helmholtz coil. Long term noise and offset stability can be tested inside a temperature controlled mu-metal can. There are additional as well as alternative ground calibration techniques which exceed the scope of this introduction (Acuña, 2002; Lohr *et al.*, 1997; Risbo *et al.*, 2003; Auster, 2002 and Hinkal, 1980).



Figure 1.21. Helmholtz coil system for ground calibration (Photo: Imperial College, London).

Another important task besides ground calibration of the magnetometer itself is the magnetic cleanliness program. At the location of the magnetometer sensor, there should be no spacecraft-generated fields or a well known stable magnetic field. This task starts with the definition of the magnetic cleanliness requirements. All components and instruments onboard the spacecraft need to have such magnetic properties that the magnetic cleanliness requirements can be reached. Common problematic devices are fuel tanks, all kinds of electric motors, electromagnetic valves, electromagnetic switches, heater currents, power supply currents and solar panel currents. For more information see Ludlam *et al.* (2008), Narvaez (2004), Lohr (1997). An example of magnetic disturbances measured in space due to heater currents can be found in Anderson *et al.* (2001). Usually a magnetic model of the spacecraft is being put together from magnetic measurements of sub-systems before launch (Mehlem, 1978). Such a model can also be used to optimally

position multiple magnetometers on a spacecraft (Delva *et al.*, 2002). The magnetic properties of spacecraft sub-systems are typically measured inside transportable Helmholtz coil systems, ground calibration facilities (see Fig. 1.21) or gradiometer setups (see Fig. 1.22).



Figure 1.22. Gradiometer setup for magnetic measurements on spacecraft sub-systems (as used for the Rosetta Lander magnetic cleanliness program).

The magnetic cleanliness requirements can be verified at large facilities that can compensate the magnetic field of Earth, thus making it possible to put the whole spacecraft into a space that is free of magnetic fields. Examples of such facilities are at the Ames Research Center in Sunnyvale (California), IABG near Munich (Germany) and another one is at Goddard Space Flight Center (Maryland). At such facilities the magnetic fields that are generated by the spacecraft can be measured at the location of the magnetometer sensor and well known reference fields can be generated. An example can be found in (Lohr, 1997). The soft-magnetic properties of the spacecraft can be analyzed as well. In some cases permanent magnets that compensate the DC-magnetic field that is generated by the spacecraft (at the location of the magnetometer sensor) are permanently attached (glued) to the spacecraft (Kügler, 2001). Some of the shortcomings of such facilities are that the conditions that the spacecraft will encounter in space cannot be simulated, such as thermal vacuum and zero gravity. Additionally not all the devices on the spacecraft that generate magnetic fields may be fully operational in such a facility (e.g. power supplies). Another important disadvantage is the very high cost of transporting the spacecraft to such a facility and renting the facility. Even if the magnetic testing in such a facility shows that not all the magnetic cleanliness requirements have been reached, required changes to spacecraft sub-systems often cannot be made due to cost and overall schedule of the mission. A cheaper solution is just to measure the sub-

systems of the spacecraft and build a magnetic model. Such reduced magnetic cleanliness programs are described in Kuhnke *et al.* (1998) and Narvaez (2004). In case of the THEMIS mission, consisting of five small satellites, a whole satellite could fit into the JPL Helmholtz coil facility (Ludlam *et al.*, 2008). After completion of the magnetic testing the spacecraft should not be exposed to very large magnetic fields. The soft-magnetic materials on the spacecraft might simply change their generated magnetic fields and the results of the magnetic testing may be obsolete. Changes of the spacecraft after magnetic testing, especially close to the magnetometer sensor, must be done with additional emphasis on magnetic cleanliness of the changes.

In a nutshell, the magnetic cleanliness program forces additional requirements onto a large number of spacecraft sub-systems and may cause design changes such as magnetic shielding of sub-systems and components, changes in the wiring diagrams of solar panels, heaters and other circuits (Acuña *et al.*, 1996; Ludlam *et al.*, 2008; Narvaez 2004; Lohr, 1997). This is the reason why a lot of space missions have reduced magnetic cleanliness programs. In some cases even magnetometer booms are too expensive or too heavy or both. Examples of missions with magnetic field experiments but without magnetometer booms are NEAR launched on 1996-02-17, where the magnetometer was placed onto the high gain antenna (Lohr, 1997) and Mars Global Surveyor (Acuña *et al.*, 1998) launched on 1996-11-07 where magnetometers were attached to the solar panels. Magnetometer data from such missions are usually not perfect and require large amounts of post processing. Examples of such post processing procedures can be found at Acuña *et al.* (2001) and Anderson *et al.* (2001). For example, magnetometer data of very high quality were obtained from the four Cluster satellites (Balogh, *et al.*, 2001). This was due to well built magnetometers, decent magnetic cleanliness program (Kügler, 2001) and a relatively long radial boom (5 m). Magnetic disturbances from dipole-like sources decrease with distance with one over distance cubed. Magnetic disturbances from higher order multipoles decrease even faster. With other words a small increase in boom length can lead to a large decrease of magnetic disturbances at the location of the magnetometer sensors.

The Venus Express (launched on 2005-11-09) magnetic field experiment had no magnetic cleanliness program and a very short boom of only 1 m. One magnetometer was directly placed onto the spacecraft surface and the other was placed at the tip of the boom. The dual magnetometer technique is described in Zhang *et al.* (2008). A very high amount of sophisticated post processing had to be done to successfully clean the data (see Pope *et al.*, 2011).

As described above actual implementations of magnetic field experiments on spacecraft are often the result of many compromises. Important factors of consideration are scientific goals, budget, weight, power consumption, risk factors (e.g. redundancy and radiation protection) and time constraints as well as communication efforts for implementation.

1.8.2. Calibration Parameters and In-flight Calibration of Space-borne Magnetometers from Natural Constraints and Comparisons to Model Fields (Thesis Overview)

After introducing various magnetometer configurations, ground calibration and magnetic cleanliness, an introduction to calibration parameters and in-flight magnetometer calibration from natural constraints and model fields will be given.

There are three major types of calibration parameters: offsets (also referred to as zero levels), gains (also referred to as scale factors) and angles. Offsets are additive errors that add or subtract a certain value from the true value of the measured quantity. Gains are multiplicative errors (scaling errors). Angles describe the misalignments of the sensor triad. Altogether there are three offsets, three gains and six angles that need to be resolved in order to calibrate the magnetometer. How the magnetic field that is measured by the magnetometer sensors and the calibrated magnetic field are related via calibration parameters is described by equation (1.1).

$$\begin{pmatrix} B_{S_1} \\ B_{S_2} \\ B_{S_3} \end{pmatrix} = \begin{pmatrix} G_1 \sin \theta_1 \cos \varphi_1 & G_1 \sin \theta_1 \sin \varphi_1 & G_1 \cos \theta_1 \\ G_2 \sin \theta_2 \cos \varphi_2 & G_2 \sin \theta_2 \sin \varphi_2 & G_2 \cos \theta_2 \\ G_3 \sin \theta_3 \cos \varphi_3 & G_3 \sin \theta_3 \sin \varphi_3 & G_3 \cos \theta_3 \end{pmatrix} \cdot \begin{pmatrix} B_x \\ B_y \\ B_z \end{pmatrix} + \begin{pmatrix} O_1 \\ O_2 \\ O_3 \end{pmatrix} \quad (1.1)$$

B_{S_1} , B_{S_2} , B_{S_3}	non-orthogonal field components as measured by the magnetometer sensors
B_x , B_y , B_z	orthogonalized field components
G_1 , G_2 , G_3	gain corrections of each of the sensors
θ_1 , θ_2 , θ_3	elevation angles of each of the sensors
φ_1 , φ_2 , φ_3	azimuthal angles of each of the sensors
O_1 , O_2 , O_3	offsets of each of the sensors

The twelve calibration parameters are determined before launch via ground calibration procedures (see Sec. 1.8.1.). The matrix in equation (1.1) is the inverse of a calibration matrix. A calibration matrix corrects the measurements in sensor coordinates (B_{S_1} , B_{S_2} and B_{S_3}). There are a number of different techniques to adjust the ground calibration parameters in-flight. Such adjustments may be necessary because the calibration parameters may change in time throughout the mission. Especially zero levels of fluxgate magnetometers have a general tendency to change. Zero levels and scale factors tend to drift due to changes in temperature, aging of the electronics and exposure to radiation. Another source of drifting zero levels that is independent of the magnetometer itself are spacecraft generated fields (see Sec. 1.8.1.). Angles can be divided into two major groups. First: angles that determine the orthogonalization of the sensor triad (see Chapter 3.). Second: angles that determine the absolute orientation of the sensor triad in space or with respect to the orientation of the spacecraft (see Chapter 4.).

Changes of the orthogonalization of the sensor triad can be due to slight mechanical changes e.g. caused by vibration during launch and fast temperature changes. Another source of changes in orthogonalization can be flipper mechanisms that do not flip the whole sensor triad but one or two individual sensors (Russell *et al.*, 1995). Changes of the absolute orientation can be caused by boom deployment mechanisms and flipper mechanisms as well as vibration during launch and temperature changes. Bending of a slightly flexible magnetometer boom can be another source of changes in absolute orientation. Such changes can occur during spacecraft maneuvers, temperature changes, change of spin period on spinning spacecraft and aging on non-radial booms on spinning spacecraft. Non-radial booms on spinning spacecraft continuously experience a centrifugal force that is not aligned with the boom axis. Boom bending can be estimated via a dual magnetometer system (Farrell *et al.*, 1995). The change of absolute orientation is smaller for the inboard magnetometer.

Chapter 2. describes the magnetometer zero level determination on three axis stabilized spacecraft as well as the zero level determination of the magnetometer sensors that are aligned with the spin axis on spinning spacecraft. Techniques are presented that can be applied inside the interplanetary magnetic field and techniques that can be applied inside a magnetosphere. To the best of the author's knowledge, there are no published techniques for finding magnetometer zero levels inside the low field regions of a magnetosphere. For the first case (inside the interplanetary magnetic field) zero levels are calculated via the property that fluctuations of the interplanetary field are primarily changes in the direction rather than in the magnitude so that the field magnitude is more constant than any of its three component axes (Ness *et al.*, 1964). Wrong zero levels lead to an increase of the fluctuations of the field magnitude (Davis and Smith 1968; Rosenberg 1971; Belcher 1973; Hedgecock, 1975; Acuña, 2002). The theory of previously published calibration methods is generalized and an improved calibration method (Leinweber *et al.*, 2008) that also provides error estimates is presented. I apply the technique to THEMIS (Auster *et al.*, 2008), STEREO (Acuña *et al.*, 2008) and Venus Express (Zhang *et al.*, 2008) magnetic field data data. For the second case (inside the low field regions of a magnetosphere), pure changes of the field magnitude are used to obtain the zero levels. Such pure changes of the field magnitude inside a magnetosphere can be caused by mirror-mode waves (Chandrasekhar, 1958; Fazakerley and Southwood, 1994) as well as drift mirror-mode waves (Hasegawa, 1969; Tsurutani *et al.*, 1982). Erroneous zero levels cause artificial changes in the direction of a field that should only change its magnitude. A novel new calibration technique for finding zero levels inside the magnetosphere is presented and applied to THEMIS data.

Chapter 3. describes the orthogonalization of the sensor triad on spinning spacecraft. The orthogonalization procedure removes the spin tone that is left when magnetometer data are transformed from a spinning to a non-spinning coordinate system. This spintone consists of first and second harmonics of the spacecraft spin frequency for the spin plane sensors and a first harmonic for the spin axis sensor. The three different types of harmonics can be linked to specific calibration parameters (Kepko *et al.*, 1996).

1. First harmonics in the spin plane sensors are produced by miscalibrated O_1 , O_2 , θ_1 and θ_2 .
2. Second harmonics in the spin plane sensors are produced by miscalibrated ΔG_{21} and $\Delta\varphi_{21}$. Where $\Delta G_{21} = G_2 - G_1$ and $\Delta\varphi_{21} = \varphi_2 - \varphi_1$, thus the second harmonics depend on the relative spin plane gains and the relative azimuthal angles of the spin plane sensors and are independent of their absolute values.
3. First harmonics in the spin axis sensor are produced by miscalibrated θ_3 and φ_3 .

The calibration parameters O_3 , G_3 , the absolute values G_1 , G_2 , the absolute values of φ_1 and φ_2 cannot be linked to spin harmonics. First, the technique described in Kepko *et al.* (1996) is presented. This technique is FFT-based and thus does not converge for fast changes of the spin harmonics. Furthermore, an improved version of the technique for fast changing magnitudes of the spin harmonics is presented which was used for recalibration of the Galileo magnetic field data (Kivelson *et al.*, 1992 and Yu *et al.*, 2010). Additionally, the theory and the application of an orthogonalization technique for relatively fast changing calibration parameters that was developed for the Cluster (Balogh *et al.*, 2001) mission is presented. Such fast changes can occur during and after eclipsed periods of a spacecraft.

Chapter 4. describes the calibration of the absolute values of gains as well as determination of absolute orientations via comparison of the magnetometer data with geophysical model fields (e.g. Tsyganenko, 2002a; b). The theory and its application to the magnetic field experiments onboard the spinning spacecraft Galileo (Kivelson *et al.*, 1992), the three axes stabilized STEREO-B (Acuña *et al.*, 2008) spacecraft as well as the attitude determination for the spinning Polar (Russell *et al.*, 1995) and THEMIS spacecraft (Angelopoulos, 2008) is described.

Chapter 5. describes the calibration of triaxial fluxgate magnetometers from accurate measurements of the field magnitude (Merayo *et al.*, 2000; Olsen, 2003; Dougherty *et al.*, 2004). This type of cross calibration can yield all calibration parameters except absolute orientation of the sensor triad. The scalar magnetic field from the Electron Drift Instrument (Paschmann *et al.*, 1997) onboard the Cluster-3 satellite to cross calibrate the fluxgate magnetometer (Balogh *et al.*, 2001) is described. Calibration parameters are calculated that are independent of orthogonalization, except those for absolute orientation. For a spinning spacecraft, the calibration parameters are absolute values of gains G_1 , G_2 , G_3 and the spin plane offset O_3 .

Chapter 6. describes inter spacecraft calibration techniques. The application of the inter spacecraft calibration technique that was first developed for the Cluster mission but with new much shorter equations that yield the same results as the original equations (Khurana *et al.*, 1996) is described. The new equations are roughly an order of magnitude shorter (76 shorter terms vs. 342 longer terms). At times when the four Cluster satellites

flew in a tetrahedron configuration it was possible to determine the curl and the divergence of the magnetic field. When the tetrahedron crosses the tail lobes both the divergence and the curl of the magnetic field should be zero. Because of small calibration errors of the calibration parameters that cannot be found by orthogonalization, the values for curl and divergence are not exactly zero. Thus the following calibration parameters can be determined: G_1 , G_2 , G_3 , φ_1 , φ_2 and O_3 . These calibration parameters can only be corrected for three spacecraft because the technique requires a so-called mother spacecraft. Additionally the orientation of the spin axes of three spacecraft (except for the mother spacecraft) can be corrected. In Appendix B, a simple technique for zero level matching of multiple spacecraft is described.

1.8.2.1. Summary

For convenience of the reader, Table 1.3 summarizes the advances of this thesis to the field of calibration of space-borne magnetometers.

	topic	previous state of the art	advance
Chapter 2	Finding magnetometer zero levels inside the interplanetary magnetic field	Various published methods	Generalization of the theory of previously published methods. Development of an improved method that provides error estimates
	Finding magnetometer zero levels inside the low field regions of a magnetosphere	No published method	Development of a new method that provides error estimates
Chapter 3	Orthogonalization of a sensor triad on a spinning spacecraft	FFT-based method	Development of a method for fast changing spin harmonics. Development of a method for fast changing calibration parameters.
Chapter 4	Model comparisons	Various published methods for attitude determination from magnetic field	Combination of attitude determination and magnetometer calibration. Recovering the attitude plus spin phase and calibration parameters e.g. during eclipsed periods, for missions that only have a Sun sensor.
Chapter 5	Calibration of a spinning fluxgate magnetometer from EDI gyro-times.	Various suggested methods that do not match the gains	Development of a method that matches the instrument gains before finding the zero levels. Analysis EDI of noise distributions.
Chapter 6	Minimizing of curl and divergence of B inside the lobe regions of a magnetosphere	Method that uses equations that have 342 longer terms.	Solve the same problem with only 76 shorter terms. Application of the minimization for the first time to measured data.

Table 1.3. Advances to the field of in-flight calibration of space-borne magnetometers.

2. In-flight Determination of Magnetometer Zero Levels

2.1. Introduction

Post-launch spacecraft magnetometer zero levels can differ from their pre-launch values for many reasons. Some of the most common issues are temperature changes of the sensor and the electronics, varying magnetic fields of the spacecraft due to electric currents or magnetic permeability, aging of electronic parts, exposure to strong radiation, and other causes. See Acuña (2002) for a general review on space-based magnetometers. A historical review on measurements of the interplanetary magnetic field can be found in Ness and Burlaga (2001). Also see Snare (1998) for historical review on vector magnetometry in space. For a spinning spacecraft the zero levels of the component axes that lie in the spin plane can be estimated by averaging in the spinning spacecraft frame over many spin periods when gains and angles are known to high enough precision and the magnetic field is constant during the averaging period. However spacecraft generated AC-magnetic fields at the spin frequency in the spinning frame will cause erroneous zero levels in the despun spacecraft frame, that cannot be found by averaging. For a discussion of the calibration of magnetometers on spinning spacecraft such as determining relative gains and orientations see Kepko *et al.* (1996). Farell *et al.* (1995) is another reference on the calibration of magnetometers on spinning spacecraft but it omits relative gains. A commonly used term for zero level is offset. Both terms are being used interchangeably throughout this chapter.

2.2. An Advanced Approach to Finding Magnetometer Zero Levels in the Interplanetary Magnetic Field

In the solar wind a simple method that can be used to determine constant or extremely slowly varying zero levels, is averaging of the magnetic field values over a few solar rotations. The averages of all three component axes should be zero since the divergence of B is zero, and the configuration of the solar magnetic field should not be correlated with the spacecraft location. However, there are field configurations that can be symmetric about the Sun's rotation axis such as those associated with the g_1^0 , g_2^0 , g_3^0 , ... coefficients of the Legendre polynomial expansion (see, for example, Altschuler *et al.* 1977 and references therein), so this technique is not foolproof. Furthermore this technique requires that the spacecraft stays in the interplanetary magnetic field continually and it returns an average zero level at most only monthly. It is desirable to determine offsets much more often and to not rely on the Sun having a favorable magnetic configuration. Fluctuations of the interplanetary field are primarily changes in direction rather than in magnitude so that the field magnitude is more constant than any of its three component axes (Ness *et al.*, 1964). See also power spectra and histograms in Coleman (1966). Fortunately, the Alfvénic nature (Belcher *et al.*, 1969) of the solar wind fluctuations allows us to determine offsets comparatively rapidly, much faster than once per month.

There are three documented methods for finding zero levels in the interplanetary magnetic field, based on the above described property of the interplanetary magnetic field to determine slowly changing zero levels. The first method developed is called the Davis-Smith method (Davis and Smith, 1968). This method optimizes the zero levels so that the variance of the squared magnitude of the magnetic field is minimized. Rosenberg (1971) provides a detailed derivation of this technique. The Davis-Smith equation (2.22) was not published until Belcher (1973) developed his own method and compared it with the Davis-Smith method. Below an alternative derivation of the Davis-Smith method and to the variant of Belcher (1973) is described, which gives greater insight into the methodology. The Belcher method optimizes the zero levels so that the maximum variance vector is orthogonal to the background field. The third method, (Hedgecock, 1975) is based on the assumption that averaged over a suitable time interval, there should be no correlation between changes in field magnitude and changes in the inclination of the field to any one of the three component axes.

All three methods must be applied with some caution because the assumptions, on which each particular method is based, might not always be true. Their results stand and fall with the appropriate selection criteria for data intervals. The Davis-Smith method has no published selection criteria. Davis and Smith selected by eye (Belcher, 1973). Belcher and Hedgecock published rather loose selection criteria that require long intervals (a few days to weeks) of input data.

In this work, the Davis-Smith method has been modified to determine magnetometer zero levels on much shorter time scales than previously possible. While

this can be useful for all missions, it is particularly useful when the spacecraft spends most of the time inside a magnetosphere and only occasionally enters the interplanetary magnetic field. The magnetic field usually is observed close to the bow shock and in many cases highly disturbed by non-Alfvénic upstream waves, or the spacecraft might observe the interplanetary field only because of very unusual solar wind conditions that have higher than average dynamic pressure values. The revised method herein can also be used for missions that require adjustment of zero levels at more frequent intervals than a few days as required for the published selection criteria of Belcher and of Hedgecock. Such missions may not have had an appropriate magnetic cleanliness program and therefore the magnetic field at the location of the magnetometer is heavily disturbed by the spacecraft's own time varying magnetic field, or they may experience diurnal variations due to changing spacecraft or sensor fields as the solar illumination or spacecraft temperature vary with orientation or orbital position.

For convenience of the reader below all three methods are reviewed. This review gives us further insight into the differences between the three techniques and serves to illuminate the new improvements. The Belcher and the Hedgecock methods are discussed first.

2.2.1. Belcher's Method

This method is based on the assumption that the fluctuations of the solar wind are predominantly transverse to the background field (2.1). It optimizes the zero levels so that the maximum variance vector (Sonnerup, 1967) is orthogonal to the background field (2.2). Triangular brackets denote averages.

$$\delta\vec{B}_{\parallel} = \delta\vec{B} \cdot \frac{\langle \vec{B}_A \rangle}{\langle \langle \vec{B}_A \rangle \rangle} \approx 0 \quad (2.1)$$

where

$\delta\vec{B}$	unit vector in maximum variance direction
$\delta\vec{B}_{\parallel}$	part of $\delta\vec{B}$ in the direction of the background field
\vec{B}_A	actual background field vector

$$\delta\vec{B}_{\parallel} \equiv 0 \quad (2.2)$$

Assuming that the measured field \vec{B}_M consists of the actual field \vec{B}_A plus a constant offset vector \vec{O} the following equation can be obtained

$$\delta\vec{B} \cdot \langle \vec{B}_M \rangle = \delta\vec{B} \cdot \vec{O} + \delta\vec{B} \cdot \langle \vec{B}_A \rangle \quad (2.3)$$

writing the sum over n data-windows (triangular brackets denote averages over single data-windows)

$$D = \sum_{i=1}^n \left(\delta \vec{B}^i \cdot \langle \vec{B}_A^i \rangle \right)^2 = \sum_{i=1}^n \left[\delta \vec{B}^i \cdot \left(\langle \vec{B}_M^i \rangle - \bar{O} \right) \right]^2 \quad (2.4)$$

and using $\frac{dD}{d\bar{O}} = 0$ Belcher's matrix equation can be obtained

$$\sum_{i=1}^n T^i \cdot \bar{O} = \sum_{i=1}^n T^i \langle \vec{B}_M^i \rangle \quad (2.5)$$

where

- | | |
|-------|--|
| i | index of data-window |
| T^i | outer product of $\delta \vec{B}^i$ (T is a matrix) |
| n | number of data-windows |

The matrix on the left hand side of (2.5) is singular for $n=1$ but (2.5) can still be used by selecting several data-windows and solving the system of equations by using a least squares approach. Belcher's method has two selection criteria that need to be applied to each data-window. The method requires the precise knowledge of the maximum variance direction and therefore one of his selection criteria is: $\lambda_3/\lambda_1 \leq 0.1$. Where λ_1, λ_2 and λ_3 are the eigenvalues (in descending magnitude) of the same covariance matrix that was used to find the maximum variance direction (Sonnerup, 1967). His other selection criterion requires the sum of the eigenvalues to be several times above the noise level. For more detailed information see Belcher (1973).

2.2.2. Hedgecock Method

This method is based on the assumption that averaged over a suitable time interval, there should be no correlation between changes in field magnitude and changes in the inclination of the field to any one of the three coordinate axes. The word "changes" refers to first differences (differences of consecutive measurements, a simple approximation to the time derivative). Figure 2.1 shows the relationship between the actual field magnitude B_{t_A} , the measured field magnitude B_{t_M} and the offset O . Using the law of cosines to write

$$B_{t_A}^2 = B_{t_M}^2 + O^2 - 2B_{t_M}O \cos(\theta) \quad (2.6)$$

where θ is the elevation angle.

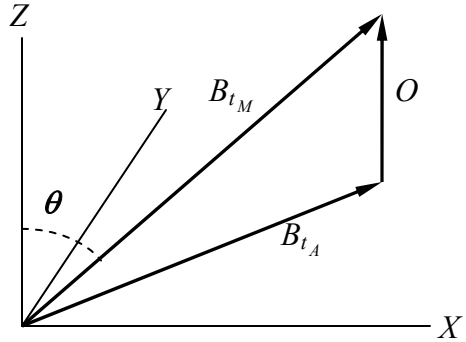


Figure 2.1. Relationship between the actual field magnitude B_{t_A} , the measured field magnitude B_{t_M} and the offset O .

Taking B_{t_A} and O as constants, differentiating and collecting terms to obtain

$$dB_{t_M} = \frac{O \sin \theta d\theta}{1 - \frac{O}{B_{t_M}} \cos \theta} \quad (2.7)$$

Assuming that the term $\frac{O}{B_{t_M}} \cos \theta$ is small (offset is small or the measured field is approximately normal to the Z-axis) to further obtain

$$\Delta B_{t_M} = O \sin \theta \Delta \theta \quad (2.8)$$

Since $\sin \theta$ is positive for $0 < \theta < 180^\circ$, the sign of ΔB_{t_M} relative to $\Delta \theta$ depends on the sign of O . The covariance $C_{(O)}$ between ΔB_{t_M} and $\Delta \theta$ changes sign as O crosses through zero ($C_{(O)} = -C_{(-O)}$ and $C_{(0)} = 0$). Writing the equation

$$C_{(O_k)} = \frac{\sum_{j=1}^N \Delta B_{t_M(O_k)_j} \Delta \theta_{(O_k)_j}}{N-1} - \frac{\sum_{j=1}^N \Delta B_{t_M(O_k)_j} \sum_{j=1}^N \Delta \theta_{(O_k)_j}}{N(N-1)} \quad (2.9)$$

where

$\Delta B_{t_M(O_k)_j}$ difference between two consecutive measured field values at k^{th} iteration

$\Delta \theta_{(O_k)_j}$ difference between two consecutive inclination angles at k^{th} iteration

$C_{(O_k)}$ covariance for the k^{th} value of O

N length of data-window

The method requires that $C_{(O_k)}$ is calculated for a range of different offsets (eg. using 0.1 nT steps for the offsets). The offset at the zero crossing of the covariances is the desired offset. Hedgecock's selection criteria are such that pairs of measurements are rejected if $\theta_{(O_k)}$ lies outside of the range $30 < \theta_{(O_k)} < 150$ or $\Delta B_{t_{M(O_k)}} > 1$ nT. For more details see Hedgecock, (1975).

2.2.3. Davis-Smith Method

The original derivation of the Davis-Smith method was never published in a refereed journal. It is based on minimization of the variance of the squared magnitude of the magnetic field of several (n) data-windows. The initially observed uncorrected variance is

$$V_i = \left\langle \left[\vec{B}_{M_i} \cdot \vec{B}_{M_i} - \langle \vec{B}_{M_i} \cdot \vec{B}_{M_i} \rangle \right]^2 \right\rangle \quad (2.10a)$$

Expanding

$$V_i = \left\langle (\vec{B}_{M_i} \cdot \vec{B}_{M_i})^2 - 2(\vec{B}_{M_i} \cdot \vec{B}_{M_i}) \langle \vec{B}_{M_i} \cdot \vec{B}_{M_i} \rangle + \langle \vec{B}_{M_i} \cdot \vec{B}_{M_i} \rangle^2 \right\rangle \quad (2.10b)$$

which reduces to

$$V_i = \left\langle (\vec{B}_{M_i} \cdot \vec{B}_{M_i})^2 \right\rangle - \langle \vec{B}_{M_i} \cdot \vec{B}_{M_i} \rangle^2 \quad (2.10c)$$

If the magnetic field measurement is corrected by subtracting an offset vector \vec{O}_i the variance of the correction becomes

$$V_i^c = \left\langle \left[(\vec{B}_{M_i} - \vec{O}_i) \cdot (\vec{B}_{M_i} - \vec{O}_i) \right]^2 \right\rangle - \langle (\vec{B}_{M_i} - \vec{O}_i) \cdot (\vec{B}_{M_i} - \vec{O}_i) \rangle^2 \quad (2.11a)$$

Expanding again

$$\begin{aligned} V_i^c = & \left\langle B_{M_i}^4 - 4B_{M_i}^2(\vec{O}_i \cdot \vec{B}_{M_i}) - 4O_i^2(\vec{O}_i \cdot \vec{B}_{M_i}) + 4\vec{O}_i(\vec{B}_{M_i} \cdot \vec{B}_{M_i})\vec{O}_i + O_i^4 + 2B_{M_i}^2O_i^2 \right\rangle \\ & - \langle B_{M_i}^2 \rangle^2 + 4\langle \vec{O}_i \cdot \vec{B}_{M_i} \rangle \langle B_{M_i}^2 \rangle + 4\langle O_i^2 \rangle \langle \vec{O}_i \cdot \vec{B}_{M_i} \rangle - 4\langle \vec{O}_i \cdot \vec{B}_{M_i} \rangle \langle \vec{O}_i \cdot \vec{B}_{M_i} \rangle - \langle O_i^2 \rangle^2 - 2O_i^2 \langle B_{M_i}^2 \rangle \end{aligned} \quad (2.11b)$$

which reduces to

$$\begin{aligned} V_i^c = & \left\langle B_{M_i}^4 \right\rangle - \left\langle B_{M_i}^2 \right\rangle^2 + 4\vec{O}_i \langle \vec{B}_{M_i} \cdot \vec{B}_{M_i} \rangle \vec{O}_i - 4\langle \vec{O}_i \cdot \vec{B}_{M_i} \rangle \langle \vec{O}_i \cdot \vec{B}_{M_i} \rangle - 4\langle B_{M_i}^2(\vec{O}_i \cdot \vec{B}_{M_i}) \rangle + 4\langle B_{M_i}^2 \rangle \langle \vec{O}_i \cdot \vec{B}_{M_i} \rangle \end{aligned} \quad (2.11c)$$

where

V_i	variance of the squared field magnitude of data-window i
V_i^c	variance after offset adjustment
\vec{B}_{M_i}	measured magnetic field vectors of data-window i
\vec{O}_i	offset vector of data-window i

Let:

$$Q_i = \langle B_{M_i}^4 \rangle - \langle B_{M_i}^2 \rangle^2 \quad \text{scalar} \quad (2.12)$$

$$W_i = \langle B_{M_i}^2 \vec{B}_{M_i} \rangle - \langle B_{M_i}^2 \rangle \langle \vec{B}_{M_i} \rangle \quad \text{vector} \quad (2.13)$$

$$D_i = \langle \vec{B}_{M_i} \vec{B}_{M_i} \rangle - \langle \vec{B}_{M_i} \rangle \langle \vec{B}_{M_i} \rangle \quad \text{dyadic (covariance matrix)} \quad (2.14)$$

The above values (2.12 to 2.14) are all constants depending only on the measured values of \vec{B}_M .

Then:

$$V_i^c = Q_i + 4\vec{O}_i(D_i)\vec{O}_i - 4\vec{O}_i W_i \quad (2.15)$$

Minimization of V_i^c by differentiating with respect to \vec{O}_i gives

$$\vec{O}_i(D_i) = \frac{\vec{W}_i}{2} \quad (2.16)$$

which is the Davis-Smith equation. For a mathematically less abstract version of this equation see (2.22). Combination of all data-windows leads to

$$\sum_{i=1}^n D_i \cdot \vec{O} = \frac{1}{2} \sum_{i=1}^n \vec{W}_i \quad (2.17)$$

where

n	number of data-windows
\vec{O}	offset for all combined data-windows

2.2.4. Mathematical Insights on the Davis-Smith Equation

2.2.4.1. Derivation of the Davis-Smith Equation using Correlations

It is instructive to show that if one starts with the assumption that $|B_M|^2$ is uncorrelated with the variance along any one of the three component axes the same result can be obtained.

Recall that the sample covariance can be written in three different ways:

$$S_{xy} = \frac{1}{N-1} \sum_{j=1}^N (x_j - \langle x \rangle)(y_j - \langle y \rangle) \quad (2.18a)$$

$$= \frac{\sum_{j=1}^N x_j y_j - \frac{\sum_{j=1}^N x_j \sum_{j=1}^N y_j}{N(N-1)}}{N-1} \quad (2.18b)$$

$$= \langle xy \rangle - \langle x \rangle \langle y \rangle \quad (2.18c)$$

Adding an offset to any or all three component axes will not alter their mutual covariances. Setting S_{xy} to zero using (2.18c) the assumption of the lack of correlation between $|B_A|^2$ and each of the three component axes implies that

$$\begin{aligned} \langle B_1 |B_A|^2 \rangle &= \langle B_1 \rangle \langle |B_A|^2 \rangle \\ \langle B_2 |B_A|^2 \rangle &= \langle B_2 \rangle \langle |B_A|^2 \rangle \\ \langle B_3 |B_A|^2 \rangle &= \langle B_3 \rangle \langle |B_A|^2 \rangle \end{aligned} \quad (2.19)$$

where $|B_A|^2$ is the actual squared magnitude of the field.

Introducing offsets O_1 , O_2 and O_3 along each of the sensors

$$|B_M|^2 = |B_A|^2 + 2O_1 B_1 + 2O_2 B_2 + 2O_3 B_3 + O_1^2 + O_2^2 + O_3^2 \quad (2.20)$$

Writing the equations

$$\begin{aligned}\left\langle B_1 \left(|B_M|^2 - 2O_1 B_1 - 2O_2 B_2 - 2O_3 B_3 \right) \right\rangle &= \left\langle B_1 \right\rangle \left(\left\langle |B_M|^2 \right\rangle - 2O_1 \left\langle B_1 \right\rangle - 2O_2 \left\langle B_2 \right\rangle - 2O_3 \left\langle B_3 \right\rangle \right) \\ \left\langle B_2 \left(|B_M|^2 - 2O_1 B_1 - 2O_2 B_2 - 2O_3 B_3 \right) \right\rangle &= \left\langle B_2 \right\rangle \left(\left\langle |B_M|^2 \right\rangle - 2O_1 \left\langle B_1 \right\rangle - 2O_2 \left\langle B_2 \right\rangle - 2O_3 \left\langle B_3 \right\rangle \right) \\ \left\langle B_3 \left(|B_M|^2 - 2O_1 B_1 - 2O_2 B_2 - 2O_3 B_3 \right) \right\rangle &= \left\langle B_3 \right\rangle \left(\left\langle |B_M|^2 \right\rangle - 2O_1 \left\langle B_1 \right\rangle - 2O_2 \left\langle B_2 \right\rangle - 2O_3 \left\langle B_3 \right\rangle \right)\end{aligned}\quad (2.21)$$

From (2.18a) it is easy to see since O_1^2 , O_2^2 and O_3^2 do not change in time they do not change the covariance and for that reason can be omitted from (2.21).

After bringing all offsets to one side one can write the equation as:

$$\begin{pmatrix} \left\langle B_1^2 \right\rangle - \left\langle B_1 \right\rangle^2 & \left\langle B_1 B_2 \right\rangle - \left\langle B_1 \right\rangle \left\langle B_2 \right\rangle & \left\langle B_1 B_3 \right\rangle - \left\langle B_1 \right\rangle \left\langle B_3 \right\rangle \\ \left\langle B_2 B_1 \right\rangle - \left\langle B_2 \right\rangle \left\langle B_1 \right\rangle & \left\langle B_2^2 \right\rangle - \left\langle B_2 \right\rangle^2 & \left\langle B_2 B_3 \right\rangle - \left\langle B_2 \right\rangle \left\langle B_3 \right\rangle \\ \left\langle B_3 B_1 \right\rangle - \left\langle B_3 \right\rangle \left\langle B_1 \right\rangle & \left\langle B_3 B_2 \right\rangle - \left\langle B_3 \right\rangle \left\langle B_2 \right\rangle & \left\langle B_3^2 \right\rangle - \left\langle B_3 \right\rangle^2 \end{pmatrix} \begin{pmatrix} O_1 \\ O_2 \\ O_3 \end{pmatrix} = \frac{1}{2} \begin{pmatrix} \left\langle B_1 |B_M|^2 \right\rangle - \left\langle B_1 \right\rangle \left\langle |B_M|^2 \right\rangle \\ \left\langle B_2 |B_M|^2 \right\rangle - \left\langle B_2 \right\rangle \left\langle |B_M|^2 \right\rangle \\ \left\langle B_3 |B_M|^2 \right\rangle - \left\langle B_3 \right\rangle \left\langle |B_M|^2 \right\rangle \end{pmatrix} \quad (2.22)$$

Equation (2.22) is the same as (2.16). This demonstrates that the Davis-Smith method is also a correlation technique. The matrix on the left hand side of (2.22) is the covariance matrix that is independent of offset.

2.2.4.2. Davis-Smith Equation for First Differences

It is similarly instructive to derive the Davis-Smith method for first differences. Equation (2.23) is the time derivative of (2.20).

$$\frac{d|B_M|^2}{dt} = \frac{d|\vec{B}_A|^2}{dt} + 2O_1 \frac{dB_1}{dt} + 2O_2 \frac{dB_2}{dt} + 2O_3 \frac{dB_3}{dt} \quad (2.23)$$

In (2.23) the terms $2O_1$, $2O_2$ and $2O_3$ are still present and $\frac{d|\vec{B}_A|^2}{dt}$ is constant for a pure rotation as well as linear change of the field magnitude. Thus making the covariance between $\frac{d|\vec{B}_M|^2}{dt}$ and $\frac{dB_1}{dt}$, $\frac{dB_2}{dt}$ and $\frac{dB_3}{dt}$ zero yields $2O_1$, $2O_2$ and $2O_3$.

Formulating equation (2.21) for first differences yields:

$$\begin{aligned}
 \langle \Delta B_1 (\Delta |B_M|^2 - 2O_1 \Delta B_1 - 2O_2 \Delta B_2 - 2O_3 \Delta B_3) \rangle &= \langle \Delta B_1 \rangle \left(\langle \Delta |B_M|^2 \rangle - 2O_1 \langle \Delta B_1 \rangle - 2O_2 \langle \Delta B_2 \rangle - 2O_3 \langle \Delta B_3 \rangle \right) \\
 \langle \Delta B_2 (\Delta |B_M|^2 - 2O_1 \Delta B_1 - 2O_2 \Delta B_2 - 2O_3 \Delta B_3) \rangle &= \langle \Delta B_2 \rangle \left(\langle \Delta |B_M|^2 \rangle - 2O_1 \langle \Delta B_1 \rangle - 2O_2 \langle \Delta B_2 \rangle - 2O_3 \langle \Delta B_3 \rangle \right) \\
 \langle \Delta B_3 (\Delta |B_M|^2 - 2O_1 \Delta B_1 - 2O_2 \Delta B_2 - 2O_3 \Delta B_3) \rangle &= \langle \Delta B_3 \rangle \left(\langle \Delta |B_M|^2 \rangle - 2O_1 \langle \Delta B_1 \rangle - 2O_2 \langle \Delta B_2 \rangle - 2O_3 \langle \Delta B_3 \rangle \right)
 \end{aligned} \tag{2.24}$$

Bringing all offsets to one side yields the same equation as (2.16) and (2.22) but for first differences as input. This means that equations (2.16) and (2.22) can be used for both magnetic field data and first differences of magnetic field data. At this point I would like to mention that there is another computationally less expensive solution to (2.24).

Assuming $\frac{d|\bar{B}_A|^2}{dt}$ is zero (which is true for a pure rotation) the offsets can be directly brought to one side which leads to a simpler equation:

$$\begin{pmatrix} \Delta B_1 & \Delta B_2 & \Delta B_3 \end{pmatrix} \begin{pmatrix} O_1 \\ O_2 \\ O_3 \end{pmatrix} = \frac{1}{2} \Delta |B_M|^2 \tag{2.25}$$

Interestingly enough for first differences equation (2.25) is identical to equation (2.16) in Acuña *et al.* (2002) even though their equation was derived completely differently.

2.2.4.3. Davis-Smith Equation for Filtered Data

It is again instructive to derive the Davis-Smith method for filtered data (see equation 2.26).

$$F(|B_M|^2) \approx F(|B_A|^2) + 2O_1 F(B_1) + 2O_2 F(B_2) + 2O_3 F(B_3) \tag{2.26}$$

Where $F(\cdot)$ denotes the filter function.

Similarly as for first differences equation (2.21) can also be formulated for filtered data. Equation (2.25) can also be used for filtered data if the filter removes the DC-components and low frequencies. The cutoff frequency needs to be higher than one divided by the length of the data-window.

Using filters makes it possible to filter out slow changes in the field magnitude. Figure 2.2 shows an example of artificially generated data by using simple mathematical functions. The data set contains pure rotations around two non-parallel axes while the magnetic field strength is smoothly decreasing (slightly non-linear). I added 2 nT offset in each component leading to small ripples in the field magnitude B_t . I then applied the Davis-Smith equation to this data set in three different ways. First I used the unfiltered data which returned $O_1 = 11.92$ nT, $O_2 = -3.08$ nT and $O_3 = 4.80$ nT. Second I used first differences which returned $O_1 = 1.58$ nT, $O_2 = 2.21$ nT and $O_3 = 1.88$ nT which is in this case a great improvement (due to the almost linear decrease of the field). Third I applied a high-pass filter to remove the decrease of the total field while keeping the ripples unchanged which yielded the correct $O_1 = 2.00$ nT, $O_2 = 2.00$ nT and $O_3 = 2.00$ nT. Additionally I calculated the offset using (2.25) which yielded $O_1 = 11.83$ nT, $O_2 = 2.87$ nT, $O_3 = 4.88$ nT. This result is in this case not as good as using the full Davis-Smith equation and first differences as input (see above). The assumption of $\frac{d|\vec{B}_A|^2}{dt} = 0$ equals zero is violated due to the continuous decrease of the field magnitude.

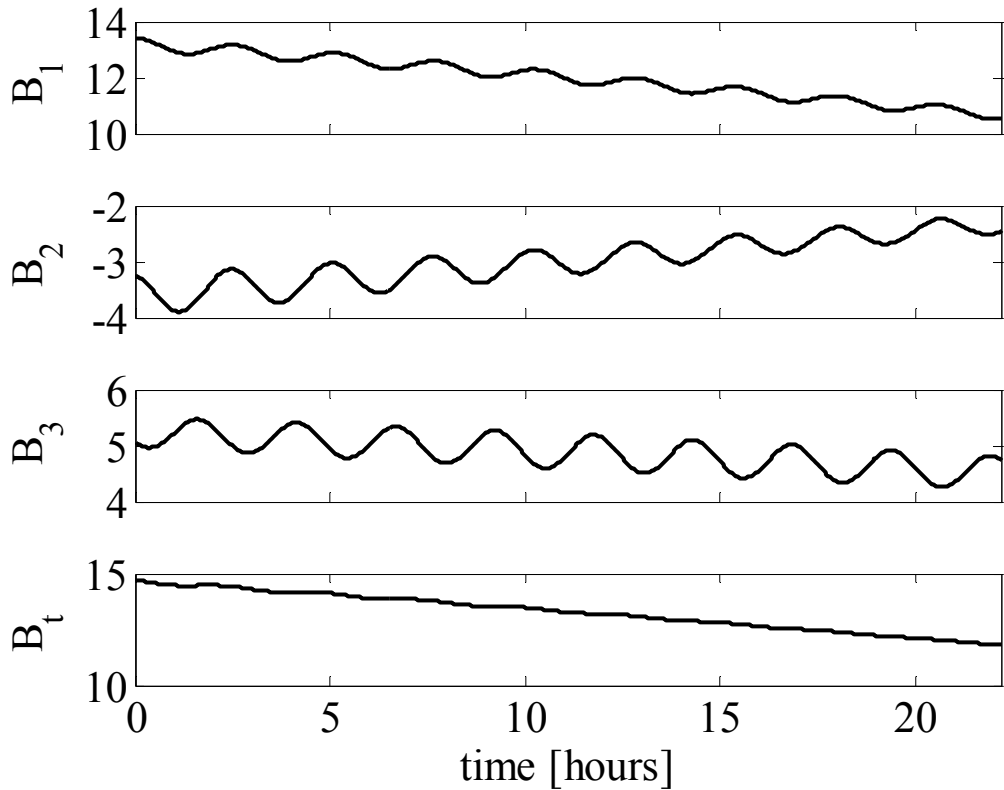


Figure 2.2. Artificially generated data that contain pure rotations while the field strength B_t is smoothly and slightly non-linearly decreasing.

At this point, a postulate stated by Hedgecock should be discussed: “A possible criticism of the above two methods (methods by Davis-Smith and Belcher) is that they tend to maximize the Alfvénic character (i.e. field magnitude conserving) of the selected fraction of observations even though there is no *a priori* reason why the disturbances should be strictly Alfvénic in nature. In the following we present a technique for zero level determination which does not suffer from this objection ”. Also the fact that Hedgecock correlates the field magnitude with an inclination angle rather than the component itself does not make a significant difference. The component and the inclination angle are directly related. However this does make it impossible to find a simple analytical solution. First differences are often very small quantities and small compressional disturbances can have an undesired influence on the outcome of zero level calculations. In general for relatively long intervals (as used by Belcher and Hedgecock) there is no significant difference if one uses first differences or not. For shorter intervals however there is often a difference (see example above).

Major advantages can be achieved when a filter is applied. This makes it possible to filter out disturbances such as slow changes in the field magnitude or stray fields caused by the spacecraft. With the exception of shocks, fast magnetosonic waves tend to smooth out compressional disturbances in the solar wind while Alfvénic structures persist. For example a high-pass filter (with a cutoff frequency of a few mHz) does not reduce the variance of the magnetic field measurements as drastically as taking the derivative. This conserves a larger range of input values. Correlations are very sensitive to phase shifts; therefore it is crucial that the filter is a zero-phase filter. Additionally, the filter should conserve the amplitude of the pass-band and thus for this work Butterworth-type filters were used. The Davis-Smith equation (2.22) can handle all types of filters (high-pass, low-pass, band-pass, and band-stop) no matter how much of the DC-components of the data are preserved.

For a spinning spacecraft with no AC-fields at the spin frequency, say due to asymmetries in the solar panel configuration, only the offset along the spin axis needs to be calculated and the Davis-Smith equation can be simplified to:

$$\left(\langle B_3^2 \rangle - \langle B_3 \rangle^2 \right) O_3 = \frac{1}{2} \left(\langle B_3 |B_M|^2 \rangle - \langle B_3 \rangle \langle |B_M|^2 \rangle \right) \quad (2.27)$$

with the assumption that the third component is the spin axis.

2.2.4.4. Mathematical Superiority of the Davis-Smith Equation

The main advantage of the Davis-Smith equation over the equations by Belcher and Hedgecock is its versatility. It works for unaltered as well as for filtered data and for first differences. Another advantage over the method by Hedgecock is that it provides analytical solutions for all three component axes if needed and therefore omitting the need for iterations through various offset values. A third major advantage over Belcher’s method is that the Davis-Smith equation is not singular if applied to just one data-

window. This is critical for establishing sophisticated selection criteria for data-windows (see Section 2.2.5). Belcher's matrix is singular for one data-window because two of its eigenvalues are zero. This means that each data-window only provides information along one direction whereas the Davis-Smith equation is capable of providing information along all three component axes of the principal coordinate system of each data-window. In other words Belcher's equation does not use all available information.

2.2.5. Selection Criteria for the Davis-Smith Method

After having established the mathematical superiority of the Davis-Smith equation the optimum selection criteria need to be found. At first, previously published selection criteria by Belcher and Hedgecock are being discussed. As mentioned above Belcher uses the criterion $\lambda_3/\lambda_1 \leq 0.1$. The eigenvalues of the covariance matrix are a measure of variance along the principal axes. As mentioned in the previous section Belcher's equation allows each data-window only to contain information along one direction (the maximum variance direction). The ratio λ_3/λ_1 is therefore a suitable criterion for his method, even though occasionally this leads to the selection of data-windows that contain pure compressions. This can happen (but not necessarily) when both λ_3 and λ_2 are small compared to λ_1 . Hedgecock's selection criteria are dependent on the zero level. This means that for each iteration the selected data set changes. This can lead to multiple zero crossings of the calculated set of covariances thus failing to provide a unique solution. The Davis-Smith equation can handle information (variance) along all three axes of the principal coordinate system therefore all three eigenvalues of each data-window should be as large as possible (additional criteria needed see below).

Figure 2.3a shows an example of STEREO-A magnetic (Acuña *et al.*, 2008) field data that start at 2007-03-26, 13:40:51 and are displayed in spacecraft coordinates. Figure 2.3b, contains the same data as Figure 2.3a but rotated into minimum variance coordinates to show that variance is present along all three principal axes. The third panel of Figure 2.3b contains the component with the smallest variance. For a pure rotation of the interplanetary magnetic field a plot of the squared field magnitude versus either one of its component axes should look like a straight line with zero gradient (assuming all zero levels are correct). Figure 2.3c shows slopes before and after the correct zero levels have been applied. The gray slopes are nonlinear because the zero levels are incorrect for all three components, the black horizontal lines are close to being linear due to the presence of rotations around various non-parallel axes and corrected zero levels. For the case that there are rotations and that the zero levels are correct for two axes but incorrect for one axis, the slope is still linear and its gradient is equal to twice the required offset correction (see black points in Figure 2.3d). If an incorrect zero level in another component is introduced, the slope becomes nonlinear (see gray points in Figure 2.3d). Application of the correct zero levels to the data in Figure 2.3a yields an extremely flat field magnitude confirming that the variances along all three components are mostly rotational (see Figure 2.3e).

In case of pure compressions along one component axis (while the other two components stay constant) the plot of the squared magnitude versus that particular component resembles a parabola (see Figure 2.4). In reality there are neither pure rotations nor pure compressions; the field behavior is somewhat in between. The task is to separate rotations that are pure enough to give reliable offset estimates from those that are too heavily disturbed by compressions. Let us take a closer look at the second case, where there are pure compressions, along one component axis. If one naively makes the correlation between the field magnitude and that component go to zero by changing the zero level, the average of that component will be removed because the derivative of x^2 (a parabola) is $2x$. For this reason the Davis-Smith method tends to remove the averages of the component axes if applied to data with too much compressional content.

For intervals that have small variance in the component axes it is difficult to decide whether a slope is truly linear. The data points from the data-window, once corrected, should lie on a straight line with zero gradient. There is a certain minimal required variance that allows us to find linear slopes. For the description of most of the criteria that are being used for finding zero levels, the term *mcs* which is the minimal compressional standard deviation that should be resolved is introduced.

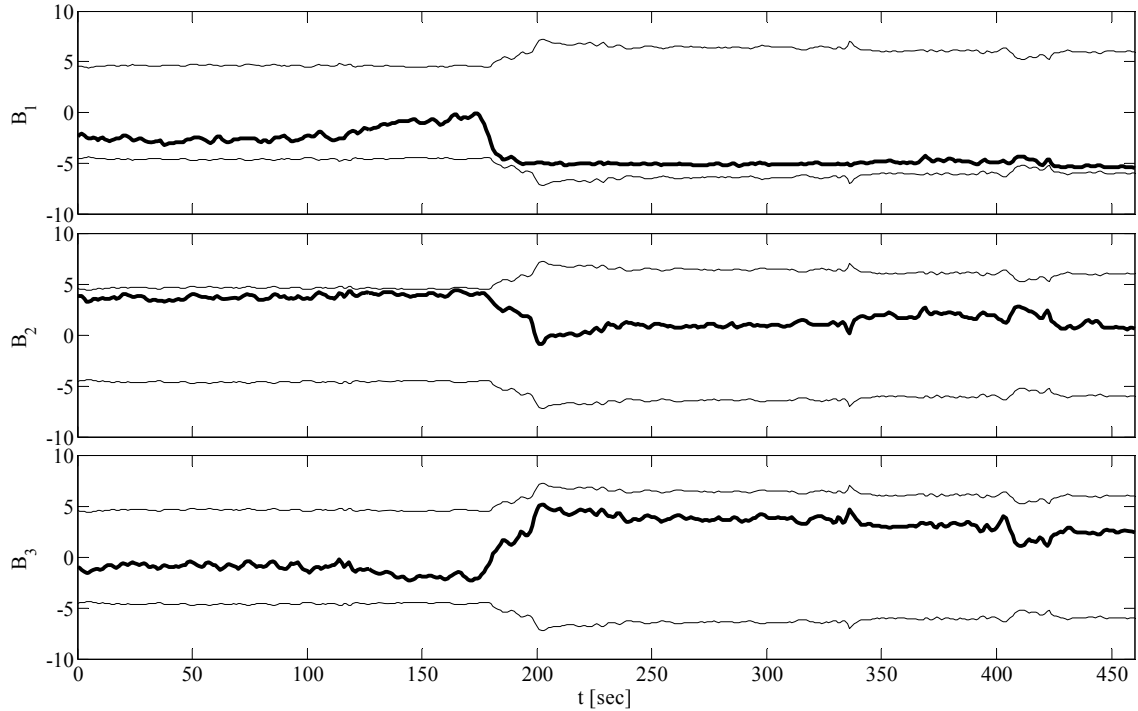


Figure 2.3a. A short example of STEREO-A data in the spacecraft coordinate system. The thin black lines are the magnetic field magnitude and its negative value plotted on the same scale to illustrate when the field was largely along or orthogonal to the sensors. The zero levels are incorrect. $O_1 = 1 \text{ nT}$, $O_2 = -1 \text{ nT}$ and $O_3 = 2 \text{ nT}$.

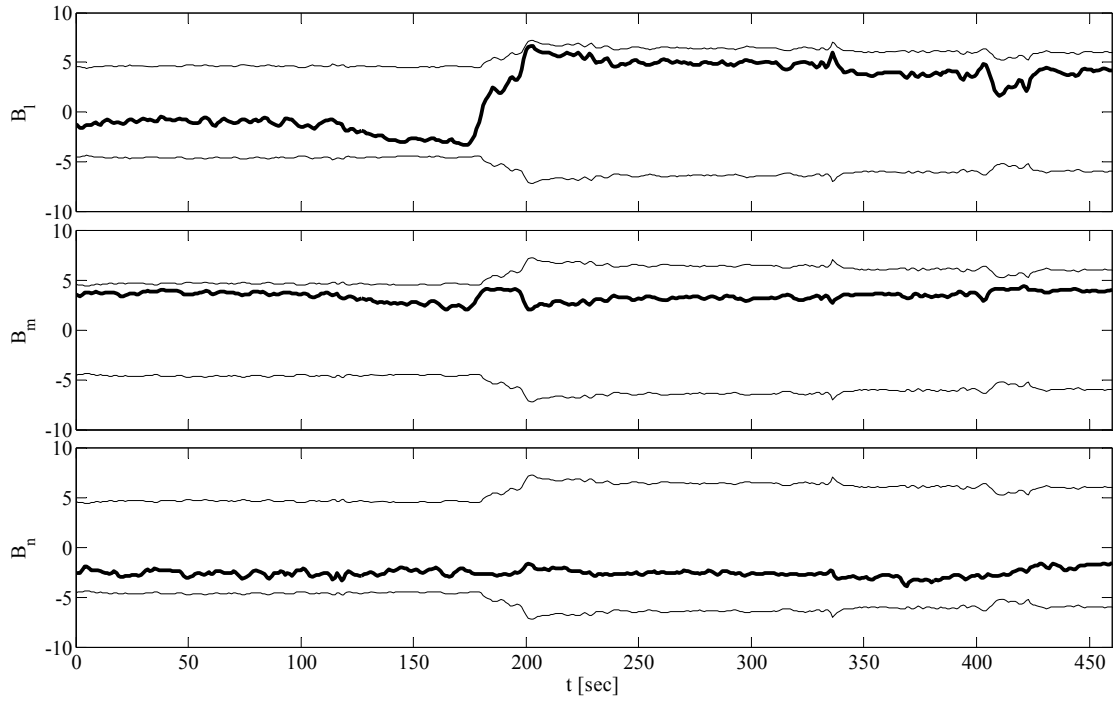


Figure 2.3b. Same data as in Figure 2.3a but rotated into the minimum variance coordinate system to show that there is variance along all three axis of the principal coordinate system. The square roots of the eigenvalues (same as standard deviations in the minimum variance coordinate system) are given in descending order: 3.03 nT, 0.48 nT and 0.38 nT.

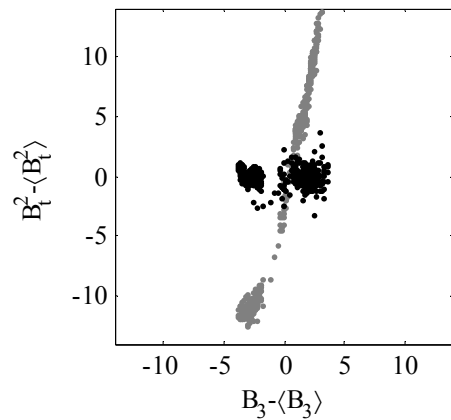
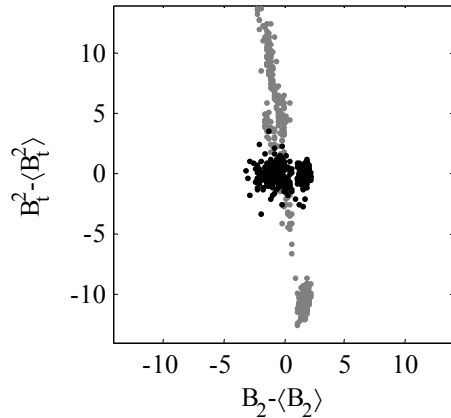
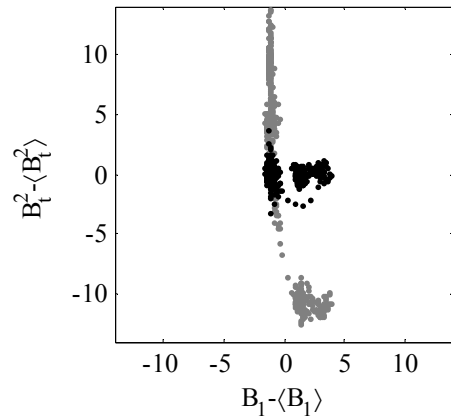


Figure 2.3c. Squared magnitude (B_t^2) versus component plots. The averages have been subtracted to center the plots at the origin.
 Gray: before zero Levels have been applied.
 Black: after zero levels have been applied.

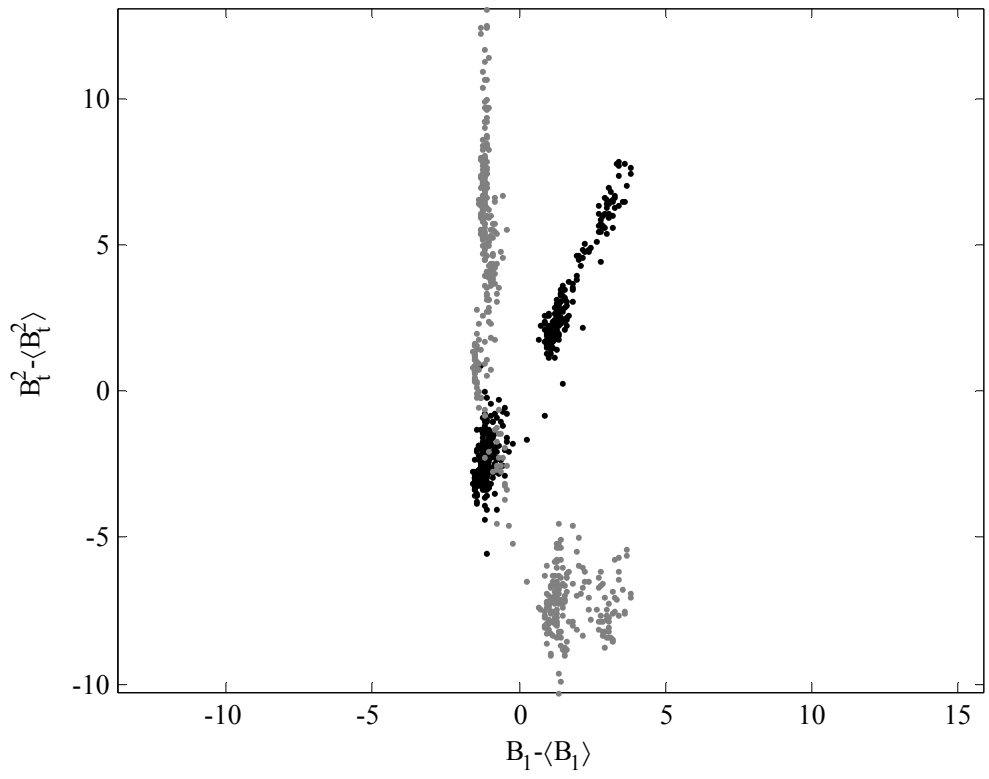


Figure 2.3d.

Black: O_1 is incorrect whereas O_2 and O_3 are correct. This causes a slope with gradient of $2O_1$ that is close to linear. $O_1=1\text{ nT}$.

Gray: O_1 and O_3 are incorrect whereas O_2 is correct. The introduction of an offset in another component causes a highly nonlinear slope. $O_1=1\text{ nT}$ and $O_3=2\text{ nT}$.

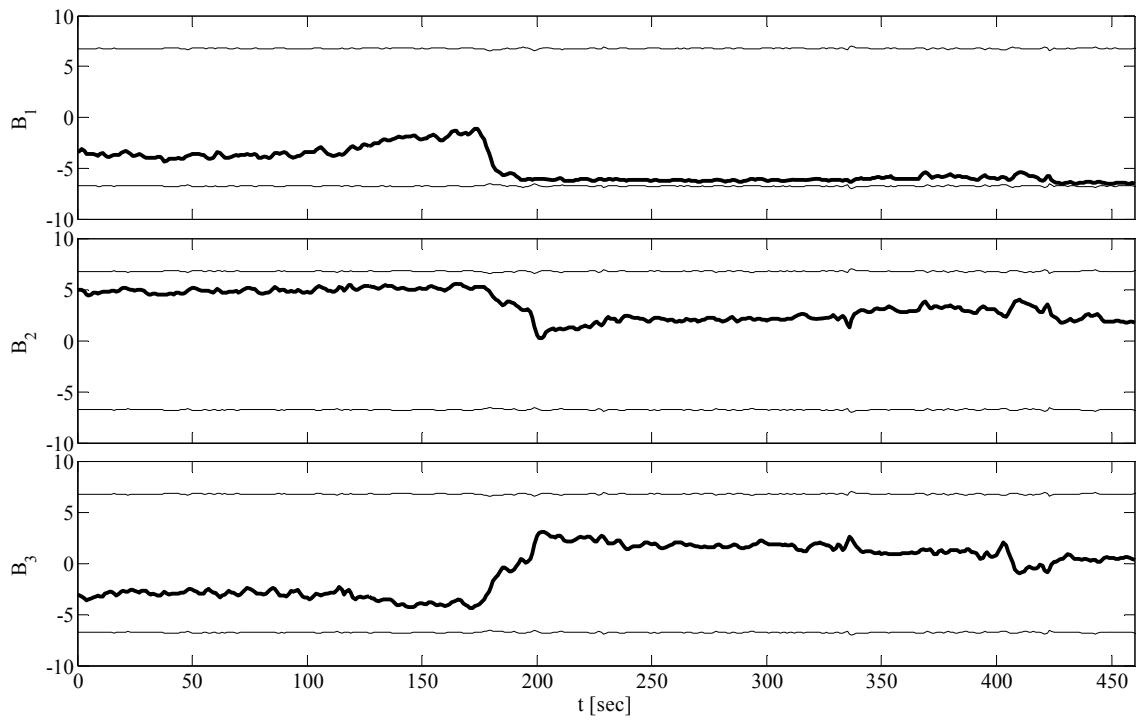


Figure 2.3e. The data in Figure 2.3a after the zero levels have been applied. The thin black traces are the mirrored field magnitude. The variance of the squared magnitude (thin black traces) has been greatly reduced compared to Figure 2.3a confirming that the variances in the component axes are mostly rotational.

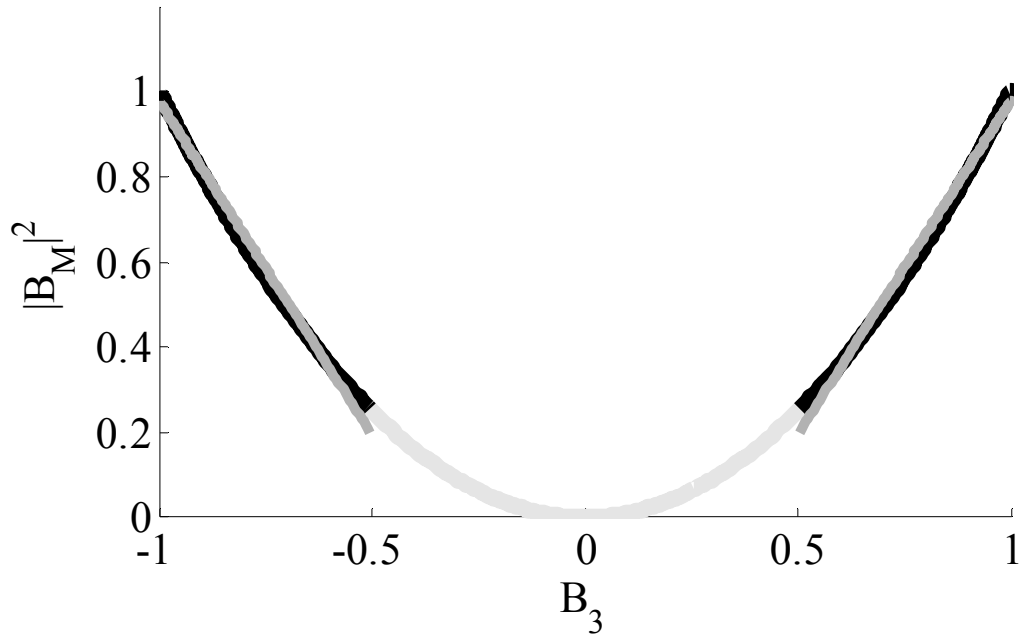


Figure 2.4. A theoretical example of a pure compression. Magnitude squared versus the component along which there is a pure compression. For this example I chose the other two components (B_1 and B_2) to be zero.

Black: upper and lower quartile of B_3 .

The straight slopes represent twice the offsets that would be calculated using only the upper and lower quartile. The difference of those offsets is used for the third selection criterion (the linearity criterion).

2.2.5.1. First Selection Criterion

In order to solve for all three zero levels significant rotations around various non-parallel axes are required. As stated above, many data-windows are being combined to perform a single large inversion. Each data-window is required to contain fluctuations that lie at least within a single plane. A combination of such data-windows can still contain fluctuations that lie inside multiple non-parallel planes. Thus the first criterion requires that the square root of the second eigenvalue of the covariance matrix is greater than a certain threshold, namely $\sqrt{\lambda_2} > \varepsilon_1$. I usually set $\varepsilon_1 = mcs$ (see Table 2.1). For a spinning spacecraft the criterion changes to $std(B_3) > \varepsilon_1$ (the third axis is assumed to be the spin axis).

2.2.5.2. Second Selection Criterion

The second selection criterion describes how “clean” particular rotations within a certain data-window are. By computing the ratio $\frac{\lambda_2}{std(|B_A|^2)} > \varepsilon_2$, a measure of this property can be obtained. I normally choose $\varepsilon_2 = 0.2$ to 0.5. This selection criterion is applied after the zero levels have been calculated using equations (2.22) or (2.27) because $std(|B_M|^2)$ changes towards $std(|B_A|^2)$ when the zero levels change towards their correct values (see black curves in Figure 2.3c or compare the thin black traces in Figure 2.3a with the corresponding traces in Figure 2.3e). For a spinning spacecraft λ_2 can be replaced by $var(B_3)$ (the third axis is assumed to be the spin axis).

2.2.5.3. Third Selection Criterion

The third selection criterion decides whether a particular slope exhibits sufficient linearity with a gradient of zero. Since this selection criterion requires much computational effort it is only applied if the first two selection criteria are fulfilled. Additionally, this selection criterion is applied after the zero levels have been calculated (using equations (2.22) or (2.27)) and subtracted from the data. The magnetic field measurements of a data-window are being sorted in three different ways, according to B_1 , B_2 and B_3 and the values of $|B_A|^2$ are always exchanged according to the corresponding sorting procedure. After the sorts have been performed B_1 , B_2 and B_3 are in ascending order and their corresponding values of $|B_A|^2$ ($|B_A|^2$ in three different sequences). For the first quarter of the values of B_1 , offset O_{11} is calculated using the Davis-Smith equation (2.27) that solves for only one component. Similarly, the offset O_{12} for the second quarter of values is calculated and so on. Then the maximum and minimum values of the four calculated offsets are taken and the criterion $abs(O_{1max} - O_{1min}) < \varepsilon_3$

(see Figure 2.4) is applied. For a long data interval with pure compressions having a standard deviation of mcs , $\text{abs}(O_{1\max} - O_{1\min})$ should be $\sim 2mcs$ (if the sum of the squares of the other two components is constant). As a conservative threshold $\varepsilon_3 = mcs$ can be used. The same procedure is applied to the other two component axes. In case of a spinning spacecraft only one component has to be taken into account.

2.2.5.3.1. Making the Third Selection Criterion Robust

It is likely that not all three component axes fulfill the third selection criterion for the same data-window. A particular data-window can still be used if at least one component passes the selection criteria. In this case the other two component axes that do not pass the selection criteria should not have a significant influence on the calculation of the offset of the component that passes. The component axes influence one another via the off-diagonal terms (covariances) in (2.22). Off-diagonal terms should not dominate the matrix in such a way that the offsets of the components that pass cannot be determined correctly. As an example, it is assumed that only the first component passes. The covariances of the other components can be checked in the following way:

$$\langle B_1^2 \rangle - \langle B_1 \rangle^2 > \text{abs}(O_{2\max} - O_{2\min}) \text{abs}(\langle B_1 B_2 \rangle - \langle B_1 \rangle \langle B_2 \rangle) + \text{abs}(O_{3\max} - O_{3\min}) \text{abs}(\langle B_1 B_3 \rangle - \langle B_1 \rangle \langle B_3 \rangle)$$

where $\text{abs}(O_{2\max} - O_{2\min})$ and $\text{abs}(O_{3\max} - O_{3\min})$ are used as estimates of how much the offsets O_2 and O_3 are being compromised. Now let's assume that the first two components pass. It is possible to check against the third component by doing two checks:

$$\langle B_1^2 \rangle - \langle B_1 \rangle^2 > \text{abs}(O_{3\max} - O_{3\min}) \text{abs}(\langle B_1 B_3 \rangle - \langle B_1 \rangle \langle B_3 \rangle)$$

$$\langle B_2^2 \rangle - \langle B_2 \rangle^2 > \text{abs}(O_{3\max} - O_{3\min}) \text{abs}(\langle B_2 B_3 \rangle - \langle B_2 \rangle \langle B_3 \rangle)$$

Similarly, checks for all other possible cases are performed.

If one looks at just one data-window, the checks of the covariances are rather loose because the estimated errors used for cross checking might not always be accurate but statistically a large error of the offset of another component combined with a large covariance reduces the chance of correct offset estimate of the component of interest. The checks are to avoid large outliers. Section 2.2.7 describes how all data-windows are combined. All data-windows are combined under the assumption that the influence of the components that did not pass cancel each other out to a large extent. For a spinning spacecraft the covariances do not need to be taken into account.

After all of the selection criteria have been applied, it is still possible to get outliers. It can be expected that the offsets that pass the third selection criterion are correct to a certain extent. The standard deviation of all offsets that pass the tests is calculated. Offsets that have a larger difference from the median than a multiple c_1 of the standard deviation are dismissed. In this work $c_1=1.25$ has usually been used. For a spinning spacecraft only one component needs to be taken into consideration.

The value that can be used for mcs is dependent on the distance from the Sun as well as noise in the data and disturbances introduced by the spacecraft's magnetic field and the chosen high-pass filter. Table 2.1, shows three example sets of criteria used in this work. The value for each criterion has been determined empirically. In general the same values are used for filtered and unfiltered data. The selection criteria were chosen in such a way that in general mcs is the only parameter that needs to be changed according to the distance from the Sun.

2.2.6. Windowing

The method works with a data-window length that varies from about 5 min to about 1 hour (parameters: wp_1 minimal data-window length, wp_2 maximal data-window length). The shift step s is constant and smaller than half of the smallest data-window length. Each data-window regardless of its length is shifted with shift step s over the whole set of input data. This means that a single data point can be part of several data-windows. The variable data-window length gives us three advantages: the method scales itself towards optimal data-window length; more accurate tracking of the beginnings and ends of pure rotations is obtained and long consistent intervals of pure rotations are more heavily weighted.

The smallest data-window length of 320 sec is increased subsequently by wp_3 percent until the largest data-window length of 3600 sec is reached. For this work $wp_3=5$ to 20 percent was used. Shift steps from $s=3$ sec. to 16 sec. were used. All selected data-windows regardless of their length are combined and one large inversion is performed. Variable data-window length greatly increases the number of data-windows and thus the number of required computations. I implemented the algorithm in such a way that cumulative sums are used as often as possible. All averages in equations (2.22), (2.24) and (2.26) can be efficiently calculated from cumulative sums. Additionally, $std(|B_A|^2)$ in the second selection criterion (see Section 2.2.5.2) can be efficiently calculated by taking equation (2.20) squared and introducing sums:

$$std(|B_A|^2) = \sqrt{\frac{1}{n-1} \sum (|B_A|^2)^2 - n \langle |B_A|^2 \rangle^2}$$

n number of data points per window

with

$$\langle |B_A|^2 \rangle = \frac{1}{n} \sum |B_A|^2$$

with previously calculated sums

$$\sum |B_A|^2 = \sum |B_M|^2 + 2O_1 \sum B_1 + nO_1^2 + 2O_2 \sum B_2 + nO_2^2 + 2O_3 \sum B_3 + nO_3^2$$

and with

$$\begin{aligned} \sum (|B_A|^2)^2 &= \sum (|B_M|^2)^2 + \\ &+ 2O_1 \sum B_1 |B_M|^2 + \\ &+ O_1^2 \sum |B_M|^2 + 2O_2 \sum B_2 |B_M|^2 + O_2^2 \sum |B_M|^2 + 2O_3 \sum B_3 |B_M|^2 + O_3^2 \sum |B_M|^2 + \\ &+ 2O_1 \sum B_1 |B_M|^2 + \\ &+ 4O_1^2 \sum B_1^2 + 2O_1^3 \sum B_1 + 4O_1 O_2 \sum B_1 B_2 + 2O_1 O_2^2 \sum B_1 + 4O_1 O_3 \sum B_1 B_3 + 2O_1 O_3^2 \sum B_1 + \\ &+ O_1^2 \sum |B_M|^2 + \\ &+ 2O_1^3 \sum B_1 + nO_1^4 + 2O_2 O_1^2 \sum B_2 + nO_1^2 O_2^2 + 2O_3 O_1^2 \sum B_3 + nO_3^2 O_1^2 + \\ &+ 2O_2 \sum B_2 |B_M|^2 + \\ &+ 4O_1 O_2 \sum B_1 B_2 + 2O_2 O_1^2 \sum B_2 + 4O_2^2 \sum B_2^2 + 2O_2^3 \sum B_2 + 4O_3 O_2 \sum B_2 B_3 + 2O_2 O_3^2 \sum B_2 + \\ &+ O_2^2 \sum |B_M|^2 + \\ &+ 4O_1 O_2^2 \sum B_1 + nO_1^2 O_2^2 + 2O_2^3 \sum B_2 + nO_1^4 + 2O_3 O_2^2 \sum B_3 + nO_3^2 O_2^2 + \\ &+ 2O_3 \sum B_3 |B_M|^2 + \\ &+ 4O_1 O_3 \sum B_1 B_3 + 2O_3 O_1^2 \sum B_3 + 4O_2 O_3 \sum B_2 B_3 + 2O_3 O_2^2 \sum B_3 + 4O_3^2 \sum B_3^2 + 2O_3^3 \sum B_3 + \\ &+ O_3^2 \sum |B_M|^2 + \\ &+ 2O_1 O_3^2 \sum B_1 + nO_1^2 O_3^2 + 2O_2 O_3^2 \sum B_2 + nO_2^2 O_3^2 + 2O_3^3 \sum B_3 + nO_3^4 \end{aligned}$$

the second criterion can be calculated using previously calculated sums.

Similarly for first differences

$$std(\Delta |B_A|^2) = \sqrt{\frac{1}{n-1} \sum (\Delta |B_A|^2)^2 - n \langle \Delta |B_A|^2 \rangle^2}$$

with

$$\langle \Delta |B_A|^2 \rangle = \frac{1}{n} \sum \Delta |B_A|^2$$

with previously calculated sums

$$\sum \Delta |B_A|^2 = \sum \Delta |B_M|^2 + 2O_1 \sum \Delta B_1 + 2O_2 \sum \Delta B_2 + 2O_3 \sum \Delta B_3$$

and with

$$\begin{aligned} \sum (\Delta |B_A|^2)^2 &= \sum (\Delta |B_M|^2)^2 + \\ &+ 2O_1 \sum \Delta B_1 \Delta |B_M|^2 + 2O_2 \sum \Delta B_2 \Delta |B_M|^2 + 2O_3 \sum \Delta B_3 \Delta |B_M|^2 + \\ &+ 2O_1 \sum \Delta B_1 \Delta |B_M|^2 + 4O_1^2 \sum \Delta B_1^2 + 4O_1 O_2 \sum \Delta B_1 \Delta B_2 + 4O_1 O_3 \sum \Delta B_1 \Delta B_3 + \\ &+ 2O_2 \sum \Delta B_2 \Delta |B_M|^2 + 4O_2 O_1 \sum \Delta B_1 \Delta B_2 + 4O_2^2 \sum \Delta B_2^2 + 4O_2 O_3 \sum \Delta B_2 \Delta B_3 + \\ &+ 2O_3 \sum \Delta B_3 \Delta |B_M|^2 + 4O_3 O_1 \sum \Delta B_1 \Delta B_3 + 4O_2 O_3 \sum \Delta B_2 \Delta B_3 + 4O_3^2 \sum \Delta B_3^2 \end{aligned}$$

the second criterion can be obtained for first differences using previously calculated sums.

For high pass filtered data the second selection criterion can be efficiently calculated in a similar fashion.

2.2.7. Combination of Data-windows and Overall Inversion

It is possible to combine all selected data-windows in a very simple way which avoids large matrices. For each data-window all the averages from B_1 , B_2 , B_3 and $|B_M|^2$ are subtracted. Then the following equation is used to combine all the values of all data-windows, which is a simpler form of (2.22).

$$\begin{pmatrix} \langle B_1'^2 \rangle & \langle B_1' B_2' \rangle & \langle B_1' B_3' \rangle \\ \langle B_2' B_1' \rangle & \langle B_2'^2 \rangle & \langle B_2' B_3' \rangle \\ \langle B_3' B_1' \rangle & \langle B_3' B_2' \rangle & \langle B_3'^2 \rangle \end{pmatrix} \begin{pmatrix} O_1 \\ O_2 \\ O_3 \end{pmatrix} = \frac{1}{2} \begin{pmatrix} \langle B_1' |B_M|^2' \rangle \\ \langle B_2' |B_M|^2' \rangle \\ \langle B_3' |B_M|^2' \rangle \end{pmatrix} \quad (2.28)$$

For a spinning spacecraft:

$$\langle B_3'^2 \rangle O_3 = \frac{1}{2} \langle B_3' |B_M|^2' \rangle \quad (2.29)$$

Where B_1' , B_2' , B_3' and $|B_M|^2'$ are all magnetic field values of all data-windows that had the averages removed.

Even after the input has passed all the selection criteria a decision must be made whether the overall inversion has produced meaningful results. Checks are performed to see if it contains rotations around various non-parallel axes by the requirement that the standard deviation of each component that went into the final inversion is greater than c_2*mcs . If a particular component fails to meet this criterion the offset for that component cannot be trusted. In this work $c_2=1.5$ to 2 has been used. Another criterion is the number of independent points $npts$ that went into the inversion (each measurement is only counted once even if it is part of several data-windows). Usually this value is set to $npts=1000$ for one second data. This value largely depends on the resolution of the data. The next criterion is the number of different data-windows ni that went into the overall inversion. This value is usually set to 10. For a spinning spacecraft the offset from all combined data-windows can be calculated using (2.29).

If none of the components fulfill the criteria of the overall inversion one could loosen criteria one, two and three so that more data-windows get selected. In some cases it is better to have more data-windows that were chosen using less tight criteria than very few data-windows chosen with strict criteria. In some cases changing the cutoff frequency of the high-pass filter can produce a higher number of valid data-windows.

2.2.8. Monte Carlo Simulation

Once the overall inversion has been performed checks are required to see if the obtained solutions are stable solutions. As a Monte Carlo simulation a modified version of the so-called Bootstrap-method (Efron, 1982) has been chosen. This method reduces the information content of the data set which consists of n independent measurements by randomly choosing n -times a measurement out of the n measurements. This leads to a new data set that has roughly $1/e$ measurements more than once. This procedure is done a large number of times and each time a new inversion is performed. The variance of the solutions is then used as a measure of stability. In the case of interplanetary magnetic field measurements, two consecutive measurements are generally not independent (e.g. for 1 sec resolution). In order to achieve some degree of independence in this work two minute intervals instead of single points were used. Since the variable window length is variable, the same two minute interval can be part of several data-windows. If a particular two minute interval was not chosen it was removed from all data-windows. For this work 300 to 500 inversions (parameter: nmc) were performed. The decision whether an offset is determined in a stable fashion is based on the difference between the maximum and the minimum estimate. The difference must be smaller than c_3*mcs . It is possible that not all three offset estimates are stable. If at least one estimate is stable, the stable offset(s) is (are) applied to the data and the overall inversion and the Monte Carlo Simulation is repeated for the remaining component(s) but the data-windows that fulfill the third selection criterion only for the stable component(s) are left out. This leads to a data set that was especially chosen in order to solve for the remaining component(s). If only one component remains the algorithm is the same as for a spinning spacecraft. The maximum and minimum estimates are used to define the error-bars.

If no stable solution can be found one could try “tweaking” the selection criteria. For example if the noise level of the data is rather low one could loosen the criteria that are based on eigenvalues or variance (ε_1 , ε_2 and c_3). One could also try lowering the shift step s in order to better track beginnings and ends of pure rotations or decrease the increment of the widow length wp_3 from e.g. 20 percent to 10 percent. Another possibility would be that too many compressions slipped through. In this case increasing mcs could help in finding stable solutions.

2.2.9. Application of the Algorithm to Space-borne Magnetometer Data

Figure 2.5, shows an example of magnetic field data where the field magnitude is continuously declining throughout the interval. The data were measured on the three-axis stabilized STEREO-A while passing through the interior of an ICME. For this interval I could only obtain zero levels by high-pass filtering the data. First differences as well as unfiltered data did not yield results because no data-windows were selected by the algorithm.

Tables 2.2a and 2.2b show the results of a calibration performed with STEREO-B data for day 224 in 2007. The input parameters are given in Table 2.1. The first run did not return a value for O_3 for the unfiltered case and for the filtered case O_1 and O_3 could not be determined. The criteria that caused the program to dismiss some of the offset calculations are marked in light gray. Since both methods (filtered and unfiltered) did not yield O_3 the software applied O_1 from the unfiltered case and the averaged O_2 from both cases to the data and reran the algorithm only to solve for O_3 . The outcome of the rerun is displayed in Table 2.2b. The algorithm finds O_3 for the unfiltered case. I chose this particular example also to show that the criteria that were chosen do not represent strict boundaries between finding accurate and inaccurate calculations. As can be seen in Table 2.2b the estimate of O_3 for the filtered case is being dismissed by the algorithm even though the value of -38.07 nT appears to be very close to the result of the unfiltered case which is -37.99 nT. The chosen selection criteria usually are on the safe side. After I had applied the calculated offsets to the data I reran the algorithm for testing purpose and all zero levels came out zero ($O_1=0.00$ nT, $O_2=0.00$ nT, $O_3=0.00$ nT). The algorithm is mathematically not iterative; thus the algorithm will run the second time (with correct offsets) exactly as the first time (same error bars, same offset calculations will be dismissed etc.). Slight differences can arise for the filtered case because the right hand side and the left hand side of equation (2.26) are not exactly equal.

Magnetic field data of THEMIS-B (Auster *et al.*, 2008) are displayed in Figure 2.6. The data show multiple bow shock crossings. The roughly seven hour long subset of the data that is marked in gray has been selected as input for an offset calculation. The selected data contain several intervals of large upstream waves which do not disturb the algorithm. The result of the offset calculation is displayed in Table 2.3. The length of the

error bar of the calculated offset is only 0.29 nT. Because of the use of spin-averaged data the accuracy of the spin-plane offsets has no influence on the calculation of the spin-axis offset.

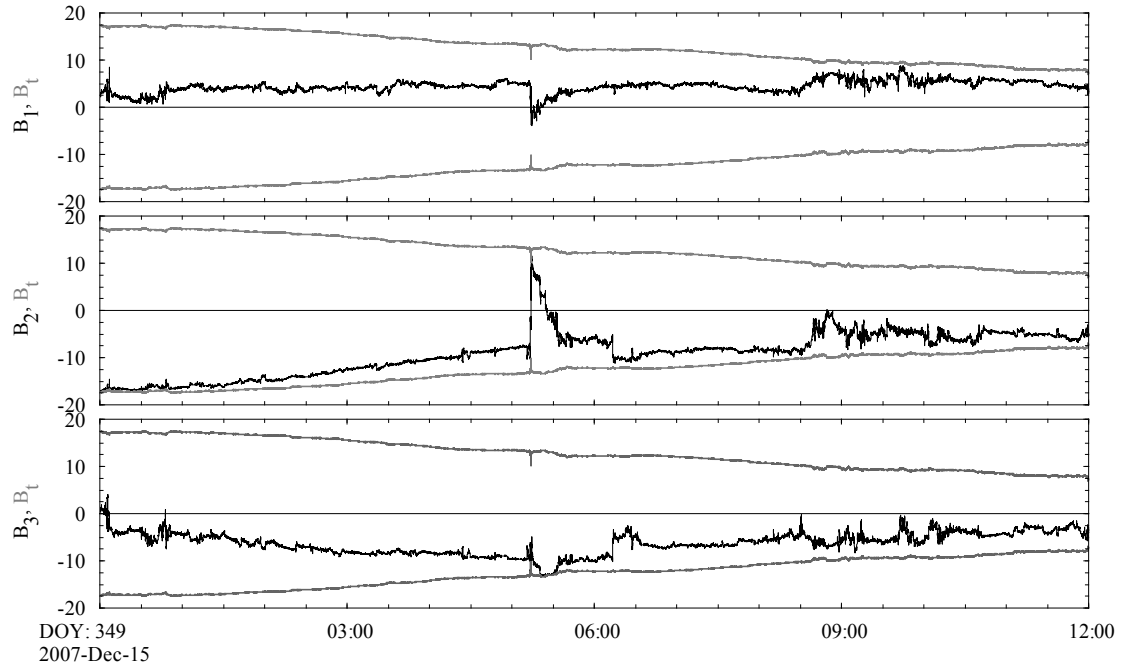


Figure 2.5. Magnetic field data of STEREO-A as it passes through the interior of an ICME. Shown in black are the outputs of the three magnetometer sensors at 1 sec resolution. The light gray lines are the magnetic field magnitude B_t and its negative value plotted on the same scale to illustrate when the field was largely along or orthogonal to the sensors. Zero-phase high-pass filtering is applied on these data before the zero level determination algorithm. The filter is a fourth order (eighth order when zero-phase filtering) butterworth-type filter with a cutoff frequency of 8.9 mHz.

mission	STEREO	THEMIS	VEX
data resolution	1 sec	3 sec	1 sec
Selection:			
mcs	0.25 nT	0.25 nT	0.3 nT
ε_1	1*mcs	1*mcs	1*mcs
ε_2	0.5	0.5	0.5
ε_3	1*mcs	1*mcs	1*mcs
c_1	1.25	1.25	1.25
Windowing:			
wp_1	320 sec	300 sec	320 sec
wp_2	3600 sec	3000 sec	3600 sec
wp_3	20%	5%	20%
s	8 sec	3 sec	8 sec
Inversion:			
c_2	1.5	1.5	2.0
$npts$	1000	300	1000
ni	10	10	10
Monte Carlo:			
nmc	300	300	300
c_3	2.0	2.0	3.0

Table 2.1. Three examples of empirically determined criteria used in calculations. STEREO is a dual-spacecraft mission with three-axis stabilization where the zero levels of all three component axes need to be calibrated. THEMIS is a five-spacecraft mission with spin stabilization where only the zero level of the component that lies along the spin axis needs to be calculated. Venus Express (VEX) is a three-axis stabilized spacecraft.

	unfiltered input data		filtered input data	
Inversion:				
Number of independent points	13648	$>npts=1000$	12727	$>npts=1000$
Number of data-windows	359	$>ni=10$	570	$>ni=10$
$std(B_1)$ (nT)	1.408	$>c_2*mcs = 0.375$	0.338	$>c_2*mcs = 0.375$
$std(B_2)$ (nT)	0.614	$>c_2*mcs = 0.375$	0.398	$>c_2*mcs = 0.375$
$std(B_3)$ (nT)	0.555	$>c_2*mcs = 0.375$	0.185	$>c_2*mcs = 0.375$
O_1 (nT)		-43.63		-43.99
O_2 (nT)		19.92		20.10
O_3 (nT)		-37.85		-37.50
Monte Carlo Simulation:				
$abs(O_{1\min} - O_{1\max})$ (nT)	0.321	$<c_3*mcs = 0.5$	---	$<c_3*mcs = 0.5$
$abs(O_{2\min} - O_{2\max})$ (nT)	0.196	$<c_3*mcs = 0.5$	0.147	$<c_3*mcs = 0.5$
$abs(O_{3\min} - O_{3\max})$ (nT)	0.525	$>c_3*mcs = 0.5$	---	$<c_3*mcs = 0.5$
Result:				
O_1 (nT)		-43.63		---
O_2 (nT)		19.92		20.10
O_3 (nT)		---		---
Error Bars:				
$O_{1\min}$ to $O_{1\max}$ (nT)		-43.89 to -43.57		---
$O_{2\min}$ to $O_{2\max}$ (nT)		19.83 to 20.02		20.03 to 20.17
$O_{3\min}$ to $O_{3\max}$ (nT)		---		---
Combined Result:				
O_1 (nT)			—43.63	
O_2 (nT)			20.01 (averaged)	
Combined Error Bars:				
$O_{1\min}$ to $O_{1\max}$ (nT)			-43.57 to -43.89	
$O_{2\min}$ to $O_{2\max}$ (nT)			19.83 to 20.17 (worst case of both estimates)	

Table 2.2a. Example of STEREO-B zero level calculations for day 224, of 2007. For the filtered case the cutoff frequency of the high-pass filter is 3.3 mHz. The fields that are marked in gray represent violations of criteria which lead to dismissal of O_1 from the filtered case and the dismissal of O_3 from both cases. The full set of selection criteria is given in Table 2.1.

	unfiltered input data	filtered input data
Inversion:		
Number of independent points	19687 $>npts=1000$	12879 $>npts=1000$
Number of data-windows	331 $>ni=10$	1035 $>ni=10$
$std(B_3)$ (nT)	0.575 $>c_2*mcs= 0.375$	0.373 $>c_2*mcs= 0.375$
O_3 (nT)	-37.99	-38.07
Monte Carlo Simulation:		
$abs(O_{3\min} - O_{3\max})$ (nT)	0.17 $<c_3*mcs= 0.5$	0.19 $<c_3*mcs= 0.5$
Result:		
O_3 (nT)	-37.99	---
Error Bars		
$O_{3\min}$ to $O_{3\max}$ (nT)	-38.06 to -37.89	---
Combined Result:		
O_3 (nT)	-37.99	
Combined Error Bars:		
$O_{3\min}$ to $O_{3\max}$ (nT)	-38.06 to -37.89	

Table 2.2b. Rerun of the algorithm in order to solve for O_3 . Before I performed the rerun I applied the corrected zero levels O_1 and O_2 as given in Table 2.2a to the input data.

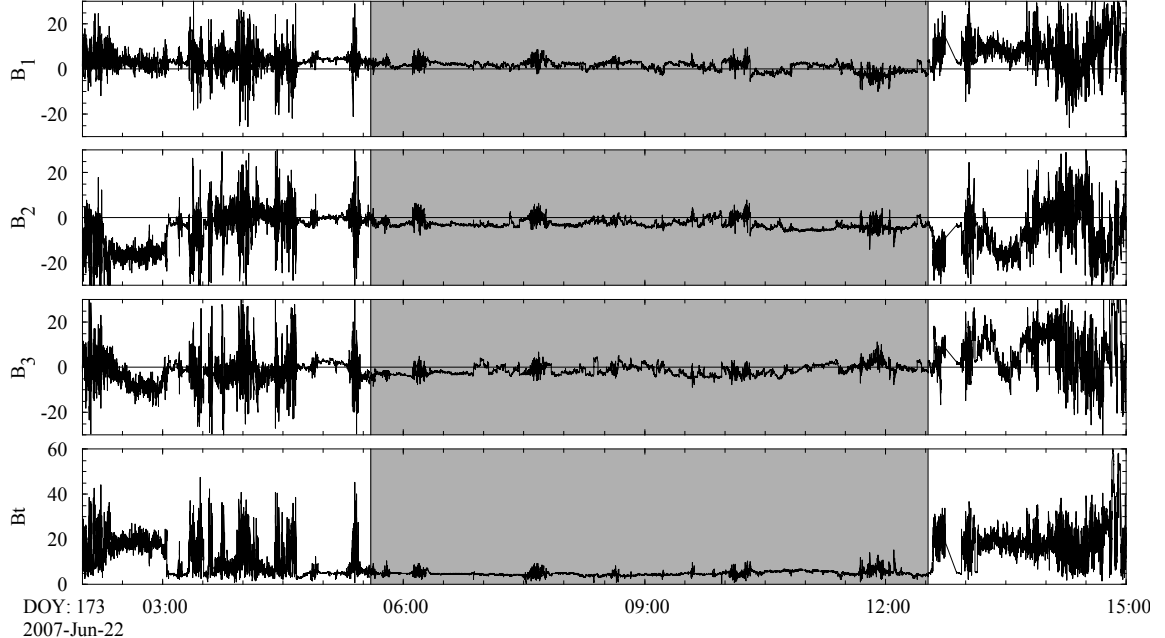


Figure 2.6. Example of spin averaged THEMIS-B data. The roughly 7 hour long subset that is marked in gray has been used as input for an offset calculation. B_3 represents the spin-plane component. The spin period of the THEMIS spacecraft is roughly 3 sec.

	unfiltered input data		filtered input data		
Inversion:					
Number of independent points	3302	$>npts=300$	3425	$>npts=300$	
Number of data-windows	215	$>ni=10$	1915	$>ni=10$	
$std(B_3)$ (nT)	1.835	$>c_2*mcs= 0.375$	1.259	$>c_2*mcs= 0.375$	
O_3 (nT)		-0.04		-0.09	
Monte Carlo Simulation:					
$abs(O_{3_{\min}} - O_{3_{\max}})$ (nT)		0.233	$<c_3*mcs= 0.5$	0.257	$<c_3*mcs= 0.5$
Result:					
O_3 (nT)		-0.04		-0.09	
Error Bars:					
$O_{3_{\min}}$ to $O_{3_{\max}}$ (nT)		-0.16 to 0.07		-0.22 to 0.04	
Combined Result:					
O_3 (nT)			-0.07 (average)		
Combined Error Bars:					
$O_{3_{\min}}$ to $O_{3_{\max}}$ (nT)		-0.22 to 0.07	(worst case of both estimates)		

Table 2.3. Example of a zero level calculation for THEMIS-B. For the filtered case the cutoff frequency of the high-pass filter is 3.3 mHz. The full set of selection criteria is given in Table 2.1.

The example that I chose for Venus Express uses a slightly different approach. Venus Express had no magnetic cleanliness program. At the positions of the magnetometers the spacecraft's magnetic field interferes with the natural magnetic field. Initial cleaning of the Venus Express data has been performed (Zhang *et al.*, 2007) using the gradiometer configuration of the dual triaxial sensors. The initial cleaning of the data provides AC-accuracy of better than 0.1 nT (Zhang *et al.*, 2007). The inboard sensor is placed directly onto the spacecraft's surface. The outboard sensor is mounted on a short boom of only one meter in length. The magnetic field strength caused by the spacecraft ranges from 2000 to 6000 nT at the inboard sensor and is roughly 200 nT at the outboard sensor. For Venus Express, detecting changes of the zero levels with as rapid a cadence as possible is necessary. The whole novel technique is applied using an overlapping three-hour window that is shifted by one hour. Whenever it is not possible to determine a zero level for a particular component the window is extended by one hour towards later times and so on. However the calculations after the next shift (one hour) again start with a three hour window (see Figures 2.7a and 2.7b). In order to be able to track offsets the selection criteria should be such that changes in offset are not mistakenly dismissed as compressions by the algorithm. Table 2.1 shows the selection criteria that I used for tracking offsets using Venus Express data. The values for mcs , c_2 and c_3 are different from the corresponding values for the other two spacecraft. A compromise between accuracy and the tracking ability was made. Large discontinuities of the zero levels occur from one day to the next because the initial data cleaning was done for day-files. An

algorithm has been applied (by the data cleaning team) to join the day- files. This algorithm occasionally leaves behind slight jumps in the offsets. I applied the technique using separate day-files so that no windows can cross day-boundaries.

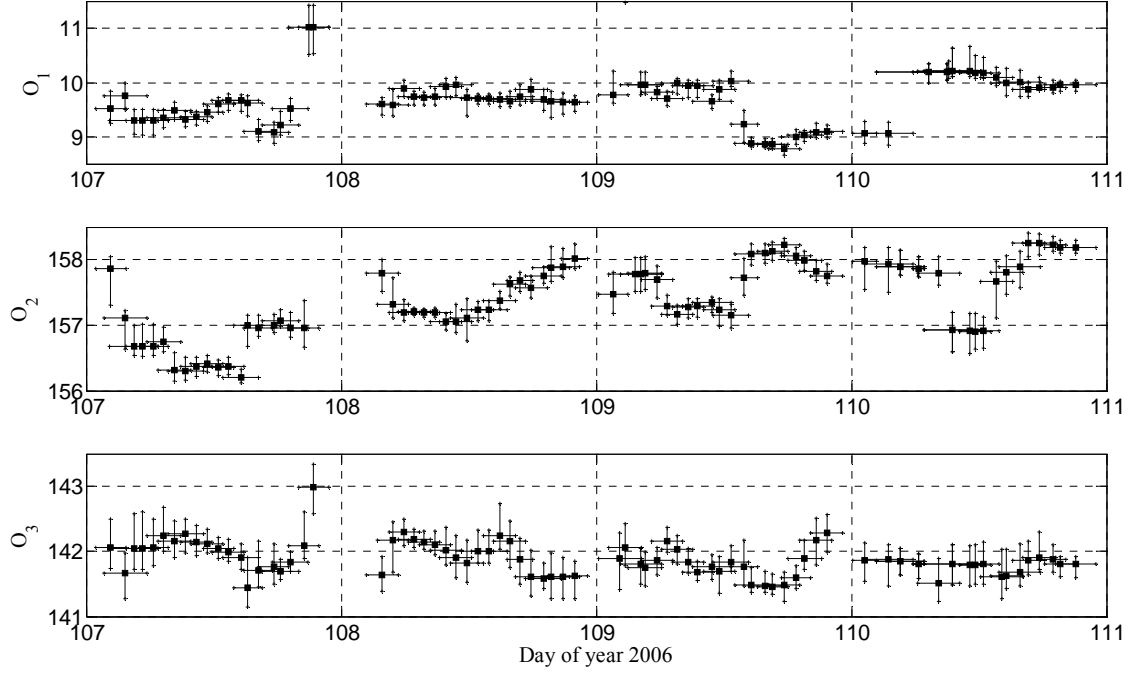


Figure 2.7a. Example of detection of changing offsets using four days of Venus Express data. The input data are unfiltered. The horizontal lines show the timeframe for a particular offset estimate. The vertical black lines represent the error bars for the offset estimates.

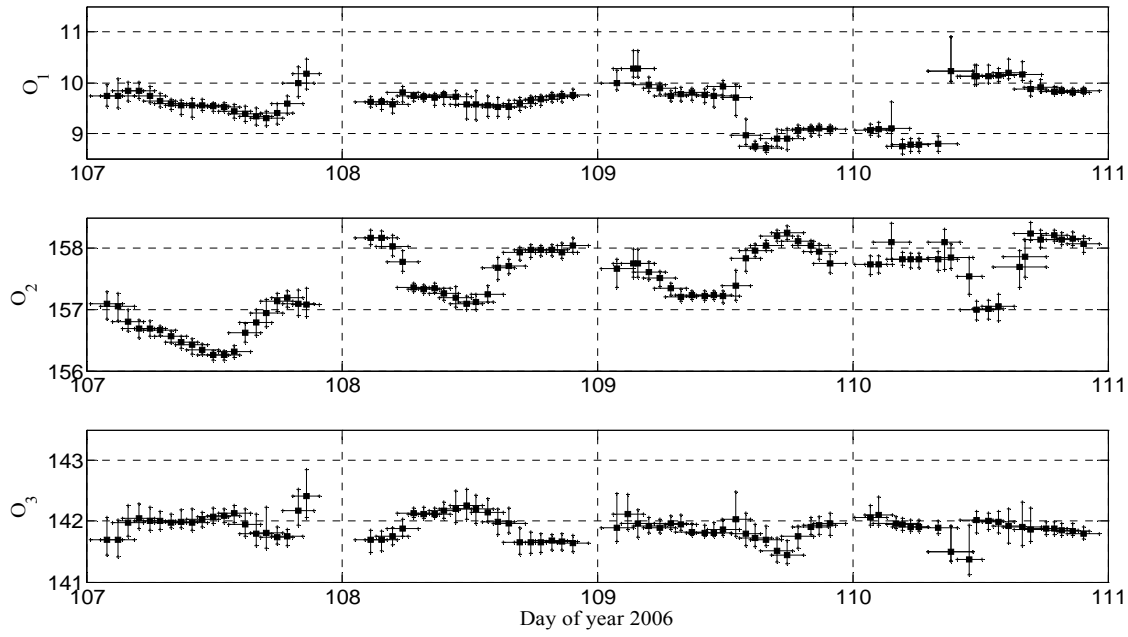


Figure 2.7b. Example of detection of changing offsets using four days of Venus Express data. The input data are high-pass filtered using a cutoff frequency of 8.9 mHz. The horizontal lines show the timeframe for a particular offset estimate. The vertical lines represent the error bars for the offset estimates.

2.3. An Advanced Approach to Finding Magnetometer Zero Levels Inside the Low-field Regions of a Magnetosphere

2.3.1. Introduction

Inside the Earth's magnetosphere, the plasma is much different from the solar-wind plasma and the magnetic fluctuations are generally not as Alfvénic as they are inside the interplanetary magnetic field. Inside a magnetosphere, magnetic field fluctuations are mostly compressional, which means that the field magnitude fluctuates strongly as the three components of the field fluctuate. In low-field regions within a magnetosphere the precision of magnetic field models is insufficient for calibration purposes. Magnetometer zero levels can be calculated from purely compressional fluctuations of the magnetic field. For a data interval that consists of pure changes of the field magnitude, the cross product of each magnetic field vector with the maximum variance vector (Sonnerup, 1967) is zero because all vectors point towards the maximum variance direction. If the zero level of the magnetometer is incorrect pure changes of the field magnitude are measured as changes of magnitude plus changes in direction of the field (see Figure 2.8). The maximum variance direction is given by the eigenvector of the covariance matrix that corresponds to the largest eigenvalue and is independent of the zero level. Geophysical phenomena that produce pure compressional fluctuations (amongst others) are mirror-mode waves, drift mirror-mode waves and magnetic nulls. The latter are observed rather scarcely and attempts to use them for zero level determination did not yield reasonable results. Mirror-mode waves are magnetic/plasma signatures that are frozen into the flowing magnetosheath plasma (Fazakerley and Southwood, 1994). Drift mirror-mode waves (Hasegawa, 1969; Tsurutani *et al.*, 1982) are as well observed in the magnetosheath and generally have larger amplitude as well as lower frequency as mirror-mode waves. Figure 2.9 depicts mirror-mode waves and Figure 2.10 drift mirror-mode waves, as observed by the THEMIS mission (Angelopoulos, 2008, Auster *et al.*, 2008).

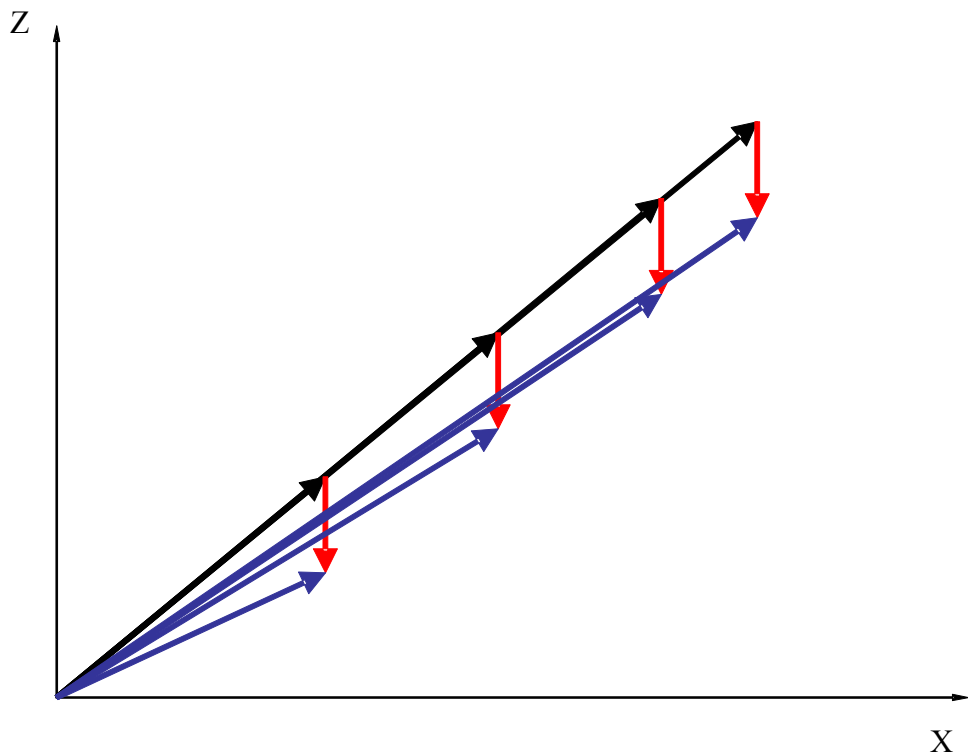


Figure 2.8. Example of an interval consisting of four magnetic field vectors in the XZ-plane. The black vectors are all aligned and represent a pure change of field magnitude. The red arrows introduce a change of the zero level along the Z-axis. The blue vectors are the result of the changed zero level. Thus the blue vectors do not have uniform direction.

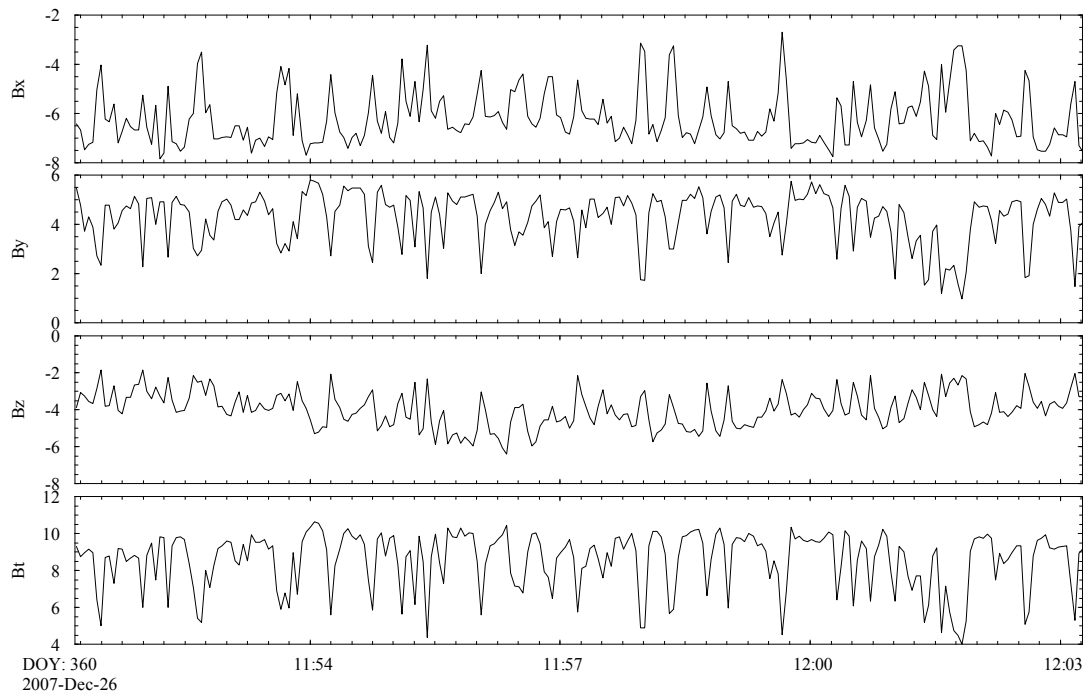


Figure 2.9. Example of mirror-mode waves as observed by the THEMIS-B spacecraft.

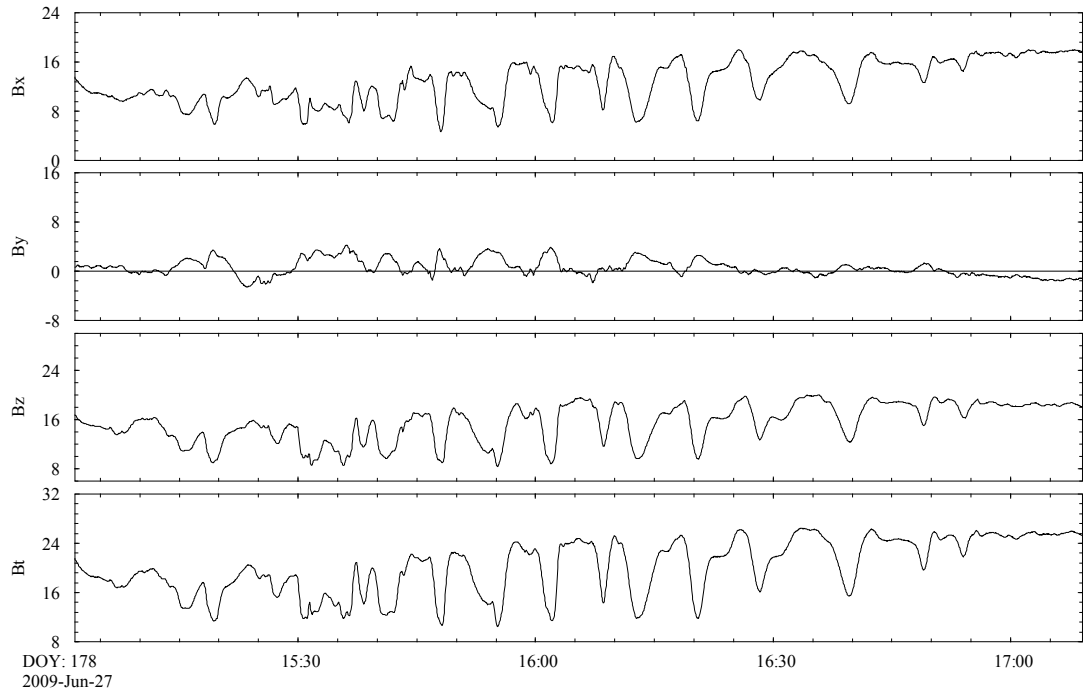


Figure 2.10. Example of drift mirror-mode waves as observed by the THEMIS-B spacecraft.

2.3.2. Algorithm

Similarly to the algorithm for finding zero levels in the interplanetary magnetic field, the algorithm in this section was designed with emphasis on automation. It searches for purely compressional changes of the magnetic field, calculates the zero level using a robust technique and checks the stability of the solution via Monte Carlo simulation. It was implemented to solve for the spin axes offsets of the five THEMIS magnetometers (Auster *et al.*, 2008).

The search algorithm for purely compressional changes of the magnetic field uses filtered as well as unfiltered data in despun spacecraft coordinates. All the given values below were determined empirically with spin averaged THEMIS magnetic field data (3 sec. resolution). Please note that the empirical values have not been tested for a different mission other than THEMIS. The filtered data are high-pass filtered with a cutoff frequency of 0.83 mHz (period of 20 minutes). The window length is variable and ranges with 30 sec. steps from 2 minutes to 10 minutes. The shift step of each window length is 3 sec.

There are two categories of criteria. The first category contains basic checks that each possible interval for zero level calculation has to pass. The second category contains checks that are applied after calculation of the zero levels for each interval separately. If an interval does not pass the checks of the first category, the checks of the second category do not need to be applied. This speeds up the whole process of finding suitable intervals. Additionally, cumulative sums are used whenever possible to shorten computation times.

2.3.2.1. Criteria: First Category

As stated above, this first set of criteria is for finding possible intervals for zero level calculation. Further checks are required for intervals that pass the checks of this category.

Criterion 1: $B_t < 30 \text{ nT}$

If the zero level O_3 is roughly known beforehand, this criterion can be used to select small fields as input.

Criterion 2: $B_{12} < 25 \text{ nT}$ ($B_{12} = \sqrt{B_1^2 + B_2^2}$)

Additional criterion that supports Criterion 1 in case of high uncertainties of O_3 before starting.

Criterion 3: $\langle F(B_{12}) \rangle < 0.25$ nT and $\langle F(B_3) \rangle < 0.25$ nT

The average of the filtered spin plane component and the spin axis component should be less than 0.25 nT. This ensures that the interval contains only varying magnetic fields (together with Criterion 4).

Criterion 4: $\frac{\lambda_2}{\lambda_1} < 0.1$ and $\lambda_1 > 1$

λ_1 and λ_2 are the eigenvalues of the covariance matrix between $F(B_{12})$ and $F(B_3)$ in descending magnitude.

F denotes the filter function

$$\text{cov}(F(B_{12}), F(B_3)) = \begin{bmatrix} \langle F(B_{12})^2 \rangle - \langle F(B_{12}) \rangle^2 & \langle F(B_{12})F(B_3) \rangle - \langle F(B_{12}) \rangle \langle F(B_3) \rangle \\ \langle F(B_3)F(B_{12}) \rangle - \langle F(B_3) \rangle \langle F(B_{12}) \rangle & \langle F(B_3)^2 \rangle - \langle F(B_3) \rangle^2 \end{bmatrix}$$

This ensures that the field changes towards a single direction and that the change is substantial.

Criterion 5: $\frac{|V_3'|}{|V_{12}'|} \leq \tan\left(65 \frac{\pi}{180}\right)$

The vector $\vec{V}' = \begin{pmatrix} V_{12}' \\ V_3' \end{pmatrix}$ is the eigenvector that corresponds to the largest

eigenvalue of the covariance matrix (Criterion 4 above). It points towards the maximum variance direction. The more the maximum variance direction points towards the spin axis, the less of an effect has a change of O_3 on the cross product between the magnetic field and the maximum variance direction. This criterion ensures that there is at least a 25 degree angle between the spin axis and the maximum variance direction.

Criterion 6: $|\text{corr}(F(B_{12}), F(B_3))| > 0.95$

The filtered components $F(B_{12})$ and $F(B_3)$ should be highly correlated.

2.3.2.2. Criteria: Second Category

This set of criteria is applied to each interval after the zero level for that interval has been calculated and applied to B_3 . Intervals that pass the checks of the first and second category are added to the set of intervals that is used for the overall least squares inversion and Monte Carlo simulation.

There are two options of how to calculate the spin axis offset. Both options yield similar results. The first option is to set $\vec{V} \times \vec{B}'$ equal to zero, whereas \vec{V} is the maximum variance direction of the filtered magnetic field data in all three dimensions (similar to matrix in Criterion 4 above but for three dimensions) and \vec{B}' is the magnetic field vector. Here, the vector \vec{B}' is a combination of filtered and unfiltered data:

$$\vec{B}' = \begin{pmatrix} F(B_1) + \langle B_1 \rangle \\ F(B_2) + \langle B_2 \rangle \\ F(B_3) + \langle B_3 \rangle \end{pmatrix}$$

This gives the following equations:

$$\vec{V} \times \vec{B}' = \begin{pmatrix} B_2' V_3 - (B_3' + O_3) V_2 \\ (B_3' + O_3) V_1 - B_1' V_3 \\ B_1' V_2 - B_2' V_1 \end{pmatrix} \quad (2.30)$$

After setting $\vec{V} \times \vec{B}'$ to zero and some algebra, two equations with one unknown are obtained:

$$\begin{pmatrix} V_2 \\ V_1 \end{pmatrix} O_3 = \begin{pmatrix} B_2' V_3 - B_3' V_2 \\ B_1' V_3 - B_3' V_1 \end{pmatrix} \quad (2.31)$$

The second option is to use the sum of the squares of the spin plane components. Writing the two dimensional cross product:

$$\vec{V}' \times \vec{B}'' = B_{12}'' V_3' - (B_3'' + O_3) V_{12}' \quad (2.32)$$

with \vec{V}' as in Criterion 5 above and $\vec{B}'' = \begin{pmatrix} F(B_{12}) + \langle B_{12} \rangle \\ F(B_3) + \langle B_3 \rangle \end{pmatrix}$

After setting $\vec{V}' \times \vec{B}''$ to zero and some algebra:

$$V_{12}' O_3 = B_{12}'' V_3' - B_3'' V_{12}' \quad (2.33)$$

Criterion 7: $RMS_{12} > 0.5 \text{ nT}$, $RMS_3 > 0.5 \text{ nT}$, $RMS_t > 0.8 \text{ nT}$

The root-mean-square deviations of three line fits to the components of \vec{B}'' and its magnitude must be larger than the above thresholds. This ensures variance of the field with respect to a line (for this purpose, this is a better criterion than variance with respect to the mean).

Criterion 8: $k_{12} < 0.15$, $k_3 < 0.15$, $k_t < 0.15$

The slopes of the linear fits in Criterion 7 must be smaller than a threshold.

Criterion 9: $c_{12,t} > 0.95$, $c_{3,t} > 0.95 \quad \forall \langle B_3 \rangle > 0$, $c_{3,t} < -0.95 \quad \forall \langle B_3 \rangle \leq 0$

$c_{12,t}$ is the correlation coefficient between B_{12}'' and $|\vec{B}''|$

$c_{3,t}$ is the correlation coefficient between B_3'' and $|\vec{B}''|$

Since $\langle B_3 \rangle$ can be positive or negative, the check of the correlation coefficient $c_{3,t}$ must be done with respect to the sign. A very high correlation between the components and the magnitude of \vec{B}'' is desired.

Criterion 10: The phase shift between the components and the magnitude of \vec{B}'' must be zero. The highest correlations or anti-correlations must be obtained without shift.

$$\text{Criterion 11: } std\left(\frac{B_{12}''}{\langle B_{12} \rangle} - \frac{B_3''}{\langle B_3 \rangle}\right) < \frac{\sqrt{\langle B_{12} \rangle^2 + \langle B_3 \rangle^2}}{m}$$

This criterion is very effective in determining whether or not an interval is supposed to be a pure compression. It relates the differences between the components to field strength, after correction of the zero level. Useful values for m range from 1000 to 2000.

2.3.2.3. Overall Inversion and Monte Carlo Simulation

The median and standard deviation of the zero levels of all intervals that pass the above eleven criteria is calculated. Intervals that have zero levels that are within one standard deviation of the median are combined to a subset of intervals that is used for the overall inversion.

For diagnostic purposes the number of all the intervals as well as the number and length of all the independent intervals is calculated. Additionally a Monte Carlo simulation is performed.

For the Monte Carlo simulation a modified blocked Bootstrap-method is used (Efron, 1982). The independent intervals are blocked to three minute intervals. Out of all n three-minute intervals, n intervals are randomly chosen. This yields a data set with reduced information that contains $1/e$ intervals more than once. For this new reduced data set the least squares solution of the zero level is calculated. This is done 1000 times. For diagnostic purposes the standard deviation, mean and median of all 1000 zero levels is computed. As error bars three times the standard deviation of the zero levels is used.

The evaluation of all the diagnostics parameters requires some experience. Tweaking the value m (see Criterion 11 above) as well as the amount of input data may be required. There are time intervals of several month of THEMIS data that do not yield a single interval that passes all 11 Criteria, which is due to absence of proper waves at the locations of the spacecraft.

2.3.2.4. Application

The algorithm was routinely applied to THEMIS data whenever a spacecraft did not go into the interplanetary field for longer periods. As an example I choose to show results for the THEMIS-A magnetometer with data from January to July 2011. The algorithm found 693 intervals (due to variable window length and overlap) that cover eight independent intervals. The independent intervals are altogether 40 minutes long and lie within a time range from March 29 to July 31, 2010. Thus, no intervals were found from January 1 to March 29. Figures 2.11 and 2.12 show two examples of such intervals. The algorithm produced results that are summarized in Table 2.4. The three sigma error bar is approximately 1 nT long. All four estimates of the zero level (-0.59 nT, -0.12 nT, -0.32 nT and -0.31 nT) are relatively close together and were calculated across 8 independent intervals that lie within a 4 month time period.

When examining the results, the outputs of the Monte Carlo simulation (error bars, mean and median), together with the number of independent intervals are most important. Additionally, the independent intervals should lie across a longer time frame. Please note that a 1 nT error bar is much better than what one would expect from model comparisons.

Number of intervals	693
Number of independent intervals	8
Combined length of independent intervals	40 min
Least squares O_3 of all 693 intervals	-0.59 nT
Least squares O_3 after cleaning (443 intervals left)	-0.12 nT (taken)
Mean least squares O_3 of Monte Carlo simulation	-0.32 nT
Median least squares O_3 of Monte Carlo simulation	-0.31 nT
Standard deviation of O_3 (Monte Carlo simulation)	0.21 nT
Three times standard deviation (error bar)	-0.32 nT \pm 0.63 nT

Table 2.4. Table of results.

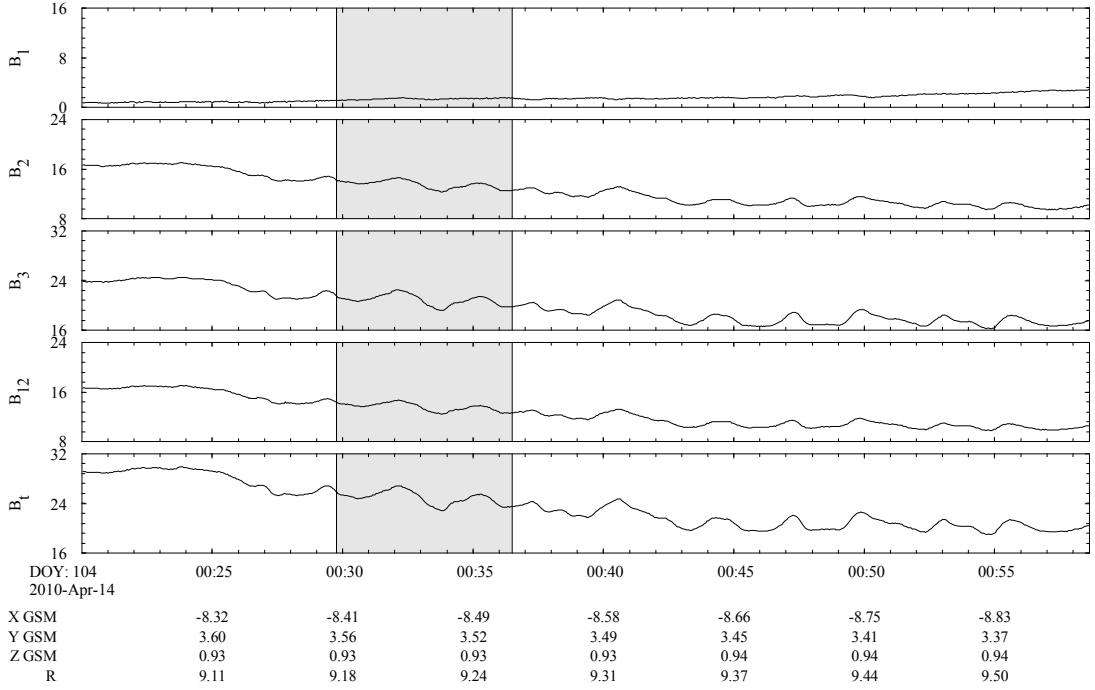


Figure 2.11. THEMIS-A magnetic field data. The area highlighted in gray is one independent interval that was chosen by the algorithm. B_{12} (4th panel) is the sum of the squares of the spin plane components.

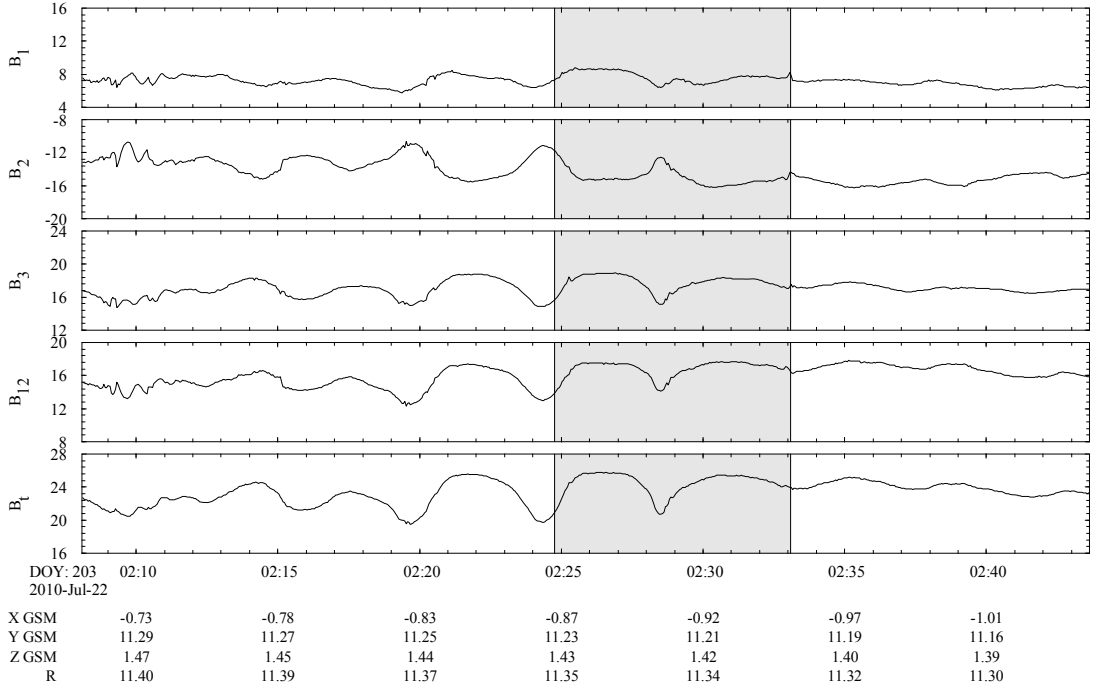


Figure 2.12. THEMIS-B magnetic field data. The area highlighted in gray is one independent interval that was chosen by the algorithm. B_{12} (fourth panel) is the sum of the squares of the spin plane components.

2.4. Conclusions

Because of its mathematical superiority (see Section 2.2.4.4.), the Davis-Smith method represents the method of choice for magnetometer calibrations inside the interplanetary magnetic field. The technique described herein is an improved implementation of the Davis-Smith method that provides error estimates. The author is aware of the fact that there are possibilities to further improve the presented novel technique. In this chapter the mathematical underpinnings of the procedure was documented and the relationship to the Belcher technique and the Hedgecock technique and their limitations were explained.

Additionally an automated technique for finding zero levels inside a magnetosphere that provides error estimates has been developed.

3. Orthogonalization of a Sensor Triad on Spinning Spacecraft

3.1. Introduction

The magnetometer sensor triad combined with the electronics produce vector measurements in sensor coordinates (S_1, S_2, S_3). This coordinate system is not perfectly orthogonal and spins with the spacecraft. Its orthogonalized version (x, y, z), as it is used in this thesis, has the z -axis aligned with the spin axis and the y -axis leads the x -axis by 90 degrees. Both coordinate systems can be transformed into non-spinning (despun) coordinate systems by multiplication with a despin matrix (see equation 3.8). After despining, the coordinate systems are called the non-orthogonal despun coordinate system (X', Y', Z') and the orthogonal despun coordinate system (X, Y, Z) which is often referred to as spacecraft coordinate system. A common definition of spacecraft coordinates is that the Sun lies in the XZ -plane with X pointing roughly towards the Sun. The Z axis is aligned with the spin axis and the Y -axis completes a right handed system. Via attitude information the spacecraft coordinates can be further transformed into various geophysical coordinate systems. Most scientific data analysis is done in geophysical coordinate systems.

There are twelve calibration parameters that are required to fully calibrate a magnetometer. The parameters are three gains (G_1, G_2, G_3), three offsets (zero levels), (O_1, O_2, O_3), and six angles. The six angles consist of three azimuthal angles ($\varphi_1, \varphi_2, \varphi_3$) and three elevation angles ($\theta_1, \theta_2, \theta_3$), as shown in Figure 3.1.

Figure 3.2 shows an example of magnetic field data as measured by one of the four Cluster satellites (Balogh *et al.*, 2001). The data are in a despun coordinate system that is slightly non-orthogonal. Data given in such a coordinate system usually contain first and second harmonics in the spin plane components and first harmonics in the spin axis component (see Figures 3.3 and 3.4). The first and second harmonics can be linked to certain calibration parameters. In the given example the magnetometer uses ranges 2, 3 and 4. The ranges are different gain states that are used to measure magnetic field values of certain values. In this example range 2 is used for small magnetic field values (-64 to 63.992 nT), range 3 for intermediate- (-256 to +255.97 nT) and range 4 for large magnetic field values (-1024 to 1023.9 nT). As can be seen from Figures 3.3 and 3.4 the spin harmonics are different at the range changes, thus each range requires a different set of calibration parameters.

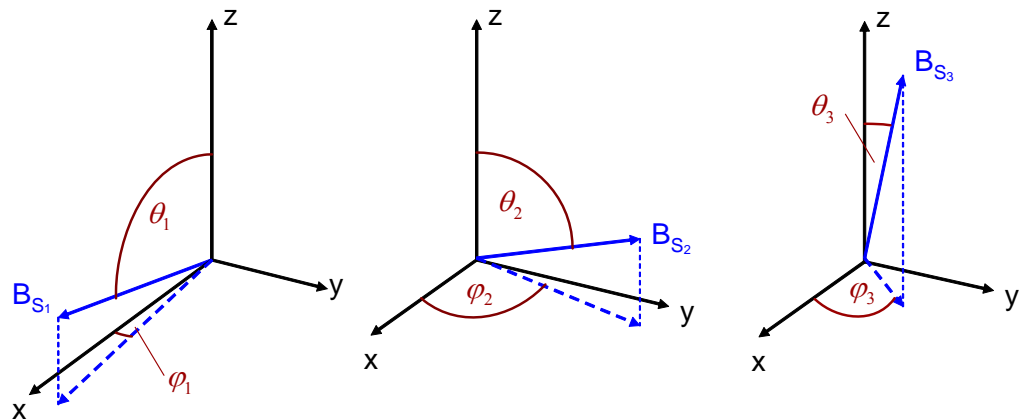


Figure 3.1. Definition of the six angles that are required to calibrate a magnetometer.

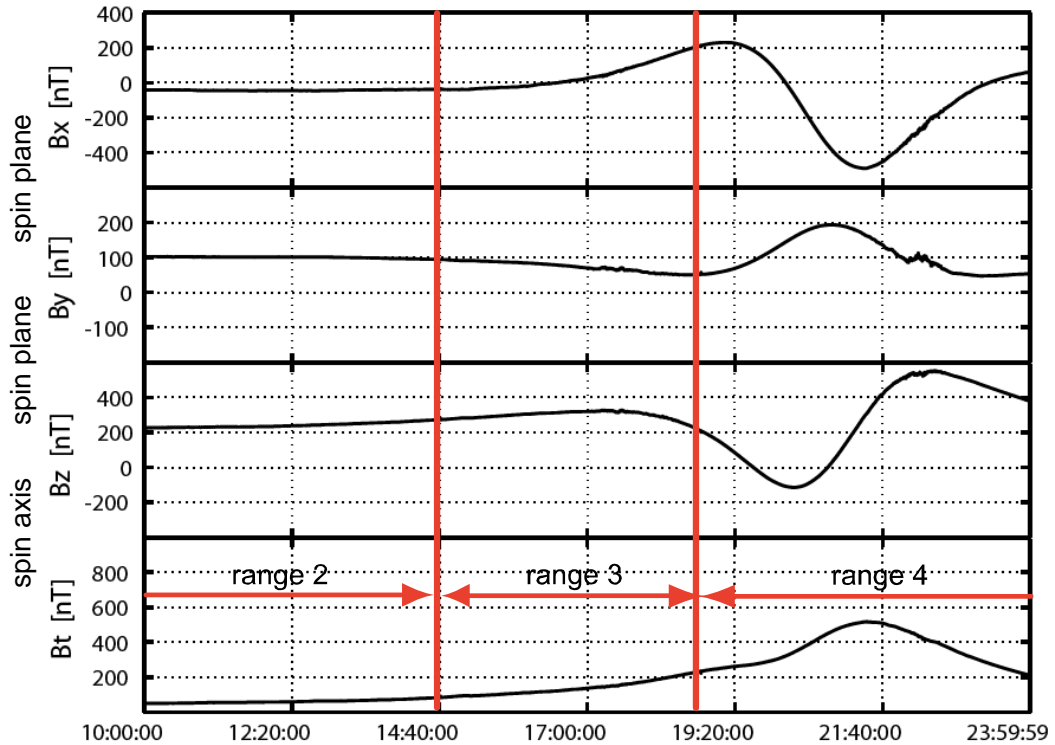


Figure 3.2. Example of Cluster magnetic field data that were measured in 3 different ranges (magnetometer gains).

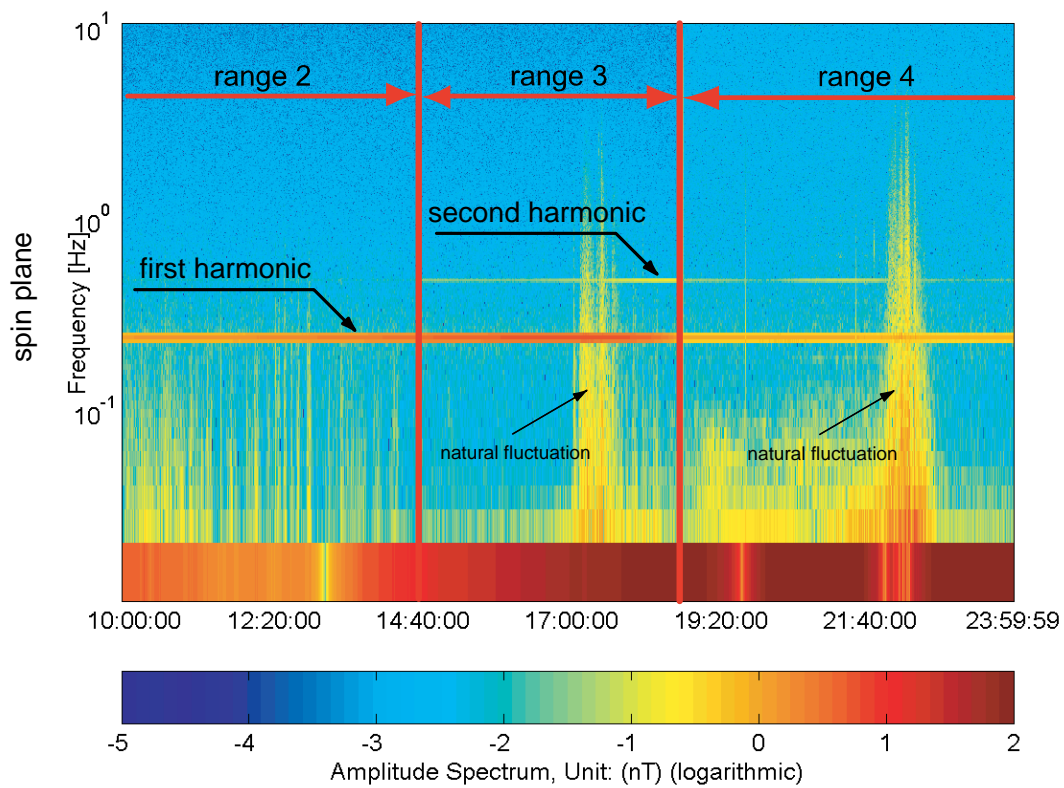


Figure 3.3. First and second harmonics in a spin plane component for three different ranges (magnetometer gains).

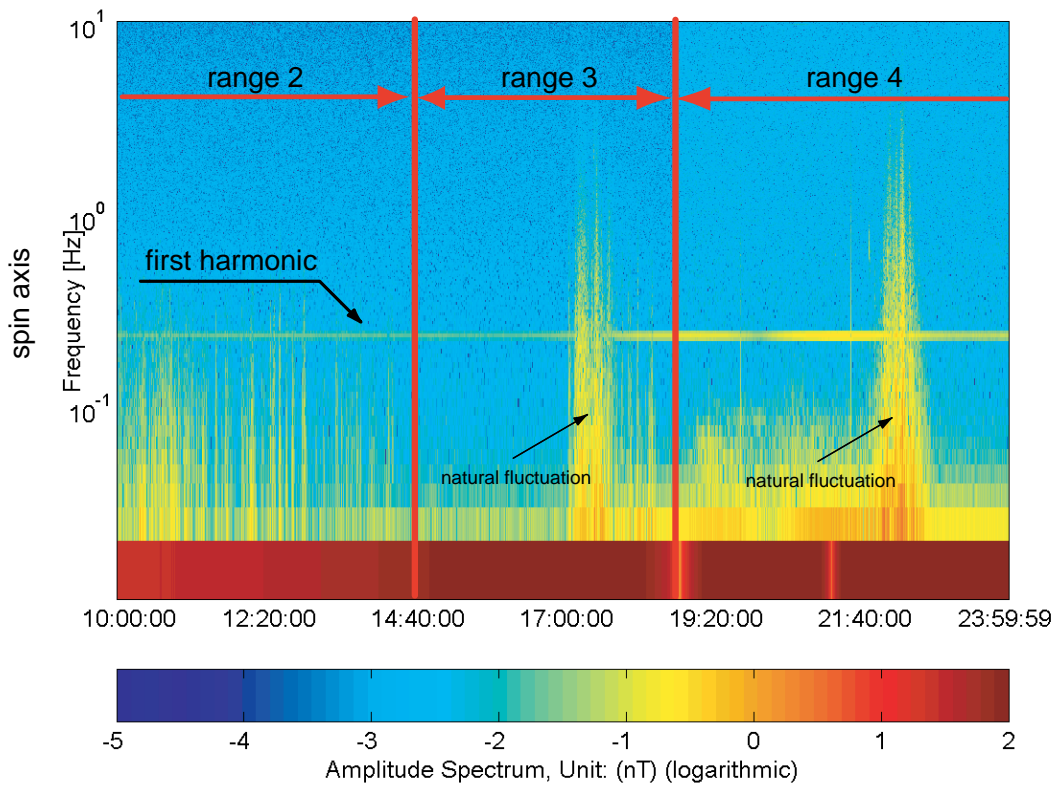


Figure 3.4. First harmonics in the spin axis component for three different ranges (magnetometer gains).

The derivation of the calibration parameters that are linked to certain harmonics is published in Kepko *et al.* (1996). Below, I provide the derivation for convenience of the reader. Equation (3.1) transforms magnetic field values that are given in orthogonal spinning coordinates back to non-orthogonal sensor coordinates.

$$\begin{pmatrix} B_{S_1} \\ B_{S_2} \\ B_{S_3} \end{pmatrix} = \begin{pmatrix} G_1 \sin \theta_1 \cos \varphi_1 & G_1 \sin \theta_1 \sin \varphi_1 & G_1 \cos \theta_1 \\ G_2 \sin \theta_2 \cos \varphi_2 & G_2 \sin \theta_2 \sin \varphi_2 & G_2 \cos \theta_2 \\ G_3 \sin \theta_3 \cos \varphi_3 & G_3 \sin \theta_3 \sin \varphi_3 & G_3 \cos \theta_3 \end{pmatrix} \cdot \begin{pmatrix} B_x \\ B_y \\ B_z \end{pmatrix} + \begin{pmatrix} O_1 \\ O_2 \\ O_3 \end{pmatrix} \quad (3.1)$$

$B_{S_1}, B_{S_2}, B_{S_3}$	non-orthogonal field components as measured by the magnetometer sensors
B_x, B_y, B_z	orthogonalized field components
G_1, G_2, G_3	gain corrections of each of the sensors
$\theta_1, \theta_2, \theta_3$	elevation angles of each of the sensors
$\varphi_1, \varphi_2, \varphi_3$	azimuthal angles of each of the sensors
O_1, O_2, O_3	offsets of each of the sensors

Please note that the matrix in equation (3.1) is the inverse of a calibration matrix. As can be seen in Figure 3.1, some of the angles are close to 90° and φ_3 can be large. The following transformations can be used to transform all angles (except for φ_3) to small values (see equations 3.2a to 3.2f).

$$\theta_1 = 90 - \Delta\theta_1 \quad (3.2a)$$

$$\varphi_1 = \Delta\varphi_1 \quad (3.2b)$$

$$\theta_2 = 90 - \Delta\theta_2 \quad (3.2c)$$

$$\varphi_2 = 90 + \Delta\varphi_2 \quad (3.2d)$$

$$\theta_3 = \Delta\theta_3 \quad (3.2e)$$

$$\varphi_3 = \varphi_3 \quad (3.2f)$$

The azimuthal angle of the spin axis φ_3 has a small effect if the corresponding elevation angle θ_3 is small (no matter how large φ_3 is). With help of small angle approximations ($\cos \Delta\alpha \approx 1$ and $\sin \Delta\alpha \approx \Delta\alpha$) and equations (3.2a) to (3.2f) it is possible to write equation (3.1) in a simpler form.

$$\begin{pmatrix} B_{S_1} \\ B_{S_2} \\ B_{S_3} \end{pmatrix} = \begin{pmatrix} G_1 & G_1 \Delta\varphi_1 & G_1 \Delta\theta_1 \\ -G_2 \Delta\varphi_2 & G_2 & G_2 \Delta\theta_2 \\ G_3 \Delta\theta_3 \cos \varphi_3 & G_3 \Delta\theta_3 \sin \varphi_3 & G_3 \end{pmatrix} \begin{pmatrix} B_x \\ B_y \\ B_z \end{pmatrix} + \begin{pmatrix} O_1 \\ O_2 \\ O_3 \end{pmatrix} \quad (3.3)$$

At this point it is worth mentioning, that using the small angle approximation for $\sin \Delta\theta_3 \approx \Delta\theta_3$ is not necessary but the equations will be given in the same form as they were published in the original publication. Not using this small angle approximation can improve convergence during iterations (the iteration process is described in Section 3.2.2).

With

$$G_2 = G_1 + \Delta G_{21} \quad (3.4)$$

and

$$\Delta\varphi_2 = \Delta\varphi_1 + \Delta\varphi_{21} \quad (3.5)$$

it is possible to write

$$\begin{pmatrix} B_{S_1} \\ B_{S_2} \\ B_{S_3} \end{pmatrix} = \begin{pmatrix} G_1 & G_1 \Delta\varphi_1 & G_1 \Delta\theta_1 \\ -G_1(\Delta\varphi_1 + \Delta\varphi_{21}) & G_1 + \Delta G_{21} & G_1 \Delta\theta_2 \\ G_3 \Delta\theta_3 \cos \varphi_3 & G_3 \Delta\theta_3 \sin \varphi_3 & G_3 \end{pmatrix} \begin{pmatrix} B_x \\ B_y \\ B_z \end{pmatrix} + \begin{pmatrix} O_1 \\ O_2 \\ O_3 \end{pmatrix} \quad (3.6)$$

The quantities $\Delta\varphi_{21}$ and $\Delta G'_{21}$ are relative corrections. As shown below (equations 3.9a to 3.9c), the absolute values of φ_1 and φ_2 cannot be linked to spin harmonics. Additionally, the absolute values of any gains (G_1 , G_2 and G_3) cannot be calculated from the equations that are given in this chapter.

With

$$B_x = B_H \cos(\omega t - \psi) \quad (3.7a)$$

$$B_y = -B_H \sin(\omega t - \psi) \quad (3.7b)$$

$$B_z = B_z \quad (3.7c)$$

it is possible relate the data in the spinning- and non-spinning frames. Where $B_H = \sqrt{B_x^2 + B_y^2}$ is the magnitude of the spin plane components. Multiplying both sides of (3.6) with the despin matrix

$$D = \begin{pmatrix} \cos \omega t & -\sin \omega t & 0 \\ \sin \omega t & \cos \omega t & 0 \\ 0 & 0 & 1 \end{pmatrix} \quad (3.8)$$

yields

$$\begin{aligned} B_{X'} = & G_1 B_H (\cos \psi + \Delta\varphi_2 \sin \psi) + G_1 \frac{B_H}{2} (\Delta G'_{21} \cos \psi - \Delta\varphi_2 \sin \psi) \\ & + \cos \omega t G_1 (B_z \Delta\theta_1 + O'_1) \\ & + \sin \omega t G_1 (-B_z \Delta\theta_2 - O'_2) \\ & + \cos 2\omega t G_1 \frac{B_H}{2} (-\Delta G'_{21} \cos \psi - \Delta\varphi_{21} \sin \psi) \\ & + \sin 2\omega t G_1 \frac{B_H}{2} (-\Delta G'_{21} \sin \psi + \Delta\varphi_{21} \cos \psi) \end{aligned} \quad (3.9a)$$

$$\begin{aligned} B_{Y'} = & G_1 B_H (\sin \psi - \Delta\varphi_2 \cos \psi) + G_1 \frac{B_H}{2} (\Delta G'_{21} \sin \psi + \Delta\varphi_2 \cos \psi) \\ & + \cos \omega t G_1 (B_z \Delta\theta_2 + O'_2) \\ & + \sin \omega t G_1 (B_z \Delta\theta_1 + O'_1) \\ & + \cos 2\omega t G_1 \frac{B_H}{2} (\Delta G'_{21} \sin \psi - \Delta\varphi_{21} \cos \psi) \\ & + \sin 2\omega t G_1 \frac{B_H}{2} (-\Delta G'_{21} \cos \psi - \Delta\varphi_{21} \sin \psi) \end{aligned} \quad (3.9b)$$

$$\begin{aligned} B_{Z'} = & G_3 (B_z + O'_3) \\ & + \cos \omega t G_3 B_H (\cos \varphi_3 \Delta\theta_3 \cos \psi + \sin \varphi_3 \Delta\theta_3 \sin \psi) \\ & + \sin \omega t G_3 B_H (-\sin \varphi_3 \Delta\theta_3 \cos \psi + \cos \varphi_3 \Delta\theta_3 \sin \psi) \end{aligned} \quad (3.9c)$$

where the magnetic phase angle in the spin plane

$$\psi = \tan^{-1}(B_Y / B_X) \quad (3.10)$$

and additional simplifications

$$O'_1 = \frac{O_1}{G_1}, \quad O'_2 = \frac{O_2}{G_1}, \quad O'_3 = \frac{O_3}{G_3} \quad \text{and} \quad \Delta G'_{21} = \frac{\Delta G_{21}}{G_1}$$

were used.

The equations (3.9a to 3.9c) are the fundamental equations for the rest of this chapter. Terms that contain $\sin \omega t$ and $\cos \omega t$ describe first harmonics. Similarly, terms that contain $\sin 2\omega t$ and $\cos 2\omega t$ describe second harmonics. From equations (3.9a) and (3.9b) one can learn that the first harmonics in the spin plane components are linked to O'_1 , O'_2 , $\Delta\theta_1$ and $\Delta\theta_2$. Additionally it can be seen that the second harmonics in the spin plane components are linked to $\Delta G'_{21}$ and $\Delta\varphi_{21}$. Furthermore it is possible to learn from equation (3.9c) that, the first harmonics in the spin axis component are linked to φ_3 and $\Delta\theta_3$. One also can learn that there are no second harmonics in the spin axis component.

In summary it is possible to state that the calibration parameters that can be resolved by removal of the spin harmonics in the despun spacecraft frame are: O'_1 , O'_2 , $\Delta\theta_1$, $\Delta\theta_2$, $\Delta G'_{21}$, $\Delta\varphi_{21}$, φ_3 and $\Delta\theta_3$.

3.2. Removal of Spin Harmonics via Fourier Transforms

This method has been described in Kepko *et al.* (1996). Herein the method is provided for convenience of the reader.

Equations (3.9a to 3.9c) contain amplitudes of various spin harmonics. Such amplitudes can be expressed by the real and imaginary terms of Fourier transformations. Fourier transforming both sides of (3.9a to 3.9c) via the relation

$$F(\omega) = 1/T \int_0^T f(t) e^{-i\omega t} dt \quad (3.11)$$

yields the following equations

$$B_{X'}(\omega=0) = B_H G_1 \cos \psi + \frac{B_H}{2} G_1 (\Delta G'_{21} \cos \psi + \Delta \varphi_{21} \sin \psi) \quad (3.12a)$$

$$\Re\{B_{X'}(\omega=\omega_{sp})\} = G_1 (B_z \Delta \theta_1 + O'_1) \quad (3.12b)$$

$$\Im\{B_{X'}(\omega=\omega_{sp})\} = G_1 (-B_z \Delta \theta_2 - O'_2) \quad (3.12c)$$

$$\Re\{B_{X'}(\omega=2\omega_{sp})\} = G_1 \frac{B_H}{2} (-\Delta G'_{21} \cos \psi - \Delta \varphi_{21} \sin \psi) \quad (3.12d)$$

$$\Im\{B_{X'}(\omega=2\omega_{sp})\} = G_1 \frac{B_H}{2} (-\Delta G'_{21} \sin \psi + \Delta \varphi_{21} \cos \psi) \quad (3.12e)$$

$$B_{Y'}(\omega=0) = B_H G_1 \sin \psi + \frac{B_H}{2} G_1 (\Delta G'_{21} \sin \psi - \Delta \varphi_{21} \cos \psi) \quad (3.12f)$$

$$\Re\{B_{Y'}(\omega=\omega_{sp})\} = G_1 (B_z \Delta \theta_2 + O'_2) \quad (3.12g)$$

$$\Im\{B_{Y'}(\omega=\omega_{sp})\} = G_1 (B_z \Delta \theta_1 + O'_1) \quad (3.12h)$$

$$\Re\{B_{Y'}(\omega=2\omega_{sp})\} = G_1 \frac{B_H}{2} (\Delta G'_{21} \sin \psi - \Delta \varphi_{21} \cos \psi) \quad (3.12i)$$

$$\Im\{B_{Y'}(\omega=2\omega_{sp})\} = G_1 \frac{B_H}{2} (-\Delta G'_{21} \cos \psi - \Delta \varphi_{21} \sin \psi) \quad (3.12j)$$

$$B_{Z'}(\omega=0) = G_3 (B_z + O'_3) \quad (3.12k)$$

$$\Re\{B_{Z'}(\omega=\omega_{sp})\} = G_3 B_H (\cos \varphi_3 \Delta \theta_3 \cos \psi + \sin \varphi_3 \Delta \theta_3 \sin \psi) \quad (3.12l)$$

$$\Im\{B_{Z'}(\omega=\omega_{sp})\} = G_3 B_H (\cos \varphi_3 \Delta \theta_3 \sin \psi - \sin \varphi_3 \Delta \theta_3 \cos \psi) \quad (3.12m)$$

The zeroth-order harmonics ($\omega=0$) represent the estimates of averages of the field in the X , Y , and Z directions. The estimates are required to calculate B_H , B_Z and ψ . The three quantities are assumed to be constant over an interval where a Discrete Fourier Transformation (DFT) is performed. This assumption is violated for fast changing fields. An alternative technique has been developed and is presented in Section 3.3.

3.2.2. Least Squares Inversions and Iterations

From (3.12b) and (3.12h) a system of equations can be formed so that it is possible to solve for O_1' and $\Delta\theta_1$.

$$U = B_Z \Delta\theta_1 + O_1' \quad (3.13)$$

Where U consists of $\Re\{B_{X'}(\omega = \omega_{sp})\}/G_1$ and $\Im\{B_{Y'}(\omega = \omega_{sp})\}/G_1$.

Similarly, from (3.12c) and (3.12g) a system of equations can be formed so that it is possible to solve for O_2' and $\Delta\theta_2$.

$$V = B_Z \Delta\theta_2 + O_2' \quad (3.14)$$

Where V consists of $\Im\{B_{X'}(\omega = \omega_{sp})\}/G_1$ and $\Re\{B_{Y'}(\omega = \omega_{sp})\}/G_1$.

From (3.12d), (3.12e), (3.12i) and (3.12j) a system of equations can be formed so that it is possible to solve for $\Delta G'_{21}$ and $\Delta\varphi_{21}$.

$$W_{j=1..4} = \Delta G'_{21} \alpha_j + \Delta\varphi_{21} \beta_j \quad (3.15)$$

With

$$W_1 = 2\Re\{B_{X'}(\omega = 2\omega_{sp})\}/(G_1 B_H)$$

$$\alpha_1 = -\cos\psi, \beta_1 = -\sin\psi$$

$$W_2 = 2\Im\{B_{X'}(\omega = 2\omega_{sp})\}/(G_1 B_H)$$

$$\alpha_2 = -\sin\psi, \beta_2 = \cos\psi$$

$$W_3 = 2\Re\{B_{Y'}(\omega = 2\omega_{sp})\}/(G_1 B_H)$$

$$\alpha_3 = \sin\psi, \beta_3 = -\cos\psi$$

$$W_4 = 2\Im\{B_{Y'}(\omega = 2\omega_{sp})\}/(G_1 B_H)$$

$$\alpha_4 = -\cos\psi, \beta_4 = -\sin\psi$$

The last system of equations can be formed from (3.12l) and (3.12m) so that it is possible to solve for φ_3 and $\Delta\theta_3$.

$$P_{j=1,2} = \cos\varphi_3 \Delta\theta_3 \gamma_j + \sin\varphi_3 \Delta\theta_3 \delta_j \quad (3.16)$$

With

$$P_1 = \Re\{B_z(\omega = \omega_{sp})\} / (G_3 B_H)$$

$$\gamma_1 = \cos \psi, \delta_1 = \sin \psi$$

$$P_2 = \Im\{B_z(\omega = \omega_{sp})\} / (G_3 B_H)$$

$$\gamma_2 = -\sin \psi, \delta_2 = \cos \psi$$

As stated above a better way of solving this equation is to use $\sin \Delta\theta_3$ instead of just the small angle approximation $\Delta\theta_3$.

$$P_{j=1,2} = \cos \varphi_3 \sin \Delta\theta_3 \gamma_j + \sin \varphi_3 \sin \Delta\theta_3 \delta_j \quad (3.17)$$

Defining in (3.17) $a = \cos \varphi_3 \sin \Delta\theta_3$, $b = \sin \varphi_3 \sin \Delta\theta_3$ and solving for a and b yields

$$\tan \varphi_3 = b/a$$

$$\sin \Delta\theta_3 = \sqrt{a^2 + b^2}$$

The described least squares equations represent approximations of the full equations, thus iterations are required in order to calculate exact calibration parameters. Each iteration yields approximate calibration parameters which are applied using the full equation (3.1). Data that have the new calibration parameters applied are then used to further calculate improved calibration parameters until convergence is reached.

3.2.3. Application of the Technique

It is important to note that the DFTs must be applied to an integral number of spin periods in order to get the best possible estimates of the amplitudes of the spin harmonics. In this work, intervals that are in the order of 20 spin periods long were used. Sets of such intervals are formed so that they cover a range of magnetic field values that is as large as possible (significant portions of a spacecraft orbit). This ensures that the equations are stable and converge. The background field of each interval should be as quiet as possible.

Figures 3.5 and 3.6 show dynamic spectra of data that were calibrated using the above technique. It is the same interval as shown in Figures 3.2, 3.3 and 3.4. Each of the three different ranges (2, 3, and 4) must be calibrated separately. The dynamic spectra show that the spin tone has been reduced greatly.

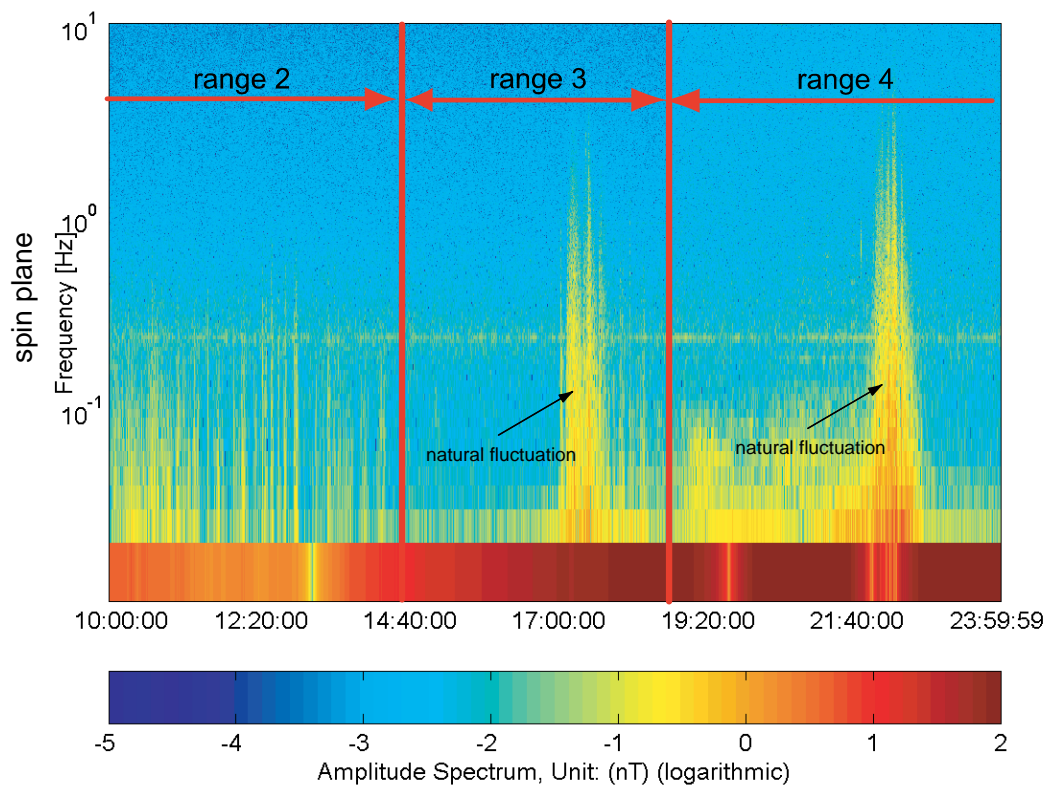


Figure 3.5. Removed spin tone in one of the spin plane components. Shown are data that cover three different ranges (magnetometer gains).

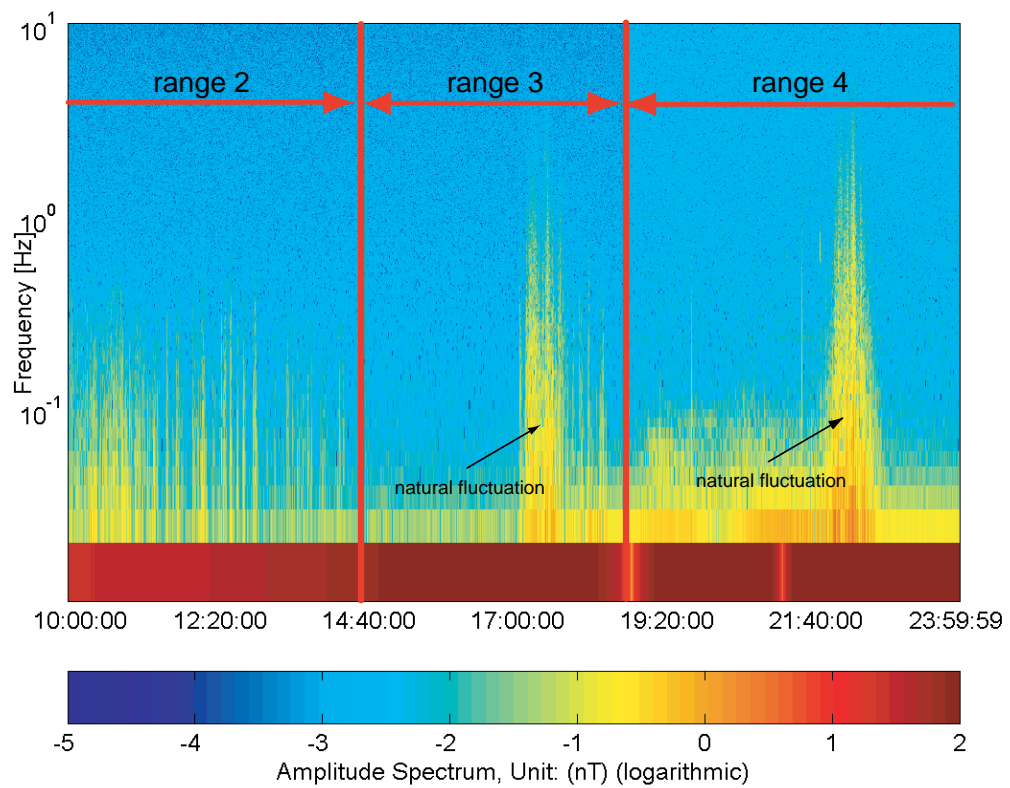


Figure 3.6. Removed spin tone in the spin axis component. Shown are data that cover three different ranges (magnetometer gains).

3.3. Removal of Spin Harmonics for Fast Changing Magnetic Fields (Envelope-Method)

3.3.1. Introduction

The technique described in the previous section is working well for slowly changing magnetic fields. I tried applying it to data that were measured during the Galileo Earth flybys. The method did not converge and for that reason, produced completely unrealistic results. The slow spin period (~ 20 sec) together with fast changing magnetic fields (as encountered by the fast moving spacecraft) are a problem for the Fourier based method. Figure 3.7 shows that not only the magnetic field changes fast but also the amplitudes of the spin harmonics change significantly even within a single spin period. The Galileo magnetometer is described in Kivelson *et al.* (1992).

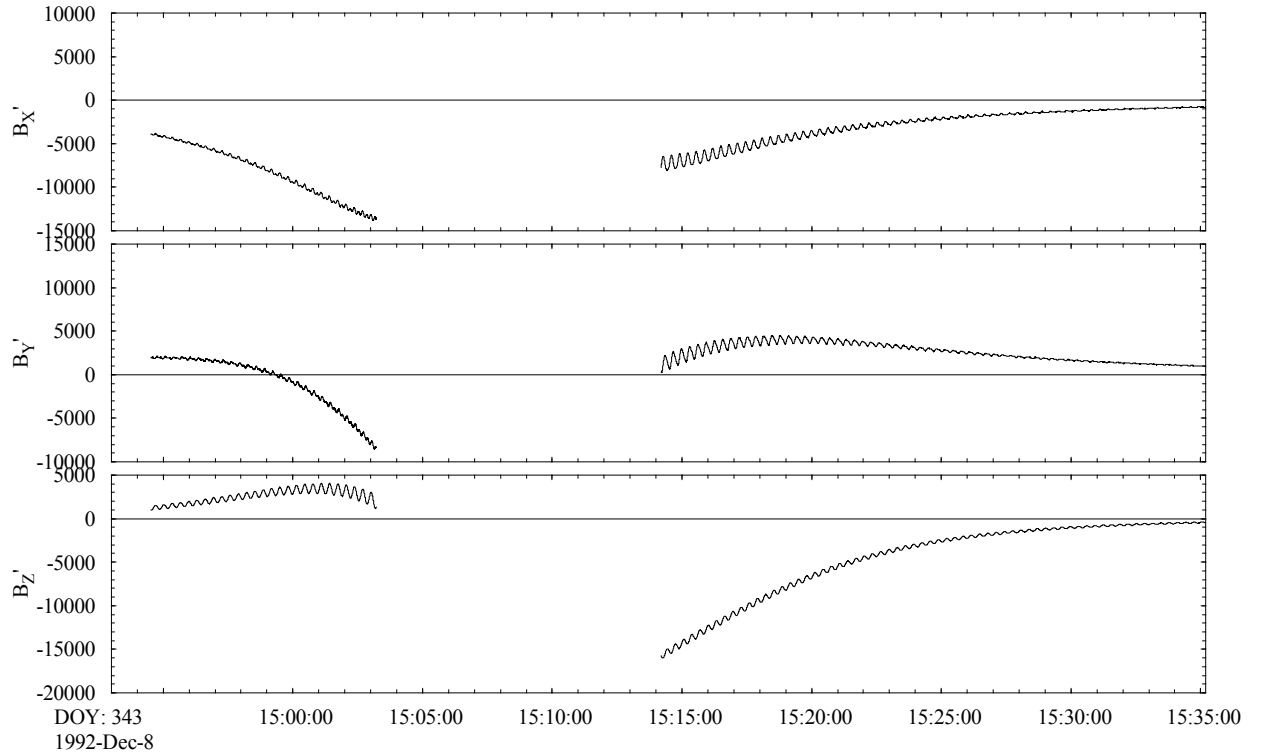


Figure 3.7. Magnetic field data in non-orthogonal despun spacecraft coordinates as measured by the Galileo spacecraft during its second Earth flyby.

Additionally, it can be seen that the noise level is very small compared to the amplitudes of the magnetic field and the spin harmonics. A better approach is to use envelopes to calculate time varying amplitudes of the magnetic field (see Figure 3.8). An example of such amplitudes of spin harmonics is shown in the bottom panel of Figure 3.8. Having amplitudes of spin harmonics for every point in time allows us to directly work with the fundamental equations (3.9a to 3.9c). It is important to point out that the amount of information that is being gained by using envelopes is extremely large.

The DFTs produce a single amplitude value for each harmonic per DFT-window. The envelope technique has as many times more values as measurements were taken during a DFT-window (usually several hundred times to thousands more). This vast increase of information easily allowed us to successfully calibrate the Galileo Earth flybys.

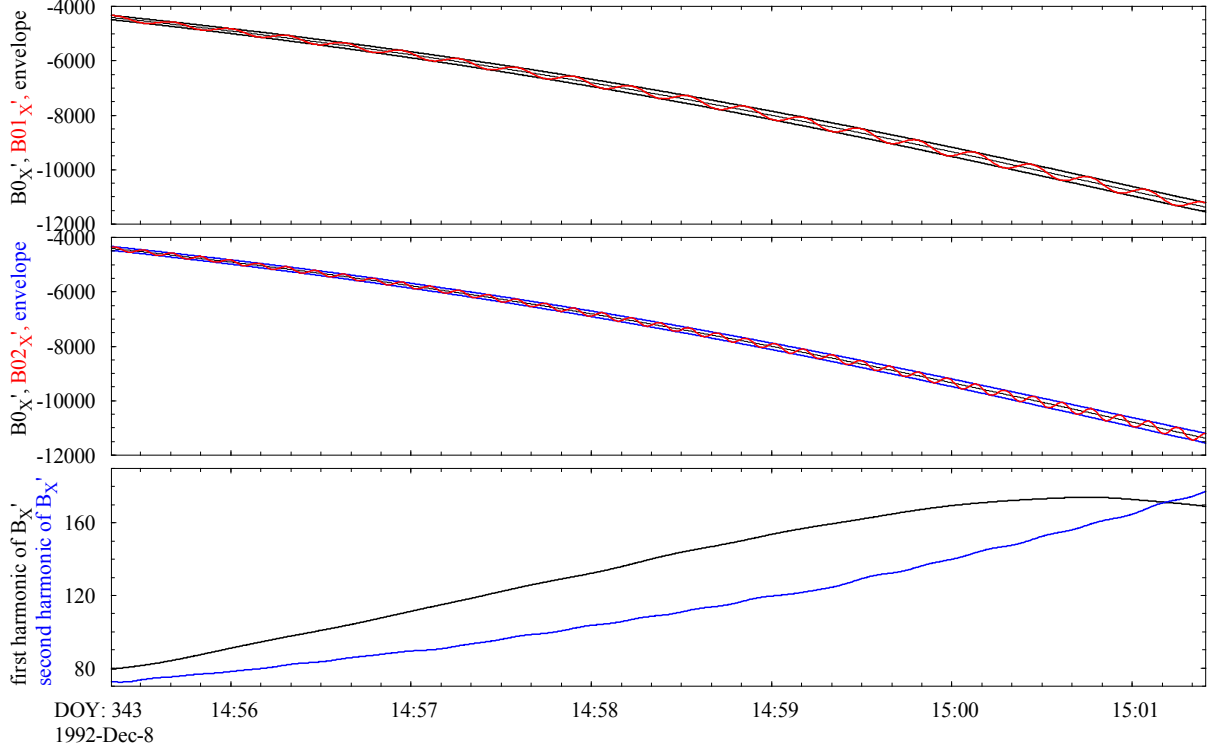


Figure 3.8. The first and second panels show magnetic field values that contain spin harmonics plus envelopes. The first panel shows the first harmonic of B_X' after filtering (see Sec. 3.3.2.). The second panel shows the second harmonic of B_X' after filtering (see Sec. 3.3.2.). The bottom panel shows the amplitudes of the spin harmonics as calculated from the envelopes.

3.3.2. Algorithm

The algorithm is fairly simple. Calculating the envelope requires a program that searches for valleys and peaks and interpolates. In the spin plane there are first and second harmonics. In order to get the first harmonics the data need to be low-pass filtered so that they do not contain second harmonics. In order to get the second harmonics the data need to be high-pass filtered so that they do not contain first harmonics. The applied filters must be zero phase filters that do not change the amplitude of the pass-band. To reduce the influence of high-frequency noise, the data can be low-pass filtered with cutoff frequencies above the frequencies of interest. From the amplitude of a certain harmonic and phase with respect to spacecraft spin phase it is easy to calculate the required sine- and cosine terms of the amplitudes as needed in the fundamental equations (3.9a to 3.9c).

3.3.3. Application of the Envelope-Method

I successfully applied the method to Galileo Earth flyby data. The equations for the Least-Squares fits (3.13, 3.14, 3.15 and 3.17) were slightly changed so that they minimize the error in percent of the field magnitude, by dividing both sides with one hundredth of the field magnitudes. Figure 3.9 shows a comparison between the non-orthogonalized and orthogonalized data.

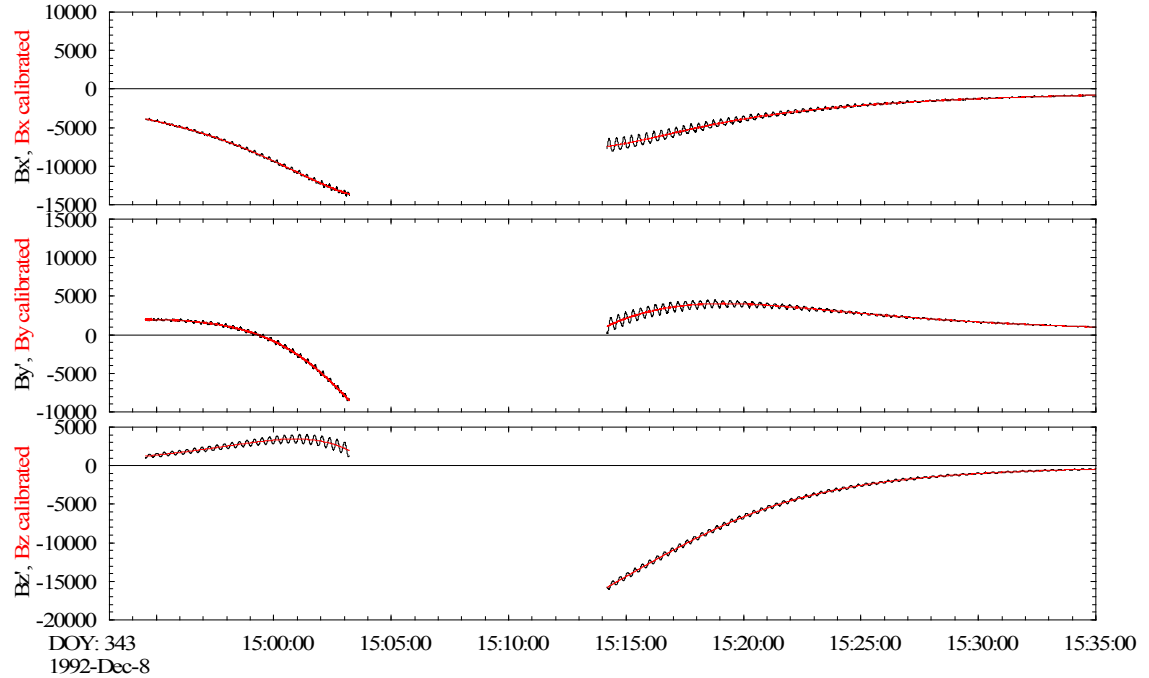


Figure 3.9. Magnetic field data in non-orthogonal despun spacecraft coordinates as well as in orthogonalized (red) despun spacecraft coordinates (measured by the Galileo spacecraft during its second Earth flyby).

3.4. Resolving Short Term Variations in the Calibration Parameters via Spin Tone Removal

3.4.1. Introduction

There are also short term variations in the calibration parameters which cannot be resolved with the least squares approaches that are described in Sections 3.2 and 3.3. One of the most common reasons for fast changing calibration parameters is fast changing temperature. Fast changes of temperatures commonly happen when a spacecraft goes into- or comes out of an eclipse. There are many other reasons why short term variations of the calibration parameters may occur. For example: a highly charged spacecraft due to photo electrons or exposure to strong radiation.

Before the method is described in greater detail a review of the used coordinate systems is given. The first coordinate system is the so-called spacecraft coordinate system (x, y, z) which is orthogonal and spins with the spacecraft. For the same coordinate system but spinning with twice the spin frequency (x'', y'', z'') is used. The z -axis is aligned with the spacecraft spin axis. The x - and y -axes (also x'' and y'') lie in the spin plane so that y leads x by 90° in the direction of rotation. The second coordinate system is the sensor coordinate system (S_1, S_2, S_3) which is similar to the spacecraft coordinate system meaning that the sensors of the triad S_1, S_2 and S_3 are roughly pointing towards x, y and z . The difference is that this coordinate system is not orthogonal due to the misalignment of the sensors. For the rest of this chapter, horizontal bars above symbols mean that the quantity represented by the symbol is averaged.

The basic principal of the new method is that the contributions of the first harmonics on the left hand sides in (3.9a, 3.9b and 3.9c) become constants in a frame which spins with the spacecraft's spin frequency. Similarly the second harmonics become constants in a frame that spins with twice the spin frequency.

The starting point for the explanations is the magnetic field data in the orthogonalized spacecraft coordinate system as expressed in equations (3.9a, 3.9b and 3.9c). The orthogonalization is done using the calibration parameters from the initial least squares solution.

3.4.2. Equations and Algorithm

Starting with the first harmonics in the spin plane, there are the terms $\cos \omega t G_1(B_z \Delta \theta_1 + O'_1)$, $\sin \omega t G_1(-B_z \Delta \theta_2 - O'_2)$ in equation (3.9a) and the terms $\cos \omega t G_1(B_z \Delta \theta_2 + O'_2)$ and $\sin \omega t G_1(B_z \Delta \theta_1 + O'_1)$ in (3.9b). Equation (3.18) shows how the inverse of the despin matrix (3.8) can be applied to the above terms of the first harmonics in order to show that the terms $G_1(B_z \Delta \theta_1 + O'_1)$ and $G_1(B_z \Delta \theta_2 + O'_2)$ are

constants in the spinning spacecraft frame. Therefore, by using running averages on B_x and B_y denoted as $\overline{B_x}$ and $\overline{B_y}$ the terms $G_1(B_z\Delta\theta_1 + O'_1)$ and $G_1(B_z\Delta\theta_2 + O'_2)$ can be calculated for each point in time.

$$\begin{pmatrix} \overline{B_x} \\ \overline{B_y} \end{pmatrix} = \begin{pmatrix} G_1(B_z\Delta\theta_1 + O'_1) \\ G_1(B_z\Delta\theta_2 + O'_2) \end{pmatrix} = \begin{pmatrix} \cos\omega t & \sin\omega t \\ -\sin\omega t & \cos\omega t \end{pmatrix} \begin{pmatrix} \cos\omega t G_1(B_z\Delta\theta_1 + O'_1) + \sin\omega t G_1(-B_z\Delta\theta_2 - O'_2) \\ \cos\omega t G_1(B_z\Delta\theta_2 + O'_2) + \sin\omega t G_1(B_z\Delta\theta_1 + O'_1) \end{pmatrix} \quad (3.18)$$

In the above equation the DC-component and the second harmonics of equations (3.9a) and (3.9b) were not rotated since they become harmonics in the spinning frame and go to zero because of the averaging.

Similarly, for resolving the second harmonics in the spin plane the data need to be transformed into a coordinate system that spins with twice the spin frequency. The DC-component in the despun frame usually becomes a big second harmonic in the frame that spins with twice the spin frequency. This big second harmonic would seriously affect any averaging, thus subtracting a running average in the orthogonal despun frame and then going into a frame that spins with twice the frequency solves this problem. The average in this frame is proportional to the second harmonics in the despun coordinate system. In the despun frame the second harmonics are expressed by the terms

$$\begin{aligned} & \cos 2\omega t G_1 \frac{B_H}{2} (-\Delta G'_{21} \cos\psi - \Delta\varphi_{21} \sin\psi), \\ & \sin 2\omega t G_1 \frac{B_H}{2} (-\Delta G'_{21} \sin\psi + \Delta\varphi_{21} \cos\psi) \end{aligned}$$

in (3.9a) and by

$$\begin{aligned} & \cos 2\omega t G_1 \frac{B_H}{2} (\Delta G'_{21} \sin\psi - \Delta\varphi_{21} \cos\psi), \\ & \sin 2\omega t G_1 \frac{B_H}{2} (-\Delta G'_{21} \cos\psi - \Delta\varphi_{21} \sin\psi) \end{aligned}$$

in (3.9b).

After transforming these terms to a spinning coordinate system that rotates with twice the spin frequency yields:

$$\begin{pmatrix} \overline{B_x} \\ \overline{B_y} \end{pmatrix} = \begin{pmatrix} A \\ B \end{pmatrix} = \begin{pmatrix} \cos 2\omega t & \sin 2\omega t \\ -\sin 2\omega t & \cos 2\omega t \end{pmatrix} \begin{pmatrix} \cos 2\omega t A + \sin 2\omega t (-B) \\ \cos 2\omega t B - \sin 2\omega t A \end{pmatrix} \quad (3.19)$$

with

$$A = G_1 \frac{B_H}{2} (-\Delta G'_{21} \cos \psi - \Delta \varphi_{21} \sin \psi) \quad (3.20a)$$

$$B = -G_1 \frac{B_H}{2} (-\Delta G'_{21} \sin \psi + \Delta \varphi_{21} \cos \psi) \quad (3.20b)$$

and

$$\begin{pmatrix} \overline{B_x} \\ \overline{B_y} \end{pmatrix} = \begin{pmatrix} \cos 2\omega t & \sin 2\omega t \\ -\sin 2\omega t & \cos 2\omega t \end{pmatrix} \begin{pmatrix} B_X - \overline{B_X} \\ B_Y - \overline{B_Y} \end{pmatrix}. \quad (3.21)$$

In equation (3.19) the terms for the first harmonics in equations (3.9a) and (3.9b) were left out since they become harmonics in the frame that spins with twice the spin frequency and become zero because of averaging.

By using

$B_x = B_H \cos \psi$ and $B_y = B_H \sin \psi$ it is possible to write

$$A = \frac{G_1}{2} (-\Delta G'_{21} B_x - \Delta \varphi_{21} B_y) \quad (3.22a)$$

$$B = -\frac{G_1}{2} (-\Delta G'_{21} B_y + \Delta \varphi_{21} B_x) \quad (3.22b)$$

This two by two system of equations can be solved for $\Delta G'_{21}$ and $\Delta \varphi_{21}$. Since previously calibrated data were used, G_1 can be set to 1.

After solving the system of equations:

$$\begin{aligned} \Delta G'_{21} &= \frac{Z_1 B_x + Z_2 B_y}{-B_y^2 - B_x^2} \\ \Delta \varphi_{21} &= \frac{Z_1 B_y - Z_2 B_x}{-B_y^2 - B_x^2} \end{aligned}$$

$$\text{with } Z_1 = \frac{2A}{G_1} \text{ and } Z_2 = -\frac{2B}{G_1}.$$

And the last type of harmonics that need to be discussed are the first harmonics in the spin axis component. Those harmonics are described in equation (3.9c), by the terms

$$\begin{aligned} & \cos \omega t G_3 B_H (\cos \varphi_3 \Delta \theta_3 \cos \psi + \sin \varphi_3 \Delta \theta_3 \sin \psi), \\ & \sin \omega t G_3 B_H (-\sin \varphi_3 \Delta \theta_3 \cos \psi + \cos \varphi_3 \Delta \theta_3 \sin \psi). \end{aligned}$$

Let us use the following simplifications

$$\begin{aligned} a &= G_3 B_H (\cos \varphi_3 \Delta \theta_3 \cos \psi + \sin \varphi_3 \Delta \theta_3 \sin \psi), \\ b &= G_3 B_H (-\sin \varphi_3 \Delta \theta_3 \cos \psi + \cos \varphi_3 \Delta \theta_3 \sin \psi). \end{aligned}$$

Equation (3.9c) now can be written as $B_{Z'} = G_3 (B_z + O'_3) + \cos \omega t a + \sin \omega t b$.

If $B_{Z'}$ is transformed into a spinning frame and averaged the following equations can be obtained

$$\overline{B_{Z'} \cos \omega t} = \overline{\cos^2 \omega t a + \cos \omega t \sin \omega t b}, \quad (3.23a)$$

$$\overline{B_{Z'} \sin \omega t} = \overline{\sin \omega t \cos \omega t a + \sin^2 \omega t b}. \quad (3.23b)$$

Because $\cos^2 \omega t = \frac{1}{2}(1 + \cos 2\omega t)$, $\sin^2 \omega t = \frac{1}{2}(1 - \cos 2\omega t)$ and $\cos \omega t \sin \omega t = \frac{1}{2}\sin 2\omega t$ equations (3.23a) and (3.23b) simplify to

$$\overline{B_{Z'} \cos \omega t} = \frac{1}{2} \bar{a} = \frac{1}{2} G_3 \overline{B_H} (\cos \varphi_3 \Delta \theta_3 \cos \psi + \sin \varphi_3 \Delta \theta_3 \sin \psi) \quad (3.24a)$$

$$\overline{B_{Z'} \sin \omega t} = \frac{1}{2} \bar{b} = \frac{1}{2} G_3 \overline{B_H} (-\sin \varphi_3 \Delta \theta_3 \cos \psi + \cos \varphi_3 \Delta \theta_3 \sin \psi) \quad (3.24b)$$

This two by two system of equations can be easily solved by again using $B_x = B_H \cos \psi$ and $B_y = B_H \sin \psi$. After some algebra

$$\varphi_3 = \arctan \frac{\overline{B_{Z'} \cos \omega t B_{Y'}} - \overline{B_{Z'} \sin \omega t B_{X'}}}{\overline{B_{Z'} \cos \omega t B_{X'}} + \overline{B_{Z'} \sin \omega t B_{Y'}}},$$

$$\Delta \theta_3 = \frac{2 \overline{B_{Z'} \cos \omega t}}{G_3 (\overline{\cos \varphi_3 B_{X'}} + \overline{\sin \varphi_3 B_{Y'}})}$$

where G_3 can be set to 1 due to previous calibration.

In case a previous calibration did not provide accurate values for G_1 and G_3 , the spin tone can still be removed because the required corrections to G_1 and G_3 are then included in the 6 parameters that are obtained in this section.

3.4.3. Application of the Technique to Cluster Data

As an example I chose Cluster magnetic field data (Balogh *et al.*, 2001) that were measured after Cluster-3 came out of an eclipse (see Figure 3.10). The eclipse lasted for roughly 43 minutes and ended at 13:45:30 on March 06, 2002. Due to rapidly changing temperature after eclipsed periods, the required zero levels, gains as well as angles change slightly. The small changes are enough to cause faint spin harmonics that vary in strength. Thus, a single calibration matrix plus a single set of three zero levels does not completely remove the spin harmonics when temperatures are changing. Figures 3.11, 3.12 and 3.13 show dynamic amplitude spectra of data that were calibrated with a single set of calibration parameters. As can be seen, there are faint changing spin harmonics left. The time varying calibration parameters that are required to completely remove the spin harmonics are given in Figure 3.14. Some outliers were detected by quick visual inspection and replaced with linearly interpolated values. The required corrections are rather small. Except for $\Delta\theta_3$ in the bottom panel, all calibration parameters show systematic changes. The top two panels of Figure 3.14 actually contain four time varying calibration parameters that do not need to be separated (see figure caption). The dynamic spectra after application of the time varying calibration parameters are given in Figures 3.15, 3.16 and 3.17.

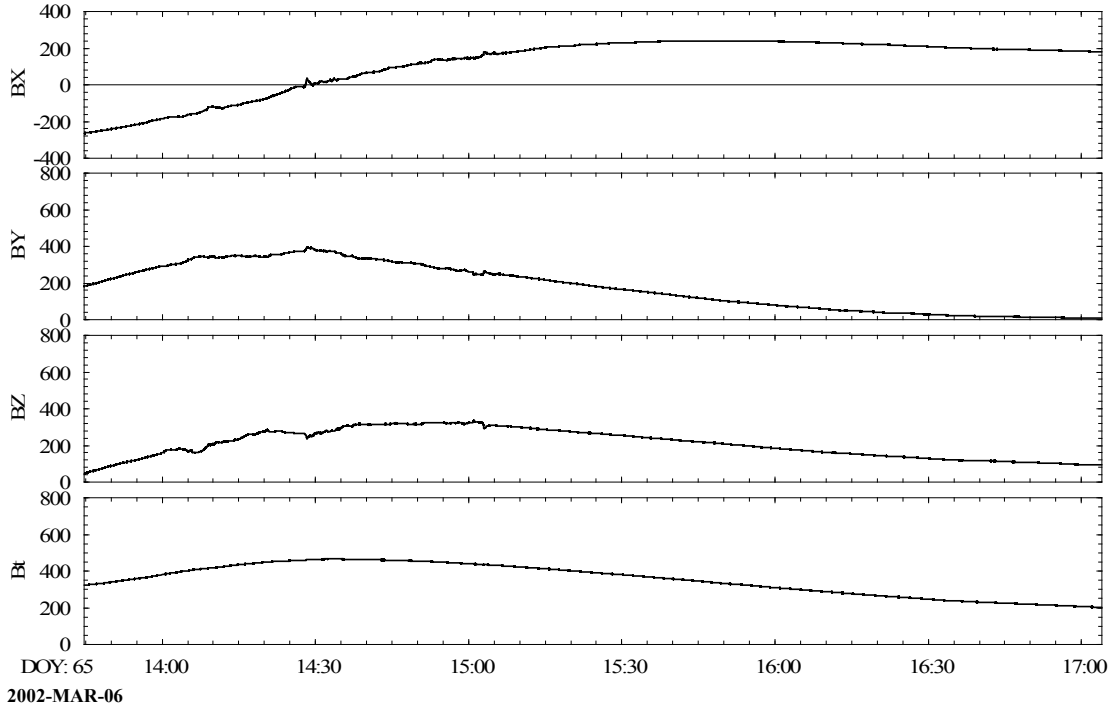


Figure 3.10. Cluster-3 magnetic field data in range 4 (range 4: ± 1024 nT).

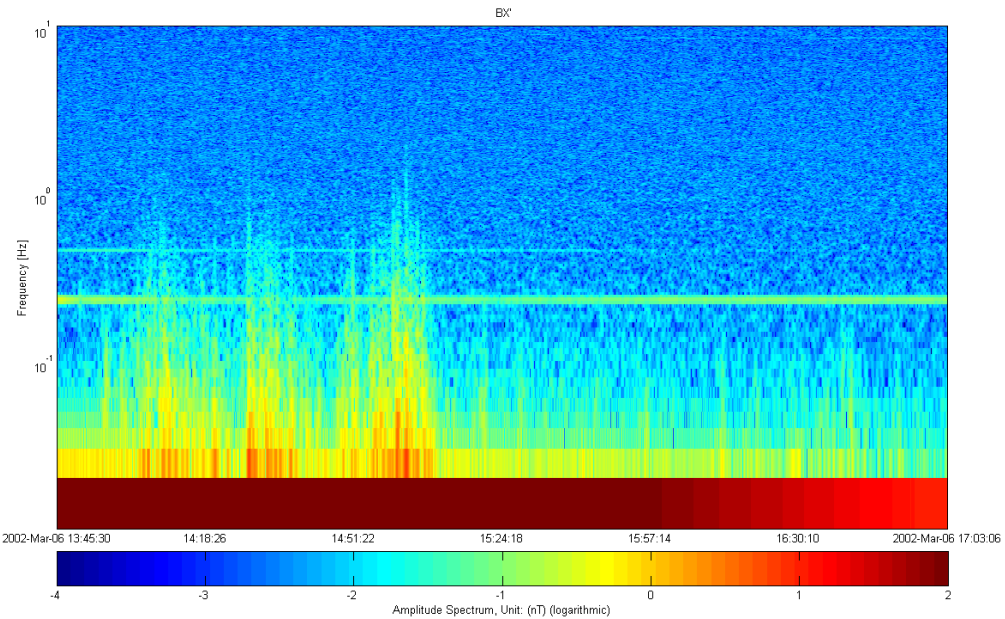


Figure 3.11. Dynamic amplitude spectrum of Cluster-3 data after application of a single set of calibration parameters, in despun spacecraft coordinates (spin plane component).

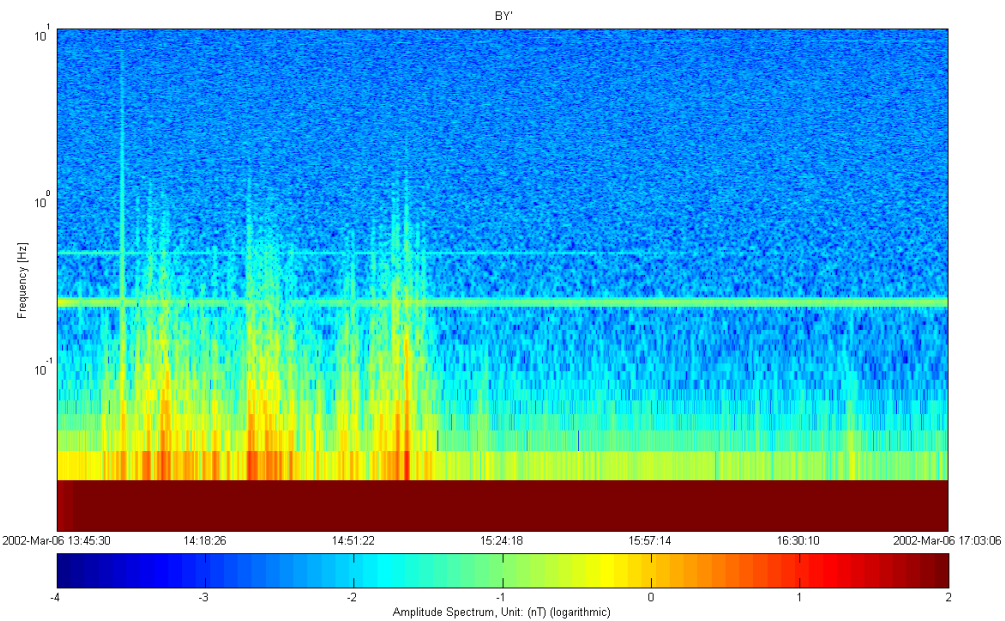


Figure 3.12. Dynamic amplitude spectrum of Cluster-3 data after application of a single set of calibration parameters, in despun spacecraft coordinates (spin plane component).

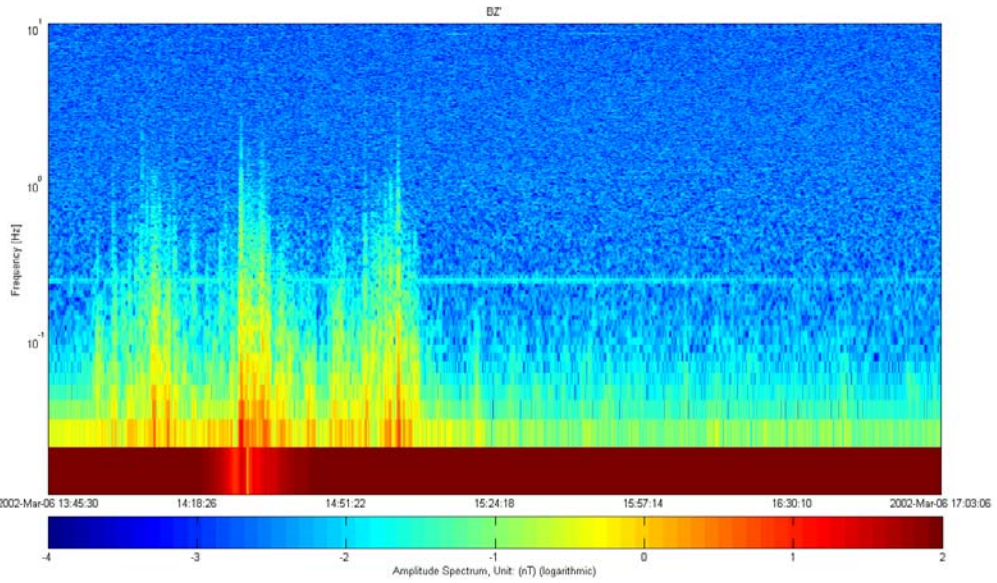


Figure 3.13. Dynamic amplitude spectrum of Cluster-3 data after application of a single set of calibration parameters, in despun spacecraft coordinates (spin axis component).

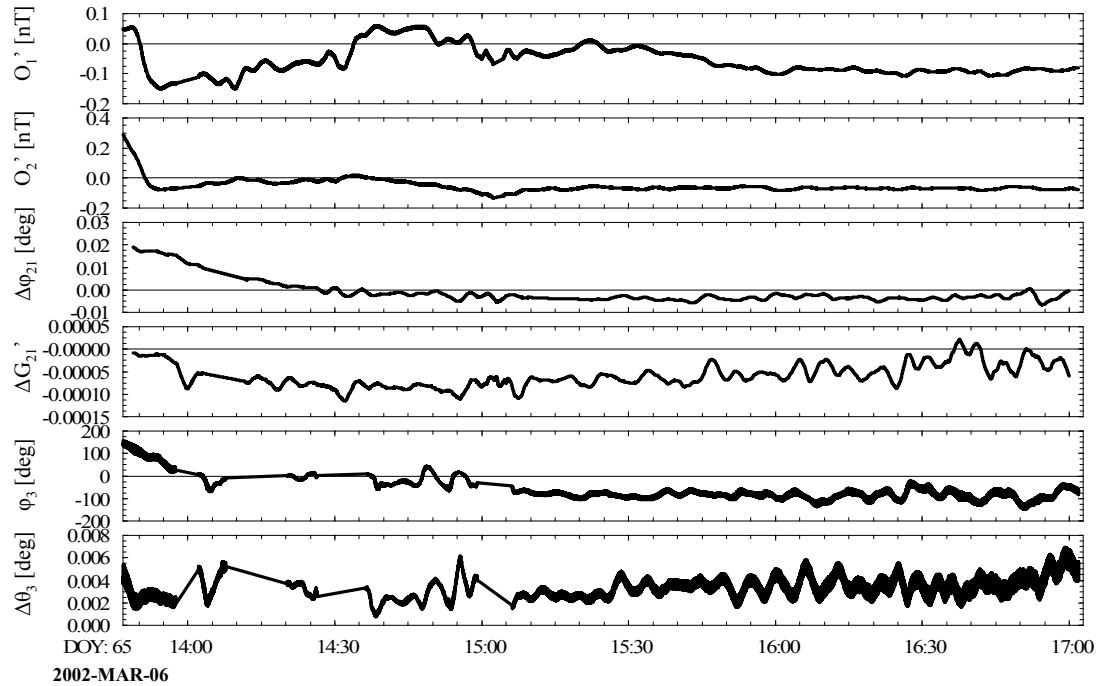


Figure 3.14. Time varying calibration parameters that are required to completely remove faint spin harmonics. The vertical labels of the top two panels (O_1' and O_2') are a simplification. The fully correct labels should be $B_z\Delta\theta_1 + O_1'$ and $B_z\Delta\theta_2 + O_2'$ which leads to altogether eight time varying parameters.

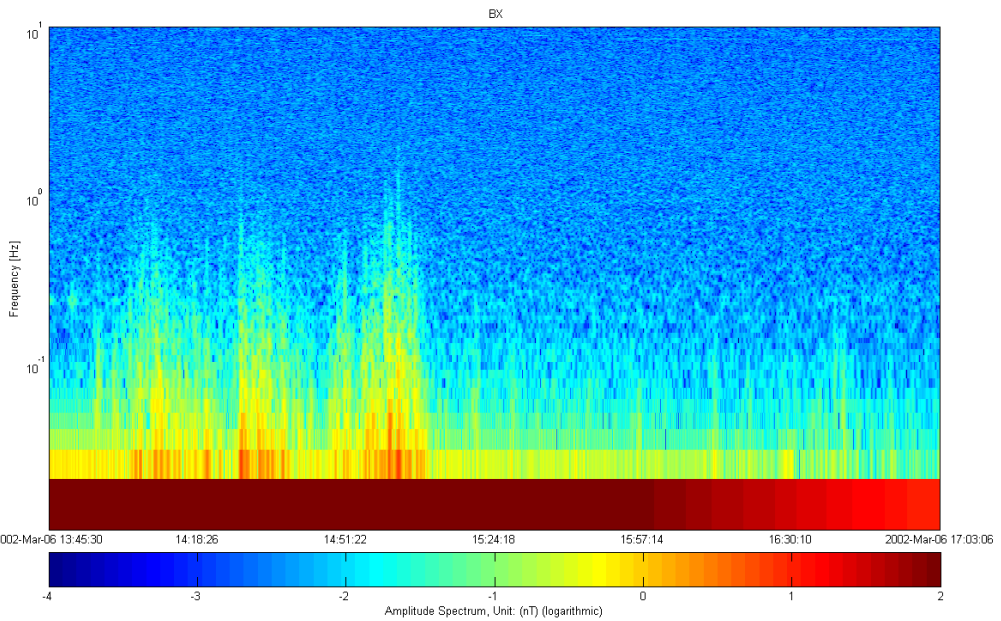


Figure 3.15. Dynamic amplitude spectrum of Cluster-3 data after application of a single set of calibration parameters, plus time varying calibration parameters, in despun spacecraft coordinates (spin plane component).

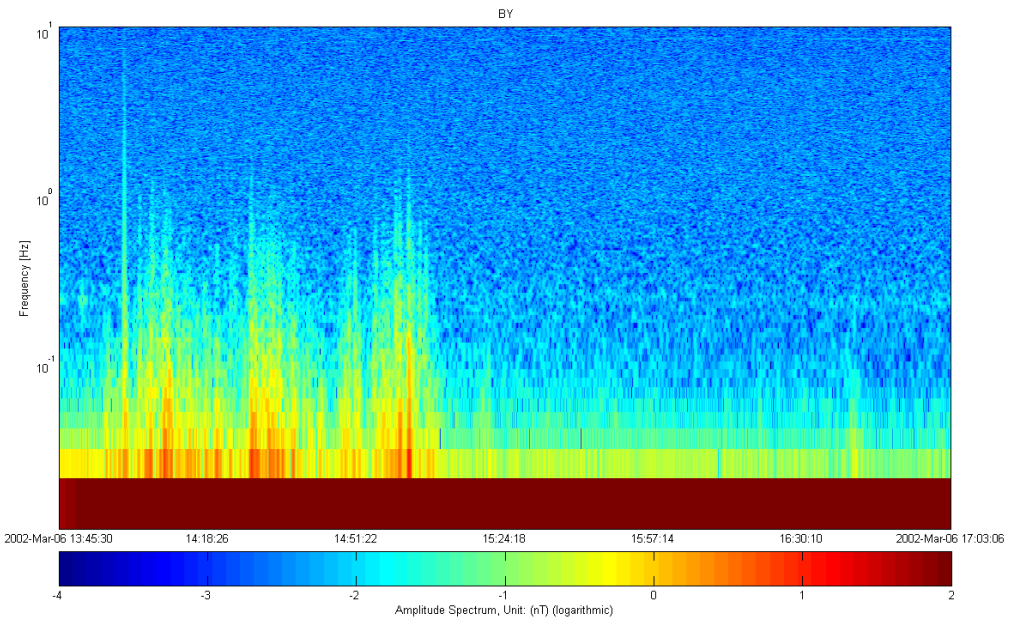


Figure 3.16. Dynamic amplitude spectrum of Cluster-3 data after application of a single set of calibration parameters, plus time varying calibration parameters, in despun spacecraft coordinates (spin plane component).

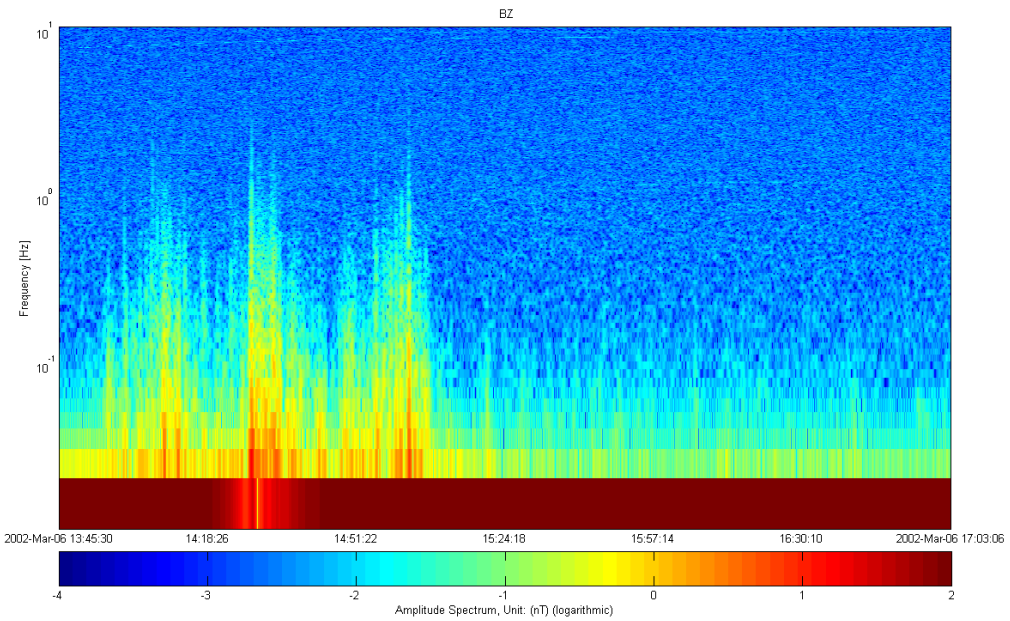


Figure 3.17. Dynamic amplitude spectrum of Cluster-3 data after application of a single set of calibration parameters, plus time varying calibration parameters, in despun spacecraft coordinates (spin axis component).

3.5. Conclusions

The method for orthogonalization of a sensor triad on a spinning spacecraft as first published by Kepko *et al.* (1996) has been improved and extended.

Small angle approximation for the spin axis elevation angle has been replaced by its full expression (see Equation 3.17). This allows convergence also for larger errors in the spin axis elevation angle.

Fourier transforms have been replaced by envelopes of spin harmonics in the despun frame. This allows orthogonalization during periods with fast changing magnetic fields such as the Galileo Earth flybys. The envelope-method may also be a method of choice for the upcoming Magnetospheric Multiscale (MMS) mission (currently scheduled to be launched on 2014-08-14). Similar to the Galileo spacecraft, the four MMS satellites will have slow spin periods of 20 sec.

Additionally, a method for resolving fast changing calibration parameters has been developed and successfully applied for time periods with large temperature changes.

4. Comparison with Model Fields

There are internal as well as external field models for the Earth's magnetic field. One commonly used internal field model is the International Geomagnetic Reference Model (IGRF) (see e.g. Maus *et al.*, 2005). Often used external field models are various so-called Tsyganenko models (e.g. Tsyganenko, 2002a; b). See also Sections 1.4. and 1.5. For a general introduction to calibration parameters see Section 1.8.2.

Model fields are usually not accurate enough to solve for magnetometer zero levels, which would require the model fields to be accurate to fractions of a nano Teslas. Only crude estimates of zero levels can be calculated via Earth field comparisons. If the spacecraft travels inside the interplanetary field or encounters mirror-mode waves, the methods described in Chapter 2 can be applied. If a magnetometer has multiple ranges, zero levels that were determined using the methods described in Chapter 2 can be propagated to magnetometer ranges for higher fields by using a method described in Appendix A.

4.1. Transformation of Model Fields into Spacecraft Coordinates

It is easiest to do the Earth field comparisons in spacecraft coordinates. Thus, the model field needs to be transformed into spacecraft coordinates. Spacecraft coordinates are usually defined that the Z axis points roughly towards north, the Sun lies inside the XZ-plane and the Y-axis completes the right handed system. The transformation is different for spinning and three axis stabilized spacecraft because of different attitude information. Spacecraft attitude is usually provided in inertial coordinates such as, for example the Geocentric Equatorial Inertial of epoch 2000 (GEI₂₀₀₀) coordinates. This coordinate system has the Z-axis pointing along the Earth's rotation axis (positive towards north). The X-axis points towards the first point of Aries. The direction of the Earth's rotation axis is not constant. This is the reason why often an epoch is defined. For more information on coordinate systems see Hapgood, M. A. (1995). Standard geophysical coordinate transformations provide transformations from inertial to the Geocentric Solar Ecliptic (GSE) system. This system has X pointing from Earth to Sun. The Y-axis lies inside the ecliptic plane and points towards dusk. The Z-axis is perpendicular to the ecliptic plane and positive towards north.

4.1.1. Spinning Spacecraft (Transformation to Spacecraft Coordinates)

The attitude information for a spinning spacecraft is given as direction of the spin axis in inertial coordinates. As a first step the inertial coordinates are being transformed into GSE coordinates and \vec{z}^{GSE} of the direction of the spin axis can be obtained. The direction of the Sun in GSE coordinates is (1,0,0). Thus, the direction of \vec{y}^{GSE} is given by:

$$\vec{y}^{GSE} = \frac{\vec{z}^{GSE} \times \begin{pmatrix} 1 \\ 0 \\ 0 \end{pmatrix}}{\left| \vec{z}^{GSE} \times \begin{pmatrix} 1 \\ 0 \\ 0 \end{pmatrix} \right|}$$

The direction of \vec{x}^{GSE} is then:

$$\vec{x}^{GSE} = \vec{y}^{GSE} \times \vec{z}^{GSE}$$

The three vectors \vec{x}^{GSE} , \vec{y}^{GSE} and \vec{z}^{GSE} are the rows of a transformation matrix:

$$T = \begin{pmatrix} \vec{x}^{GSE} & \vec{y}^{GSE} & \vec{z}^{GSE} \end{pmatrix}^T$$

The magnetic field can be transformed to despun spacecraft coordinates (DSL) as follows:

$$\vec{B}^{DSL} = T \vec{B}^{GSE}$$

The transformation from DSL back to GSE can be done by using the transpose of T . The three vectors \vec{x}^{GSE} , \vec{y}^{GSE} and \vec{z}^{GSE} are then columns of the matrix T^T .

4.1.2. Three Axis Stabilized Spacecraft (Transformation to Spacecraft Coordinates)

For a three axis stabilized spacecraft an attitude matrix is given. The matrix contains the directions of all three axes in inertial coordinates. The model field can be transformed into inertial coordinates and then brought directly into spacecraft coordinates via the attitude matrix.

4.2. Spinning Spacecraft (Model Comparison)

Removal of spin harmonics (see Chapter 3) can not resolve four calibration parameters. These calibration parameters are absolute value of the azimuthal angles φ_{12} , absolute value of the spin plane gains G_{12} , absolute value of the spin axis gain G_3 and the spin axis offset O_3 . Please note that model fields are usually not accurate enough to solve for magnetometer zero levels.

For resolving calibration parameters the model, as well as the data need to be transformed into orthogonal despun spacecraft coordinates.

$$\begin{pmatrix} B_{m1} \\ B_{m2} \\ B_{m3} \end{pmatrix} = \begin{pmatrix} \cos \varphi_{12} & \sin \varphi_{12} & 0 \\ -\sin \varphi_{12} & \cos \varphi_{12} & 0 \\ 0 & 0 & 1 \end{pmatrix} \begin{pmatrix} G_{12} & 0 & 0 \\ 0 & G_{12} & 0 \\ 0 & 0 & G_3 \end{pmatrix} \begin{pmatrix} B_{sc1} \\ B_{sc2} \\ B_{sc3} + dO_3 \end{pmatrix} \quad (4.1)$$

B_{m1}, B_{m2}, B_{m3}	model field in orthogonal despun spacecraft coordinates
$B_{sc1}, B_{sc2}, B_{sc3}$	measured field in pseudo orthogonal despun spacecraft coordinates

Equation (4.1) can be split into two parts.

$$\begin{pmatrix} B_{sc1} & B_{sc2} \\ B_{sc2} & -B_{sc1} \end{pmatrix} \begin{pmatrix} G_{12} \cos \varphi_{12} \\ G_{12} \sin \varphi_{12} \end{pmatrix} = \begin{pmatrix} B_{m1} \\ B_{m2} \end{pmatrix} \quad (4.2)$$

and

$$(B_{sc3} + 1) \begin{pmatrix} G_3 \\ G_3 dO_3 \end{pmatrix} = B_{m3} \quad (4.3)$$

with

$$dO_3 = \frac{G_3 dO_3}{G_3}$$

The calibration parameters can be calculated as follows:

$$\varphi_{12} = \tan^{-1} \left(\frac{G_{12} \sin \varphi_{12}}{G_{12} \cos \varphi_{12}} \right)$$

$$G_{12} = \sqrt{(G_{12} \cos \varphi_{12})^2 + (G_{12} \sin \varphi_{12})^2}$$

If the spin axis offset O_3 is not required equation (4.3) becomes:

$$B_{sc3}G_3 = B_{m3}$$

4.2.1. Application to Galileo's Second Earth flyby

The Galileo magnetometer is described in Galileo Kivelson *et al.* (1992). After removal of the spin harmonics (orthogonalization), the magnetic field data were compared with the Earth's magnetic field model (Tsyganenko, 2002a; b). I solved for φ_{12} , G_{12} , and G_3 . The equations for the Least-Squares fits were slightly changed (4.2 and 4.3) so that they minimize the error in percent of the field magnitude, by dividing both sides with one hundredth of the field magnitudes. As can be seen from Figure 4.1, the residuals are generally better than 0.2 percent of the field magnitude. For more details see Z. J. Yu *et al.* (2010).

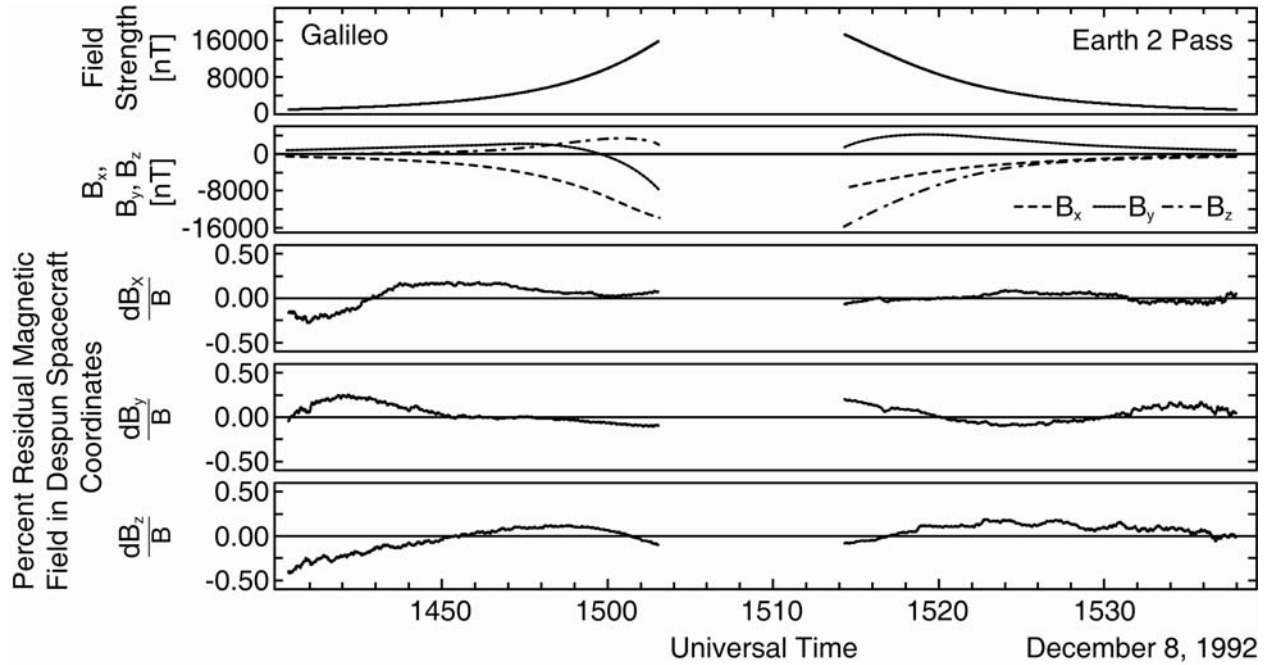


Figure 4.1. Galileo's second Earth flyby: Top two panels show the field magnitude and the field values of the three components. The bottom three panels show the residuals in percent of the field magnitude.

4.3. Three Axis Stabilized Spacecraft (Model Comparison)

It is possible to solve for all twelve calibration parameters via model comparison. Please note that model fields are usually not accurate enough to solve for magnetometer zero levels.

First, the model field needs to be transformed into spacecraft coordinates (see Section 4.1). The equations can be written as follows (without solving for offsets):

$$\vec{B}_{sc} = A \vec{B}_m \quad (4.1)$$

\vec{B}_m	model field in spacecraft coordinates
\vec{B}_{sc}	measured field in pseudo spacecraft coordinates
A	transformation matrix

The matrix A can be calculated from n measurements as follows:

$$\vec{B}_{sc_{[1,n]}} \vec{B}_{m_{[1,n]}}^T = A \vec{B}_{m_{[1,n]}} \vec{B}_{m_{[1,n]}}^T \quad (4.2)$$

$$A = \vec{B}_{sc_{[1,n]}} \vec{B}_{m_{[1,n]}}^T [\vec{B}_{m_{[1,n]}} \vec{B}_{m_{[1,n]}}^T]^{-1}$$

From the elements of A, various calibration parameters can be calculated (see equation 1.1). The gains are the norms of the row-vectors.

$$G_1 = \sqrt{a_{11}^2 + a_{12}^2 + a_{13}^2}$$

$$G_2 = \sqrt{a_{21}^2 + a_{22}^2 + a_{23}^2}$$

$$G_3 = \sqrt{a_{31}^2 + a_{32}^2 + a_{33}^2}$$

The azimuthal angles are

$$\varphi_1 = \tan^{-1} \left(\frac{a_{12}}{a_{11}} \right)$$

$$\varphi_2 = \tan^{-1} \left(\frac{a_{22}}{a_{21}} \right)$$

$$\varphi_3 = \tan^{-1} \left(\frac{a_{32}}{a_{31}} \right)$$

The elevation angles are

$$\theta_1 = \tan^{-1} \left(\frac{\frac{a_{11}}{\cos \varphi_1}}{a_{13}} \right)$$

$$\theta_2 = \tan^{-1} \left(\frac{\frac{a_{21}}{\cos \varphi_2}}{a_{23}} \right)$$

$$\theta_3 = \tan^{-1} \left(\frac{\frac{a_{31}}{\cos \varphi_3}}{a_{33}} \right)$$

Equation (4.1) is written so that A corrects the model field. Usually, the measured data need to be corrected. This can be done with the inverse of A as calibration matrix.

If zero levels must be calculated as well, the equations can be written as follows:

$$\begin{pmatrix} B_{sc1} + dO_1 \\ B_{sc2} + dO_2 \\ B_{sc3} + dO_3 \end{pmatrix} = \begin{pmatrix} a_{11} & a_{12} & a_{13} \\ a_{21} & a_{22} & a_{23} \\ a_{31} & a_{32} & a_{33} \end{pmatrix} \begin{pmatrix} B_{sc1_{TSY}} \\ B_{sc2_{TSY}} \\ B_{sc3_{TSY}} \end{pmatrix} \quad (4.3)$$

After some algebra:

$$\begin{pmatrix} B_{sc1} \\ B_{sc2} \\ B_{sc3} \end{pmatrix} = \begin{pmatrix} B_{sc1_{TSY}} & B_{sc2_{TSY}} & B_{sc3_{TSY}} & 0 & 0 & 0 & 0 & 0 & -1 & 0 & 0 \\ 0 & 0 & 0 & B_{sc1_{TSY}} & B_{sc2_{TSY}} & B_{sc3_{TSY}} & 0 & 0 & 0 & -1 & 0 \\ 0 & 0 & 0 & 0 & 0 & 0 & B_{sc1_{TSY}} & B_{sc2_{TSY}} & B_{sc3_{TSY}} & 0 & -1 \end{pmatrix} \begin{pmatrix} a_{11} \\ a_{12} \\ a_{13} \\ a_{21} \\ a_{22} \\ a_{23} \\ a_{31} \\ a_{32} \\ a_{33} \\ dO_1 \\ dO_2 \\ dO_3 \end{pmatrix} \quad (4.4)$$

The calibration parameters can be calculated the same way as described above.

4.3.1. Application to STEREO Data

The closest magnetic field measurements to Earth were taken on Nov. 06, 2006, during a perigee pass that took place a relative short time period after launch on Oct. 25, 2006. This perigee pass was used to calculate alignments and gain factors, since the largest possible range of magnetic field values were measured during this pass. During the pass, the magnetometer was in high range ($\pm 65,536$ nT). For more information on the STEREO triaxial fluxgate magnetometers see Acuña *et al.* (2008). The zero levels were determined according to Leinweber *et al.* (2008), at a later stage of the mission when the spacecraft was inside the solar wind, in low range (± 512 nT).

The zero levels were propagated from the low range to the high range by removing the steps that occur when a magnetometer switches from one range to another. The propagated zero levels were used as input for the Earth field comparison. Thus, only alignments and gain factors needed to be determined. The obtained calibration matrix was applied to both ranges and the steps at the range changes were double checked.

Figure 4.2 shows the residuals of the Earth field comparison for STEREO-B. At relevant field strength, the residuals stay well within 0.3 percent. The residuals (in percent) increase towards smaller fields but their absolute values stay small. The RMS errors for all three components are: $RMS_1 = 4.5$ nT; $RMS_2 = 11.7$ nT; $RMS_3 = 9.0$ nT;

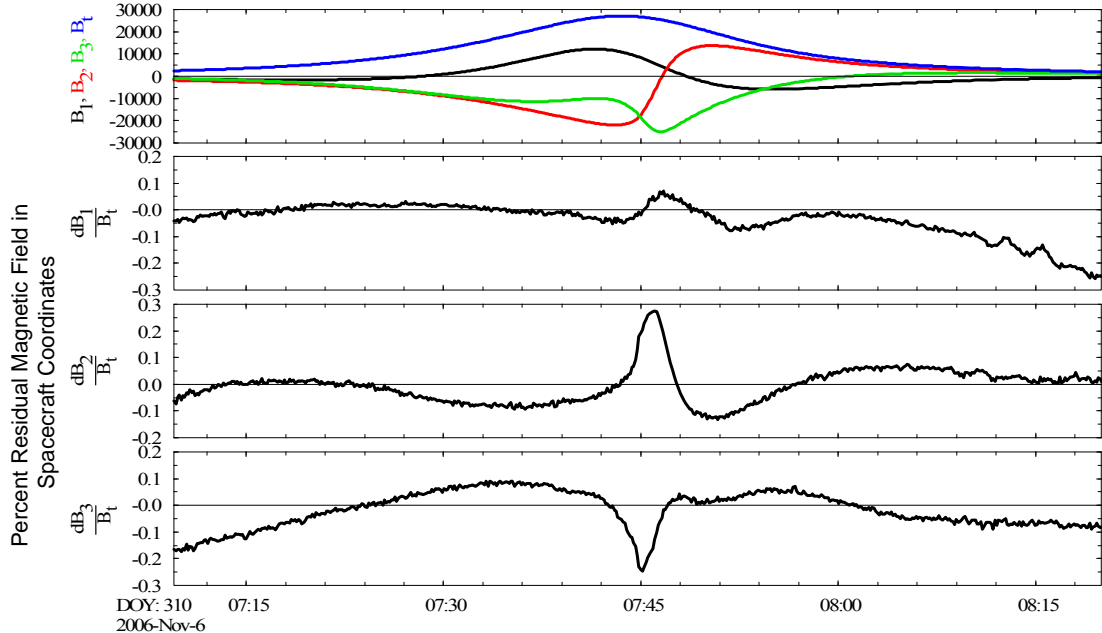


Figure 4.2. The top panel shows the perigee pass of STEREO-B with the closest magnetic field measurements to Earth. The bottom three panels show the residuals of the Earth field comparison in percent of the field magnitude.

4.4. Attitude Determination of a Spinning Spacecraft (First Method)

In some cases space probes are not equipped with accurate star sensors but with Sun sensors instead. Sun sensors are cheaper but not as accurate. At low enough perigee passes the spacecraft attitude can be refined using Earth field comparisons. Besides the refined attitude, magnetometer calibration parameters can be determined as well. It is useful to calculate calibration parameters that can not be found by spin tone removal (see Chapter 3). The calibration parameters are absolute value of the azimuthal angles φ_{12} , absolute value of the spin plane gains G_{12} , absolute value of the spin axis gain G_3 and the spin axis offset O_3 . Please note that model fields are usually not accurate enough to solve for magnetometer zero levels.

First a different way of transforming the model field from GSE coordinates into spacecraft coordinates must be found. The method described in Section 4.1.1 is not useful for refining attitude information. A mathematical formulation that is based on rotations instead of cross products can be used (see Figure 4.3).

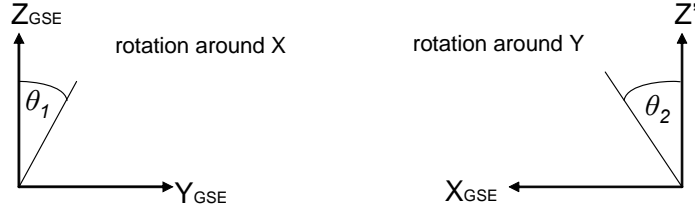


Figure 4.3. Required rotations for transformation into spacecraft coordinates.

The first rotation is around the X_{GSE} -axis. The angle θ_1 can be calculated from the projection of the attitude vector onto the YZ_{GSE} -plane. The second rotation is around the new Y -axis. The angle θ_2 can be calculated from the projection onto the XZ_{GSE} -plane.

The full equation can be written as follows

$$\begin{pmatrix} B_{sc1_{TSY}} \\ B_{sc2_{TSY}} \\ B_{sc3_{TSY}} \end{pmatrix} = \begin{pmatrix} 1 & 0 & 0 \\ 0 & \cos d\theta_1 & \sin d\theta_1 \\ 0 & -\sin d\theta_1 & \cos d\theta_1 \end{pmatrix} \begin{pmatrix} \cos d\theta_2 & 0 & \sin d\theta_2 \\ 0 & 1 & 0 \\ -\sin d\theta_2 & 0 & \cos d\theta_2 \end{pmatrix} \begin{pmatrix} \cos d\varphi_{12} & \sin d\varphi_{12} & 0 \\ -\sin d\varphi_{12} & \cos d\varphi_{12} & 0 \\ 0 & 0 & 1 \end{pmatrix} \begin{pmatrix} G_{12} & 0 & 0 \\ 0 & G_{12} & 0 \\ 0 & 0 & G_3 \end{pmatrix} \begin{pmatrix} B_{sc1} \\ B_{sc2} \\ B_{sc3} + dO_3 \end{pmatrix} \quad (4.5)$$

The three rotations in equation (4.5) represent a valid set of Euler angle rotations. Since model field ($B_{sc1_{TSY}}$, $B_{sc2_{TSY}}$, $B_{sc3_{TSY}}$) and the measured field (B_{sc1} , B_{sc2} , B_{sc3}) are both close to true spacecraft coordinates, small angle approximations ($\sin \alpha \approx \alpha$ and $\cos \alpha \approx 1$) can be used and the gains can be written as differences.

$$\begin{pmatrix} B_{sc1_{TSY}} \\ B_{sc2_{TSY}} \\ B_{sc3_{TSY}} \end{pmatrix} = \begin{pmatrix} 1 & 0 & 0 \\ 0 & 1 & d\theta_1 \\ 0 & -d\theta_1 & 1 \end{pmatrix} \begin{pmatrix} 1 & 0 & d\theta_2 \\ 0 & 1 & 0 \\ -d\theta_2 & 0 & 1 \end{pmatrix} \begin{pmatrix} 1 & d\varphi_{12} & 0 \\ -d\varphi_{12} & 1 & 0 \\ 0 & 0 & 1 \end{pmatrix} \begin{pmatrix} 1-dG_{12} & 0 & 0 \\ 0 & 1-dG_{12} & 0 \\ 0 & 0 & 1-dG_3 \end{pmatrix} \begin{pmatrix} B_{sc1} \\ B_{sc2} \\ B_{sc3} + dO_3 \end{pmatrix} \quad (4.6)$$

After some algebra and neglecting second order terms an equation that is suitable for least squares inversion can be obtained.

$$\begin{pmatrix} B_{sc1_{TSY}} - B_{sc1} \\ B_{sc2_{TSY}} - B_{sc2} \\ B_{sc3_{TSY}} - B_{sc3} \end{pmatrix} = \begin{pmatrix} -B_{sc1} & 0 & B_{sc2} & 0 & B_{sc3} & 0 \\ -B_{sc2} & 0 & -B_{sc1} & B_{sc3} & 0 & 0 \\ 0 & -B_{sc3} & 0 & -B_{sc2} & -B_{sc1} & 1 \end{pmatrix} \begin{pmatrix} dG_{12} \\ dG_3 \\ d\varphi_{12} \\ d\theta_1 \\ d\theta_2 \\ dO_3 \end{pmatrix} \quad (4.7)$$

Since small angle approximations were used and second order terms were neglected, iterations are required. The preliminary parameters can be calculated using equation (4.7). Then the full equation (4.5) is used to calculate a new model field as well as a new spacecraft field. The parameters $d\theta_1$ and $d\theta_2$ are used to calculate the new model field. The other parameters $d\varphi_{12}$, dG_{12} , dG_3 and dO_3 are magnetometer calibration parameters and are used to calculate the new spacecraft field. Iterations are performed until convergence of the system.

4.4.1. Attitude Determination of a Spinning Spacecraft with Variable Phase Angle Correction (Second Method)

For a large number of perigee passes it was necessary to allow time varying corrections to the phase angle. This is especially important during eclipsed periods where the Sun sensor cannot operate. Additionally, slight uncertainties in timing or inaccuracies of the Sun sensor can be causes for the need of time varying corrections of the phase angle, during perigee passes. For example a timing uncertainty of 1/128 sec on a spacecraft that spins with 3 sec (e.g. THEMIS) causes an apparent 0.94 degree error in phase angle.

In case a variable phase angle correction is required, the direction of the measured spin plane component can be matched with the direction of the spin plane component of the model field. This can be done for every point (see equation 4.8).

$$\begin{pmatrix} B_{sc1_{TSY}} \\ B_{sc2_{TSY}} \end{pmatrix} = \begin{pmatrix} \cos d\varphi_{12} & \sin d\varphi_{12} \\ -\sin d\varphi_{12} & \cos d\varphi_{12} \end{pmatrix} \begin{pmatrix} B_{sc1} \\ B_{sc2} \end{pmatrix}$$

After some algebra:

$$\begin{pmatrix} B_{sc1_{TSY}} \\ B_{sc2_{TSY}} \end{pmatrix} = \begin{pmatrix} B_{sc1} & B_{sc2} \\ B_{sc2} & -B_{sc1} \end{pmatrix} \begin{pmatrix} \cos d\varphi_{12} \\ \sin d\varphi_{12} \end{pmatrix}$$

Since only the direction needs to be corrected, normalization with the field magnitudes is applied

$$\begin{pmatrix} \frac{B_{sc1_{TSY}}}{|B_{sc12_{TSY}}|} \\ \frac{B_{sc2_{TSY}}}{|B_{sc12_{TSY}}|} \end{pmatrix} = \begin{pmatrix} \frac{B_{sc1}}{|B_{sc12}|} & \frac{B_{sc2}}{|B_{sc12}|} \\ \frac{B_{sc2}}{|B_{sc12}|} & -\frac{B_{sc1}}{|B_{sc12}|} \end{pmatrix} \begin{pmatrix} \cos d\varphi_{12} \\ \sin d\varphi_{12} \end{pmatrix} \quad (4.8)$$

with

$$|B_{sc12_{TSY}}| = \sqrt{|B_{sc1_{TSY}}|^2 + |B_{sc2_{TSY}}|^2}$$

$$|B_{sc12}| = \sqrt{|B_{sc1}|^2 + |B_{sc2}|^2}$$

After solving the 2 by 2 system, the phase angle can be calculated as follows:

$$d\varphi_{12} = \tan^{-1} \left(\frac{\sin d\varphi_{12}}{\cos d\varphi_{12}} \right)$$

As one can see, there is no small angle approximation required. Thus, this method can be used for very large errors of the phase angle (e.g. during eclipsed periods when a Sun sensor cannot operate).

Additionally, it can be used to double check shadow correction models (models of the moments of inertia of a spacecraft for varying temperature) during perigee passes. When a spacecraft cools down during eclipse, mechanical contractions occur so that the spin period decreases slightly. Such models are used to correct phase information during eclipsed periods. This has been done for the THEMIS mission (Angelopoulos, 2008) and goes beyond the scope of this thesis. For more details see Georgescu *et al.* (2011).

After the spin phase components are aligned, a simpler system of equations that does not contain phase corrections, can be solved.

$$\begin{pmatrix} B_{sc1_{TSY}} \\ B_{sc2_{TSY}} \\ B_{sc3_{TSY}} \end{pmatrix} = \begin{pmatrix} 1 & 0 & 0 \\ 0 & 1 & d\theta_1 \\ 0 & -d\theta_1 & 1 \end{pmatrix} \begin{pmatrix} 1 & 0 & d\theta_2 \\ 0 & 1 & 0 \\ -d\theta_2 & 0 & 1 \end{pmatrix} \begin{pmatrix} 1-dG_{12} & 0 & 0 \\ 0 & 1-dG_{12} & 0 \\ 0 & 0 & 1-dG_3 \end{pmatrix} \begin{pmatrix} B_{sc1}' \\ B_{sc2}' \\ B_{sc3} + dO_3 \end{pmatrix} \quad (4.9)$$

With B_{sc1}' and B_{sc2}' containing the time varying phase corrections.

Since the system of equations contains small angle approximations and second order terms were neglected, iterations are necessary. The iterations are similar to the ones in Sec. 4.4, except that the phase correction is left out of the full equation (4.5). The parameters $d\theta_1$ and $d\theta_2$ are used to calculate the new model field. The other parameters dG_{12} , dG_3 and dO_3 are magnetometer calibration parameters and are used to calculate the new spacecraft field. The iterations also contain recalculation of the time varying phase corrections every time before equation (4.9) is being solved. Iterations are performed until convergence of the system.

4.4.2. Application to Polar Data with Constant Phase Corrections

The Polar spacecraft has a Sun sensor instead of a more expensive star sensor. The polar magnetic field investigation is described in Russell *et al.* (1995). Sun sensors are not as accurate as star sensors. I applied the above techniques to data from February 2004 to December 2004. During this time period, perigee was roughly at 1.5 Re distance from Earth's center. The field strength at perigee was about 12000 nT. This field strength is generally large enough for model comparisons during a "quieter" magnetosphere. The spin period of Polar is ~6 sec which is fast enough so that small uncertainties in timing can cause large angular errors in the spin plane (e.g. a timing error of 1/64 sec causes a 0.94 degree error).

The above described methods (see Sec. 4.4 and 4.4.1) have been applied to all perigee passes between February, 2004 to December, 2004. Data inside 2 Re distance from the center of Earth were used. The spacecraft stayed inside 2 Re for about 50 minutes. Even though the second method does not provide a constant phase correction, the mean of the time varying phase was calculated. The RMS error of the spin plane components was used as indicator if the mean value can be used for calibration. A threshold of

$$\max\left(\sqrt{B_1^2 + B_2^2}\right) * 0.003 > \sqrt{RMS_1^2 + RMS_2^2}$$

was chosen.

The second method often converges better than the first one. If both methods provided a valid constant phase correction, the one with the smaller RMS error was chosen. When both methods failed to provide valid constant phase corrections, the other parameters (dG_{12} , dG_3 , dO_3 , $d\theta_1$ and $d\theta_2$) of the second method were often valid.

All parameters that were calculated from least square fits needed to pass a Monte Carlo simulation. A blocked Bootstrap-method (Efron, 1982) was used. The block size was calculated dynamically for every perigee pass.

$$nblock = 3 * \sqrt[3]{nperig}$$

<i>nblock</i>	number of points per block
<i>nperig</i>	number of points for each perigee pass

Spin averaged data were used (~ 6 sec period). Out of all n intervals with length of $nblock$, n intervals are randomly chosen. This yields a data set with reduced information that contains $1/e$ intervals more than once (for each perigee pass). For this new reduced data set the least squares solutions of the calibration parameters is calculated. This is done 1000 times. The thresholds are given in Table 4.1.

Parameter	threshold
$3 * \text{std}(dG_{12})$	< 0.002
$3 * \text{std}(dG_3)$	< 0.002
$3 * \text{std}(d\varphi_{12})$	< 0.25 deg (first method only)
$3 * \text{std}(dRAS)$	< 0.35 deg
$3 * \text{std}(dDEC)$	< 0.25 deg
$3 * \text{std}(dO_3)/(B_3 \text{ range})$	< 0.0008

Table 4.1. Thresholds for interpreting the Monte Carlo simulation.

The angles $dRAS$ and $dDEC$ are the corrections to right ascension and declination in geophysical coordinates. The quantity $B_3 \text{ range}$ is the range of B_3 across a perigee pass. The threshold for $dRAS$ was chosen to be larger than the one for $dDEC$ because the spin axis during the chosen one year period was closer to be perpendicular to the ecliptic plane than parallel to the ecliptic plane.

Figure 4.4 shows the results for the chosen one year period. The obvious long gap from mid of February to beginning of April, 2004 is due to self similarities of the magnetic field components (see Figure 4.5). The least squares fit has many possible sets of calibration parameters that make the RMS error small. The Monte Carlo simulation identifies such perigee passes.

Another obvious feature is that the phase correction has long intervals with the same value. The same values come from nearest neighbor interpolation. Those are the cases where both methods did not find a valid constant phase but the second method produced five other calibration parameters that passed the thresholds of the Monte Carlo simulation, thus variable phase corrections would be required for those intervals. At the time of writing, large time intervals of Polar magnetic field data are being recalibrated.

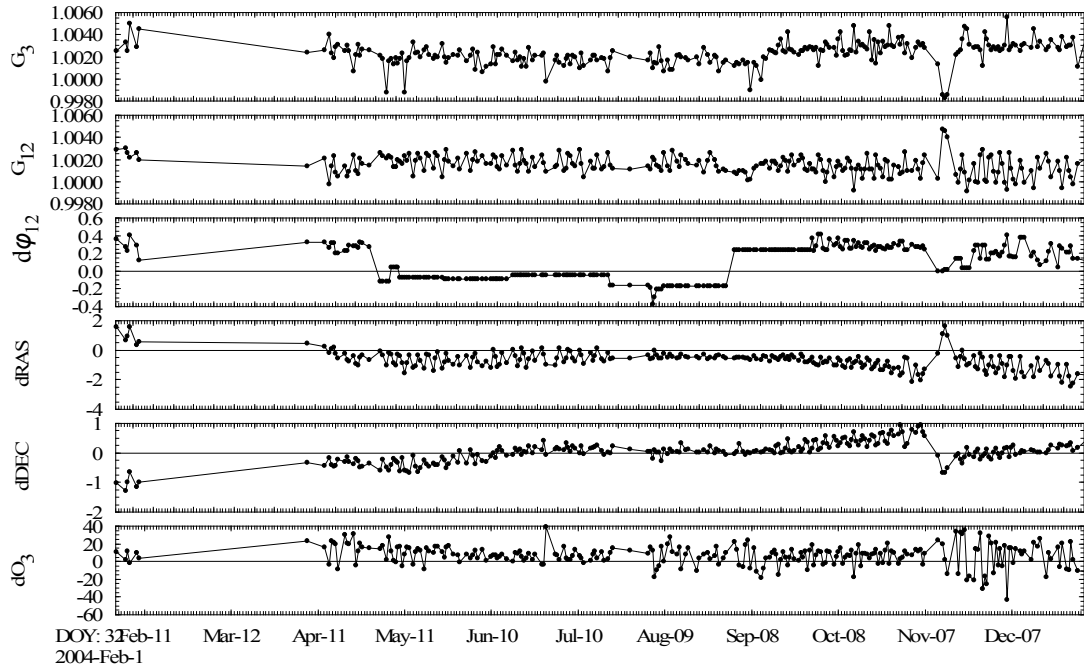


Figure 4.4. Combined results from the first and second methods. The quantities $d\varphi_{12}$, $dRAS$ and $dDEC$ are in degree and dO_3 is in nano Tesla.

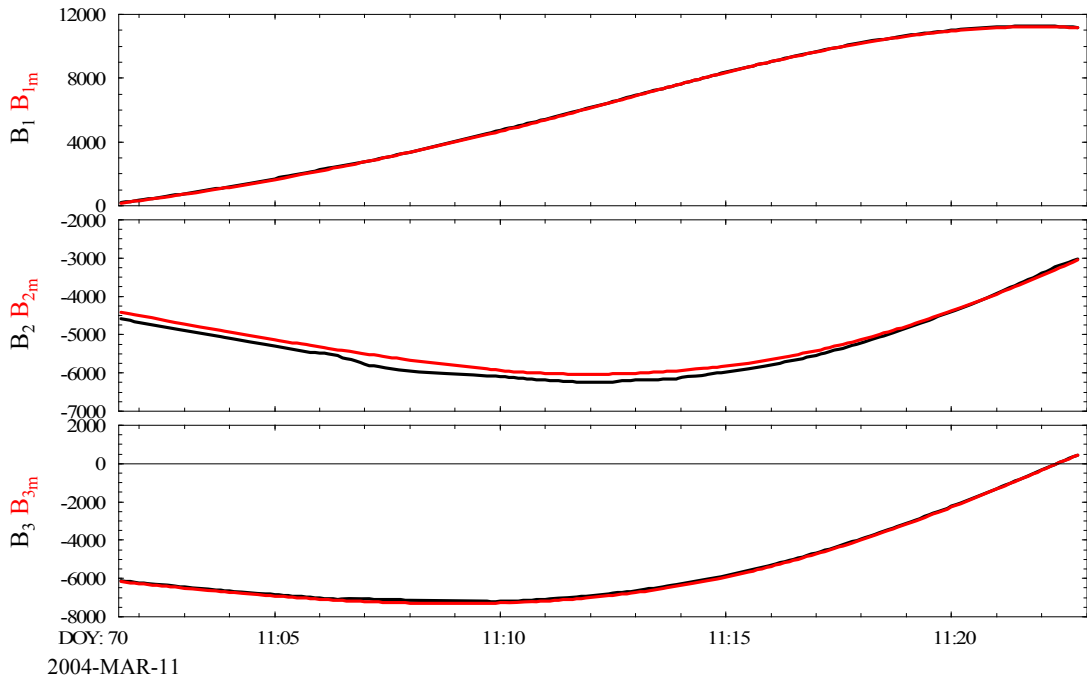


Figure 4.5. A perigee pass with only ~ 25 min of data. The second and third component are similar in shape (panels 2 and 3). Data are black and the model is red.

4.4.3. Application to THEMIS Data with Variable Phase Corrections

Correction of THEMIS data (Auster *et al.*, 2008) during eclipses is being done by models of the moments of inertia of a spacecraft for varying temperature. For more information see Georgescu *et al.* (2011). For THEMIS, time varying phase corrections have only been used for double checking of the models of moments of inertia.

Figure 4.6 shows that the data and the model of the spin plane components have large deviations during an eclipsed perigee pass. The bottom panel shows the required time varying phase angle correction. Figure 4.7 shows the calibrated data after application of the second method.

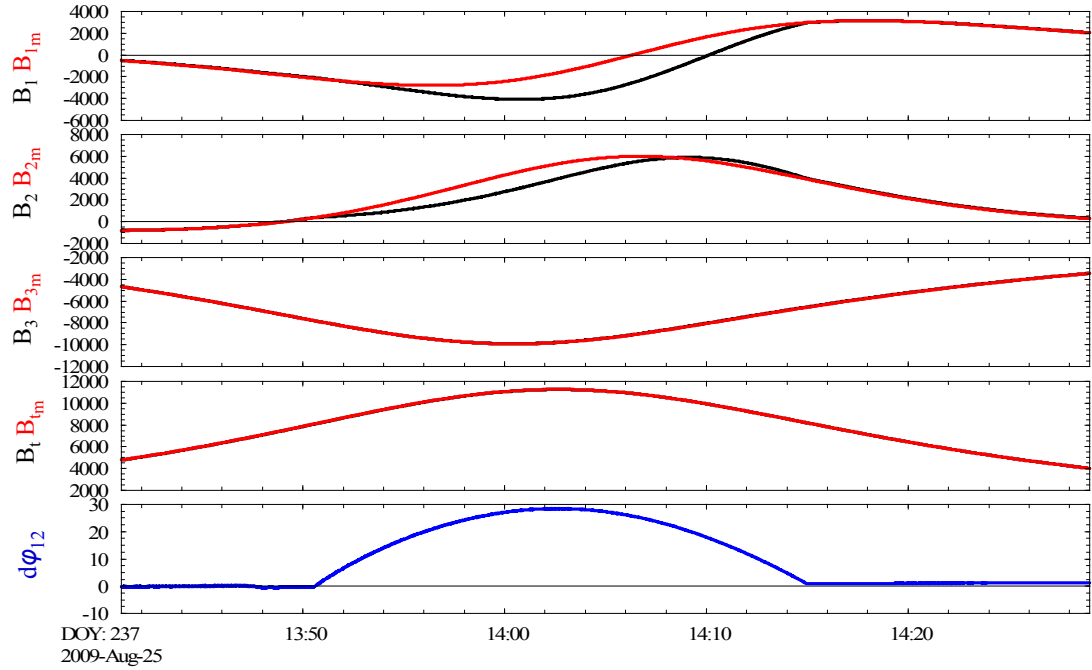


Figure 4.6. Data (black) and the model (red) before calibration with the second method. The required time varying correction to the phase angle ($d\varphi_{12}$) is given in degree.

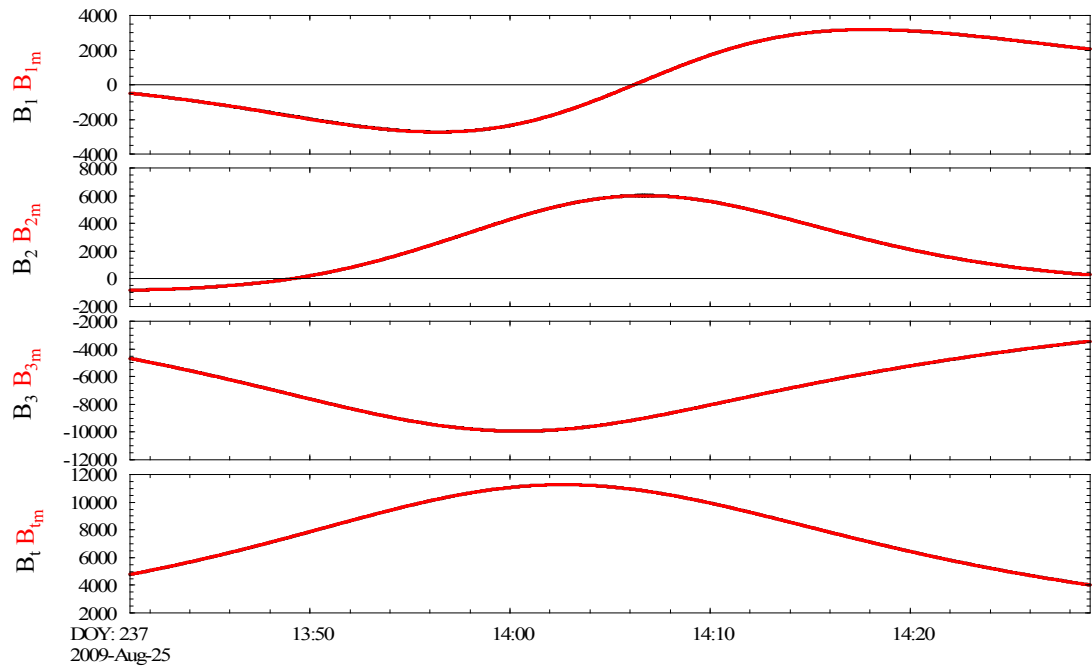


Figure 4.7. Data (black) and the model (red) after calibration with the second method. The black traces are below the red traces.

4.5. Conclusions

The required equations for resolving calibration parameters from Earth field comparisons for spinning as well as three axes stabilized spacecraft were described. Furthermore, equations for solving for calibration parameters as well as attitude for spinning spacecraft, including error estimates were derived. Additionally, a method for large and time varying Sun-angle corrections was developed.

5. Calibration of Triaxial Fluxgate Magnetometers from Accurate Measurements of the Field Magnitude

Precise scalar magnetic field measurements provided by magnetometers as well as the Electron Drift Instrument can be used to calibrate triaxial magnetometers. Fluxgate magnetometers as well as vector helium magnetometers are known to have small drifts of the zero levels. In case of a three axis stabilized spacecraft, 9 calibration parameters can be resolved. The ones for absolute orientation cannot be resolved. The method was derived by Merayo *et al.* (2000) and applied e.g. to calibrate the triaxial magnetometer onboard the Ørsted satellite (Olsen *et al.*, 2003). For a spinning spacecraft it makes sense to solve for absolute spin plane gains (G_{12}), spin axis gain (G_3) and spin axis offset (O_3).

In this chapter the field magnitude measured by the Electron Drift Instrument (Paschmann *et al.*, 1988 and 1997) onboard the spinning Cluster-3 satellite was used to calibrate its triaxial fluxgate magnetometer (e.g. Balogh *et al.*, 2001).

5.1. Measuring Scalar Magnetic Fields with the Electron Drift Instrument (EDI)

The basic principle of an electron drift instrument is that, if a beam of electrons is sent away from a spacecraft, the electrons gyrate inside the ambient magnetic field, and deviations from a spiral-shaped trajectory as one expects in a uniform magnetic field indicate the presence of an electric field and possibly also a gradient of the magnetic field. The energy of the electrons varies between 0.5 to 1 keV in the Cluster EDI. For the right starting direction of the beam, the right combination of electric field and magnetic field, the beam can be detected again on the other side of the spacecraft. Additionally the angular velocity of the spacecraft has to be compensated. The electrons do not have circular orbits because they drift with a drift velocity. This velocity consists of two parts. The first part is caused by the electric field and the second part is caused by the gradient of the magnetic field according to equation (5.1).

$$v_d = v_E + v_{\nabla B} \quad (5.1)$$

$$v_E = \frac{E \times B}{B^2}$$

$$v_{\nabla B} = \frac{W}{e} \frac{B \times \nabla B}{B^3}$$

with

W	energy of the electrons
e	charge of an electron

The drift velocity causes a drift step

$$d = v_d T_g$$

with

T_g	time of flight
-------	----------------

If there are two electron guns and two detectors (see Figure 5.1), the drift step can be continuously monitored via triangulation (see Figure 5.2).

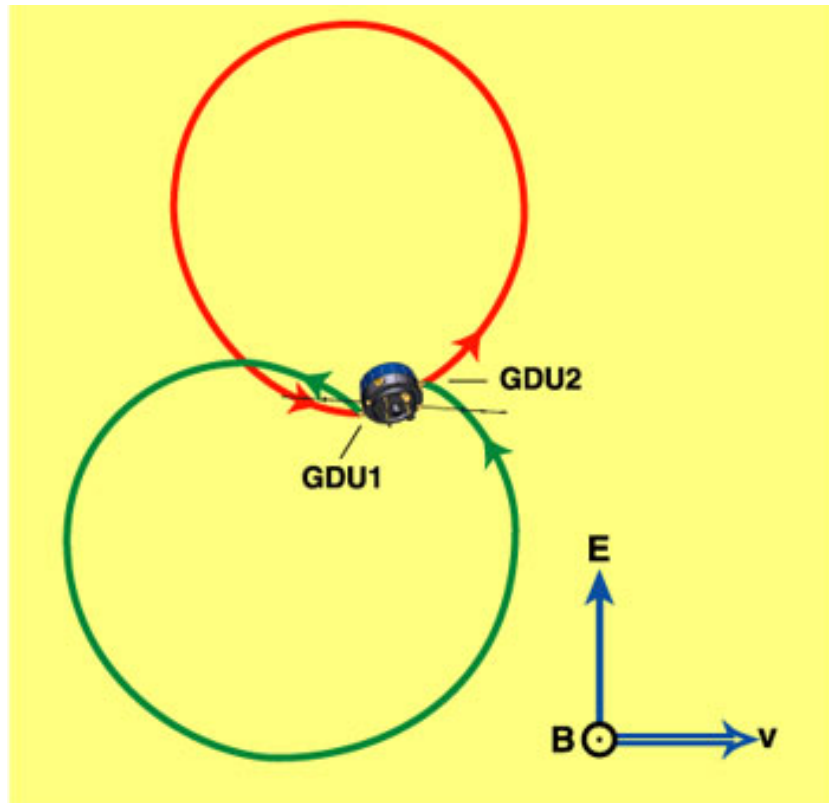


Figure 5.1. The basic operating principle of an electron drift instrument.

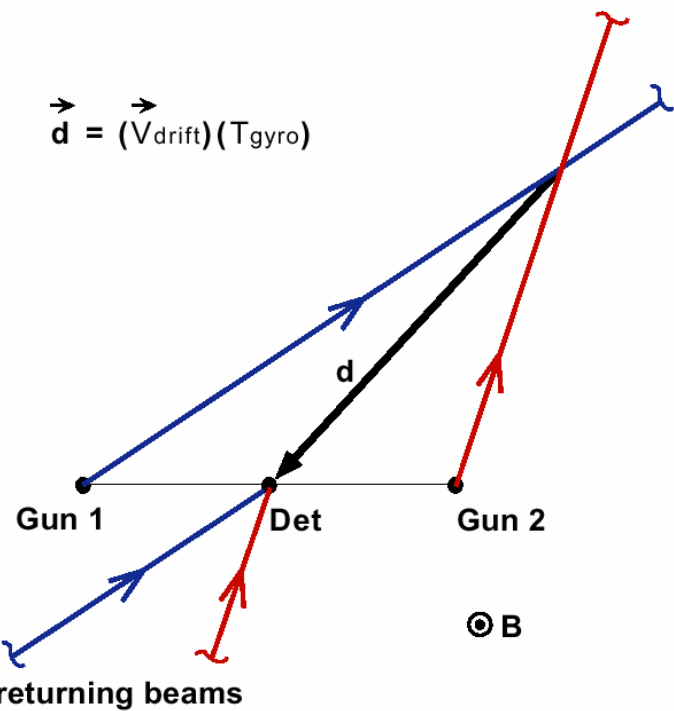


Figure 5.2. The triangulation process.

For small fields (and therefore large gyro radii) the triangulation becomes less accurate but the measured times of flight, which are important for calculating the field magnitude, increase in accuracy. Additionally the difference of the times of flight for the two beams increases in accuracy, thus the drift velocity can be calculated more precisely.

Electrons that are emitted parallel to v_d have shorter times of flight than electrons that are emitted anti-parallel to v_d .

$$T_{l,2} = T_g \left(1 \pm \frac{v_d}{v_e} \right)$$

The drift due to the electric field is independent of the energy of the electrons. Thus, by using different energies the part of the drift that is caused by the electric field and the part that is caused by the gradient of the magnetic field can be separated.

For $W_2 = 2W_1$ the equations can be written as:

$$\begin{aligned} v_E &= 2v_1 - v_2 \\ v_{VB}(W_1) &= v_2 - v_1 \end{aligned}$$

The difference of the times of flight yields the drift velocity

$$\Delta T = T_l - T_2 = 2T_g \frac{v_d}{v_e} = 2 \frac{d}{v_e}$$

with

$$T_g = \frac{T_l + T_2}{2}$$

the magnitude of the magnetic field can be calculated

$$T_g = \frac{2\pi m_e}{eB} \quad (5.2)$$

m_e mass of an electron

For more information on the Electron Drift Instrument see Paschmann *et al.* (1988 and 1997).

5.2. Calibration of a Triaxial Magnetometer with the Electron Drift Instrument (EDI) Onboard a Spinning Spacecraft

After EDI data has undergone appropriate data cleaning procedures, magnetometer spin axes offsets can be cross checked by comparison of the field magnitude as derived from EDI times of flight with the field magnitudes as measured by the magnetometer (see equation 5.2). The used EDI times of flight as well as magnetometer data were downloaded from the Cluster data archive. For information on the archiving and cleaning of EDI data see Georgescu *et al.* (2005) and for Cluster magnetometer (FGM) data see Gloag *et al.* (2005).

Figures 5.3, 5.4 and 5.5 show a comparison between EDI field magnitudes and FGM spin averaged field magnitudes for different field strengths. The figures show that there is a dramatic increase of noise towards higher fields in the EDI data.

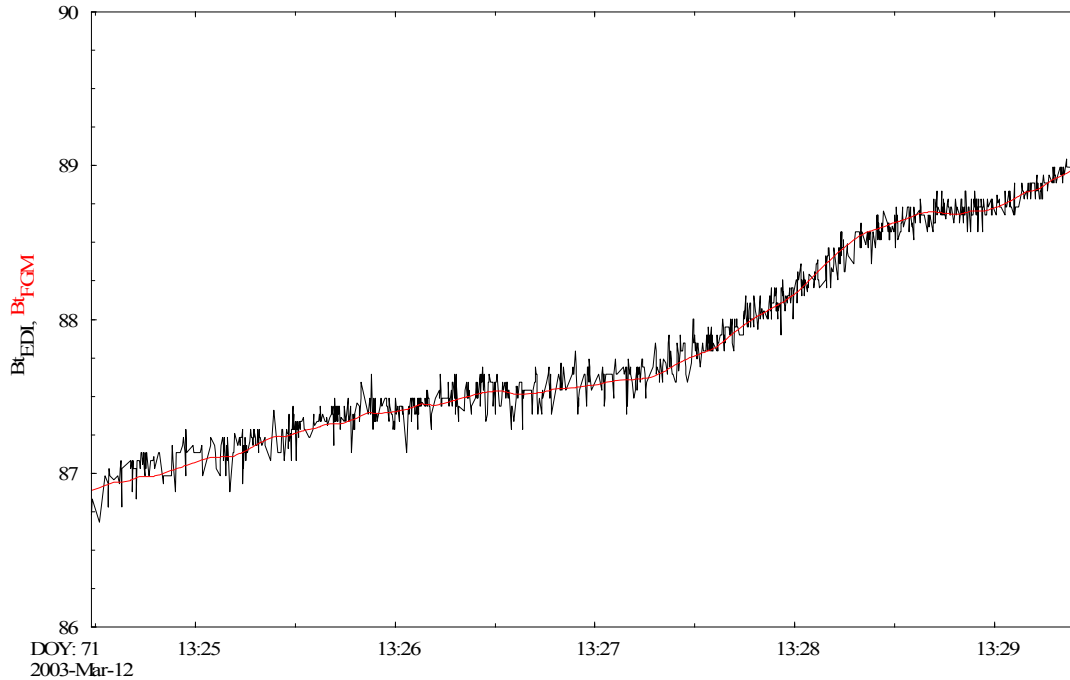


Figure 5.3. Comparison of EDI magnetic field magnitude and FGM magnetic field magnitude (red) at ~ 88 nT.

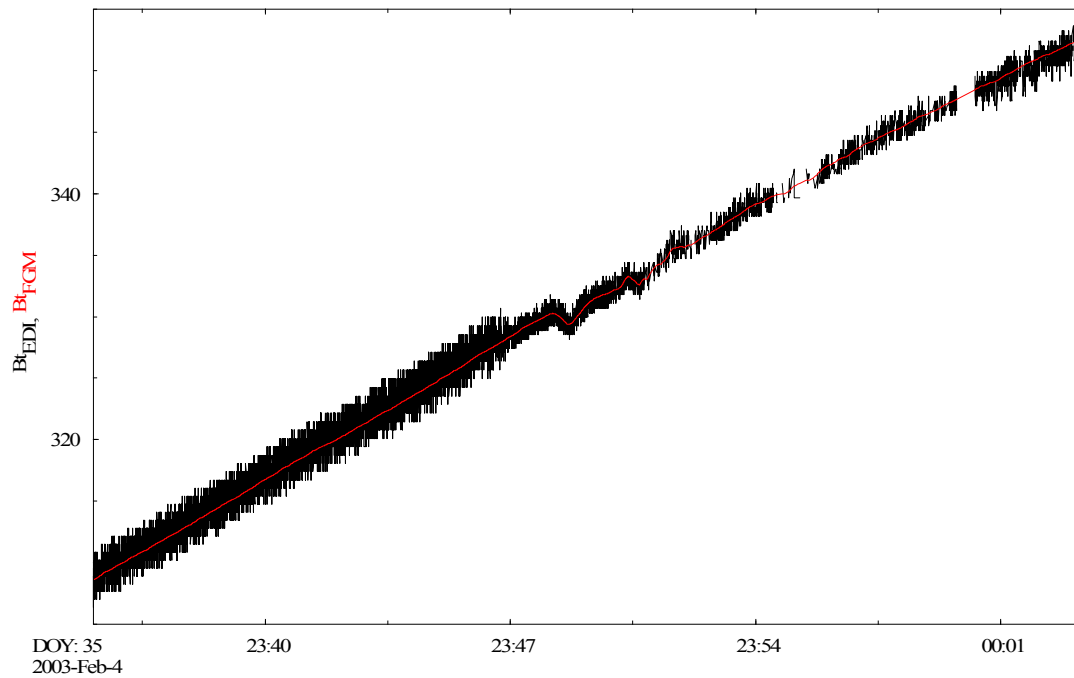


Figure 5.4. Comparison of EDI magnetic field magnitude and FGM magnetic field magnitude (red) at ~ 325 nT. EDI changes ranges at 325 nT.

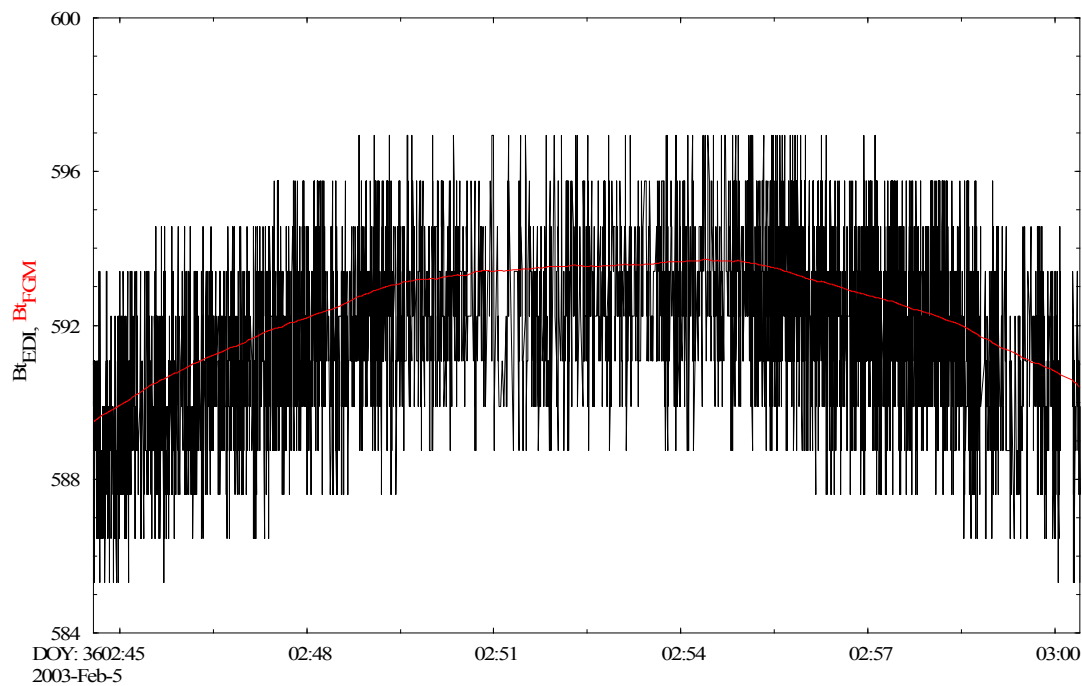


Figure 5.5. Comparison of EDI magnetic field magnitude and FGM magnetic field magnitude (red) at ~ 590 nT.

To better characterize the noise behavior for calibration work I used EDI and FGM data that were measured during relatively quiet times between Jan. 02, 2003 and Mar. 22, 2003. Within this interval EDI measured ~5.4 million valid data points. The spin averaged FGM data were interpolated to match the points in time of EDI. The measurements were binned to 40 nT bins. Figure 5.6 shows the number of measurements per bin. For each bin the RMS difference between the field magnitudes of EDI and FGM was calculated (see Figure 5.7). For the bins with the highest fields the RMS differences are above 3 nT. Additionally, the distributions (via histograms) of the RMS differences for each of the bins were analyzed. Figure 5.8 shows systematic deviations from zero towards positive differences that increase with the field. To find if the increase is linear, I did a linear fit to the averages of all the differences for each bin. Figure 5.9 shows that the increase of the differences is generally along a straight line. This suggests that there is a significant difference of the gains between EDI and FGM.

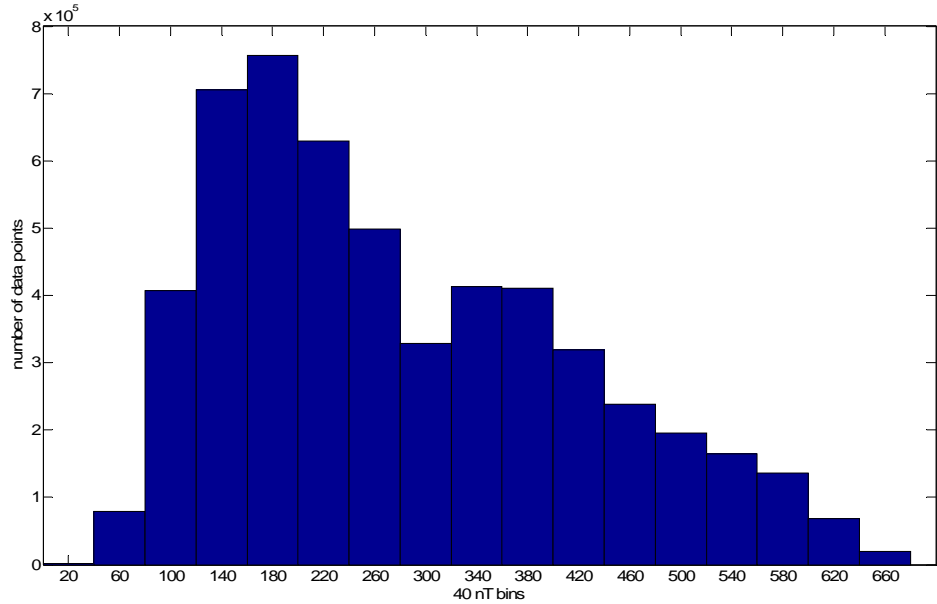


Figure 5.6. Number of EDI measurements per bin.

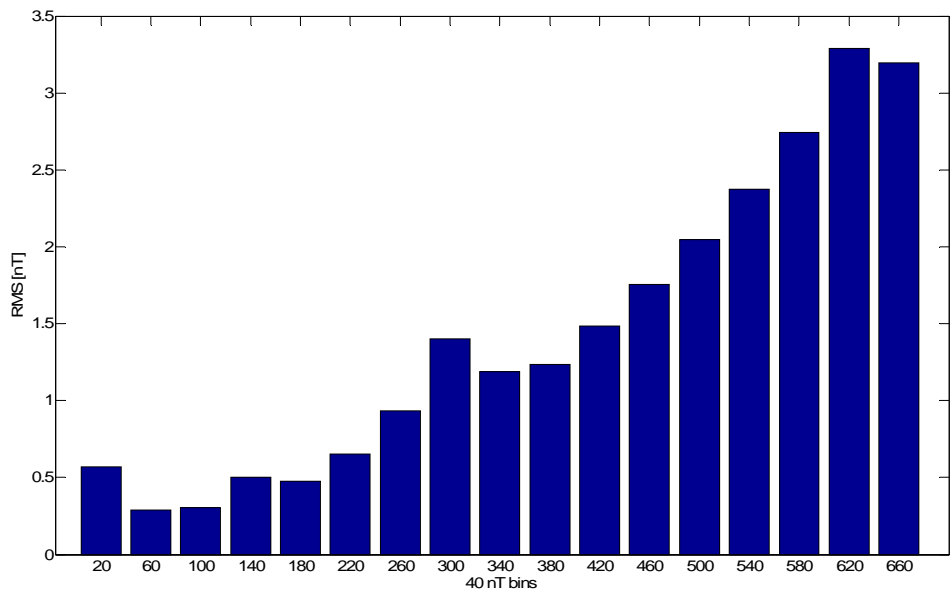
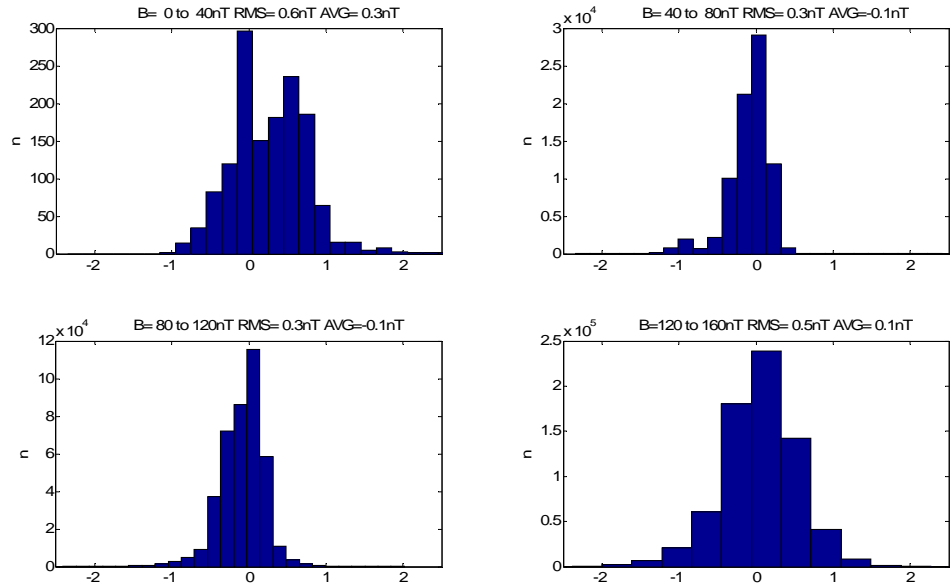
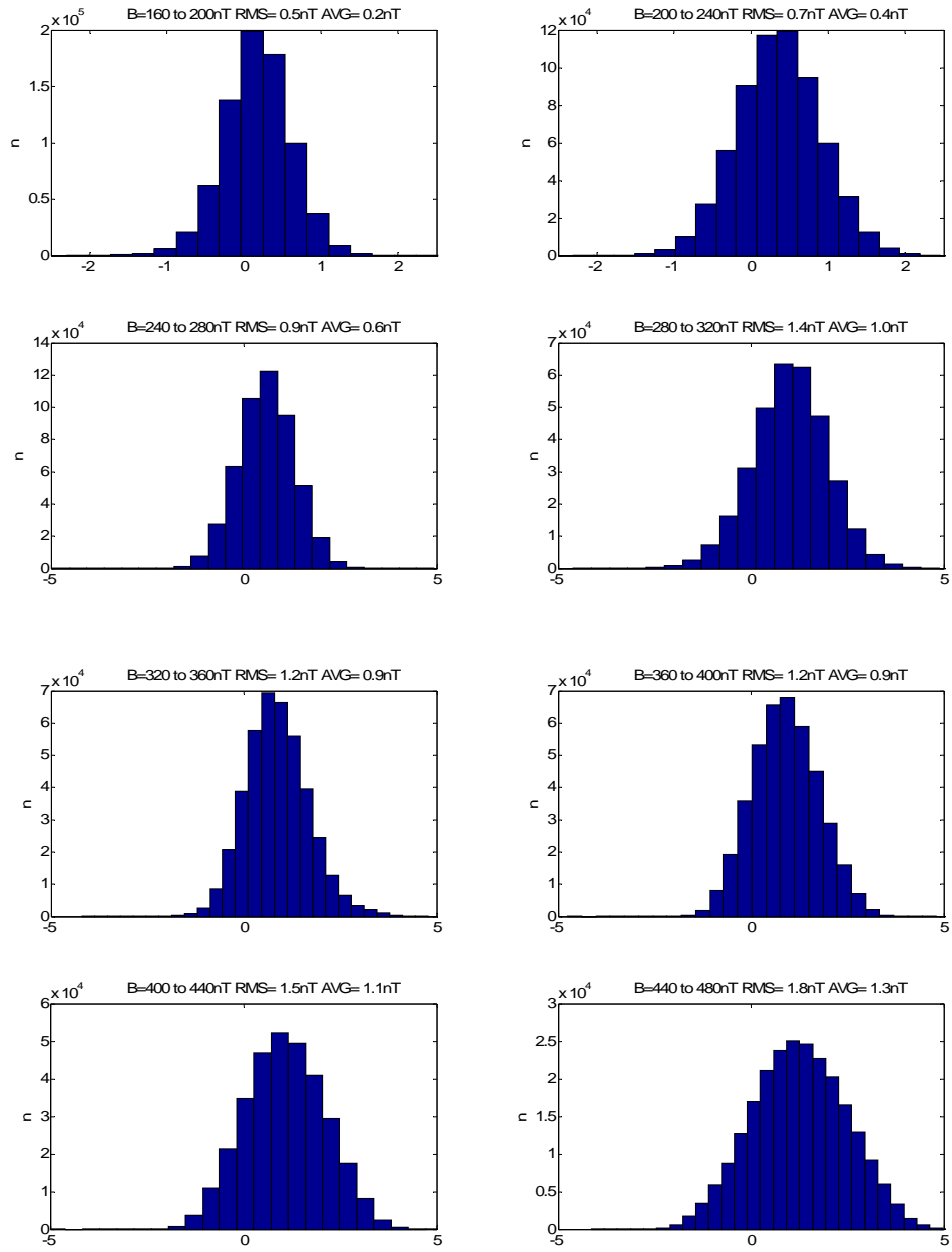


Figure 5.7. RMS differences between EDI and FGM per bin (before calibration).





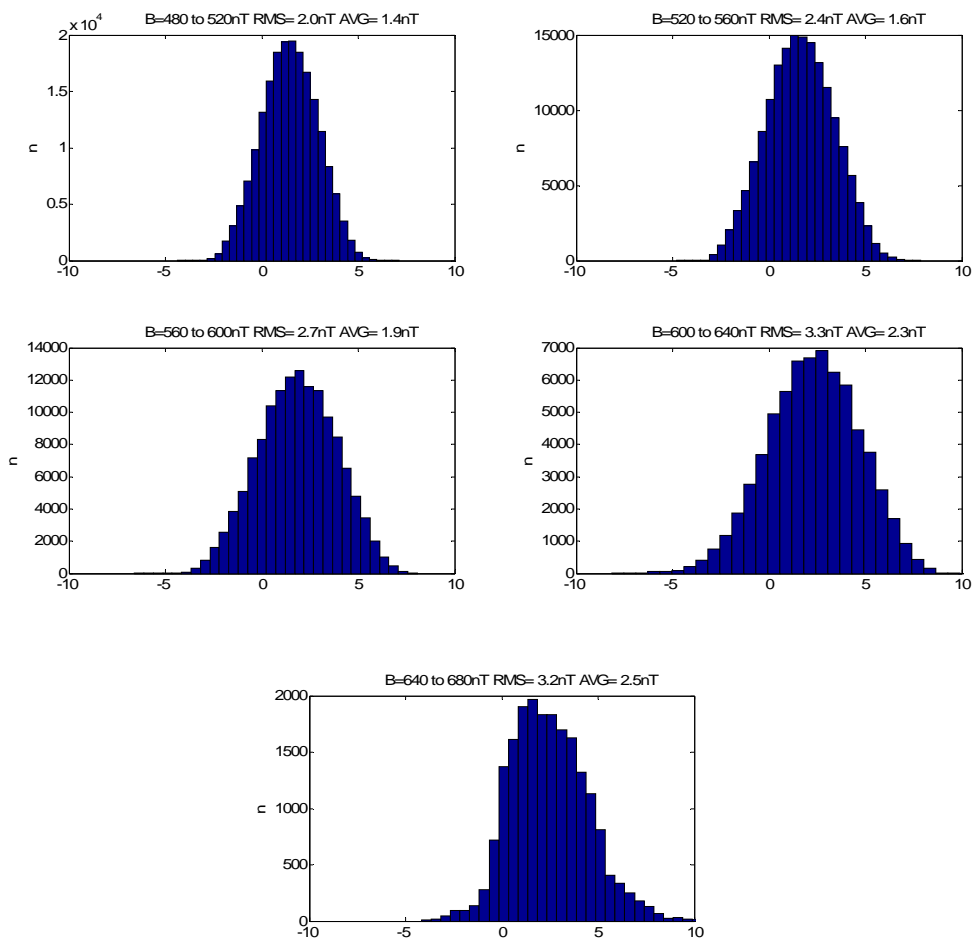


Figure 5.8. Histograms of differences between EDI and FGM (before calibration).

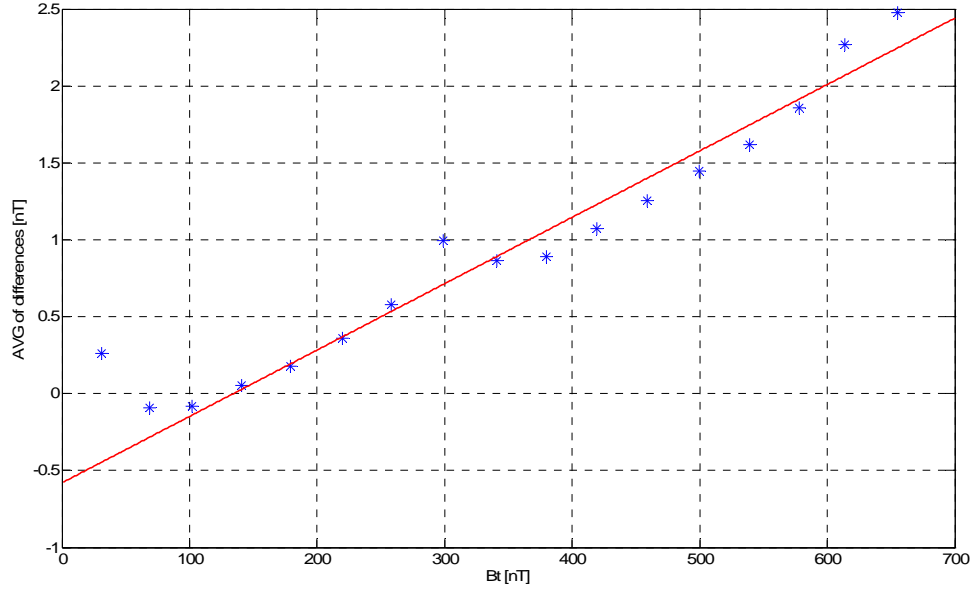


Figure 5.9. Linear fit across all the mean differences between EDI and FGM of all the bins (before calibration).

Since there are almost no measurements of EDI in low fields, finding zero levels is not possible without matching the gains between the two instruments. The equation for the gains and offsets can be written as shown below. A decision was made to change the gains for FGM but there is no proof that the FGM gains are incorrect.

$$B_{tEDI}^2 = G_{12}^2 B_{1FGM}^2 + G_{12}^2 B_{2FGM}^2 + G_3^2 (B_{3FGM} + O_3)^2$$

which transforms to

$$B_{tEDI}^2 = G_{12}^2 (B_{1FGM}^2 + B_{2FGM}^2) + G_3^2 B_{3FGM}^2 + 2G_3^2 O_3 B_{3FGM} + G_3^2 O_3^2$$

A simple linear fit can be used to solve for four unknowns. The unknowns are: $x_1 = G_{12}^2$, $x_2 = G_3^2$, $x_3 = G_3^2 O_3$ and $x_4 = G_3^2 O_3^2$. Since the gains are always positive values it is possible to calculate

$$G_{12} = \sqrt{x_1}$$

$$G_{3p} = \sqrt{x_2}$$

$$O_{3p} = \frac{x_3}{x_2}$$

where the last term $x_4 = G_3^2 O_3^2$ was neglected because the zero level can be positive and negative. It can be assumed that the result for G_{12} is correct and final because the neglected term does not contain G_{12} . Since the fourth term was neglected, the results for G_{3p} and O_{3p} can still be improved. After application of G_{12} a simple two dimensional minimum search algorithm can be used to find the final G_3 and O_3 . The finest steps for offset and gain are 0.02 nT and 0.05%, respectively. Table 5.1 shows the results of the fits. The first fit has the lowest RMS value and the highest number of parameters (four) but yields only starting values for G_3 and O_3 . After application of the results of the first fit the RMS goes up again. After the minimum search the RMS is almost as low as for the first fit but with altogether one parameter less.

	RMS	Parameters
before fit	1.2275 nT	N/A
after first fit	0.9045 nT	$G_{12}=1.0034, G_{3p}=1.0030, O_{3p}=-0.15$ nT
after application of G_{3p} and O_{3p}	0.9184 nT	same
after minimum search	0.9049 nT	$G_{12}=1.0034, G_3=1.0025, O_3=-0.28$ nT
after using data below 120 nT	0.2872 nT	$G_{12}=1.0034, G_3=1.0025, O_3=-0.41$ nT

Table 5.1. Results of various fits.

For the data with applied calibration parameters the box chart of the RMS values for each bin is depicted in Figure 5.10. This figure shows that the differences are smallest up to 120 nT. After matching the gains, I did another fit only with data below 120 nT and solved only for O_3 via a simple one dimensional minimum search algorithm with a finest step size of 0.01 nT. I get a new value of $O_3=-0.41$ nT (see also Table 5.1).

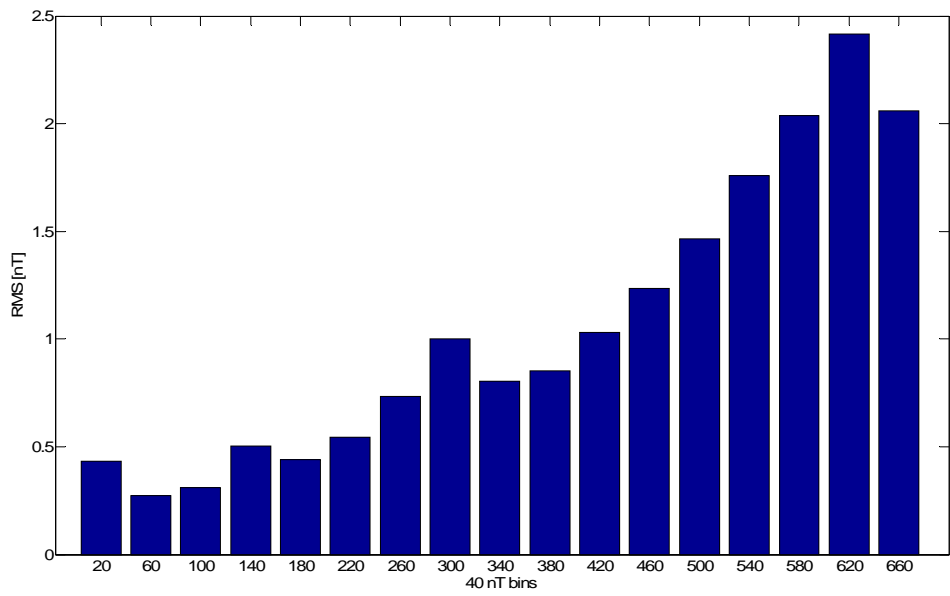
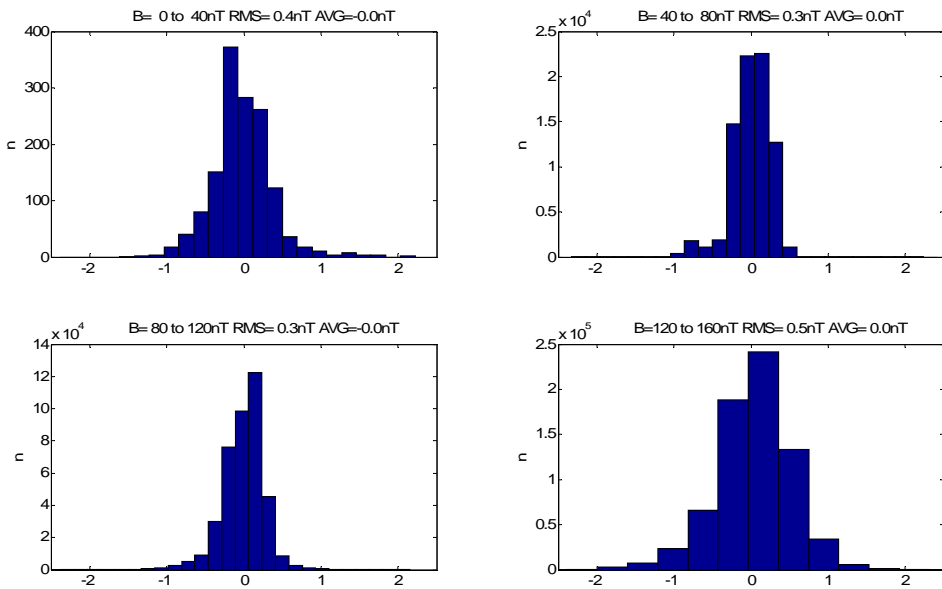
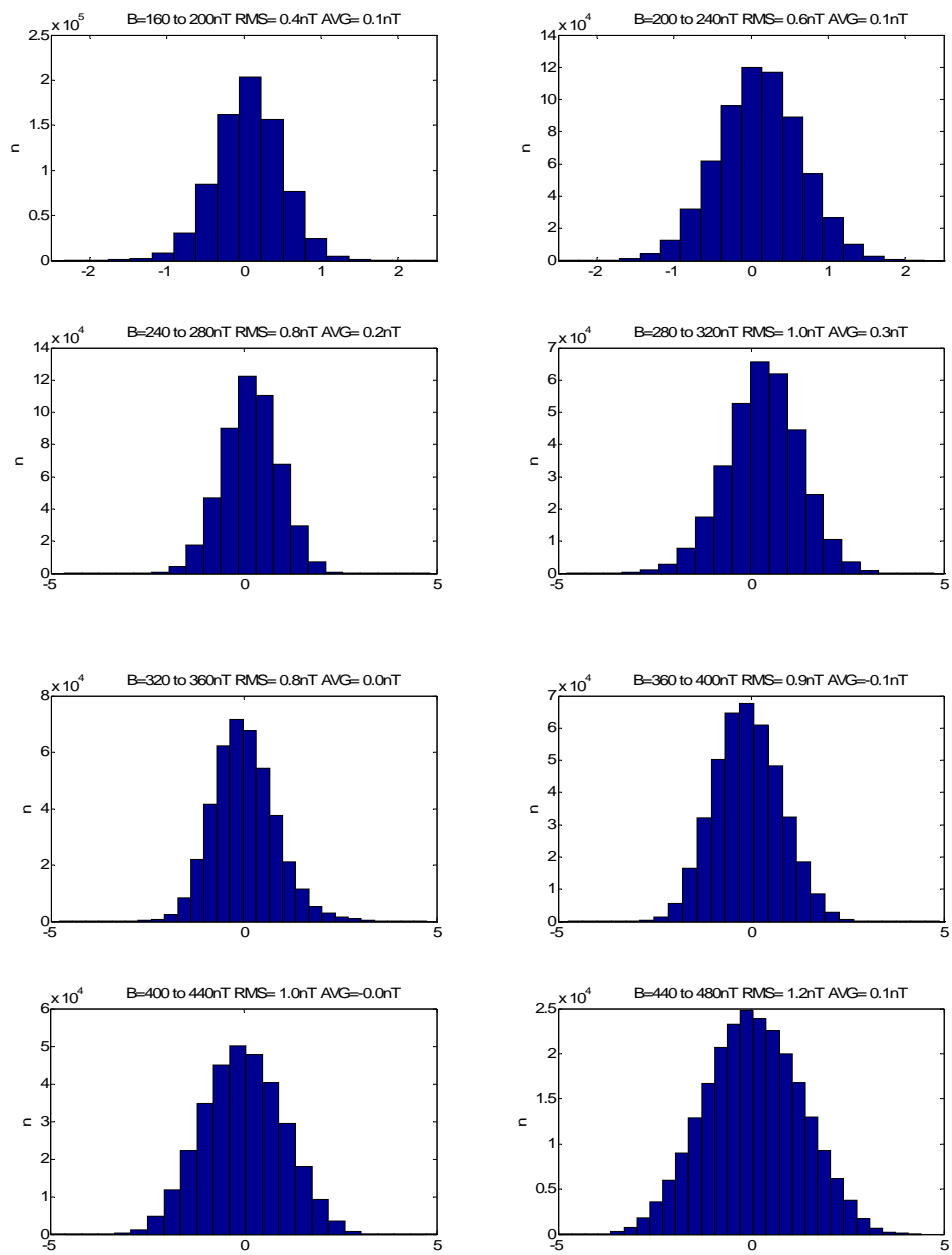


Figure 5.10. RMS differences between EDI and FGM for each bin after minimum search.





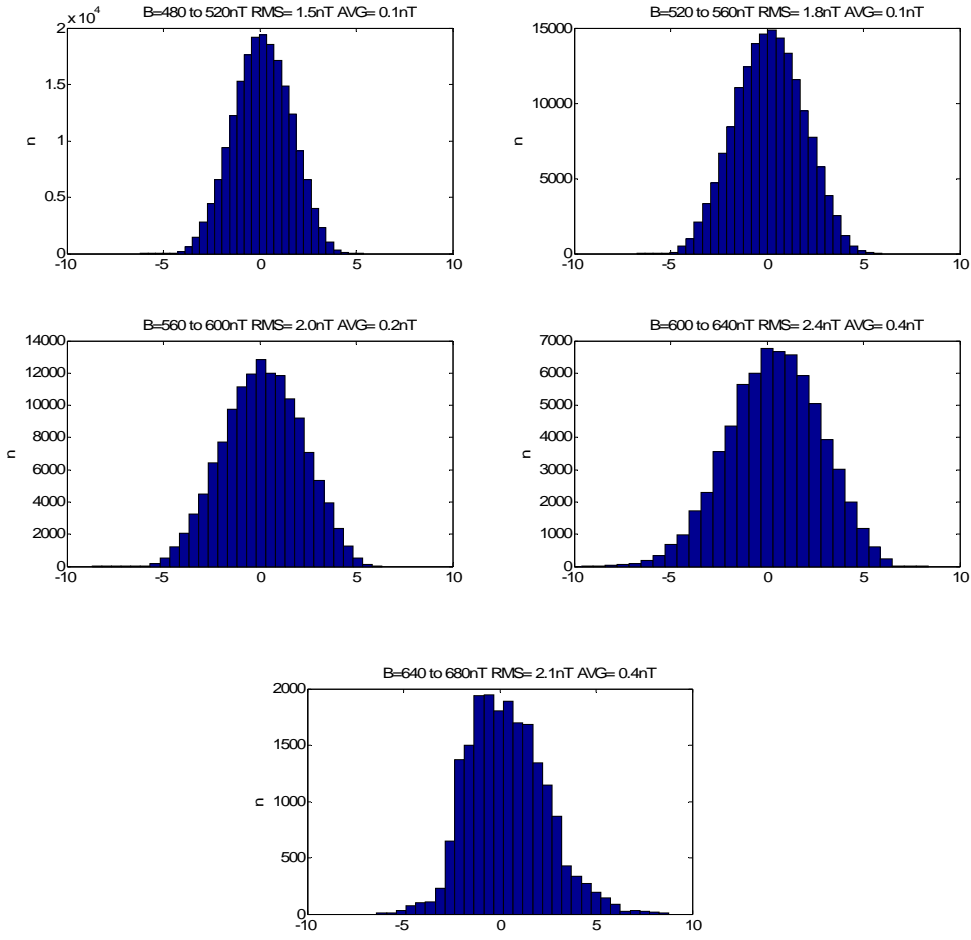


Figure 5.11. Histograms of differences between EDI and FGM (after calibration).

After application of all the calibration parameters in the last row of Table 5.1, the distributions for each bin have shifted towards zero. The distributions look symmetric except for the one for the highest fields (see Figure 5.11). This could be because EDI gives the times of flight in coarse steps for higher fields (see Figure 5.5).

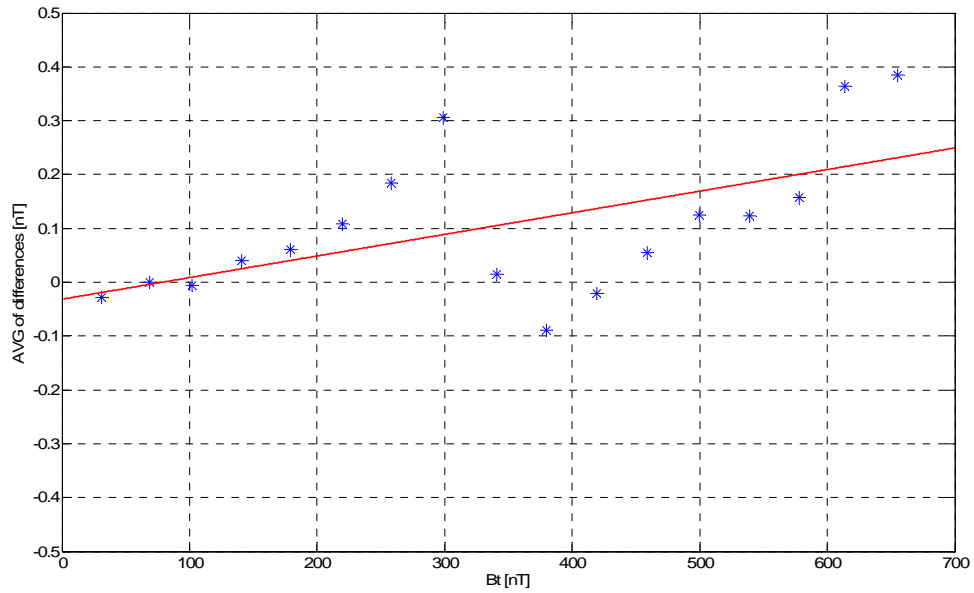


Figure 5.12. Linear fit across all the mean differences between EDI and FGM of all the bins (after calibration).

Additionally the line fit across the mean differences of all the bins (see Figure 5.12) is repeated. It has dramatically improved. The steepness of the slope is now very small. The larger deviations from the line before and after ~ 325 nT could be due to a range change of EDI at 325 nT. The magnetometer shows extremely linear behavior of the spin plane sensors, as can be seen in Figures 3.15 and 3.16. If the magnetometer would be non-linear, various higher harmonics of the spin frequency would be visible. There is no strong reason to assume that the spin axis sensor is non-linear.

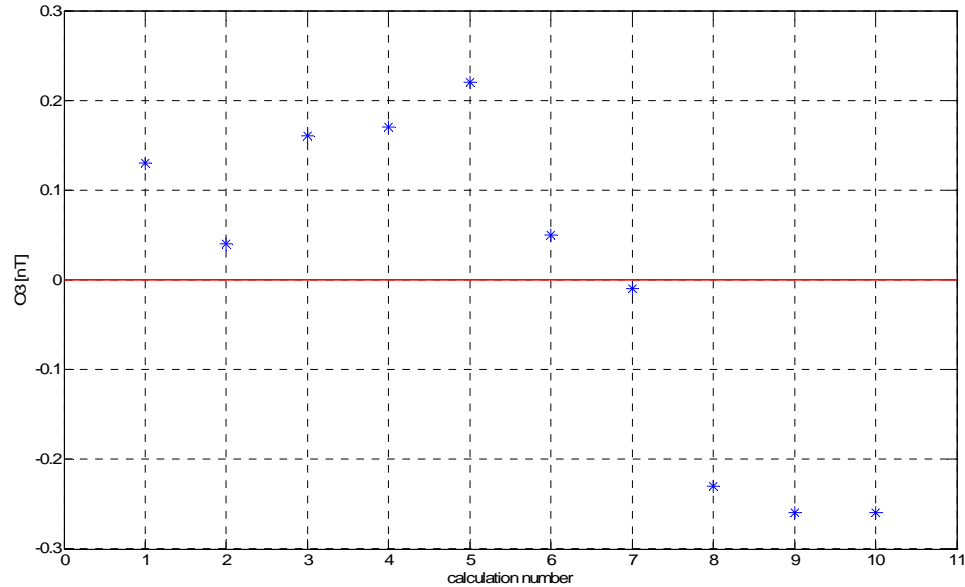


Figure 5.13. Zero level calculations for fields smaller 120 nT. The data were binned to 10 bins with equal number of points. The data in the first bin were measured before the data in the second bin and so forth.

Additionally, I bin the newly calibrated data that are smaller than 120 nT to 10 bins with equal number of measurements but this time I bin according to time. This means that the data in the first bin were measured before the data in the second bin and so forth. I calculate the zero levels (O_3) for each bin and see if a trend can be seen. Figure 5.13 shows the results. It can be seen that the offset values are not random but follow a trend. This trend could be due to a number of eclipses that occurred during the selected test interval.

It is possible to conclude that after the gains between EDI and FGM have been matched, the spin axis zero levels can be calculated for relatively short time intervals.

5.3. Conclusions

This chapter shows that the noise distributions of EDI (differences to spin averaged magnetic field data) are mostly symmetric, which is important for least squares fitting. There is a significant difference in gains between the magnetometer (FGM) and EDI on Cluster 3. For this work, I used data from the official Cluster data archive. After the gains between EDI and FGM have been matched, the spin axis zero levels can be calculated for relatively short time intervals. The technique and the results herein may be useful for the upcoming Magnetospheric Multiscale (MMS) mission (currently scheduled to be launched on 2014-08-14). Each of the four MMS satellites will be equipped with two fluxgate magnetometers as well as an Electron Drift Instrument.

6. Precise Calculation of Current Densities via Four Spinning Spacecraft in a Tetrahedron Configuration

The European Cluster mission was the first mission specifically designed to measure spatial gradients of physical quantities in three dimensions. Four spacecraft were flying in a tetrahedron configuration which allowed calculation of spatial gradients such as current densities. Ampere's law provides an equation that allows the calculation of current densities

$$\nabla \times \vec{B} = \mu_0 \vec{J}$$

$$\nabla \times \vec{B} \quad \text{curl of the magnetic field often expressed as } \frac{nT}{\text{Re}}, \frac{nT}{\text{km}} \text{ or } \frac{nT}{m}$$

μ_0 permeability of free space (physical constant)

$$4 \cdot \Pi \cdot 10^{-7} \frac{Vs}{Am}$$

$$\vec{J} \quad \text{current density often expressed as } \frac{nA}{m^2}$$

Similar to Khurana *et al.* (1996), the derivation herein also starts with first order Taylor-series expansion but the method below is derived differently and the problem is solved with only four relatively short equations compared to 18 long equations in the Khurana paper. If measurements from four spacecraft are obtained the curl of \vec{B} can be calculated from Taylor Series expansion (first order)

$$B_x^i = B_x^0 + \frac{\partial B_x}{\partial x} dx^{i0} + \frac{\partial B_x}{\partial y} dy^{i0} + \frac{\partial B_x}{\partial z} dz^{i0}$$

$$B_y^i = B_y^0 + \frac{\partial B_y}{\partial x} dx^{i0} + \frac{\partial B_y}{\partial y} dy^{i0} + \frac{\partial B_y}{\partial z} dz^{i0}$$

$$B_z^i = B_z^0 + \frac{\partial B_z}{\partial x} dx^{i0} + \frac{\partial B_z}{\partial y} dy^{i0} + \frac{\partial B_z}{\partial z} dz^{i0}$$

i index of spacecraft (1 to 4)

B_x^0, B_y^0, B_z^0 magnetic field at center of the tetrahedron (center of mass)

$dx^{i0}, dy^{i0}, dz^{i0}$ spacecraft distances from the center of the tetrahedron.

$$\frac{\partial B_x}{\partial x}, \frac{\partial B_x}{\partial y}, \frac{\partial B_x}{\partial z},$$

$$\begin{aligned} & \frac{\partial B_y}{\partial x}, \frac{\partial B_y}{\partial y}, \frac{\partial B_y}{\partial z}, \\ & \frac{\partial B_z}{\partial x}, \frac{\partial B_z}{\partial y}, \frac{\partial B_z}{\partial z} \end{aligned} \quad \text{nine first order gradients of the magnetic field}$$

After subtraction of the equation for spacecraft 1

$$B_x^{21} = \frac{\partial B_x}{\partial x} dx^{21} + \frac{\partial B_x}{\partial y} dy^{21} + \frac{\partial B_x}{\partial z} dz^{21} \quad (6.1a)$$

$$B_x^{31} = \frac{\partial B_x}{\partial x} dx^{31} + \frac{\partial B_x}{\partial y} dy^{31} + \frac{\partial B_x}{\partial z} dz^{31} \quad (6.1b)$$

$$B_x^{41} = \frac{\partial B_x}{\partial x} dx^{41} + \frac{\partial B_x}{\partial y} dy^{41} + \frac{\partial B_x}{\partial z} dz^{41} \quad (6.1c)$$

Where B_x^{il} is the difference of the x-component between the i^{th} spacecraft and the first spacecraft. Similarly dx^{il} is the difference in the x-direction between the i^{th} spacecraft and the first spacecraft. The equations for the y- and the z-components of the magnetic fields (B_y^{il} and B_z^{il}) are similar. Equations (6.1a to 6.1c) can be written in matrix form

$$\begin{pmatrix} dx^{21} & dy^{21} & dz^{21} \\ dx^{31} & dy^{31} & dz^{31} \\ dx^{41} & dy^{41} & dz^{41} \end{pmatrix} \cdot \begin{pmatrix} \frac{\partial B_x}{\partial x} \\ \frac{\partial B_x}{\partial y} \\ \frac{\partial B_x}{\partial z} \end{pmatrix} = \begin{pmatrix} B_x^{21} \\ B_x^{31} \\ B_x^{41} \end{pmatrix} \quad (6.2)$$

The 3x3-matrix in equation (6.2) is called distance matrix. The spatial gradients can be calculated via the inverse of the distance matrix

$$\begin{pmatrix} \frac{\partial B_x}{\partial x} \\ \frac{\partial B_x}{\partial y} \\ \frac{\partial B_x}{\partial z} \end{pmatrix} = \begin{pmatrix} ax^{21} & ay^{21} & az^{21} \\ ax^{31} & ay^{31} & az^{31} \\ ax^{41} & ay^{41} & az^{41} \end{pmatrix}^{-1} \begin{pmatrix} B_x^{21} \\ B_x^{31} \\ B_x^{41} \end{pmatrix} \quad (6.3)$$

The curl and the divergence of \vec{B} can be calculated as follows

$$\begin{aligned}(\nabla \times \mathbf{B})_x &= \frac{\partial B_z}{\partial y} - \frac{\partial B_y}{\partial z} \\(\nabla \times \mathbf{B})_y &= \frac{\partial B_x}{\partial z} - \frac{\partial B_z}{\partial x} \\(\nabla \times \mathbf{B})_z &= \frac{\partial B_y}{\partial x} - \frac{\partial B_x}{\partial y} \\\nabla \cdot \mathbf{B} &= \frac{\partial B_x}{\partial x} + \frac{\partial B_y}{\partial y} + \frac{\partial B_z}{\partial z}\end{aligned}$$

As can be seen from the above equations, the spatial gradients only depend on differences of magnetic field measurements and inter spacecraft distances. An assumption was made that the inter spacecraft distances are determined with high enough accuracy. As can be seen from equations 6.1a to 6.1c, the inter spacecraft distances are being multiplied with the spatial gradients. Any errors in inter spacecraft distances directly influence the accuracy of the spatial gradients. Small uncertainties in the magnetometer calibration can introduce very large errors in the differences of magnetic field values and thus errors in the spatial gradients.

There are regions inside the Earth's magnetosphere where the current density is negligibly small. Such regions are inside the tail lobes and high latitude regions in the middle magnetosphere (but away from the cusp regions). Without performing inter spacecraft calibration the measured current density is usually not zero at such regions. Calibration parameters can be calculated by minimizing curl of \vec{B} and divergence of \vec{B} at regions where these quantities are negligibly small.

After spacecraft one was chosen as the mother spacecraft, an assumption was made that the other three spacecraft have slight errors in their absolute orientations with respect to the mother spacecraft. These errors can be expressed as Euler angle rotations. Contrary to Khurana *et al.* (1996), the same rotations as in equation (4.5) were used. Two rotations (angles $d\theta_1$ and $d\theta_2$) were used to adjust the directions of the spin axes of three spacecraft and another rotation was used (angle $d\varphi_{12}$) to adjust the azimuthal angles of the spin plane components. Similarly as in equation (4.5) the same gain matrix (gains G_{12} and G_3) was used and the spin axes offset (dO_3) was added. These calibration parameters cannot be found by spin tone removal (see Chapter 3).

$$\begin{pmatrix} B_x \\ B_y \\ B_z \end{pmatrix} = \begin{pmatrix} 1 & 0 & 0 \\ 0 & \cos d\theta_1 & \sin d\theta_1 \\ 0 & -\sin d\theta_1 & \cos d\theta_1 \end{pmatrix} \begin{pmatrix} \cos d\theta_2 & 0 & \sin d\theta_2 \\ 0 & 1 & 0 \\ -\sin d\theta_2 & 0 & \cos d\theta_2 \end{pmatrix} \begin{pmatrix} \cos d\varphi_{12} & \sin d\varphi_{12} & 0 \\ -\sin d\varphi_{12} & \cos d\varphi_{12} & 0 \\ 0 & 0 & 1 \end{pmatrix} \begin{pmatrix} G_{12} & 0 & 0 \\ 0 & G_{12} & 0 \\ 0 & 0 & G_3 \end{pmatrix} \begin{pmatrix} B_x' \\ B_y' \\ B_z' + dO_3 \end{pmatrix} \quad (6.4)$$

After small angle approximations and writing the gains as deltas yields

$$\begin{pmatrix} B_x \\ B_y \\ B_z \end{pmatrix} = \begin{pmatrix} 1 & 0 & 0 \\ 0 & 1 & d\theta_1 \\ 0 & -d\theta_1 & 1 \end{pmatrix} \begin{pmatrix} 1 & 0 & d\theta_2 \\ 0 & 1 & 0 \\ -d\theta_2 & 0 & 1 \end{pmatrix} \begin{pmatrix} 1 & d\varphi_{12} & 0 \\ -d\varphi_{12} & 1 & 0 \\ 0 & 0 & 1 \end{pmatrix} \begin{pmatrix} 1-dG_{12} & 0 & 0 \\ 0 & 1-dG_{12} & 0 \\ 0 & 0 & 1-dG_3 \end{pmatrix} \begin{pmatrix} B_x' \\ B_y' \\ B_z' + dO_3 \end{pmatrix} \quad (6.5)$$

Combination of the three rotation matrices to a single matrix yields

$$\begin{pmatrix} B_x \\ B_y \\ B_z \end{pmatrix} = \begin{pmatrix} 1 & d\varphi_{12} & d\theta_2 \\ -d\varphi_{12} & 1 & d\theta_1 \\ -d\theta_2 & -d\theta_1 & 1 \end{pmatrix} \begin{pmatrix} 1-dG_{12} & 0 & 0 \\ 0 & 1-dG_{12} & 0 \\ 0 & 0 & 1-dG_3 \end{pmatrix} \begin{pmatrix} B_x' \\ B_y' \\ B_z' + dO_3 \end{pmatrix} \quad (6.6)$$

Writing without matrix form and neglecting second order terms yields

$$\begin{aligned} B_x &= B_x' - dG_{12}B_x' + d\varphi_{12}B_y' + d\theta_2B_z' \\ B_y &= B_y' - dG_{12}B_y' - d\varphi_{12}B_x' + d\theta_1B_z' \\ B_z &= B_z' - dG_3B_z' - d\theta_1B_y' - d\theta_2B_x' + dO_3 \end{aligned}$$

Equation (6.3) shows that the spatial gradients only depend on differences of magnetic field values between spacecraft, thus the field of spacecraft one can be subtracted out.

$$\begin{aligned} B_x^{il} &= B_x^{il} - dG_{12}^{il}B_x^{i'} + d\varphi_{12}^{il}B_y^{i'} + d\theta_2^{il}B_z^{i'} \\ B_y^{il} &= B_y^{il} - dG_{12}^{il}B_y^{i'} - d\varphi_{12}^{il}B_x^{i'} + d\theta_1^{il}B_z^{i'} \\ B_z^{il} &= B_z^{il} - dG_3^{il}B_z^{i'} - d\theta_1^{il}B_y^{i'} - d\theta_2^{il}B_x^{i'} + dO_3^{il} \end{aligned}$$

with $i = 2, 3, 4$

Inserting the equations into (6.3) yields

$$\begin{pmatrix} \frac{\partial B_x}{\partial x} \\ \frac{\partial B_x}{\partial y} \\ \frac{\partial B_x}{\partial z} \end{pmatrix} = \begin{pmatrix} ax^{21} & ay^{21} & az^{21} \\ ax^{31} & ay^{31} & az^{31} \\ ax^{41} & ay^{41} & az^{41} \end{pmatrix} \begin{pmatrix} B_x^{21} - dG_{12}^{21}B_x^{2'} + d\varphi_{12}^{21}B_y^{2'} + d\theta_2^{21}B_z^{2'} \\ B_x^{31} - dG_{12}^{31}B_x^{3'} + d\varphi_{12}^{31}B_y^{3'} + d\theta_2^{31}B_z^{3'} \\ B_x^{41} - dG_{12}^{41}B_x^{4'} + d\varphi_{12}^{41}B_y^{4'} + d\theta_2^{41}B_z^{4'} \end{pmatrix} \quad (6.7)$$

Similarly

$$\begin{pmatrix} \frac{\partial B_y}{\partial x} \\ \frac{\partial B_y}{\partial y} \\ \frac{\partial B_y}{\partial z} \end{pmatrix} = \begin{pmatrix} ax^{21} & ay^{21} & az^{21} \\ ax^{31} & ay^{31} & az^{31} \\ ax^{41} & ay^{41} & az^{41} \end{pmatrix} \begin{pmatrix} B_y^{21}, -dG_{12}^{21}B_y^2, -d\varphi_{12}^{21}B_x^2 + d\theta_1^{21}B_z^2 \\ B_y^{31}, -dG_{12}^{31}B_y^3, -d\varphi_{12}^{31}B_x^3 + d\theta_1^{31}B_z^3 \\ B_y^{41}, -dG_{12}^{41}B_y^4, -d\varphi_{12}^{41}B_x^4 + d\theta_1^{41}B_z^4 \end{pmatrix} \quad (6.8)$$

and

$$\begin{pmatrix} \frac{\partial B_z}{\partial x} \\ \frac{\partial B_z}{\partial y} \\ \frac{\partial B_z}{\partial z} \end{pmatrix} = \begin{pmatrix} ax^{21} & ay^{21} & az^{21} \\ ax^{31} & ay^{31} & az^{31} \\ ax^{41} & ay^{41} & az^{41} \end{pmatrix} \begin{pmatrix} B_z^{21}, -dG_3^{21}B_z^2, -d\theta_1^{21}B_y^2 - d\theta_2^{21}B_x^2 + dO_3^{21} \\ B_z^{31}, -dG_3^{31}B_z^3, -d\theta_1^{31}B_y^3 - d\theta_2^{31}B_x^3 + dO_3^{31} \\ B_z^{41}, -dG_3^{41}B_z^4, -d\theta_1^{41}B_y^4 - d\theta_2^{41}B_x^4 + dO_3^{41} \end{pmatrix} \quad (6.9)$$

After introducing the calibration parameters that need to be calculated, equations that minimize curl of \vec{B} and divergence of \vec{B} can be written.

Setting curl of \vec{B} and divergence of \vec{B} equal to zero yields four equations

$$\begin{aligned} \frac{\partial B_y}{\partial z} &= \frac{\partial B_z}{\partial y} \\ \frac{\partial B_z}{\partial x} &= \frac{\partial B_x}{\partial z} \\ \frac{\partial B_x}{\partial y} &= \frac{\partial B_y}{\partial x} \\ \frac{\partial B_x}{\partial x} + \frac{\partial B_y}{\partial y} + \frac{\partial B_z}{\partial z} &= 0 \end{aligned}$$

After writing equations (6.7 to 6.9) in non-matrix form, inserting the appropriate terms into the above four equations and after some algebra four equations with 18 unknowns can be obtained.

$$\begin{pmatrix}
dG_{12}^{21} \\
dG_{12}^{31} \\
dG_{12}^{41} \\
dG_3^{21} \\
dG_3^{31} \\
dG_3^{41} \\
d\varphi_{12}^{21} \\
d\varphi_{12}^{31} \\
d\varphi_{12}^{41} \\
d\theta_1^{21} \\
d\theta_1^{31} \\
d\theta_1^{41} \\
d\theta_2^{21} \\
d\theta_2^{31} \\
d\theta_2^{41} \\
dO_3^{21} \\
dO_3^{31} \\
dO_3^{41}
\end{pmatrix} = X \begin{pmatrix}
(\nabla \times \vec{B}')_x \\
(\nabla \times \vec{B}')_y \\
(\nabla \times \vec{B}')_z \\
\nabla \cdot \vec{B}'
\end{pmatrix} \quad (6.10)$$

With $\nabla \times \vec{B}'$ and $\nabla \cdot \vec{B}'$ calculated from $(B_x^{i1'}, B_y^{i1'}, B_z^{i3'})$, $i = 2, 3, 4$ and the inverse distance matrix (see equation 6.3). The elements of matrix X are given in Appendix C.

Small angle approximations were made and second order terms were neglected. Thus iterations must be used to accurately calculate the calibration parameters. Estimates of calibration parameters are calculated using approximate equations (6.10). The estimates are then applied using the full equations (6.4). The approximate equations are used again but with the corrected data as input. This is done until the system converges.

The above derived equations yield exactly the same results as the equations published in Khurana *et al.* (1996), however the equations herein are much more compact (roughly by an order of magnitude).

6.1. Application to Cluster Data

Inter spacecraft calibration is most important for small separations of the four Cluster spacecraft. During the so-called: “2003 Cluster tail season”, the inter spacecraft distances were roughly only 100 km. For this season inter spacecraft calibration had a large effect on the calculation of current densities. For more information on the Cluster magnetic field investigation see Balogh *et al.* (2001).

Figure 6.1 shows an example of current density before and after inter spacecraft calibration. The figure shows a typical plasma sheet crossing with B_x changing sign. One can easily see that without inter spacecraft calibration there is a large current density in the quiet lobe regions. In the figure caption the term “best effort calibration” is used. This calibration consists of orthogonalization via spin tone removal (see Sec. 3.2), calculation of the spin axes offsets inside the solar wind (similar to Sec. 2.2) and removal of the jumps between range changes (see Appendix A).

Inter spacecraft calibrations were done with roughly one to two weeks of input data that contain several plasma sheet crossings. From the data regions in the lobes of the magnetosphere where the curl and the divergence should be zero were selected. It is also important to try to get an as high as possible range of input data. Additionally, paying attention to the tetrahedron quality factor Q is important.

$$Q=1+(\text{true volume})/(\text{ideal volume})+(\text{true area})/(\text{ideal area})$$

The “ideal volume” and the “ideal area” are calculated for a regular tetrahedron with the mean separation as base. When $Q = 1$ all spacecraft are collinear; when $Q = 2$ all spacecraft are planar; $Q=3$ for a regular tetrahedron. In this work, input data at times when Q is greater than 2 were used. For doing the minimization of curl and divergence all four spacecraft were transformed into spacecraft coordinates of the mother spacecraft.

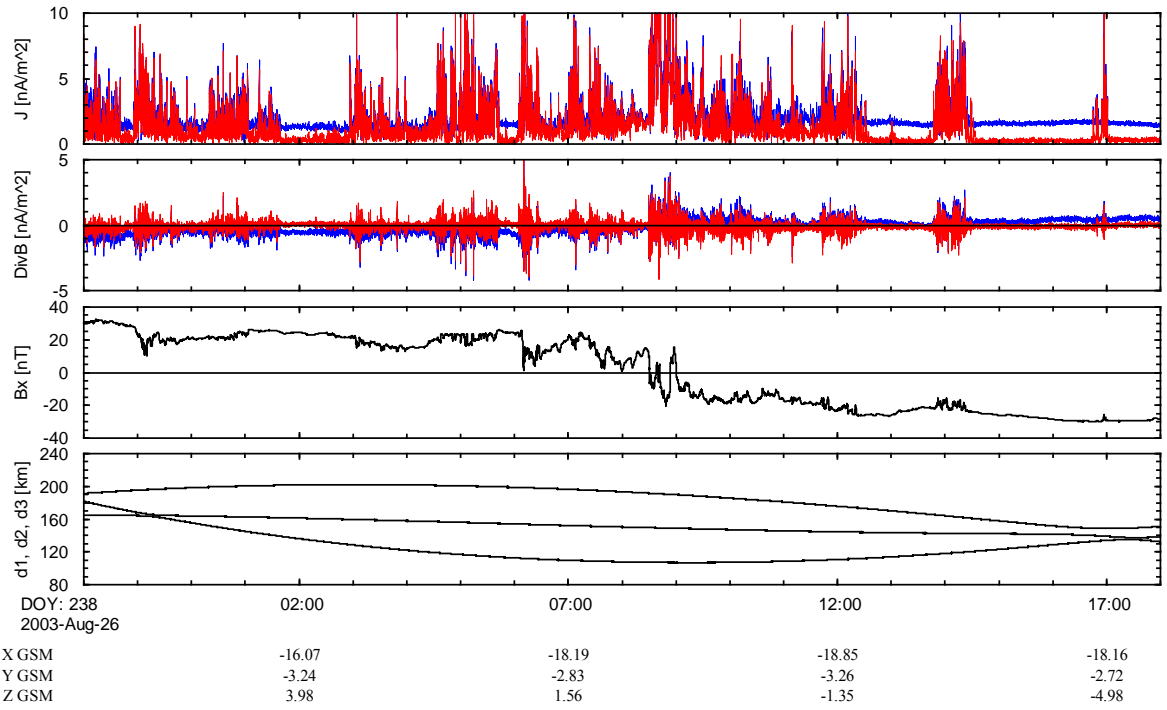


Figure 6.1. Blue: best effort calibration; Red: best effort calibration plus inter spacecraft calibration. The top panel shows a comparison of current density before and after inter spacecraft calibration. The second panel shows a comparison of divergence before and after inter spacecraft calibration. The third panel shows B_x and the bottom panel shows the inter spacecraft distances from a principal coordinate system. The three traces are largest, intermediate and smallest spacecraft distance.

6.2. Conclusions

Much shorter equations as previously published in Khurana *et al.* (1996) were derived that yield the same results. Additionally, I successfully applied the technique to measured data for the first time and show its importance. Current density as well as divergence of the magnetic field inside the tail lobes is significantly improved (much closer to zero) especially for 100 km spacing. The upcoming Magnetospheric Multiscale (MMS) mission (currently scheduled to be launched on 2014-08-14) will have much smaller spacecraft separations of <25 km. The method described herein may be crucial for calculating spatial gradients with MMS.

7. Discussion and Future Work

7.1. Chapter 2.2

In Section 2.2.4.4, the mathematical superiority of the Davis-Smith equation is pointed out. Based on this knowledge, a novel new technique is presented. Zero level calibrations of past missions might profit from the application of the technique herein but the recalibration must be done on the data in sensor coordinates and not all investigators have chosen to archive data in this coordinate system.

When a spacecraft is in a planetary magnetosheath or even an ICME magnetosheath the field variations along a component direction may correlate with the magnetic field magnitude for long periods because the shock changes the field only in the direction perpendicular to the shock normal. Inside a planetary magnetosphere a similar situation arises but with three-axis stabilized spacecraft, rolls or rocking of the spacecraft about its axes can be effective in determining the zero levels. Further studies need to be done for the application of the novel new technique to data from rocking or rolling spacecraft inside a magnetosphere. For example the change of the Earth's internal field strength at the position of the spacecraft could be filtered out leaving only the pure rotations of the magnetic field data from rocking or rolling. Additionally the technique could be applied to purely Alfvénic transverse waves inside a magnetosphere (Cummings *et al.*, 1969) while filtering out the Earth's internal field. For a spin stabilized spacecraft this is generally not possible to rock or roll the spacecraft perpendicular to the spin-axis but in multiple spacecraft missions it is sometimes possible to fly with spin axes at a large angle to one another. This was done on ISEE 1 and 2 for brief periods and recently on THEMIS (Angelopoulos, personal communication, 2007). Another technique to obtain the offset of the third axis is to rotate the sensor along the spin axis into the rotational plane of the spacecraft. This was done on ISEE 1 and 2 (Russell, 1978) and Polar (Russell *et al.*, 1995).

Further work could also be done by validating the presented novel technique using cross-instrument calibrations on a single spacecraft. For example a vector magnetometer can be calibrated using a reference scalar field strength (Merayo *et al.*, 2000, Chapter 5 of this thesis) such as provided by the gyro-times of an electron drift instrument (e.g. Paschmann *et al.*, 1997) or a precise scalar magnetometer. See Olsen *et al.* (2003) for information on the scalar calibration of the Ørsted vector magnetometer.

Analysis of the Alfvénic nature of the solar wind (Belcher *et al.*, 1969) as well as Alfvénic transverse waves inside a magnetosphere (Cummings *et al.*, 1969) could be done with emphasis on calibration e.g. for finding ideal frequency bands for zero level determination. Those studies could include data from particle instruments as well. For further information see e.g. Tsurutani and Ho, (1999) and Russell, (2000).

7.2. Chapter 2.3

An automated technique for finding zero levels inside a magnetosphere that provides error estimates was developed. Similarly, as stated in the previous section: past missions could benefit from the application of the new technique herein.

Cross checks between the new technique and the technique in Leinweber *et al.* (2008) could be performed with missions that go through the magnetosheath and into the interplanetary field within shorter time periods. Additional cross checks could be done by applying Leinweber *et al.* (2008) to rolling and rocking spacecraft inside the magnetosphere. Furthermore, all other cross checks (EDI, precise scalar field measurements and perpendicular spin axes) described in the previous section could be done as well. Another cross check could also be done by solving for the spin plane offsets of spinning spacecraft after orthogonalization (see Chapter 3).

Future research could also include solving for all three zero levels on three axis stabilized spacecraft.

7.3. Chapter 3

It is often necessary to determine in flight, the deviation of the actual direction of the spin axis with respect to a mechanical axis of the spacecraft. For example, comparisons of data between different instruments may require precise knowledge of such a deviation. Orthogonalization provides the angular deviations between the true spin axis and the magnetometer sensor that is (more or less) aligned with the spin axis. Measurements on ground provide information on the orientation of the magnetometer sensors versus spacecraft body axes. Unfortunately, there are some uncertainties that arise after launch. For example, the deployment of the boom was not exactly as it was on ground or a non-radial boom can bend due to a constant force. Effects of gravity may have compromised measurements on ground and temperatures were different. Knowing the spin axis with respect to one of the sensor axes may not necessarily provide very accurate information on spacecraft spin axis versus body axes.

Housekeeping data of a spacecraft often contain temperature measurements at various positions on a spacecraft. The method for resolving short term variations of calibration parameters (described in Section 3.4.) could be used to track changes (in flight) due to varying temperatures.

The envelope-method could be further tested with data that have higher noise levels. Filtering out noise may improve the versatility of the method. The limits of the envelope- as well as the DFT-based method could be further investigated. There may be situations where the DFT-based method is advantageous.

The algorithm for resolving short term variations of calibration parameters as described in Sec. 3.4.2., has worked well for a large number of applications. However, modifications to the algorithm seem possible. First: Instead of averaging in various coordinate systems, envelopes could be used to get the time-varying harmonics (similar to Sec. 3.3.). Second: Running sine wave fits seem to be another possibility.

7.4. Chapter 4

This chapter describes various methods for comparisons of magnetic field data with model fields in order to resolve magnetometer calibration parameters, attitude information as well as Sun angle information. It would be interesting to study the results of comparisons with different models. Additional studies on the stability of the obtained parameters versus varying perigee distances could be done. The influence of the accuracy of the input parameters of a model on the results could also be explored.

7.5. Chapter 5

Matching the gain factor between EDI and the fluxgate magnetometer is necessary in order to obtain correct magnetometer zero levels. The described method could be double checked with Leinweber *et al.* (2008) for Cluster orbits that pass quickly from higher fields into the interplanetary magnetic field. Such further research could potentially be very valuable for the upcoming Magnetospheric Multiscale (MMS) mission (currently scheduled to be launched on 2014-08-14). Each of the four MMS satellites will be equipped with two fluxgate magnetometers as well as an Electron Drift Instrument. MMS orbits will be such that entering the interplanetary field will only occur during unusual solar wind conditions.

7.6. Chapter 6

This chapter points out that current density as well as divergence of the magnetic field inside the tail lobes was significantly improved especially for 100 km spacing. The upcoming MMS-mission will have spacecraft spacing that is much smaller (<25 km). The method described herein may be crucial for calculating spatial gradients with MMS.

Since MMS will have much lower perigee passes than the Cluster mission, changing gains and angles with the method herein may be problematic. The field inside the tail lobes is relatively small (\sim 30 nT). This could lead to high uncertainties of gains and angles. Further research is necessary to combine the method described herein with Earth field comparisons so that gains and angles stay well defined.

Appendix A

Removing the jumps between the range changes

After orthogonalization calibration parameters that were impossible to determine via spin tone removal can be used, to remove jumps between range changes. The jumps can be fixed for the spin plane sensors by changing their gain and their azimuthal angle. The same gain and angle is applied to both spin plane sensors. The gain correction is applied to the lower range and the angle correction is applied to the higher range. For the spin axis a change of the zero level and a gain change can be used to fix jumps. The gain correction is applied to the lower range and the zero level correction is applied to the higher range. Information from several jumps is combined and a least squares solution, to derive the calibration parameters is performed. Combination of several jumps yields a range of input data which is required to derive stable solutions. Especially combining range changes at increasing fields with range changes at decreasing fields is important, since those range changes occur at different levels of the field.

Spin Plane:

The spin plane magnetic fields of the lower range are denoted as B_{PL1} and B_{PL2} . Similarly for the upper range: B_{PU1} and B_{PU2} . The subscript P means “prime” and is used to denote uncorrected values. The subscripts 1 and 2 denote the spin plane sensors.

First calculating the gain

$$\Delta G_{12} = \frac{\sqrt{B_{PU1}^2 + B_{PU2}^2}}{\sqrt{B_{PL1}^2 + B_{PL2}^2}}$$

Second calculating the angle:

$$\Delta\varphi_1 = \tan^{-1} \frac{\Delta G_{12} B_{PU1} B_{PL2} - \Delta G_{12} B_{PU2} B_{PL1}}{\Delta G_{12}^2 B_{PL1} B_{PL2} + B_{PU1} B_{PU2}}$$

The changes are applied as follows:

Upper range:

$$\begin{pmatrix} B_{U1} \\ B_{U2} \end{pmatrix} = \begin{pmatrix} \cos \Delta\varphi_1 & -\sin \Delta\varphi_1 \\ \sin \Delta\varphi_1 & \cos \Delta\varphi_1 \end{pmatrix} \begin{pmatrix} B_{PU1} \\ B_{PU2} \end{pmatrix}$$

Lower range:

$$\begin{pmatrix} B_{L1} \\ B_{L2} \end{pmatrix} = \begin{pmatrix} \Delta G_{12} & 0 \\ 0 & \Delta G_{12} \end{pmatrix} \begin{pmatrix} B_{PL1} \\ B_{PL2} \end{pmatrix}$$

Spin Axis:

The magnetic field of the uncorrected lower range spin axis sensor is denoted as B_{PL3} . Similarly for the upper range: B_{PU3} . The subscript 3 denotes the spin axis sensor.

The following equation can be solved in the least squares sense:

$$B_{PL3}\Delta G_3 = B_{PU3} - \Delta O_3$$

The changes are applied as follows:

Upper range:

$$B_{U3} = B_{PU3} + \Delta O_3$$

Lower range:

$$B_{L3} = \Delta G_3 B_{PL3}$$

Please note that the delta gains are close to one, whereas the delta angle and delta offsets are close to zero.

Appendix B

Matching of zero levels from multiple spacecraft

E.g. in the solar wind, differences of the magnetic fields measured at two points that are relatively close together are zero over sufficient long time periods. If the magnetometers have offsets the measured differences do not go to zero. For a cluster of four spacecraft 6 differences between the spin axes components can be used to correct the offsets.

In terms of equations this can be expressed as follows:

$$B_{31} + O_{31} - (B_{32} + O_{32}) = 0$$

$$B_{31} + O_{31} - (B_{33} + O_{33}) = 0$$

$$B_{31} + O_{31} - (B_{34} + O_{34}) = 0$$

$$B_{32} + O_{32} - (B_{33} + O_{33}) = 0$$

$$B_{32} + O_{32} - (B_{34} + O_{34}) = 0$$

$$B_{33} + O_{33} - (B_{34} + O_{34}) = 0$$

where e.g. B_{31} means the spin axis component of spacecraft 1 and similarly O_{32} means the spin axis offset of spacecraft 2 and so on.

Written as matrix equation of the form $Ax = b$ the above becomes:

$$\begin{pmatrix} 1 & -1 & 0 & 0 \\ 1 & 0 & -1 & 0 \\ 1 & 0 & 0 & -1 \\ 0 & 1 & -1 & 0 \\ 0 & 1 & 0 & -1 \\ 0 & 0 & 1 & -1 \end{pmatrix} \begin{pmatrix} O_{31} \\ O_{32} \\ O_{33} \\ O_{34} \end{pmatrix} = \begin{pmatrix} B_{32} - B_{31} \\ B_{33} - B_{31} \\ B_{34} - B_{31} \\ B_{33} - B_{32} \\ B_{34} - B_{32} \\ B_{34} - B_{33} \end{pmatrix}$$

This matrix equation can be solved by singular value decomposition (SVD). The rank of A is only 3 which means that there is one free parameter. The free parameter will be set to zero. In other words the method chooses automatically a mother spacecraft. The mother spacecraft can be easily changed to another spacecraft by subtracting its offset from all spacecraft. E.g. the mother spacecraft can be chosen so that the overall change of the zero levels is smallest.

Figure B.1 shows the 6 differences for all four Cluster spacecraft for all three components of the magnetic field. The spin plane components (upper two panels) show no systematic differences whereas the bottom panel shows small systematic differences.

After matching the zero levels the bottom panel in Figure B.2 shows no systematic differences anymore.

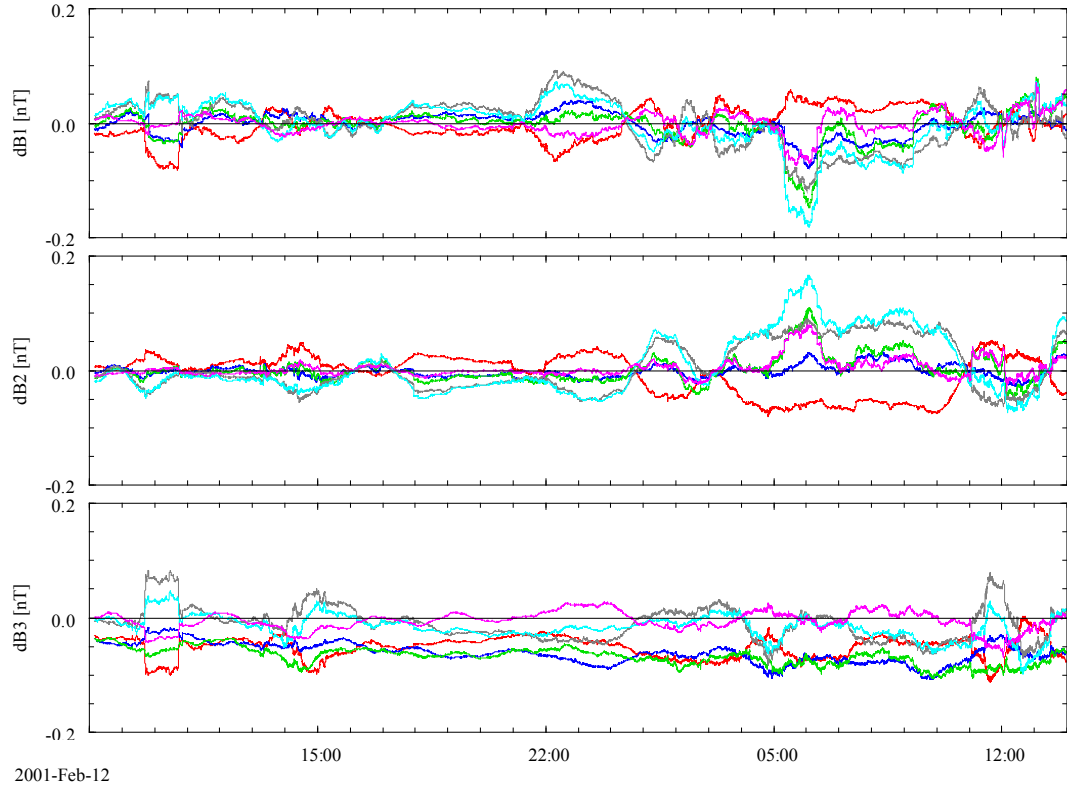


Figure B.1. Six differences before zero level matching, of three components of four Cluster spacecraft (one component per panel).

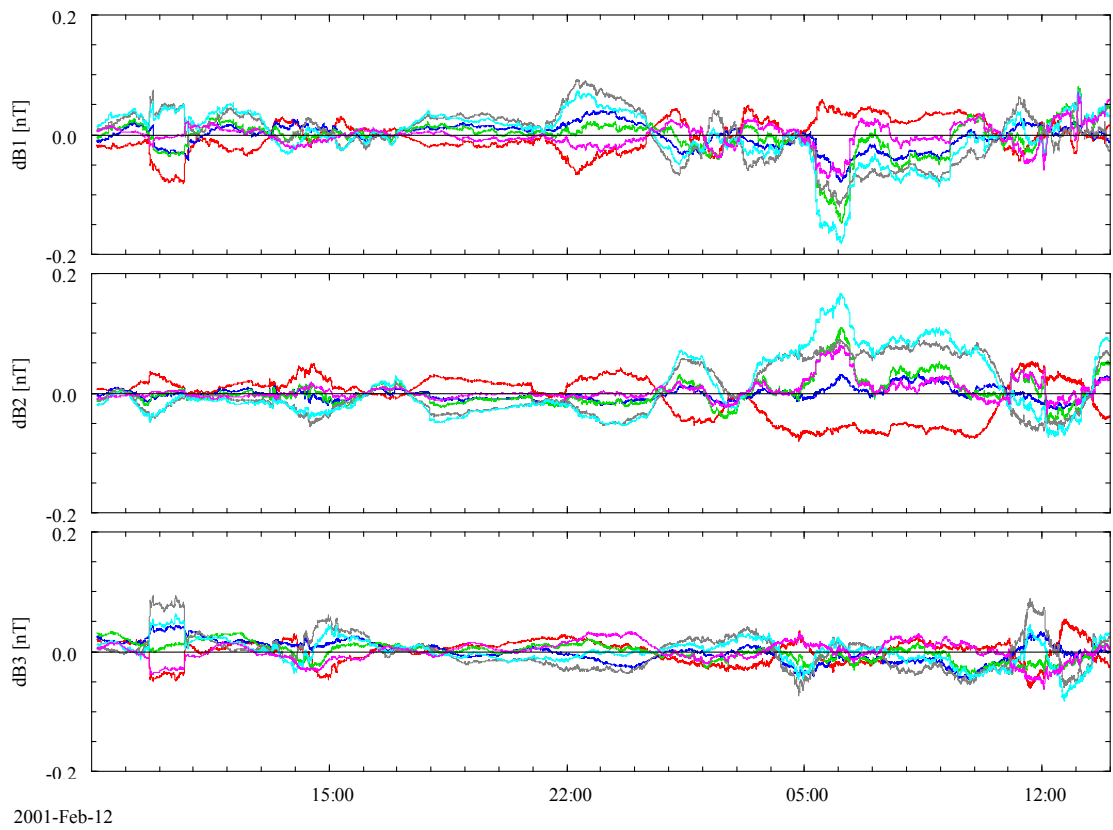


Figure B.2. Six differences after zero level matching, of three components of four Cluster spacecraft (one component per panel).

Appendix C

Elements of matrix X in equation (6.10):

Row 1:

$$\begin{aligned}
 x_{1,1} &= -ax^{41}B_y^2, \\
 x_{1,2} &= -ay^{41}B_y^3, \\
 x_{1,3} &= -az^{41}B_y^4, \\
 x_{1,4} &= ax^{31}B_z^2, \\
 x_{1,5} &= ay^{31}B_z^3, \\
 x_{1,6} &= az^{31}B_z^4, \\
 x_{1,7} &= -ax^{41}B_x^2, \\
 x_{1,8} &= -ay^{41}B_x^3, \\
 x_{1,9} &= -az^{41}B_x^4, \\
 x_{1,10} &= ax^{41}B_z^2 + ax^{31}B_y^2, \\
 x_{1,11} &= ay^{41}B_z^3 + ay^{31}B_y^3, \\
 x_{1,12} &= az^{41}B_z^4 + az^{31}B_y^4, \\
 x_{1,13} &= ax^{31}B_x^2, \\
 x_{1,14} &= ay^{31}B_x^3, \\
 x_{1,15} &= az^{31}B_x^4, \\
 x_{1,16} &= -ax^{31}, \\
 x_{1,17} &= -ay^{31}, \\
 x_{1,18} &= -az^{31}
 \end{aligned}$$

Row 2:

$$\begin{aligned}
 x_{2,1} &= ax^{41}B_x^2, \\
 x_{2,2} &= ay^{41}B_x^3, \\
 x_{2,3} &= az^{41}B_x^4, \\
 x_{2,4} &= -ax^{21}B_z^2, \\
 x_{2,5} &= -ay^{21}B_z^3, \\
 x_{2,6} &= -az^{21}B_z^4,
 \end{aligned}$$

$$\begin{aligned}
x_{2,7} &= -ax^{41}B_y^2, \\
x_{2,8} &= -ay^{41}B_y^3, \\
x_{2,9} &= -az^{41}B_y^4, \\
x_{2,10} &= -ax^{21}B_y^2, \\
x_{2,11} &= -ay^{21}B_y^3, \\
x_{2,12} &= -az^{21}B_y^4, \\
x_{2,13} &= -ax^{21}B_x^2 - ax^{41}B_z^2, \\
x_{2,14} &= -ay^{21}B_x^3 - ay^{41}B_z^3, \\
x_{2,15} &= -az^{21}B_x^4 - az^{41}B_z^4, \\
x_{2,16} &= ax^{21}, \\
x_{2,17} &= ay^{21}, \\
x_{2,18} &= az^{21}
\end{aligned}$$

Row 3:

$$\begin{aligned}
x_{3,1} &= -ax^{31}B_x^2 + ax^{21}B_y^2, \\
x_{3,2} &= -ay^{31}B_x^3 + ay^{21}B_y^3, \\
x_{3,3} &= -az^{31}B_x^4 + az^{21}B_y^4, \\
x_{3,4} &= 0, \\
x_{3,5} &= 0, \\
x_{3,6} &= 0, \\
x_{3,7} &= ax^{31}B_y^2 + ax^{21}B_x^2, \\
x_{3,8} &= ay^{31}B_y^3 + ay^{21}B_x^3, \\
x_{3,9} &= az^{31}B_y^4 + az^{21}B_x^4, \\
x_{3,10} &= -ax^{21}B_z^2, \\
x_{3,11} &= -ay^{21}B_z^3, \\
x_{3,12} &= -az^{21}B_z^4, \\
x_{3,13} &= ax^{31}B_z^2, \\
x_{3,14} &= ay^{31}B_z^3, \\
x_{3,15} &= az^{31}B_z^4, \\
x_{3,16} &= 0, \\
x_{3,17} &= 0
\end{aligned}$$

$$x_{3,18} = 0$$

Row 4:

$$\begin{aligned}
x_{4,1} &= ax^{21}B_x^2 + ax^{31}B_y^2, \\
x_{4,2} &= ay^{21}B_x^3 + ay^{31}B_y^3, \\
x_{4,3} &= az^{21}B_x^4 + az^{31}B_y^4, \\
x_{4,4} &= ax^{41}B_z^2, \\
x_{4,5} &= ay^{41}B_z^3, \\
x_{4,6} &= az^{41}B_z^4, \\
x_{4,7} &= ax^{31}B_x^2 - ax^{21}B_y^2, \\
x_{4,8} &= ay^{31}B_x^3 - ay^{21}B_y^3, \\
x_{4,9} &= az^{31}B_x^4 - az^{21}B_y^4, \\
x_{4,10} &= ax^{41}B_y^2 - ax^{31}B_z^2, \\
x_{4,11} &= ay^{41}B_y^3 - ay^{31}B_z^3, \\
x_{4,12} &= az^{41}B_y^4 - az^{31}B_z^4, \\
x_{4,13} &= ax^{41}B_x^2 - ax^{21}B_z^2, \\
x_{4,14} &= ay^{41}B_x^3 - ay^{21}B_z^3, \\
x_{4,15} &= az^{41}B_x^4 - az^{21}B_z^4, \\
x_{4,16} &= -ax^{41}, \\
x_{4,17} &= -ay^{41}, \\
x_{4,18} &= -az^{41}
\end{aligned}$$

References

- Acuña, M. H., J. L. Scheifele, P. Stella , C. Kloss, B. Smith, G. Heinshohn, and K. Sharmit, Magnetic field cancellation techniques for the Mars Global Surveyor solar array, *Conference Record of the Twenty Fifth IEEE Photovoltaic Specialists Conference - 1996*, 325-328, 1996.
- Acuña, M. H., J. E. P. Connerney, P. Wasilewski, R. P. Lin, K. A. Anderson, C. W. Carlson, J. McFadden, D. W. Curtis, D. Mitchell, H. Reme, C. Mazelle, J. A. Sauvaud, C. d'Uston, A. Cros, J. L. Medale, S. J. Bauer, P. Cloutier, M. Mayhew, D. Winterhalter, and N. F. Ness, Magnetic field and plasma observations at Mars: Initial results of the Mars global surveyor mission, *Science* 279(5357), 1676-1680, 1998.
- Acuña, M. H., J. E. P. Connerney, P. Wasilewski, R. P. Lin, D. Mitchell, K. A. Anderson, C. W. Carlson, J. McFadden, H. R. Reme, C. Mazelle, D. Vignes, S. J. Bauer, P. Cloutier, and N. F. Ness, Magnetic field of Mars: Summary of results from the aerobraking and mapping orbits, *J. Geophys. Res.* 106(E10), 23403-23417, 2001.
- Acuña, M. H., Space-based magnetometers, *Rev. Sci. Instrum.* 73, 3717, 2002.
- Acuña, M. H., D. Curtis, J. L. Scheifele, C. T. Russell, P. Schroeder, A. Szabo, and J. G. Luhmann. The STEREO/IMPACT magnetic field experiment, *Space Sci. Rev.* 136(1-4), 203-226, 2008.
- Altschuler, M. D., R. H., Levine, M. Stix, and Harvey J., High resolution mapping of the magnetic field of the solar corona, *Sol. Phys.* 51, 345, 1977.
- Anderson, B. J., L. J. Zanetti, D. H. Lohr, J. R. Hayes, M. H. Acuña, C. T. Russell, and T. Mulligan, In-flight calibration of the NEAR magnetometer, *IEEE T. Geosci. Remote.* 39(5), 907-917, 2001.
- Angelopoulos, V., The THEMIS mission, *Space Sci. Rev.* 141(1–4), 5 –34, doi:10.1007/s11214-008-9336-1, 2008
- Auster, H. U., K. H. Fornacon, E. Georgescu, K. H. Glassmeier, and U. Motschmann, Calibration of flux-gate magnetometers using relative motion, *Meas. Sci. Technol.* 13(7), 1124-1131, 2002.
- Auster, H. U., K. H. Glassmeier, W. Magnes, O. Aydogar, W. Baumjohann, D. Constantinescu, D. Fischer, K. H. Fornacon, E. Georgescu, P. Harvey, O. Hillenmaier, R. Kroth, M. Ludlam, Y. Narita, R. Nakamura, K. Okrafka, F. Plaschke, I. Richter, H. Schwarzl, B. Stoll, A. Valavanoglou, and M. Wiedemann, The THEMIS Fluxgate Magnetometer, *Space Sci. Rev.* 141(1-4), 235-264, 2008.

Balogh, A., T. J. Beek, R. J. Forsyth, P. C. Hedgecock, R. J. Marquedant, E. J. Smith, D. J. Southwood, and B. T. Tsurutani, The Magnetic-Field Investigation on the Ulysses Mission - Instrumentation and Preliminary Scientific Results, *Astron. Astrophys. Sup.* 92(2), 221-236, 1992.

Balogh, A., C. M. Carr, M. H. Acuña, M. W. Dunlop, T. J. Beek, P. Brown, K. H. Fornacon, E. Georgescu, K. H. Glassmeier, J. Harris, G. Musmann, T. Oddy, and K. Schwingenschuh, The Cluster Magnetic Field Investigation: overview of in-flight performance and initial results, *Ann. Geophys.* 19(10-12), 1207-1217, 2001.

Barry, J. D. and R. C. Snare, A Fluxgate Magnetometer for the Application Technology Satellite, *IEEE Transactions on Nuclear Science NS-13*(6), 326-331, 1966.

Behannon, K. W., M. H. Acuña, L. F. Burlaga, R. P. Lepping, N. F. Ness and F. M. Neubauer, Magnetic Field Experiment for Voyagers 1 and 2, *Space Sci. Rev.* 21, 235-257, 1977.

Belcher, J. W., L. Davis, Jr., and E. J. Smith, Large Amplitude Alfvén Waves in the Interplanetary Medium: Mariner 5, *J. Geophys. Res.* 77, 2302, 1969.

Belcher, J. W., A variation of the Davis-Smith method for in-flight determination of spacecraft magnetic fields, *J. Geophys. Res.* 78, 6480, 1973.

Bennett, J.O., The Cosmic Perspective: The Solar System, *Addison Wesley*, 2004.

Blanc, M., R. Kallenbach, and N. V. Erkaev, Solar system magnetospheres, *Space Sci. Rev.* 116, 227-298, 2005.

Burlaga, L.F., N.F. Ness, M.H. Acuña, R.P. Lepping, J.E.P. Connerney, E.C. Stone, and F.B. McDonald, Crossing the termination shock into the heliosheath, magnetic fields. *Science* 309, 2027–2029, 2005.

Burlaga, L.F., N.F. Ness, M.H. Acuña, R.P. Lepping, J.E.P. Connerney, and J.D. Richardson, Observations of magnetic fields at the termination shock by Voyager 2. *Nature* 454, 75–77, 2008.

Cahill, L. J., Magnetic Field Measurements in Space, *Space Sci. Rev.* 1(3), 399-414, 1963.

Cain, J. C., J. D. Stolarik, J. P. Heppner, I. R. Shapiro, Vanguard 3 Magnetic-Field Observations, *J. Geophys. Res.* 67(13), 5055, 1962

Chandrasekhar, S., K. Watson, and A. Kaufman, The Stability of the Pinch, *Proceedings of the Royal Society of London. Series A, Mathematical and Physical Sciences* 245(1243), 435-455, 1958.

Coleman, Jr., P. J., Davis, Jr., L., and Sonett, C. P., Steady Component of the Interplanetary Magnetic Field: Pioneer V, *Phys. Rev. Lett.* 5, 43-46, 1960.

Coleman, P. J., Variations in the Interplanetary Field: Mariner 2, 1. Observed Properties, *J. Geophys. Res.* 71, 5509-5531, 1966.

Connor, B., Space Magnetics - Mariner 5 Magnetometer Experiment, *IEEE T. Magn. MAG4*(3), 391-., 1968.

Cornilleau-Wehrlin, N., P. Chauveau, S. Louis, A. Meyer, J. M. Nappa, S. Perraut, L. Rezeau, P. Robert, A. Roux, C. DeVilledary, Y. DeConchy, L. Friel, C. C. Harvey, D. Hubert, C. Lacombe, R. Manning, F. Wouters, F. Lefevre, M. Parrot, J. L. Pincon, B. Poirier, W. Kofman, and P. Louarn, The Cluster spatio-temporal analysis of field fluctuations (STAFF) experiment, *Space Sci. Rev.* 79(1-2), 107-136, 1997.

Cummings, W. D., R. J. O'Sullivan, and P. J. Coleman, Standing Alfvén Waves in the Magnetosphere, *J. Geophys. Res.* 74 (3): 778-, 1969.

Davis, L., Jr., and E. J. Smith, 1968, The In-Flight Determination of Spacecraft Magnetic Field Zeros, *EOS Trans., AGU* 49, 257, 1968.

Delva, M., H. Feldhofer, K. Schwingenschuh, and K. Mehlem, A new multiple sensor magnetic compatibility technique for magnetic field measurements in space, *EMC Europe 2002. International Symposium on Electromagnetic Compatibility*, 523-, 2002.

Dolginov, Sh. Sh., L. N. Zhuzgov, and V. A. Selyutin, Magnetometers in the Third Soviet Earth Satellite, *Iskusstvennyye Sputniki Zemli* 4, 135-160 (*Artificial Earth Satellites*, 358-396), 1960.

Dolginov, Sh. Sh., L. N. Zhuzgov, N. V. Pushkov, L. O. Tyurmina, and I. V. Fryazinov, Some Results of Measuring the Constant Magnetic Field of the Earth with the Third Artificial Sputnik of the Earth Above the Territory of the U.S.S.R., *Geomagn. Aeron+* 1061-1075, 877-889, 1962.

Dougherty, M. K., S. Kellock, , D. J. Southwood, A. Balogh, E. J. Smith, B. T. Tsurutani, B. Gerlach, K. H. Glassmeier, F. Gleim, C. T. Russell, G. Erdős, E. M. Neubauer, S. W. H. Cowley, The Cassini magnetic field investigation, *Space Sci. Rev.* 114(1-4), 331-383, 2004.

Dungey, J. W., Interplanetary Magnetic Field and the Auroral Zones, *Phys. Rev. Lett.* 6, 47-49, 1961.

Dungey, J.W., The structure of the exosphere, or adventures in velocity space. In: DeWitt, C., J. Hiebert, and A. Lebeau, Editors, 1963. *Geophysics., the Earth's Environment, Gordon Breach, New York*, 505–550, 1963.

Duret, D., J. Bonzom, M. Brochier, M. Frances, J. M. Leger, R. Odru, C. Salvi, T. Thomas, and A. Perret, Overhauser Magnetometer for the Danish Oersted Satellite, *IEEE T. Magn.* 31(6), 3197-3199, 1995.

Efron, B., The Jackknife, the Bootstrap, and other Resampling Plans, (*Philadelphia: S.I.A.M.*), 1982.

Farrell, W. M., R. F. Thompson, R. P. Lepping, and J. B. Byrnes, A Method of Calibrating Magnetometers on a Spinning Spacecraft, *IEEE T. Magn.* 31, 996, 1995.

Fazakerley, A., and D. Southwood, Mirror Instability in the Magnetosheath, *Adv. Space Res.* 14(7), 65-68, 1994.

Frandsen, A. M. A., B. V. Connor, J. Van Amersfoort, E. J. Smith, ISEE-C Vector Helium Magnetometer, *IEEE T. Geosci. Remote.* 16(3), 195-198, 1978.

Georgescu, E., G. Paschmann, H. Vaith, J. Quinn, P. Puhl-Quinn, M. Chutter and R. Torbert, Archiving of the Cluster EDI Data, in *Proceedings of the Cluster and Double Star Symposium 5th Anniversary of Cluster in Space*, ESTEC, Noordwijk, 2005.

Georgescu, E., F. Plaschke, U. Auster, K.-H. Fornaçon, and H. U. Frey, Modelling of spacecraft spin period during eclipse, *Ann. Geophys.* 29, 875-882, doi:10.5194/angeo-29-875-2011, 2011.

Gloag, J. M., C. Carr, B. Forte, and E. A. Lucek, The status of Cluster FGM data submissions to the CAA, in *Proceedings of the Cluster and Double Star Symposium 5th Anniversary of Cluster in Space*, ESTEC, Noordwijk, 2005.

Hapgood, M.A., Space physics coordinate transformations: the role of precession, *Ann. Geophys.* 13, 713-716, 1995.

Hasegawa, A., Drift Mirror Instability in Magnetosphere, *Physics of Fluids* 12(12P1), 2642-, 1969.

Hedgecock, P. C., A Correlation Technique for Magnetometer Zero Level Determination, *Space Sci. Instrum.* 1, 83-90, 1975.

Heppner, J. P., N. F. Ness, C. S. Scearce and T. L. Skillman, Explorer 10 Magnetic Field Measurements, *J. Geophys. Res.* 68, 46, 1963.

Hinkal, S., Magnetic field satellite (MAGSAT) spacecraft vector magnetometer calibration, *Proceedings of the Society of Photo-optical Instrumentation Engineers* 251, 190-6, 1980.

Hurwitz, L, and J. Nelson, Proton Vector Magnetometer, *J. Geophys. Res.* 65(6), 1759-1765, 1960.

Irwin, W. P., Horner, A. and K. J. Lohmann, Magnetic field distortions produced by protective cages around sea turtle nests: unintended consequences for orientation and navigation?, *Biol. Conserv.* 118, 117-120, 2004.

Kallenrode, M.-B., Current views on impulsive and gradual solar energetic particle events, *J. Phys. G Nucl. Partic.* 29, 965-981, 2003.

Kepko, E. L., K. K. Khurana, and M. G. Kivelson, Accurate determination of magnetic field gradients from four point vector measurements: 1. Use of natural constraints on vector data obtained from a single spinning spacecraft, *IEEE T. Magn.* 32, 377, 1996.

Khurana, K. K., E. L. Kepko, M. G. Kivelson, and R. C. Elphic, Accurate determination of magnetic field gradients from four point vector measurements: 2. Use of natural constraints on vector data obtained from four spinning spacecraft, *IEEE T. Magn.* 32, 5193, 1996.

Kirschvink, J.L. Magnetoreception: Homing in on Vertebrates. *Nature* 390 (6658): 339-340, 1997.

Kivelson, M. G., K. K. Khurana, J. D. Means, C. T. Russell, and R. C. Snare, The Galileo Magnetic Field Investigation, *Space Sci. Rev.* 60, 357-383, 1992.

Kivelson, M. G., Russell, C. T. (Eds.), *Introduction to Space Physics*, Cambridge University Press, Cambridge, 1995.

Kivelson, M. G., Planetary Magnetospheres. In: Y. Kamide/A. Chian, *Handbook of the Solar-Terrestrial Environment*, 469-492, doi: 10.1007/11367758_19 © Springer-Verlag Berlin Heidelberg, 2007

Kristjansson, J. E., Kristiansen J., and E. Kaas, Solar activity, cosmic rays, clouds and climate - an update, *Adv. Space Res.* 34, 407-415, 2004.

Kügler, H., Lessons Learned during the Magnetic Cleanliness Programmes of the Cluster Projects, *Fourth International Symposium Environmental Testing for Space Programmes*, Meeting held June 12-14, 2001, at the Palais de Congrès, Liège, Belgium. Edited by Brigitte Schürmann, European Space Agency, ESA SP-467, ISBN: 92-9092-7097, 69, 2001.

Kuhnke, F., M. Menvielle, G. Musmann, J. F. Karczewski, H. Kugler, C. Cavoit, and P. Schibler, The OPTIMISM/MAG Mars-96 experiment: magnetic measurements onboard landers and related magnetic cleanliness program, *Planet. Space Sci.* 46(6-7), 749-767, 1998.

Langel, R., G. Ousley, J. Berbert, J. Murphy, and M. Settle, The MAGSAT Mission, *Geophys. Res. Lett.* 9(4), 243-245, 1982.

Lanzerotti, L., D. Thomson, and C. MacLennan, Wireless at high altitudes - Environmental effects on space-based assets. *Bell Labs Tech. J.* 2(3), 5-19, 1997.

Leinweber, H. K., C. T. Russell, K. Torkar, T. L. Zhang, and V. Angelopoulos, An advanced approach to finding magnetometer zero levels in the interplanetary magnetic field, *Meas. Sci. Technol.* 19(5), 2008.

Lohmann, K. J., N. D. Pentcheff, G. A. Nevitt, G. D. Stetten, R. K. Zimmerfaust, H. E. Jarrard, and L. C. Boles, Magnetic orientation of spiny lobsters in the ocean: Experiments with undersea coil systems, *J. Exp. Biol.* 198, 2041-2048, 1995.

Lohr, D. A., L. J. Zanetti, B. J. Anderson, T. A. Potemra, J. R. Hayes, R. E. Gold, R. M. Henshaw, F. F. Mobley, and D. B. Holland, NEAR magnetic field investigation, instrumentation, spacecraft magnetics and data access. *Space Sci. Rev.* 82(1-2), 255-281, 1997.

Ludlam, M., V. Angelopoulos, E. Taylor, R. C. Snare, J. D. Means, Y. S. Ge, P. Narvaez, H. U. Auster, O. Le Contel, D. Larson, and T. Moreau, The THEMIS Magnetic Cleanliness Program. *Space Sci. Rev.* 141(1-4), 171-184, 2008.

Manoj, C., A. Kuvshinov, S. Maus, and H. Luhr, Ocean circulation generated magnetic signals, *Earth Planets Space* 58, 429–437, 2006.

Maus, S., S. Macmillan, F. Lowes, and T. Bondar, Evaluation of candidate geomagnetic field models for the 10th generation of IGRF, *Earth Planets Space* 57, 1173–1181, 2005.

Mehlem, K., Multiple Magnetic Dipole Modeling and Field Prediction of Satellites, *IEEE T. Magn.* 14(5), 1064-1071, 1978.

Melzner, F., D. Antrack, and G. Metzner, The GEOS electron beam experiment S 329, *Space Sci. Instrum.* 4(1), 45-55, 1978.

Merayo, J. M. G., P. Brauer, F. Primdahl, J. R. Petersen, and O. V. Nielsen, Scalar calibration of vector magnetometers, *Meas. Sci. Technol.* 11(2), 120-132 2000.

Narvaez, P., The magnetostatic cleanliness program for the Cassini spacecraft, *Space Sci. Rev.* 114, 385, 2004.

Ness, N. F., C. S. Scearce, and J. B. Seek, Initial results of the IMP-1 magnetic field experiment, *J. Geophys. Res.* 69, 3531, 1964.

Ness, N. F., C. S. Scearce and S. Cantarano, Preliminary Results from the Pioneer 6 Magnetic Fields Experiment, *J. Geophys. Res.* 71, 3305-3313, 1966.

Ness, N. F., K. W. Behannon, S. C. Cantaran, and C. S. Scearce, Observations of Earths Magnetic Tail and Neutral Sheet at 510,000 Kilometers by Explorer 33, *J. Geophys. Res.* 72(3), 927-, 1967.

Ness, N. F., Magnetometers for Space Research, *Space Sci. Rev.* 11, 111-222, 1970.

Ness, N. F., K. W. Behannon, R. P. Lepping and K. H. Schatten, Use of two Magnetometers for Magnetic Field Measurements on a Spacecraft, *J. Geophys. Res.* 76, 3565-3573, 1971.

Ness, N. F. and L. F. Burlaga, Spacecraft studies of the interplanetary magnetic field, *J. Geophys. Res.* 106, 15803, 2001.

Neubauer, F. M., Optimization of Multimagnetometer Systems on a Spacecraft, *J. Geophys. Res.* 80, 3235-3240, 1975.

Olsen, N., L. Toffner-Clausen, T. J. Sabaka, P. Brauer, J. M. G. Merayo, J. L. Jorgensen, J. M. Leger, O. V. Nielsen, F. Primdahl, and T. Risbo, Calibration of the Ørsted vector magnetometer, *Earth Planets Space* 55(1), 11-18, 2003.

Parker, E.N., Cosmical Magnetic Fields: Their Origin and Their Activity, *Oxford University Press*, New York, 841, 1979.

Parks, G. K., Physics of Space Plasmas, *Addison-Wesley*, CA, 1991.

Paschmann, G., F. Melzner, G. Haerendel, O. H. Bauer, W. Baumjohann, M. Boehm, M. Nakamura, N. Sckopke, R. Treumann, C. E. McIlwain, W. Fillius, E. C. Whipple, R. B. Torbert, J. M. Quinn, V. Formisano, E. Amata, A. Pedersen, K. Tsuruda, and H. Hayakawa, The electron drift instrument, *Cluster Mission. Scientific and Technical Aspects of the Instruments* 55-, 1988.

Paschmann, G., F. Melzner, R. Frenzel, H. Vaith, P. Parigger, U. Pagel, O. H. Bauer, G. Haerendel, W. Baumjohann, N. Scopke, R. B. Torbert, B. Briggs, J. Chan, K. Lynch, K. Morey, J. M. Quinn, D. Simpson, C. Young, C. E. McIlwain, W. Fillius, S. S. Kerr, R. Mahieu and E. C. Whipple, The Electron Drift Instrument for Cluster, *Space Sci. Rev.* 79 (1-2), 233-269, 1997.

Paschmann, G., N. Sckopke, H. Vaith, J. M. Quinn, O. H. Bauer, W. Baumjohann, W. Fillius, G. Haerendel, S. S. Kerr, C. A. Kletzing, K. Lynch, C. E. McIlwain, R. B. Torbert, and E. C. Whipple, EDI electron time-of-flight measurements on Equator-S, *Ann. Geophys.* 17, 1513-1520, 1999.

Pollinger, A., R. Lammegger, W. Magnes, M. Ellmeier, W. Baumjohann, L. Windholz, Control Loops for a Coupled Dark State Magnetometer, *2010 Ninth IEEE Sensors Conference (SENSORS 2010)*, 779-784, 2010.

Pope, S. A., T. L. Zhang, M. A. Balikhin, M. Delva, L. Hvizzdos, K. Kudela, and A. P. Dimmock, Exploring planetary magnetic environments using magnetically unclean spacecraft: A systems approach to VEX MAG data analysis, *Ann. Geophys.* 29, 639-647, doi:10.5194/angeo-29-639-2011, 2011.

Risbo, T., P. Brauer, J. M. G. Merayo, O. V. Nielsen, J. R. Petersen, F. Primdahl, I. Richter, Orsted pre-flight magnetometer calibration mission. *Meas. Sci. Technol.* 14(5), 674-688, 2003.

Roederer, J. G., Are magnetic storms hazardous to your health? *EOS Trans., AGU* 76, 441–445, 1995.

Rosenberg, R. L., Automatic Calculation of Zero Levels for Interplanetary Spacecraft Magnetometers by the Davis Method, *Publ. No. 903, Inst. of Geophysics & Planetary Physics*, UCLA, 1971.

Roux, A., O. Le Contel, C. Coillot, A. Bouabdellah, B. de la Porte D., Alison, S. Ruocco, and M. C. Vassal, The Search Coil Magnetometer for THEMIS. *Space Sci. Rev.* 141(1-4), 265-275, 2008.

Russell, C. T., The ISEE1 and ISEE2 Fluxgate Magnetometer, *IEEE T. Geosci. Elect. GE-16*, 239-242, 1978.

Russell, C. T., R. C. Snare, J. D. Means, and R. C. Elphic, Pioneer Venus Orbiter fluxgate magnetometer, *IEEE T. Geosci., Remote GE-18*(1), 32-36, 1980.

Russell, C. T., R. C. Snare, J. D. Means, D. Pierce, D. Dearborn, M. Larson, G. Barr, and G. Le, The GGS/Polar Magnetic Fields Investigation, *Space Sci. Rev.* 71(1-4), 563-582, 1995.

Russell, C. T., The solar wind interaction with the Earth's magnetosphere: a tutorial, *IEEE T. Plasma Sci.* 28(6), 1818 – 1830, 2000.

Russell, C. T., Solar wind and interplanetary magnetic field: A tutorial, in *Space Weather, Geophys. Monog. Series 125*, edited by P. Song, H. J. Singer, and G. L. Siscoe, 73–89, doi:10.1029/GM125p0073, AGU, Washington, D. C., 2001.

Russell, C. T., The coupling of the solar wind to the Earth's magnetosphere, chapter in, *Space Weather - Physics and Effects*, editors: Bothmer V., and I. A. Daglis., Springer Berlin Heidelberg, 2007.

Scheffel, A., M. Gruska, D. Faivre, A. Linaroudis, J. M. Plitzko, D. Schüler, An acidic protein aligns magnetosomes along a filamentous structure in magnetotactic bacteria, *Nature* 440(7080):110-4, 2006.

Scherer, K., H. Fichtner, T. Borrmann, J. Beer, L. Desorgher, E. Flückiger, H.-J. Fahr, S. E. S. Ferreira, U. Langner, M. S. Potgieter, B. Heber, J. Masarik, N. Shaviv, and J. Veizer, Erratum: Interstellar-terrestrial relations: the variable cosmic environments, the dynamic heliosphere, and their imprints on terrestrial archives, *Space Sci. Rev.* 127(1-4), 467, 2006.

Shapiro, I. R., J. D. Stalarik and J. P. Heppner, The Vector Field Proton Magnetometer for IGY Satellite Ground Stations, *J. Geophys. Res.* 65, 913-920, 1960.

Slavin, J., Mercury's magnetosphere, *Adv. Space Res.* 33, 1859, 2004.

Smith, E. J., The global heliospheric magnetic field, book chapter in, The Heliosphere through the Solar Activity Cycle, Balogh A., Lanzerotti L. J., and Suess S. T., editors, *Springer Berlin Heidelberg*, ISBN 978-3-540-74302-6 (online), 2007.

Snare, R. C., A History of Vector Magnetometry in Space, *Geophys. Monog. Series 103*, 101, 1998.

Sonnerup, B. U. Ö., and L. J. Cahill, Magnetopause Structure and Attitude from Explorer 12 Observations, *J. Geophys. Res.* 72, 171, 1967.

Sonett, C., Sims, A., and Abrams, I., Distant Geomagnetic Field .1. in Finitesimal Hydromagnetic Waves, *J. Geophys. Res.* 67(4), 1191-, 1962.

Southwood, D., E. Smith, and A. Balogh, Dual technique magnetometer experiment for the Cassini Orbiter spacecraft, *J. Brit. Inter. Soc.* 45(9), 371-4, 1992.

Temuriantz, N. A., V. S. Martinyuk, N. G. Ptitsyna, G. Villoresi, N. Iucci, Yu. Kopytenko, M. I. Tyasto, L. I. Dorman, Complex-spectrum magnetic environment enhances and/or modifies bioeffects of hypokinetic stress condition: An animal study, *Adv. Space Res.* 40(11), 1758-1763, 2007.

Treumann, R. A., Nakamura, R., and Baumjohann, W., Collisionless reconnection: mechanism of self-ignition in thin plane homogeneous current sheets, *Ann. Geophys.* 28, 1935–1943, 2010.

Tsurutani, B. T., E. J. Smith, R. R. Anderson, K. W. Ogilvie, J. D. Scudder, D. N. Baker, and S. J. Bame, Lion Roars and Nonoscillatory Drift Mirror Waves in the Magnetosheath, *J. Geophys. Res.* 87(NA8), 6060-6072, 1982.

Tsurutani, B. T., and C. M. Ho, A review of discontinuities and Alfvén waves in interplanetary space: Ulysses results, *Rev. Geophys.* 37(4): 517-541, 1999.

Tsurutani, B. T., Solar/Interplanetary Plasma Phenomena Causing Geomagnetic Activity at Earth, in *Proceedings of the International School of Physics "Enrico Fermi,"* edited by B. Coppi, A. Ferrari, and E. Sindoni, IOS Press, Amsterdam, 2000.

Tsyganenko, N., A model of the near magnetosphere with a dawn-dusk asymmetry - 1. Mathematical structure, *J. Geophys. Res.* 107(a8), 1179-, 2002.

Tsyganenko, N., A model of the near magnetosphere with a dawn-dusk asymmetry - 2. Parameterization and fitting to observations, *J. Geophys. Res.* 107(a8), 1176-, 2002.

Van Allen, J. A., The Geomagnetically Trapped Corpuscular Radiation, *J. Geophys. Res.* 64(11), 1683–1689, 1959.

Vanselow, K.H. and K. Ricklefs, Are solar activity and sperm whale Physeter macrocephalus strandings around the North Sea related?, *J. Sea Res.* 53, 319–327, 2005.

Walker, M. M., C. E. Diebel, C. V. Haugh, P. M. Pankhurst, J. C. Montgomery and C.R. Green, Structure and function of the vertebrate magnetic sense. *Nature* 390, 371–376, 1997.

Wei, Z.-G. and W.-Y. Xu, Drift and intensity variations of the geomagnetic field, *Chinese J. Geophys.* 44(4), 496–505, 2001.

Winterhalter, D., Acuña, M., and Zakharov, A. (editors), Mars' Magnetism and its Interaction with the Solar Wind, *Space Sci. Rev.* 111, Kluwer Academic Publishers, Dordrecht, NL, 2004.

Yu, Z. J., H. K. Leinweber, and C. T. Russell, Galileo constraints on the secular variation of the Jovian magnetic field, *J. Geophys. Res.* 115, E03002, doi:10.1029/2009JE003492, 2010.

Zhang, T. L., M. Delva, W. Baumjohann, M. Volwerk, C. T. Russell, S. Barabash, M. Balikhin, S. Pope, K. -H. Glassmeier, K. Kudela, C. Wang, Z. Voeroes, and W. Zambelli, Initial Venus Express magnetic field observations of the Venus bow shock location at solar minimum, *Planet. Space Sci.* 56(6), 785-789, 2008.

Zhang, T. L., M. Delva, W. Baumjohann, M. Volwerk, C. T. Russell, H. Y. Wei, C. Wang, M. Balikhin, S. Barabash, H.-U. Auster, and K. Kudela, Induced magnetosphere and its outer boundary at Venus, *J. Geophys. Res.* 114(E09), 2009.